



POLITECNICO
MILANO 1863

SCUOLA DI INGEGNERIA INDUSTRIALE
E DELL'INFORMAZIONE

Image-based finite element modelling of tricuspid valve biomechanics

TESI DI LAUREA MAGISTRALE IN
BIOMEDICAL ENGINEERING
INGEGNERIA BIOMEDICA

Author: **Simona Vailetta**

Student ID: 975218

Advisor: Prof. Emiliano Votta

Co-advisor: Davide Tondi

Academic Year: 2022-23

Abstract

Tricuspid regurgitation (TR) affects approximately 1.6 million people in the USA, develops secondary to right heart disease in 90% of cases, and is associated with an increased risk of mortality. There are few studies in the literature that have investigated the biomechanics of the tricuspid valve (TV), and the interest of the scientific community has only recently increased.

The herein thesis is focused on a finite element analysis (FEA) methodological study to assess the importance of modelling the CTs of the TV. The numerical model of the valve was reconstructed based on TV echocardiographic images acquired on an ex-vivo porcine heart with TR. The main structures such as annulus, free margin, leaflets, and papillary muscles (PMs) were manually segmented at end-diastole (ED) and systolic peak (SP) frames.

The numerical model comprised four key structures: leaflets at ED, leaflets at SP, PMs, and CTs. The meshes of the leaflets were generated through a multistep process comprising filtering, resampling, and triangulation. The apices of the PMs were reconstructed through tracing and anatomical information, and they served as a point from which CTs branched out. CTs were not visible on echocardiographic images, prompting the exploration of two reconstruction strategies: a parametric model for TV based on existing literature, and an alternative functionally equivalent model previously employed solely for mitral valves, featuring uniformly distributed chordae insertions on the leaflet surface. The leaflets at SP were modelled as a rigid surface, whereas the leaflets at ED were modelled with a hyperelastic constitutive material model. For CTs Weiss and Saint Venant-Kirchhoff constitutive models were investigated.

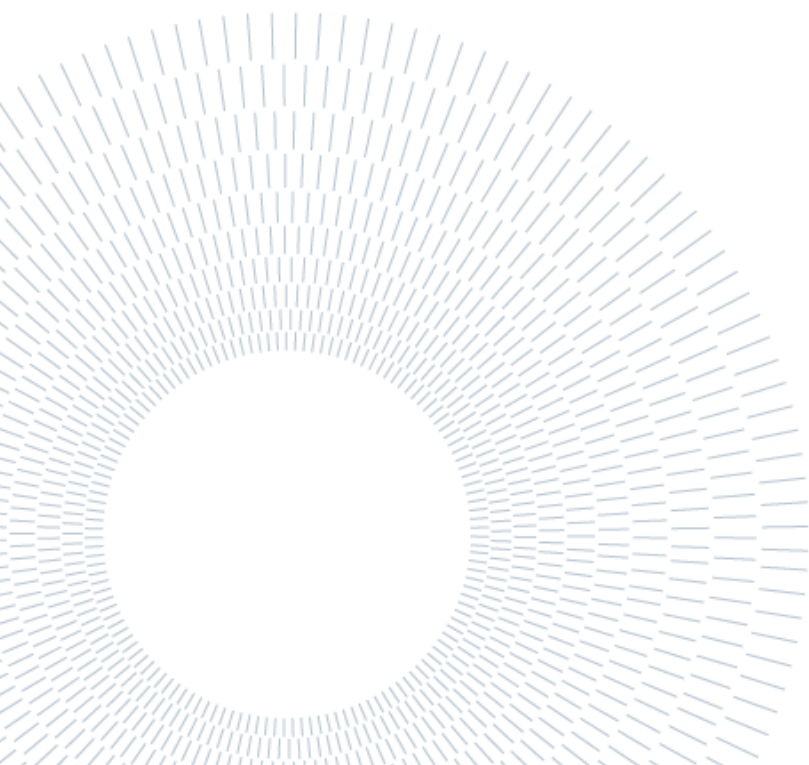
To establish the effectiveness of the parameters evaluated in the reproduction of valvular biomechanics, it is first necessary to calibrate the CTs lengths to ensure the reproduction of the TV PS configuration. For this purpose, a pipeline consisting in a sequence of 3 simulations was implemented: 1) the ED TV configuration was morphed onto the mid-systolic leaflet surface, yielding the new position of CT insertions; 2) simulating the CTs as inextensible, the TV model was pressurized to 30 mmHg, extracting the true force distribution in the chordae to infer their initial length at ED. TV closure was finally simulated from ED to SP, applying a physiologic pressure load.

Moreover, the model resulting from this pipeline was used to validate the effect on TV morphology of free wall approximation (FWA), which involves the mutual approximation of the PMs to correct regurgitation.

Four combinations of CTs modelling were executed to assess the bests simulation strategy. The Weiss material constitutive model demonstrated effectiveness in both capturing the biomechanics of the TV and assessing the impact of surgical procedures. Conversely, the functionally equivalent model showed promise in representing the TV biomechanics, whereas the parametric TV model proved more reliable in assessing the effects of surgical interventions.

Overall, the herein work provides an initial insight in the definition of a complete workflow for modelling a patient-specific pathological TV and lays the basis for the evaluation and validation of a surgical procedure from echocardiographic data.

Key-words: Tricuspid Valve; Tricuspid Regurgitation; Finite Element Analysis; Echocardiography; Patient-Specific Modelling.



Abstract in italiano

Il rigurgito tricuspide (TR) colpisce circa 1,6 milioni di persone negli Stati Uniti, nel 90% dei casi si sviluppa secondariamente a una patologia del cuore destro ed è associato a un aumento del rischio di mortalità. In letteratura esistono pochi studi che hanno analizzato la biomeccanica della valvola tricuspide (TV) e l'interesse della comunità scientifica è aumentato solo recentemente.

Il lavoro di questa tesi si basa su uno studio metodologico di analisi agli elementi finiti (FEA) per valutare l'importanza della modellazione delle chordae tendineae (CTs) della TV. Il modello numerico della valvola è stato ricostruito sulla base di immagini ecocardiografiche della TV acquisite su un cuore porcino ex-vivo con TR. Le strutture principali, come l'annulus, il margine libero, i lembi e i muscoli papillari (PMs), sono state segmentate manualmente in corrispondenza dei frame di fine diastole (ED) e di picco sistole (SP).

Il modello numerico comprende quattro strutture chiave: i lembi a ED, i lembi a SP, PMs e CTs. La mesh dei lembi è stata generata attraverso un processo a più fasi che comprende il filtraggio, il ricampionamento e la triangolazione. Gli apici delle PMs sono stati ricostruiti utilizzando i tracciamenti e le informazioni anatomiche. I PMs sono serviti come punto da cui si diramano le CTs. Le CTs non sono visibili dalle immagini ecocardiografiche, il che ha indotto a esplorare due strategie di ricostruzione: un modello parametrico per la TV basato sulla letteratura esistente e un modello alternativo funzionalmente equivalente, precedentemente utilizzato solo per le valvole mitrali, caratterizzato da inserzioni di corde uniformemente distribuite sulla superficie del lembo. I lembi di SP sono stati modellati come una superficie rigida, mentre i lembi di ED sono stati modellati con un modello costitutivo di materiale iperelastico. Per le CTs sono stati studiati i modelli costitutivi di Weiss e di Saint Venant-Kirchhoff.

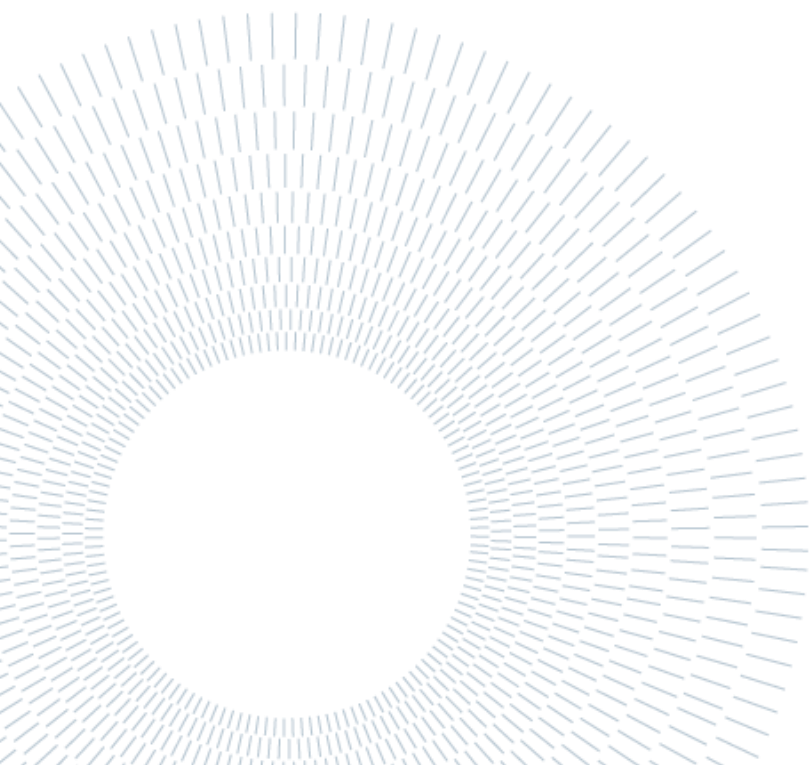
Per stabilire l'efficacia dei parametri valutati nella riproduzione della biomeccanica valvolare, è stato necessario innanzitutto calibrare le lunghezze delle CTs per garantire la riproduzione della configurazione della TV a PS. A tal fine, è stata implementata una pipeline costituita da una sequenza di 3 simulazioni: 1) la configurazione della TV a ED è stata caricata affinché si adagiasse sulla superficie ricostruita a PS, ottenendo la nuova posizione delle inserzioni delle CTs; 2) simulando le CTs come inestensibili, il modello della TV è stato pressurizzato a 30 mmHg, la vera distribuzione della forza nelle CTs è stata estratta per dedurre la loro lunghezza iniziale a ED. La chiusura del TV è stata infine simulata da ED a SP, applicando un carico pressorio fisiologico.

Inoltre, il modello risultante da questa pipeline è stato utilizzato per convalidare l'effetto sulla morfologia TV dell'approssimazione della parete libera (FWA), che comporta l'approssimazione reciproca dei PM per correggere il rigurgito.

Sono state eseguite quattro combinazioni di modellazione CTs per valutare la migliore strategia di simulazione. Il modello costitutivo di Weiss per la descrizione del materiale si è dimostrato efficace sia nel catturare la biomeccanica della TV sia nel valutare l'impatto della procedura chirurgica. Al contrario, il modello funzionalmente equivalente si è dimostrato promettente nel rappresentare la biomeccanica della TV, mentre il modello parametrico della TV si è dimostrato più affidabile nel valutare gli effetti degli interventi chirurgici.

Nel complesso, il presente lavoro fornisce una prima definizione di un flusso di lavoro completo per la modellazione di una TV patologica paziente-specifica e pone le basi per la valutazione e la validazione di una procedura chirurgica a partire dai dati ecocardiografici.

Parole chiave: Valvola tricuspide; Rigurgito tricuspide; Analisi ad Elementi Finiti; Ecocardiografia; Modellazione Paziente-Specifica.



Contents

| | |
|--|-----------|
| Abstract | 3 |
| Abstract in italiano | 5 |
| Contents | 7 |
| Introduction | 10 |
| 1 Clinical background | 12 |
| 1.1. Tricuspid valve | 12 |
| 1.1.1. Annulus | 13 |
| 1.1.2. Leaflets..... | 15 |
| 1.1.3. Papillary Muscles | 18 |
| 1.1.4. Chordae Tendinea..... | 19 |
| 1.2. Pathologies and treatments..... | 23 |
| 1.2.1. Functional Tricuspid Valve Disease..... | 23 |
| 1.2.2. TR treatment | 25 |
| 1.2.3. New approach | 25 |
| 1.3. Mock Circulatory Loops..... | 27 |
| 1.4. Noninvasive cardiovascular imaging techniques | 29 |
| 1.4.1. Echocardiography | 29 |
| 2 State-of-the-art | 31 |
| 2.1. Numerical schemes | 31 |
| 2.2. Geometric models | 33 |
| 2.2.1. Parametric models | 33 |
| 2.2.2. Models based on clinical image segmentations..... | 35 |
| 2.3. Mechanical properties | 37 |
| 2.3.1. Leaflets: biomechanical characterisation | 37 |
| 2.3.2. Leaflets: constitutive models | 41 |
| 2.3.3. CTs: biomechanical characterisation..... | 43 |
| 2.3.4. CTs: constitutive models..... | 45 |
| 2.4. Computational models for TV..... | 49 |
| 3 Methodology | 57 |
| 3.1. Aims and objectives of the thesis..... | 57 |

| | | |
|----------|--|------------|
| 3.2. | Echocardiographic Data | 59 |
| 3.3. | Data preparation workflow | 59 |
| 3.4. | Radial segmentation | 61 |
| 3.4.1. | Radial GUI development | 61 |
| 3.4.2. | Identification and tracing of reference structures | 63 |
| 3.5. | Short-axis segmentation | 67 |
| 3.6. | TV model generation | 68 |
| 3.6.1. | TV open surface, at ED | 68 |
| 3.6.2. | TV close surface, at SP | 78 |
| 3.6.3. | PMs..... | 80 |
| 3.6.4. | CTs..... | 82 |
| 3.7. | Simulation of systolic TV closure: TR case | 87 |
| 3.7.1. | Systolic closure with single step FE..... | 88 |
| 3.7.2. | Systolic closure with CTs calibration | 90 |
| 3.8. | Simulation of systolic TV closure: post-surgery | 98 |
| 4 | Results | 100 |
| 4.1. | Analysis of TV with TR | 102 |
| 4.1.1. | CTs insertion density: sensitivity analysis | 102 |
| 4.1.2. | Engineering mechanics and clinically-relevant geometry metrics | 107 |
| 4.2. | Analysis of TV after FWA AP60 | 119 |
| 4.2.1. | Quality of the images..... | 119 |
| 4.2.2. | Functional equivalent model..... | 123 |
| 4.2.3. | Chung-Hao Lee parametric model..... | 129 |
| 5 | Discussion | 132 |
| 5.1. | Initial data | 132 |
| 5.1.1. | Limitation..... | 132 |
| 5.1.2. | Future developments..... | 133 |
| 5.2. | Manual tracing..... | 133 |
| 5.2.1. | Future developments..... | 133 |
| 5.3. | Reconstruction and Simulations | 134 |
| 5.3.1. | Limitations and future developments | 138 |
| | Bibliography..... | 141 |
| A | Appendix: Additional results | 147 |
| A.1. | TV with TR: clinically relevant analysis plots..... | 147 |
| A.2. | TV with TV: leaflets maximum principal stresses..... | 149 |
| A.3. | TV with TR: leaflets maximum principal strains..... | 151 |

| | | |
|------------------------------|--|------------|
| A.4. | TV-AP60: leaflets maximum principal stresses | 153 |
| A.5. | TV-AP60: leaflets maximum principal strains | 155 |
| List of Figures..... | | 159 |
| List of Tables..... | | 171 |
| List of symbols..... | | 173 |
| List of acronyms..... | | 174 |
| Acknowledgments..... | | 175 |

Introduction

The tricuspid valve (TV) is a complex three-dimensional structure that separates the right atrium (RA) from the right ventricle (RV) ensuring the unidirectional flow of blood. The function of the TV can be affected by various pathologies. In Western society, TV regurgitation (TR) is the most common valvular lesion, affecting an estimated 1.6 million people in the US in a moderate to severe form [1]. In 90% of cases, this condition develops secondary to left heart disease [2], [3]. Recently, studies have shown that secondary TR, if left untreated, leads to an increased risk of mortality [4].

For decades, TV was little studied, and TR was considered a benign condition and was therefore undertreated. Growing recognition of the importance of the condition has led to the development of numerous treatments, mainly minimally invasive [5]. Nevertheless, there are few studies aimed at quantifying the biomechanical characteristics of the TV apparatus [6]–[9].

The aim of this thesis is to implement a reliable reconstruction workflow for the development of a finite element (FE) model of the regurgitant valve that is as accurate as possible with respect to the patient-specific geometry detected by echocardiography. Subsequently, the model will be used to test a valve treatment technique to reduce the TR proposed by Jaworek et al. [10].

Chapter 1: Clinical background.

It will provide the basic information regarding the clinical background necessary to understand the development of the thesis work. The main anatomical structures of the TV will be described: annulus, leaflets, papillary muscles (PMs) and the chordae tendineae (CTs). The diseases specific to the valve, with a focus on the TR, and the currently available clinical treatments. The reconstruction work is based on echocardiographic images acquired on a beating porcine heart on a test bench. The experimental set-up and the main cardiovascular imaging techniques, with a focus on echocardiography, will then be described.

Chapter 2: State-of-the-art

The quantification of valvular biomechanical characteristics is possible through the development of computational models. The main existing numerical schemes, methods for defining valve geometry, material characterisation and constitutive models for leaflets and CTs will be described. At the end of the chapter, the TV FE models developed are described in chronological order.

Chapter 3: Methodology

Detailed description of the strategies, hypotheses and techniques used to obtain an accurate in-silico 3D model of the TV with TR, the generation of the computational

grid or mesh, the description of the tissue properties and the boundary conditions imposed to obtain the most accurate simulations possible. Furthermore, the simulation workflow for analysing and testing parametric and constitutive models of CTs will be explored. At the end of the chapter, the in-silico testing method applied to test a new idea of TV repair surgery with TR will be discussed.

Chapter 4: Results

The main outcomes of systolic TV closure simulations with TR and post-surgery TV are reported. The results were presented using clinically relevant engineering metrics and interesting clinically-evaluation parameters. The results have been structured in such a way that the main variations of the tested parameters are compared.

Chapter 5: Discussion

The discussion chapter will analyse the results, limitations, and possible future developments of three macro-areas on which the thesis work was focused. Firstly, it will analyse the issues and weaknesses found in the echocardiographic data and the in tools that were used to make the data exploitable in the next steps. The second part will deal with the topic of manual tracing of the main structures of the TV, its current limitations, and suggestions for reducing inaccuracies. The last part will discuss the reconstruction and simulation phases, the heart of the thesis.

1 Clinical background

The TV has been historically deemed of lesser significance despite its intricate structure and colloquially referred to as the ‘forgotten or neglected valve’. TV pathologies were interpreted as a response to mitral valve (MV) dysfunction; therefore, it was conventionally believed that addressing the MV dysfunction would inherently restore TV physiological function. Recent studies, however, have indicated that specific TV diseases, including TR, are widespread in the population and independently predict mortality in individuals [1], [4]. This evidence has led to an increased acknowledgement among scientists, prompting recommendations for interventions targeting the TV.

The following sections will comprehensively detail the primary TV structures, elucidate their anatomical and morphological characteristics, provide an in-depth analysis of prevalent pathologies and examine the available state-of-the-art tools to enhance understanding, evaluate devices, and assess TV-related surgical procedures related to the TV.

1.1. Tricuspid valve

The TV is the most apical and largest valve of the four heart valves. Its physiological function consists in guaranteeing the unidirectional blood flow from the RA to the RV during RV filling, while preventing from backflow during RV systole. The large size of the TV orifice, whose area ranges between 7 cm² and 9 cm² during the cardiac cycle [11] is consistent with the low pressure levels characterizing the right heart: it allows for a minimal trans-valvular pressure drop, by less than 2 mmHg [11], during RV diastolic filling, and for low trans-valvular velocities, with peak values below 1 m/s [11].

The main structures of the TV are the annulus, the three leaflets (septal (TVSL), anterior (TVAL) and posterior (TVPL)), the CTs and the PMs ([Figure 1.1](#)) [11]

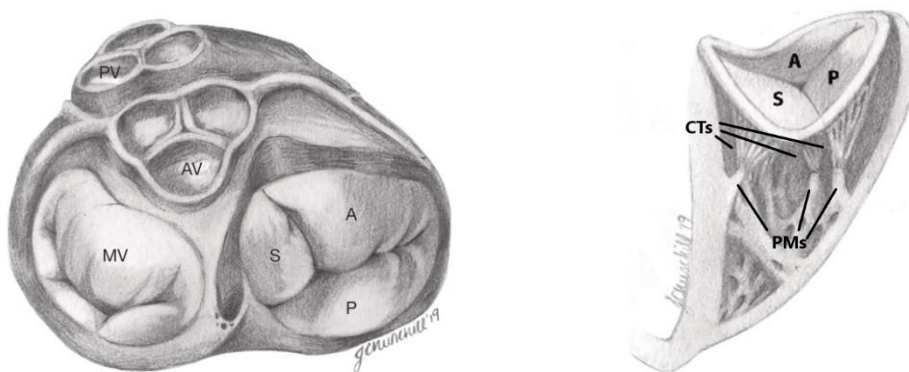


Figure 1.1: Left: representation of the valvular plane and all four valves of the heart: the TV is at the bottom right of the sketch; the three leaflets of the TV are indicated: P=posterior leaflet, A=anterior leaflet, S=septal leaflet; MV=mitral valve; PV= pulmonary valve; AV= aortic valve. Right: cross-section of the right ventricle, where the TV is visible. The three leaflets of the TV are highlighted again, the PMs and the chordae that connect the TV to the ventricular wall are also represented. Image adapted from Evin Yucel et al. [2]

1.1.1. Annulus

For any heart valve, the annulus is a ring-shaped fibrous structure that connects the valve to the walls of the heart. This structure is not clearly defined and can be difficult to identify during surgical or anatomical inspection. The annulus of a healthy TV looks D-shaped when observed from the RA, shows a non-planar profile when observed in 3D and it is asymmetrical. The D-shape can be further divided into two parts: the rounded C-shaped part that is associated with the free wall of the RA and RV, and a shorter, roughly straight segment that is located near the atrio-ventricular septum. [11]

3D-echocardiographic data indicate that, under physiological conditions, the non-planar shape of the valve is consistent between individuals: two points of maximum, i.e., most distant from the RV apex, are located adjacent to the AV in postero-lateral and antero-septal position, respectively; two points of minimum, i.e., closest to the RV apex, are located in poster-septal and antero-lateral position, respectively ([Figure 1.2](#)). [12]

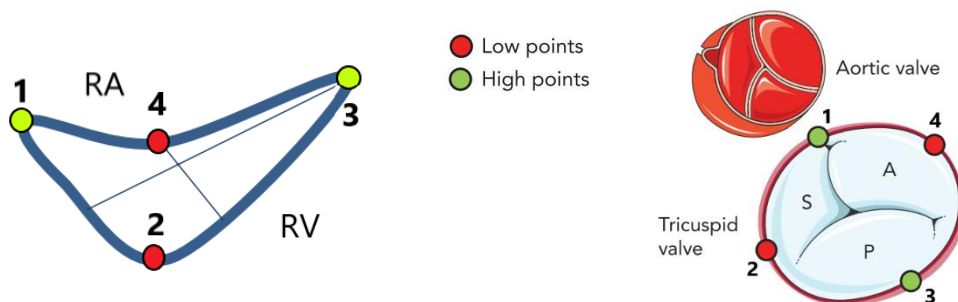


Figure 1.2: Left: non-planar shape of the physiological tricuspid valve: the highest and lowest points of the annular profile with respect to RA and RV, are highlighted; Right: positions of points in the TV annulus line with respect to AV. Image adapted from Besler et al. [12]

The microscopic structure of the annulus reveals the presence of intertwined muscle bands between 2 and 4 mm in diameter, which are hypothesised to provide support for the valve. Histological analyses have shown that muscle bands are connected through fibrous tissue and collagen. The fibrous tissue of the annulus is clearly identifiable along the free wall of the RV, while on the septal side the leaflet tissue connects with the interventricular tissue without any evident transition zones. [11], [13]

The TV annulus is a very dynamic structure, undergoing significant changes in shape and area during the cardiac cycle. From systole to diastole, the C-shaped zone, which is associated with the free wall dilates, while the straight zone is more stable due to the presence of the fibrous trigons, i.e., two highly collagenous regions where the

annulus is anchored to the valvular plane ([Figure 1.3](#)). Owing to this change in configuration, the annular area can increase by 30% from systole to diastole. Of note, excessive dilatation is limited by the presence of the heart's fibrous skeleton. [11]

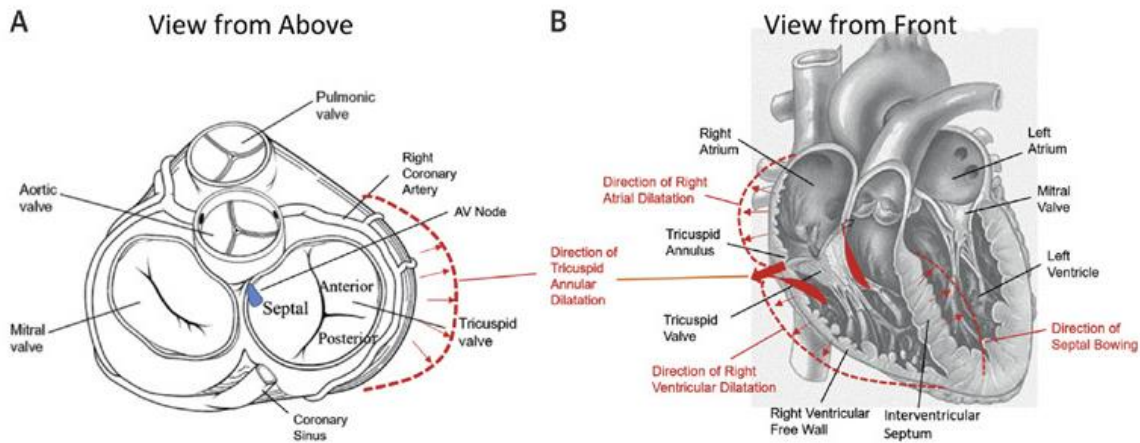


Figure 1.3: (A) Valve plan: identification of the TV with the leaflets. The dotted lines point out the direction of expansion during the cardiac cycle; (B) Frontal view of the heart: the dotted lines show the direction of expansion of the right heart structures. Image taken from Dahou et al. [11]

Over time, several studies have analyzed the geometric features of the annulus.

In 1971, Silver et al. analysed ex-vivo TV in a total of 50 hearts exported from human patients. In half of the samples, they made a cut with the knife from the RA to the apex of the RV to extract the TV. In the other samples, the valve was opened medially. The heart was then fixed in 10% formalin brine and the RV was flattened between two heavy glass plates. At this point it was possible to extract some anatomical data, including the length of the annulus circumference. It had a value of 11.4 ± 1.1 cm (mean value \pm standard deviation) in men ($n=27$) men and of 10.8 ± 1.3 cm in women ($n=23$). [13]

A more recent study by Francesco Maffessanti et al. provided a complete morphological and functional description of the annulus based on cardiac magnetic resonance imaging (MRI) [14]; The study was conducted on 13 healthy subjects and 9 patients. The results obtained on the healthy controls are reported in [Table 1.1](#). The article does not explain how the systolic and diastolic moments were chosen. Analyses conducted on the 3D and projected area of the TV show a significant increase in area from the systolic to the diastolic moment; this apparently non-logical change is associated with a concomitant elongation of the perimeter of the TV. The two annular diameters shown refer to observations with respect to the short and radial axis of the valve, respectively. The longest diameter did not change significantly from systole to diastole, whereas the shortest diameter elongated quite significantly in diastole. Eccentricity was greater during diastole than during systole. Comparing the eccentricity value of the TV annulus to that of the MV (whose average values are

minimum 0.73, maximum 0.92, systolic 0.82, diastolic 0.85), the TV annulus is more circular. The differences between heights and diameters implied a more planar shape of the annulus in diastole than in systole.

| | Minimum | Maximum | Systolic | Diastolic |
|--|------------------|------------------|------------------|------------------|
| Three-dimensional area (cm²) | 10.3 (8.4–11.0) | 13.0 (10.4–15.0) | 11.2 (8.8–13.2) | 11.9 (9.2–13.5) |
| Projected area (cm²) | 10.0 (7.9–10.6) | 12.7 (10.3–14.1) | 10.6 (7.9–12.0) | 11.3 (8.6–12.7) |
| Perimeter (mm) | 114 (105–124) | 128 (116–142) | 119 (107–128) | 123 (111–131) |
| Shortest diameter (mm) | 32 (29–34) | 38 (35–40) | 33 (31–36) | 36 (33–39) |
| Longest diameter (mm) | 33 (31–33) | 42 (36–47) | 37 (33–41) | 39 (33–43) |
| Eccentricity | 0.85 (0.81–0.91) | 0.97 (0.88–1.00) | 0.91 (0.81–0.97) | 0.93 (0.87–0.99) |
| Height (mm) | 3.7 (2.4–3.8) | 7.2 (6.3–9.2) | 5.6 (4.4–7.1) | 5.0 (4.0–6.0) |
| Planarity index (%) | 9 (6–10) | 20 (17–25) | 16 (11–20) | 12 (11–14) |

Table 1.1: Geometric characteristics of the TV physiological annulus from a study conducted by Maffessanti et al. [14]. The table shows the geometric characteristics expressed as median value (1st–3rd quartile). Data are reported for healthy subjects only.

1.1.2. Leaflets

The name of the TV stems from its tripartite leaflet structure, whose structures are characterized by distinct sizes and are named as septal, anterior, and posterior leaflets. Yet, the TV may not consistently exhibit three leaflets; instances exist, as shown in [Figure 1.4](#), even among healthy individuals, where the leaflet count deviates to either two or exceeds three. For instance, in a study conducted by Lama et al. [15] where 36 formalin-fixed adult human hearts were evaluated, the number of TV leaflets spanned from three to more than seven, and the location of the leaflets differed among subjects. Indeed, the authors stated that TVs with exactly three leaflets are relatively rare, while the presence of accessory leaflets is widespread. This is explained by the fact that the free margins of some leaflets, especially that of the TVPL, are not so regular; if the indentations of the free margin are highly pronounced, the leaflet is considered as split into several parts.

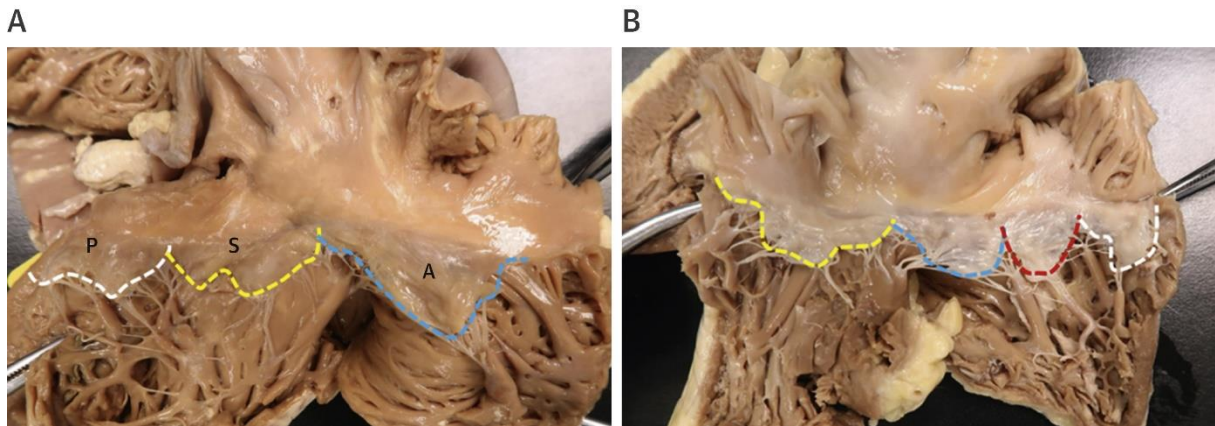


Figure 1.4: The number of leaflets of the TV may vary. (A) The three-leaflet configuration: the white line indicates the TVPL, the yellow line the TVSL and the blue line the TVAL. (B) Case with 4 leaflets. Image taken from Dahou et al. [11]

Despite the reported anatomical variability, from here on the TV anatomy will be described with reference to the three-leaflet TV paradigm.

The leaflets are separated by deep incisions or indentations, called commissures. The free margin of the commissures has usually an arch shape. There are 3 commissures, each one named after the two leaflets it separates ([Figure 1.5](#)):

- The antero-septal commissure is located at the membranous interventricular septum where the anterior and septal walls of the RV join. This corresponds to the most apical point of the valve and can be identified by a deep indentation of the leaflet tissue.
- The antero-posterior commissure is generally identified anatomically by the presence of a particular type of CTs that takes the name of fan-shaped chorda (the main characteristics of these CTs are described in subsection [1.1.4.1. Fan-Shaped Chordae](#)). These CTs fits into a deep indentation of tissue separating the TVAL and TVPL. This commissure is usually the largest of the three.
- The postero-septal commissure is also a deep indentation and has a few more landmarks for its identification: the presence of a fan-shape CTs, the PM positioned medially on the posterior wall, and the presence of a TVSL fold running towards the free margin of the leaflet. [13]

From a macroscopic analysis, the surface of the leaflets can be divided into three zones ([Figure 1.5](#)):

- the rough zone extending from the free margin to the coaptation line, i.e., the line that where the leaflets touch each other when observed from the RA. This zone is absent in the commissures, where the insertions of most of the tendon cords are located.
- the basal zone: it usually extends by a few millimeters from the annulus towards the free margin.

- the clear zone is a thin, translucent zone extending from the coaptation line to the basal zone. [13]

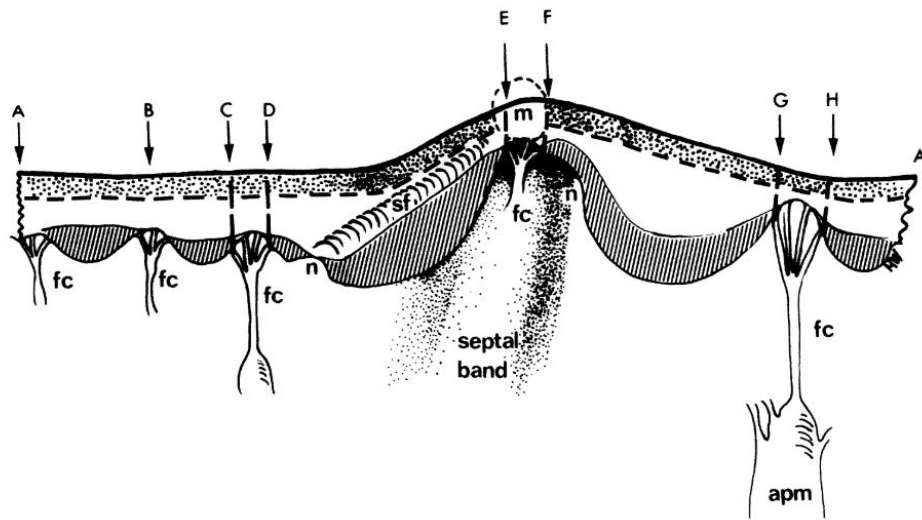


Figure 1.5: Representation of the TV leaflets cut open and distended on a planar surface. E-F = anteroseptal commissure; C-D = postero-septal commissure, where fan-shaped chordae (fc) insert; G-H = anteroseptal commissure at the Anterior Papillary Muscle (APM,) where fan-shaped chordae (fc) insert; H-C = TVPL with its multiple indentations, each one characterized by the insertion of fan-shaped chordae (fc); D-E = TVSL identified by the presence of the fold (sf); F-G = TVAL. In the illustration, the basal zone is stippled, the rough zone is dotted, and the area in between is the zone. Image taken from the Silver et al. [13]

The microscopic analysis of TV leaflet surface shows a particular organisation of the cells that appear to be intertwined and overlapping in a fibrous skeleton. This organization seems to allow cells to follow the movement of the leaflets and of the annulus.[16]

A 2019 study by Kramer et al. [17] on the TVAL of a porcine valve highlighted the predominant components as collagen fibers, GAG, elastin, and proteoglycans. The study further demonstrated that the organizational pattern of these constituents allows the identification of four distinct layers from the ventricular surface to the atrial surface. These layers include the ventricularis, where elastin fibers exhibit a radial arrangement, i.e., are mostly aligned with the annulus-to-free margin direction; the fibrosa, primarily composed of collagen; the spongiosa, characterized by proteoglycans and GAGs; and the atrialis, where elastin fibers are arranged circumferentially, i.e., parallel to the annular profile. Tissue characterization in the study revealed that the atrialis and spongiosa layers exhibit anisotropic properties and greater extensibility as compared to the ventricular and fibrosa layers, which display a more isotropic behavior.

The leaflets do not have a uniform thickness with respect to their longitudinal axis. The thickest zones are the basal zone, because of the orientation of the collagen fibres originating from the annulus, and the rough zone because it is where the greatest

number of CTs penetrate the leaflets. The clear zone that lies between the basal and the rough zone is the thinnest one with the least thickness. There are also variations between TVAL, TVPL and TVSL as shown in [Table 1.2](#) [18]

| | TVAL | TVPL | TVSL |
|---|-----------------|-----------------|-----------------|
| Thickness \pm standard deviation (mm) | 0.69 \pm 0.45 | 0.55 \pm 0.28 | 0.63 \pm 0.23 |

Table 1.2: Average thickness of TVAL, TVPL and TVSL in porcine valves

The TVAL is the one with the greatest radial extension and size and has the highest capacity for displacement. Its shape can be semicircular or quadrangular and its free margin is regular, only in some cases displaying some small indentations. [11], [13]

The TVPL, on the other hand, has the smallest circumferential extent and is characterized by an irregular free margin. Incisions are also reached by fan-shape CTs.

The TVSL has the shortest extent in the radial direction, and it is the least mobile leaflet because it attaches to the tricuspid annulus directly below the interventricular septum. The insertion point of the TVSL on the septum is located approximately 10 mm more apically than the insertion point of the TVAL. [11]

In the thesis work by A. Colombo [19], human TV valves were analyzed and leaflet thickness was measured with a micrometer. In human TV the average value of 0.396 ± 0.086 was obtained, without significant differences among leaflets.

1.1.3. Papillary Muscles

The PMs stem from the wall of the RV; each PM consists of a single or multiple heads, each one with the shape of a truncated cone ([Figure 1.6](#)). The heads of the PMs house the origin of most CTs. PMs and CTs together form the so-called subvalvular apparatus of the TV, which is aimed to prevent excessive leaflet motion towards the RA and hence leaflet prolapse during ventricular systole. PMs are characterized by great inter-subject variability in terms of point of origin, size, conformation, morphology and number of CTs originating from the PM heads [20]. Yet, the most frequent configuration, observed in about 20% of 79 human hearts under physiological conditions, is characterized by three PMs: anterior (APM) and septal (SPM), both with a single head, and posterior (PPM) with two heads [21] Also, the following observations were reported on the three PMs:

- The APM is usually the largest PM and may have one or two heads. In the latter case, the heads are always joined by a muscular bridge. The APM is the origin of the chordae that insert into the TVPL and TVAL. The length of this muscle can range from 5 mm to 41 mm.

- The PPM is characterized by high anatomical variability, as it can have one to four heads. Its length ranges from 2 mm to 30 mm and it is the origin of the chordae that support the TVPL and TVSL.
- The SPM is not always present, as is absent in 20% of subjects. When present, it stems from the septal wall and it is usually the smallest PM, with a length ranging from 2 mm to 14 mm. It can have one to four heads, which give origin to chordae that insert in the TVAL and TVSL. [11], [21]

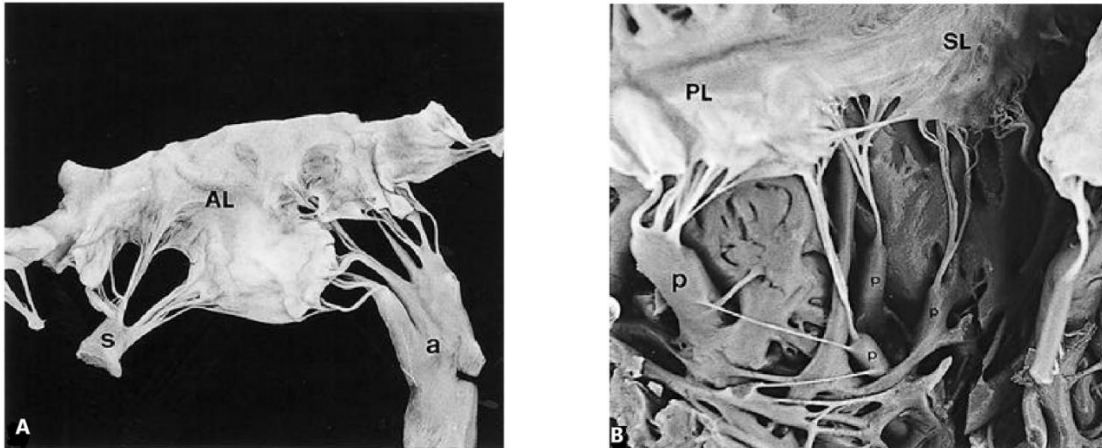


Figure 1.6: (A) Photograph of the APM and SPM. The morphology of the APM is atypical, but the difference in size between the anterior and SPM is clear. (B) Picture of a PPM with four heads. Image taken from the Silver et al. article [13]

In the study by Nigri et al. (2000), in which the morphological characteristics of the tensor apparatus of 79 human hearts under normal conditions were analysed, it was found that the most frequent combination, which corresponds to approximately 20% of the cases analysed, is that with an APM and a SPM both with a single head and a bifid PPM. [21]

Although PMs have a crucial role in valve function, there is great variability with respect to their point of origin, size, conformation, morphology and number of tendon cords to which they give rise. The study conducted by Saha et al. (2018) confirms this, considering these highly patient-specific structures. [20]

1.1.4. Chordae Tendinea

The CTs are filiform elements of different lengths, that are parts of the subvalvular apparatus. Most chordae connect the TV leaflets to the PMs, although some CTs may link the leaflets directly to the RV wall or to the septomarginal trabecula. On both cases, these CTs are classified as true chordae, as opposed to the so-called false chordae that link two PMs, or a PM to the RV wall or two points of the RV wall.

CTs have a fibrous structure, characterized by an 80% collagen content, the remaining 20% being associated to elastin and endothelial cells [11], [13]. This structure provides CTs with a non-linear elastic and stiff mechanical response. Therefore, the length of each CT undergoes small changes over the cardiac cycle, and any pathology that

causes RV dilation and outwards dislocation of the lateral or septal RV wall typically induces the hyper affect the coaptation of the valve leaflets.

Literature studies report that the average number of CTs is 25, but this amount can vary from 17 to 36. Furthermore, the CTs of the tricuspid valve are characterized by a large number of branches. [11] CTs are classified based on the placement position of their insertion on the leaflets and on the number of branches; there are five CT types: fan-shaped chordae, rough zone, free edge, deep, and basal. Of note, free edge and deep CTs are found only in the tricuspid valve.

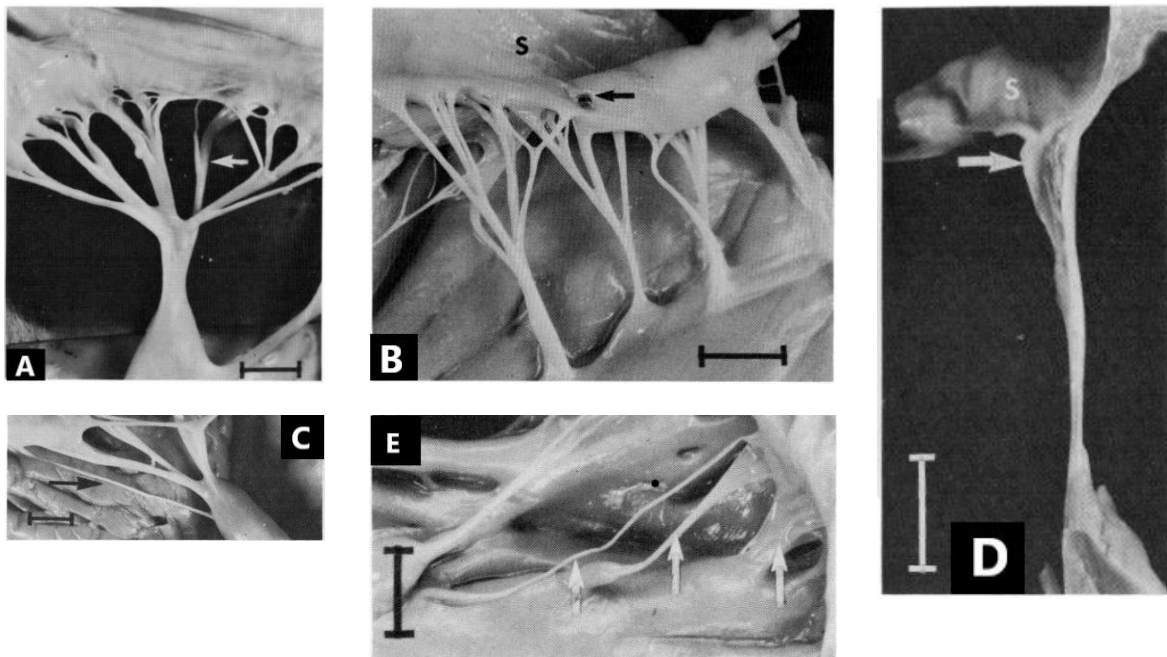


Figure 1.7: (A) Fan-shaped chordae (the arrow indicates the sub-branches of this chord just before insertion into the leaflet); (B) rough zone chordae (the arrow indicates the rough zone); (C) free-edge chordae (the arrow indicate the only free-edge chordae with its thin structure); (D) deep chordae (the arrow indicated the triangular fold); (E) basal chordae (the arrow indicated this type of CTs). Image adapted from the Silver et al. article [13]

1.1.4.1. Fan-shaped Chordae

Fan-shaped CTs are inserted into the free margin of the commissural zones, or of the indentations of the TVPL, and are used to identify the separation between the TVAL and TVPL. These CTs have a main stem that branches radially, the insertion is generally at the level of the free margin, but in some cases, they can run deep and insert into the adjacent rough area ([Figure 1.7 – A](#)). [13]

1.1.4.2. Rough Zone Chordae

Rough zone CTs insert in the rough area of the leaflets, on the ventricular side. Each of these CTs branches into three sub-branches just after the origin: the first one inserts

at the upper edge of the rough area, the third one inserts on the free edge of the leaflet, although it tends to branch further similarly to fan-shaped CTs, and the second one inserts in an intermediate location ([Figure 1.7 - B](#)). [13]

1.1.4.3. Free-edge Chordae

Free-edge chordae are usually very thin and almost unbranched: small branches are visible only right at the insertion. They originate from the apex of the PM and insert into the free margin of the leaflets. Only in rare cases do they insert into the commissures or incisures of the TVPL ([Figure 1.7 - C](#)). [13]

1.1.4.4. Deep Chordae

Deep CTs exhibit considerable length as single entities or may feature a limited number of branches immediately preceding their insertion. The point of insertion occurs either within the clear zone on the ventricular side or deep within the rough zone. The characteristic feature of these CTs is the triangular fold, i.e., a membranous tissue covering the branching zone ([Figure 1.7 - D](#)). [13]

1.1.4.5. Basal Chordae

They are single chordae and to be classified as basal chordae must not have folds of membranous tissue adhering to the wall of the ventricle. The morphology of the chord can be highly variable, the section can be flattened or rounded, the chord can be short and thick or long and thin. Their point of origin is not the PM, but they may arise from the wall of the myocardium or from small trabeculae carnae. They insert close to the annular region and before insertion widen into thin membranous bands ([Figure 1.7 - E](#)). [13]

Morphological features of the CTs

In 1971, Silver, M. D. et al. [13] measured the length and the thickness of the five CT types of 50 human hearts with healthy TVs ([Table 1.3](#)). The authors highlighted a great inter-subject anatomical variability, even when clustering chordae by subject gender; for instance, the number of rough chordae inserting on the TVAL ranged from 2 to 6 in males and from 2 to 7 in females.

| | Insertion | Length (cm) | Thickness (mm) |
|-------------------|--------------------------|---------------|----------------|
| Fan-shape | AP commissure | 1.2 ± 0.3 | 1.0 ± 0.3 |
| | AS commissure | 1.4 ± 0.4 | 0.9 ± 0.3 |
| | AS commissure | 0.7 ± 0.3 | 1.0 ± 0.3 |
| | Posterior leaflet clefts | 1.3 ± 0.4 | 0.9 ± 0.3 |
| Rough zone | TVAL | 1.5 ± 0.4 | 1.1 ± 0.4 |
| | TVPL | 1.4 ± 0.3 | 0.9 ± 0.2 |
| | TVSL | 1.7 ± 0.5 | 0.9 ± 0.2 |
| Free edge | TVAL | 1.4 ± 0.4 | 0.8 ± 0.2 |
| | TVPL | 1.3 ± 0.4 | 0.8 ± 0.2 |
| | TVSL | 1.4 ± 0.5 | 0.8 ± 0.3 |
| Deep | TVAL | 1.7 ± 0.4 | 1.0 ± 0.4 |
| | TVPL | 1.4 ± 0.4 | 0.9 ± 0.3 |
| | TVSL | 1.4 ± 0.5 | 0.8 ± 0.3 |
| Basal | TVAL | 0.6 ± 0.3 | 0.9 ± 0.4 |
| | TVPL | 0.5 ± 0.2 | 0.9 ± 0.4 |
| | TVSL | 0.6 ± 0.3 | 1.0 ± 0.5 |

Table 1.3: length and thickness of CTs evaluated in the Silver et al. study on 50 human heart.

Table adapted from Silver et al [13]. The data in the table show the mean \pm standard deviation.

In the same study, samples from male and female subjects were divided. The variability found within the same sex was in some cases high, e.g. for TVAL rough zone chordae for male subjects ranged from 2 to 6, for female subjects from 2 to 7. In conclusion, the number of CTs and insertion pattern is extremely variable from subject to subject, making the chordal apparatus patient specific.

1.2. Pathologies and treatments

Pathologies affecting the TV and its functionality can be divided into two categories:

- Primary, when they are inherent and intrinsic pathologies of the valve.
- Secondary, when they are a response to another pathology already present and affecting another structure.

Primary diseases can be divided into congenital diseases, rheumatic valve disorders, tumor or infections. Congenital diseases are structural abnormalities of the valve that individuals present from birth and that often affect certain functions. These diseases have a low prevalence, e.g. Ebstein's anomaly is a rare congenital heart disorder, which accounts for less than 1% of congenital heart defects and occurs in about 1 in 200,000 live births [22], [23]. Rheumatic valve disorders, such as tricuspid atresia and congenital tricuspid stenosis, are more common. These disorders, although considered primary, are often associated with a rheumatic MV disorder. Finally, infections include infective endocarditis, an infection that affects the inner lining of the heart and often also damages the valve.

The main secondary TV pathology is Functional Tricuspid Valve Disease (FTVD). This pathology is the most common response to advanced myocardial disorders of the left heart that may be due to pathologies of the left ventricle, MV, or aorta. It is characterized by TV annular dilatation and changes in its three-dimensional conformation. This condition does not allow TV competence and causes regurgitation of blood into the RA during the systolic contraction of the RV. [24]

1.2.1. Functional Tricuspid Valve Disease

Tricuspid regurgitation (TR) is the most common right heart lesion in adults. This disorder is primary in about 10% of cases in adults, the remaining 90% of cases are consequences of a left heart disease [2], [3]. A mild lesion is so common that it has been considered for decades to be benign and anatomically normal. The literature reports that of all patients undergoing an echocardiogram, approximately 88% have TR of varying degrees [1]. In 2019, Yan Topilsky analysed Doppler echocardiography data of approximately 13,000 patients, who were subject to strict inclusion criteria, in order to define the incidence of TR in the population. Prevalence rates were 0.59% for women and 0.47% for men, suggesting around 1.6 million affected individuals in the entire US population. [1]

Since the year 2000, research has consistently demonstrated that, even when TR a secondary condition of the left heart, insufficient treatment can lead to persistent RV dysfunction. This, in turn, emerges as a significant contributor to mortality in individuals who have undergone MV treatment. For instance, in 2019 Benfari Giovanni et al. emphasized managing TR's importance: examining 13,026 adult

patients with heart failure and reduced ejection fraction, the study highlighted the impact of functional TR on survival [4].

Anatomically, a disturbance of the left heart involves a shift in the septum between the right and left heart. The TV annulus is directly connected to this structure. As compared to the MV annulus, it is larger and less rigid, so a displacement of the septum results in dilation of the annulus. The dilatation makes the annulus more planar and circular (Figure 1.8), the most affected annular regions being the insertions of the TVAL and of the TVPL. TR can be graded by four categories of severity: mild, moderate, severe or very severe. Significant TR is evident in the presence of 40% dilatation of the annulus. Marked annular enlargement results in reduced leaflet coaptation and alters the relationship between PMs and leaflets. [2], [12]

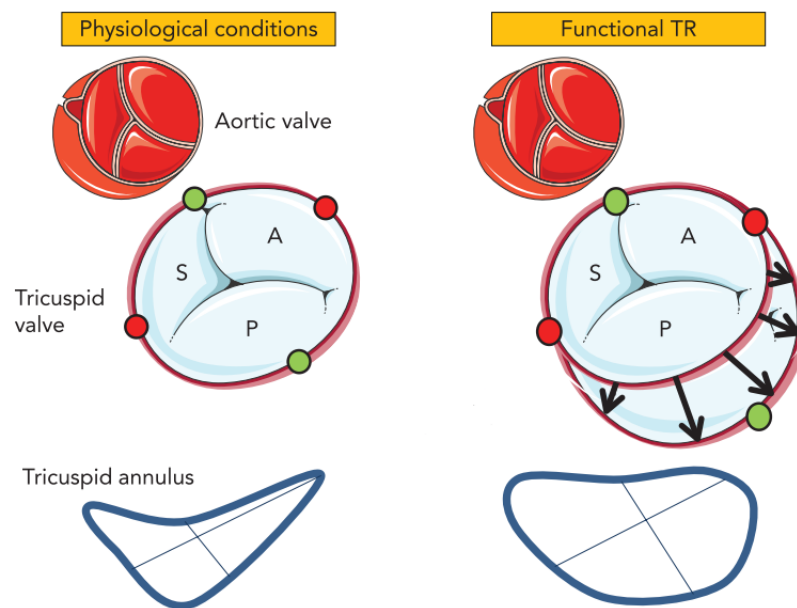


Figure 1.8: On the left is a representation of the physiological annulus with its typical cell shape. On the right is a representation of a more planar and circular annulus typical of the TR. Image adapted from Besler et al. [12]

1.2.2. TR treatment

TR treatment may vary depending on the severity of the condition, and may include drug therapies, surgery to repair or replace the TV, and minimally invasive surgical procedures. Although the number of patients suffering from moderate or severe TR is high, only 0.5% of patients undergo surgery for repair or replacement.

The main surgical procedures are:

- Ring Annuloplasty: a flexible ring-shaped prosthesis ([Figure 1.9 – A](#)) is placed and sutured close to the dilated annulus with the aim of restoring its physiological shape and size, thus allows the leaflets to properly occlude the TV orifice [5], [25].
- Surgical reconstruction: CTs or leaflets are reconfigured to restore TV function. In the case of leaflets, this is a patient-specific operation that may require removal of damaged tissue, suturing of certain components or replacement of the tissue with appropriate prostheses ([Figure 1.9 – B and C](#)). [5], [25].
- Percutaneous repair: in recent years, percutaneous repair techniques have become increasingly popular. Thanks to the use of guided catheters this technique is less invasive, not requiring open-heart surgery. Many devices are being developed for transcatheter repair of TV, although limited clinical data are available to date. Among the best known devices are the Trialign system (Mi-tralign, Inc.), the PASCAL Repair System (Edwards Lifesciences, Irvine, CA, USA), the Cardioband annuloplasty systems (Edwards Lifesciences) and the TriCinch system (4Tech Cardio Ltd.) [5][26][27].
- TV replacement: if the TV is severely damaged and it is not possible to act on the native tissue, it is replaced by a mechanical or biological valve prosthesis [25].

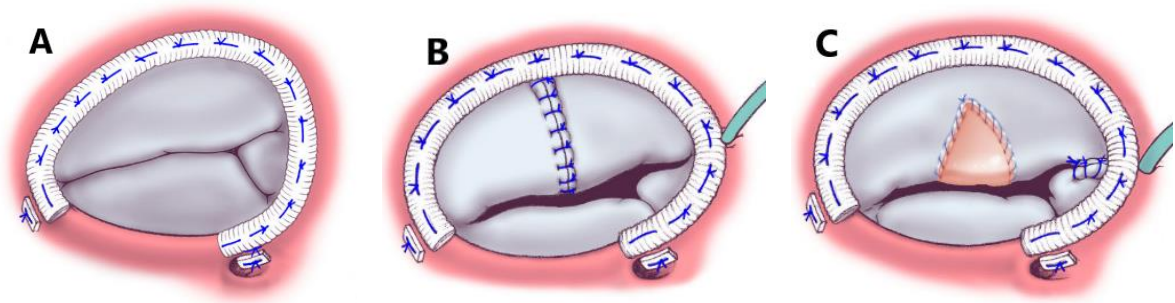


Figure 1.9: (A) Ring Annuloplasty, (B and C) Surgical reconstruction of the leaflet. Images adapted from Nishant Saran et al. [25]

1.2.3. New approach

Jaworek et al. [10] recently proposed a new type of treatment for secondary TR. Left heart disease results in dilation of the RV volume and enlargement of the TV annulus, usually due to pressure overload. Both phenomena cause TR due to increased leaflets spacing and tethering. The treatments presented in section 1.2.2. TR treatment act

directly on the annulus or on the leaflets, but do not consider RV dilatation. In this study, the effect on RV morphology of free wall approximation (FWA) was quantified using an ex-vivo experimental set-up to analyse beating porcine hearts.

FWA was analysed in three anatomical configurations ([Figure 1.10](#) - a):

- A. between the APM and PPM (A-P)
- B. between APM and SPM (A-S)
- C. between the midpoint of the PPM and the APM and the septal wall (A-SW)

In each tested direction, a mechanical device allowed the length of the suture point attached on the side of the RV free wall to be adjusted. Porcine hearts with TR were placed on the experimental set-up ([Figure 1.10](#) - b) on which resting conditions were simulated: mean pulmonary arterial pressure 15 mmHg, 60 bpm and ejected volume 70 mL. FWA was performed in configurations A, B, and C of 30% and 60% ([Figure 1.10](#) - c).

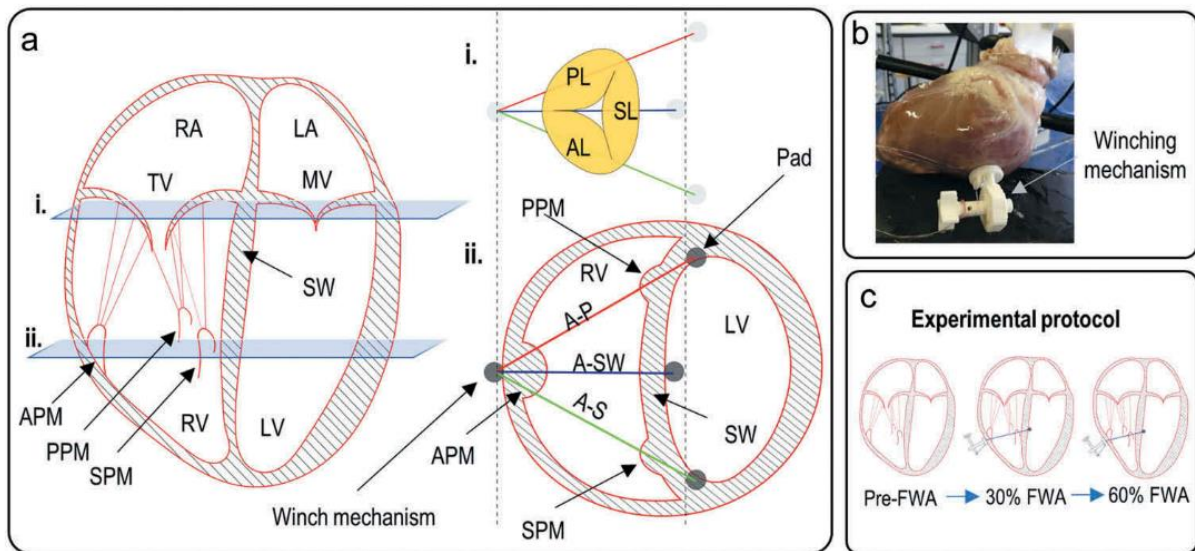


Figure 1.10: (a) Illustration of the directions of the FWA technique. i. View with respect to the valve levels. ii. View with respect to the short axis on the PMs level; (b) Representation of the experimental set-up; (c) Experimental protocol: for each heart sample, data were recorded in three pre-FWA or TR conditions, post-FWA with 30% and 60% approximation. Below are the acronyms shown in the figure: TV = tricuspid valve, RA = right atrium, RV = right ventricle, SW = septal wall, AL = anterior leaflet, PL = posterior leaflet, SL = septal leaflet, APM = anterior papillary muscle, PPM = posterior papillary muscle, SPM = septal papillary muscle, A-P = anterior-posterior approximation direction, A-S = anterior-septal approximation direction, A-SW = anterior-septal wall approximation direction, MV = mitral valve, LA = left atrium, LV = left ventricle.

The results of the article show that increasing the degree of FWA leads to macroscopic changes in morphology and haemodynamic. Papillary displacement reduces tenting in a direction-dependent manner. The A-P configuration enhances an elevation of the free margin of the leaflets adjacent to the posterior-septal commissure. The A-S

configuration reduces tenting between the septal and anterior leaflets. The A-SW configuration, on the other hand, acts by improving the tenting of all three leaflets equally. This implies that the type of FWA should be chosen according to the specific patient case. In addition, a reduction of the annulus diameter was noted. However, this improvement seems to be conditioned by the degree of deformation of the structure.

1.3. Mock Circulatory Loops

In engineering to test, analyse and evaluate a component, device or system, test benches are often set up; these are systems or structures that simulate real conditions or specific situations and allow to obtain accurate and specific data under controlled conditions. In the medical field, test benches are often used, and, in many cases, the associated *in vitro* tests are an essential step in verifying that the designed system meets the standards required for certification.

In the context of cardiovascular applications, mock circulatory loops can be designed to simulate the key features blood circulation in an anatomical district of interest. These set-ups are also often used to obtain more information about biological systems or to allow surgeons to simulate an operation. Mock loops can be divided into two categories according to whether they present biological specimens or are based exclusively on artificial structures. Depending on the intended purpose, an animal heart or a pump imitating the heart can be inserted, hoses mimic veins and arteries, sensors detect parameters of interest, and other elements can be added to achieve the desired conditions.

In their thesis, Castagna and Lentini developed a hybrid mock circulatory loop specifically to study the TV [28] it reproduces the cardiopulmonary circulation, and it includes a passive porcine right heart, which is set in motion by an external pulsatile pumping system, an after-load that simulates the hydraulic impedance of the pulmonary circulation, as well as pressure and flow transducers ([Figure 1.11](#)). To avoid unrealistic RV wall motion due to RV chamber pressurization while allowing to simulate TR, bands were positioned on the outer surface of the RV wall ([Figure 1.12](#)). Also, the pulsatile pump was connected to the RV chamber through an *ad hoc* connector inserted in the septal wall ([Figure 1.12](#)) [28], [29], [30]. Different physiological and pathological conditions were simulated by adjusting the parameters of the afterload, i.e., compliance, characteristic resistance, and peripheral resistance. Relevant parameters that were replicated were the flow waveform, in the case where physiological conditions were simulated the heart rate of 70 bpm and the ejection volume of 70 ml. Of note, during tests 3D echocardiographic imaging was acquired, obtaining the data that provide the starting point of the present thesis project.

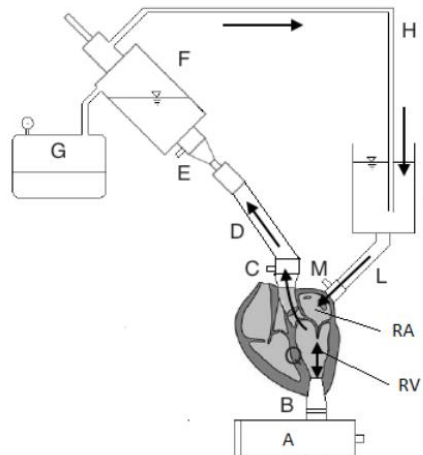


Figure 1.11: Schematic representation of the experimental set-up developed in [28]. The pump (A) is connected to the heart by means of a connector (B) which was inserted directly into the septal wall. The preload simulator is connected to the atrium (C), while the afterload simulator (I) was connected downstream of the PV (M).

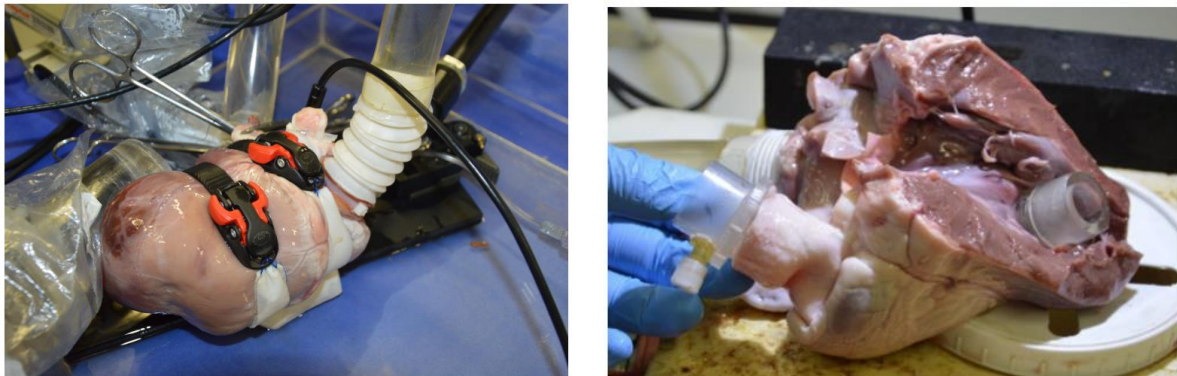


Figure 1.12: Left: RV restraining bands to control the RV motion. Right: Connector positioning in the septal wall and removing the LV. Images adapted from Castagna and Lentini's thesis [28]

1.4. Noninvasive cardiovascular imaging techniques

Medical imaging techniques allow for the visualization of organs and tissues within the body. These techniques are widely used and allow the identification of abnormalities and pathological changes that would otherwise be difficult to diagnose and assess. In the cardiovascular field, thanks to technological advances in recent years, there are many sophisticated imaging methods that allow to obtain detailed images of cardiac structures.

The most widespread ones are echocardiography, acquired through transthoracic (TTE) or transesophageal (TEE) exams, cardiac magnetic resonance imaging (MRI), cardiac computed tomography (CT), coronary angiography and cardiac nuclear imaging techniques (Cardiac PET and myocardial scintigraphy).

Recently, imaging data have increasingly been used as source data for the implementation of computational models to obtain models with high geometric realism, TTE and CT being among the most used imaging techniques [7], [29], [30], [31]. Furthermore, such models can in the future be used for patient-specific analyses that can support clinical decisions by providing additional quantitative information or predicting the impact of a potential intervention. In the current state of the art, models still have considerable limitations.

1.4.1. Echocardiography

Among the different imaging modalities, echocardiography is key to the present thesis project. It hence important to summarize the key aspects of this technology and the key features of echocardiographic images, which inherently impact the subsequent modelling pipeline.

Echocardiography is widely used to study cardiac structures and function, in particular for the sake of first diagnoses or for repeated monitoring, because it is cost- and time-efficient, and it does not require contrast agents nor ionizing radiations.

Echocardiography is based on the use high-frequency sound waves: the echocardiograph probe has a grid of densely packed piezoelectric transducers, called phase arrays, which when stimulated emit a high-frequency (2-12 MHz) directional beam and receive the waves that are scattered back. Based on the timing of the reflected waves, the anatomy in the region scanned by the beam is reconstructed. The region of interest (ROI) scanned by the pressure wave has the shape of a sector of a circle (in 2D) or sphere (in 3D) with its centre in the probe. Consequently, the acquisition of anatomical structures covering a large ROI requires the probe to be positioned relatively far from them (otherwise they end up in the 'tip' of the ROI and are cut off). This peculiarity is less evident on images acquired on a subject, as the subject itself requires a certain distance to be maintained. In the case of echocardiographic image acquisition on the test bench, the probe is placed on the first

useful surface, which corresponds to the epicardium. Consequently, the images may not contain annulus, leaflets and PMs in their entirety. From this analysis it could be deduced that the further away the probe, the more structures can be included in the image. In reality, the wave emitted by the probe and the reflected wave attenuate in space, so the further away an anatomical structure is from the probe, the less sharp the signal obtained from the reflected wave. The spatial resolution of the data is rather high, usually less than a millimetre, with values from 0.3 to 0.7 depending on the quality of the ultrasound scanner. This does not translate into equally high accuracy in the recognition of the edges of structures, because the images are always affected by blurring or hazing that make these edges 'blurred'. In the specific case of analysing very thin structures, such as valve structures, this may limit the correct definition of the various structures. Finally, the presence of artificial objects can generate artefacts: shadowing or light beams. These artefacts are related to the position of the object and the material they are made of.

The [Table 1.4](#) summarizes the main features of cardiac echocardiography:

| Main features | |
|-------------------------|--|
| Acquisition Time | Real-time It is possible to acquire several cardiac cycles in 5 sec. |
| Type Data | Volumetric |
| Space Resolution | Isotropic, less than 1 mm on linear distances |
| Time Resolution | 25-30 data/cardiac cycle |
| Cost | From 60-90 k€ to 200-300 k€ for new machines |
| Pro | Images are available immediately Can be used with in vitro set-ups, but with some limitations |
| Cons | Probe position affects image quality Difficult to discriminate adjacent structures Anatomical structures and artificial objects may interfere with signal acquisition It is possible to have artifacts (scattering, reverberations, ...) Image format require decrypting |

Table 1.4: Main features of cardiac echocardiography

2 State-of-the-art

Computational modelling of the atrioventricular heart valves has emerged as a powerful tool for understanding the complex biomechanical interactions that govern their functions. By using advanced mathematical and computational techniques, researchers can simulate the behaviour of the valves under different conditions and explore how changes in valve geometry, material properties, and loading conditions affect their performances.

The first application of a numerical model of a heart valve dates back to 1987 in a study by Hamid et al. [32] in which they wanted to study the effects of stiffening, calcification and leaflet perforation on bioprosthetic aortic valves. In the case of the mitral valve, the first model published in the literature on the development of a FEM model of the valve was developed by Kunzelman et al. in 1993 [66]. Interest in the TV came later than the other valves because the medical community has always been much more sensitive to diseases of the left heart whose impact is more evident. The first TV model was developed by Stevanella et al. in 2010 [6].

A proper computational model requires the definition of an adequate numerical scheme, a precise description of the geometry, a considered choice regarding its discretization, the attribution of the most realistic possible properties to the tissues and an application of boundary conditions that reflect the clinical scenario to be simulated and the interactions with the surrounding structures. [30]

2.1. Numerical schemes

The numerical schemes mainly used for the study of heart valves can be divided, depending on the aspect examined, into three categories:

1. Computational fluid dynamics (CFD) models focus on the dynamics of blood flow through valves. Based on numerical resolutions of mathematical equations, they describe fluid motion in terms of velocity, pressure, and energy in the fluid dynamic system. In the case of valves, they make it possible to study the behaviour of blood in the event of turbulence and vortex formation both in physiological and pathological situations or after the implantation of a heart valve or prosthesis in general. They are often used in the design of heart valves to study their impact on blood fluid dynamics.
2. Finite element (FE) structural models are dedicated to the analysis of the structural characteristics of valves under specific load and deformation conditions. This type of analysis is based on the idea of subdividing the

structure to be analysed into smaller elements. Each individual element is analysed, and its contribution is integrated into the system. They make it possible to study the stresses and deformations acting under various loading conditions. It is possible to simulate blood pressure, the forces generated by the contraction of chambers during the cardiac cycle under both in physiological and pathological conditions. In addition, they can be used to evaluate the effectiveness of surgical interventions or medical devices designed to repair or replace defective heart valves.

3. Fluid-structure interaction (FSI) models combine fluid-dynamic and structural analyses to predict the interaction between fluid flow and the solid component of valves. They are highly advanced models that allow us to understand the complex behaviour of valves by considering the dynamic interaction between blood flow and valve structure.

The following sections will discuss the FE models of the TV that are available in the literature to date, and which have been considered as the basis for the development of this thesis project. [30]

2.2. Geometric models

To accurately simulate a biomechanical response, the TV intricate three-dimensional geometry must be thoroughly characterized. Existing models in the literature are categorized into two main types:

- Parametric models that utilize anatomical data from ex-vivo experimental studies on human or animal samples.
- Image-based models created through manual or semi-automated segmentation of clinical images, using primary imaging techniques like ultrasound, computed axial tomography (CAT), magnetic resonance imaging (MRI), and micro-CT, the latter being applicable only to ex-vivo specimens.

2.2.1. Parametric models

The first three-dimensional FE model of the TV developed by Stevanella et al. in 2010 [6] is a parametric model. The information used to create it came from an experimental analysis of five human hearts from subjects with an average age of 75 years, without major valve disease, and twenty porcine hearts. Many data were extracted from the specimens, including: the total length of the annulus and its individual traits as well as the annulus-margin free extension at characteristic valve positions. In addition, a statistical analysis was performed to test the hypothesis that porcine valves could be used as a model for human valves.

The construction of the unloaded geometric model, depicted in the [Figure 2.1](#), was guided by experimental measurements on human valves, integrating measurements on porcine valves and sonomicrometric data from the literature [33], for dimensions that required the presence of a complete heart.

The annular profile was reconstructed from the quantitative in vivo data reported by Hiro et al. [33] for seven sheep by interpolating the coordinates of six ultrasonic crystals using a natural cubic spline method. This approach resulted in a profile consistent with echocardiographic measurements reported in the literature [34], [35]. All measured geometric dimensions were normalised to the length of the reconstructed annular profile. The free margin profile of the laminae was defined based on the extensions of the leaflets from annulus to free margin measured at 12 points, which were then interpolated with natural cubic splines. The tendon cords were modelled as unbranched cords with a constant cross-sectional area and the papillary muscles were modelled as single nodes. The coordinates of the papillary muscles were set consistent with the sonomicrometric data reported in Hiro et al. article [33].

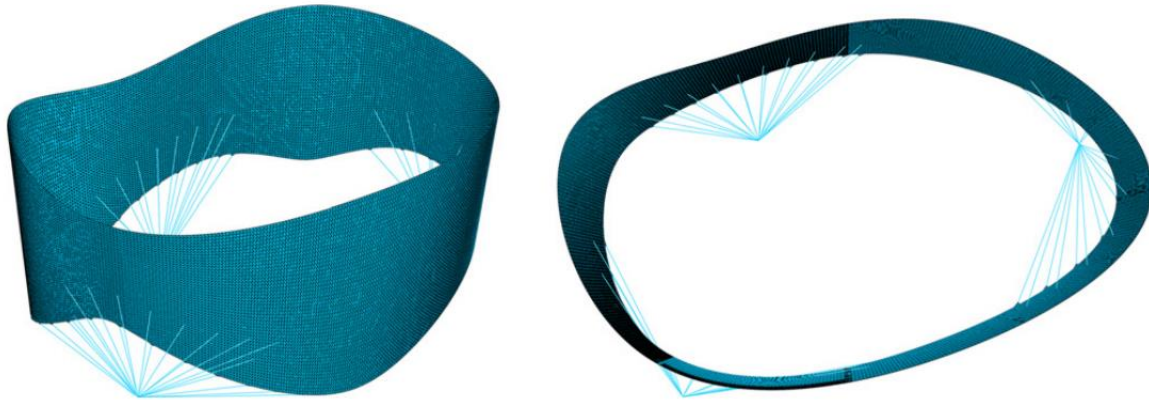


Figure 2.1: Representation of the TV unloaded configuration using a parametric model developed by Stevanella et al. Image adapted from Stevanella et al. article [6]

The study by Johnson, Laurence et al. of 2021 [36] proposed a new parametric approach to TV modelling. The aim was to create a parametric system that could repeatably and reliably reconstruct a significant number of different geometries and configurations with little variations of specific parameters.

The model is detailed within a cylindrical three-dimensional reference framework, as illustrated in [Figure 2.2](#) which visually represents the steps to create the parametric model. The initial component established is the annulus, described geometrically via a B-spline. This spline is a parametric polynomial curve formulated from a weighted linear blend of 18 spline basis functions. Adjusting the control points for these basic functions allows for shaping the annulus as desired. The antero-septal commissure marks the curve's beginning and end, while the remaining commissures are parametrically determined based on this. The location of these commissures influences the leaflet spans and their commissural positions on the free margin. The leaflet's offset direction is set perpendicular to the plane of the ring, with offset points generating a series of cubic B-splines whose extremities are interpolated to form the free margin. It's possible to parametrically set a leaflet development direction that differs from being perpendicular to the annulus plane. Papillary muscles and chordae tendineae groups are also parametrically related to the annulus, with the number of chordae and their spacing within each group determined by a B-spline surface reflecting the valve leaflets' circumferential orientation.

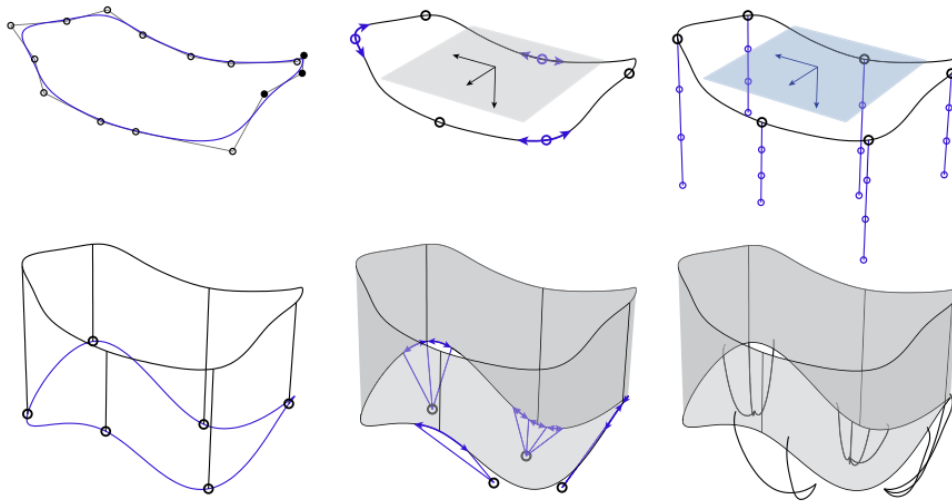


Figure 2.2: Basic sequence for the realization of the parametric model proposed by Johnson. The promo step is the definition of the 18 characteristic points of the annulus, which are interpolated by a B-spline. The initial point of the curve corresponds to the antero-septal commissure. Identifying the position of the commissures is fundamental to defining the annulus-free margin extension. Parametrically, the position of the papillary muscles and the characteristics of the main tendon groups are defined. Image adapted from Johnson et al. article [36]

2.2.2. Models based on clinical image segmentations

The decision to base a computational model on clinical imaging provides a detailed view of biological structures and precise dimensional information on the shape, size and position of organs, tissues and anatomical structures. Clinical images can be obtained directly from patients, allowing computational models to be customised to suit the specific anatomical and pathological characteristics, resulting in patient-specific models. This can lead to greater precision and effectiveness in patient-specific medical and surgical treatments.

In 2017, Aversa and Careddu [37] carried out the first imaging-based attempt to reconstruct TV geometry. Specifically, in their work they acquired 3D real-time echocardiographic (RT3DE) images of porcine heart on a test bench. The images were then manually segmented using specially developed tools. The [Figure 2.3](#) shows the steps leading from echocardiographic data to a 3D reconstruction of the valve.

This work was based not on patient images, but on images acquired in-vitro. The artificial circulation circuit they used proved to be suitable for conducting experimental TV surveys, allowing them to replicate physiological working conditions of the valve, in terms of pulsatile flow, frequency and pressure acting on the system. In addition, they carried out experimental measurements on the biological samples that were used. As a result, the in-silico model generated proved to be geometrically reliable.

Following the acquisition of the images and their segmentation, however, reworking is necessary to obtain a reconstructed model of the valve. In their model to reconstruct the 3D geometry of the valve leaflets and valve ring, the plotted points were interpolated using cubic splines, resampled and filtered using Fourier functions.

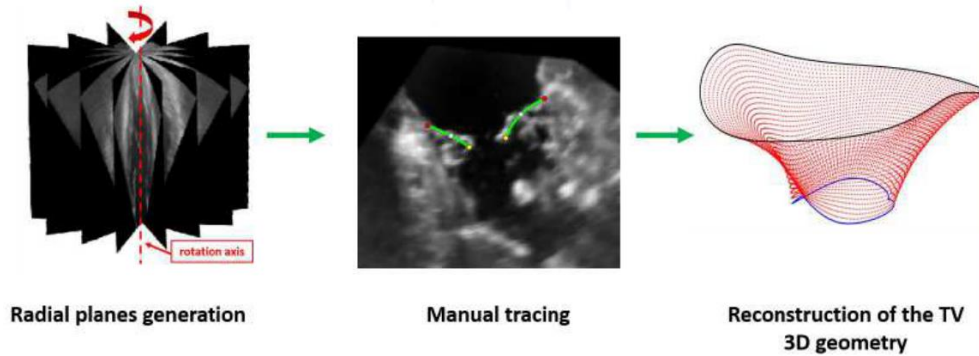


Figure 2.3: steps leading from acquisition of echocardiographic data to three-dimensional valve reconstruction. Image adapted from Aversa and Careddu thesis [37].

Kong's model [7] was the first model that reconstructed a patient-specific geometry by segmenting images from computed tomography (MSCT). The model was aimed at analysing the forces acting on the tensor apparatus and the field of forces acting on the leaflets.

Finally, Pouch et al. [38] in 2017 developed the first semi-automated echocardiographic image segmentation workflow of TVs of pediatric patients with hypoplastic left heart syndrome. Starting with the manual definition of some landmarks, the code was able to reconstruct accurate geometric models of the valve, as depicted in the [Figure 2.4](#).

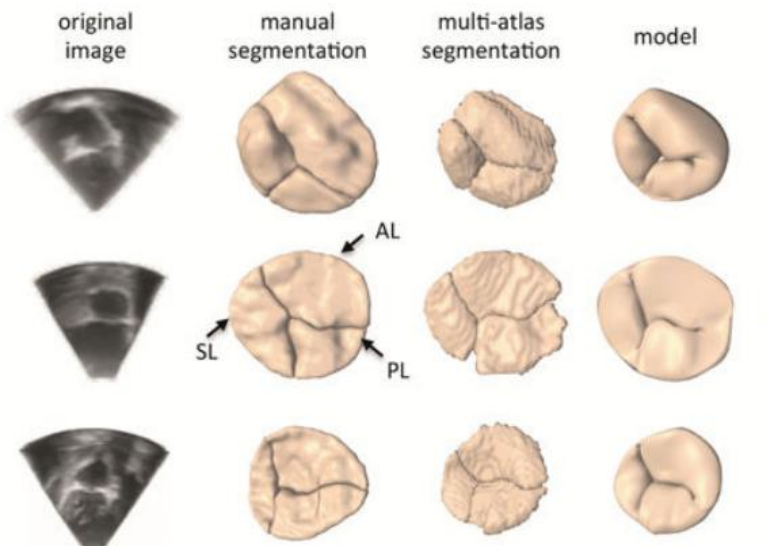


Figure 2.4: The first column represents the source image, the second the manual segmentation and the third column the result obtained with the MALF (multi-atlas label fusion) technique, the fourth column the model obtained. Image adapted from Pouch article [38].

2.3. Mechanical properties

In the development of a model based on FE analysis, the identification of a consistent constitutive model and appropriate parameters for the biomechanic description of the material is crucial to accurately simulate the mechanical behaviour of the structure.

Biological systems are extremely complex and heterogeneous. Moreover, they generally exhibit a multi-scale structure that may vary significantly when analysed at microscopic or macroscopic levels. Furthermore, there is great variability between subjects, variability that affects the mechanical properties of tissues.

In the case of the TV, the first constitutive models and the respective parameters used were derived from studies of the mitral valve, mainly due to the lower interest in this valve compared to the mitral valve and the limited number of data available. The description of the constitutive model and the identification of characterising parameters is crucial for obtaining an accurate and predictive model.

In the following sections, the main material characterisation studies of leaflets and CTs and the constitutive models used in computational models will be discussed.

2.3.1. Leaflets: biomechanical characterisation

The first material characterisation study of TV leaflets was published only a few years ago. It is a 2016 study by K. Amini Khoiy et al. [39] in which a biaxial test protocol was used to measure the ex-vivo stress and strain response of porcine TV leaflets. The tissues were preconditioned with 10 cycles of equibiaxial loading. Subsequently, 5 different test protocols were performed for each leaflet. Only the first test involved an equibiaxial protocol with a maximum value of 100 N/m, while the other four were non-equibiaxial protocols. The [Figure 2.5](#) shows the test results with equibiaxial protocol for the TVAL, TVPL and TVSL respectively, so with the first protocol. The stress-stretch curves show a highly non-linear response in both radial and circumferential directions. There is an initial stretch of elastic response followed by a rapid transition to a much stiffer condition. The non-linear trend is present in both radial and circumferential directions, but the leaflets appear much stiffer in the circumferential direction. This behaviour is also evident due to the high level of stress imposed on the tissue. The stress value under physiological conditions is approximately 40 N/m, whereas up to 100 N/m were stressed in the test. On the TVAL and TVPL, there was no significant change in thickness, but the TVAL was much stiffer. The TVSL was found to be significantly thicker, but more yielding in the circumferential direction than the other two leaflets. The tests show that all three leaflets have an anisotropic characterisation, with peak values in the TVPL.

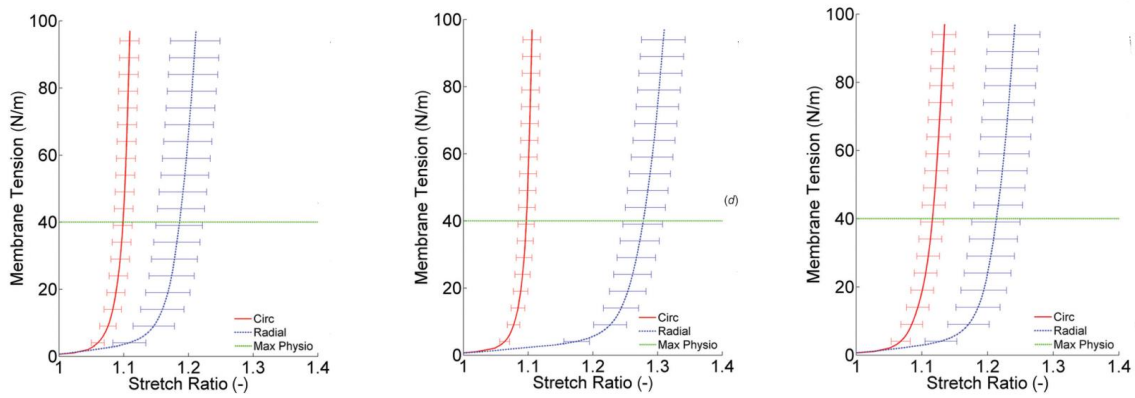


Figure 2.5: The graphs shown are the results of biaxial tests on the TVAL, TVPL and TVSL respectively, imposing different levels of tension. The circumferential direction (Circ) is highlight in red and the radial direction (Radial) in blue. The main line is the average value obtained and the horizontal bars are the standard errors. The green horizontal line indicates the maximum level of physiological tension, while the tests go up to 100N/m to simulate the condition of hypertension. Images adapted from K. Amini Khoiy et al. article [39]

In 2017, Pham et al. [40] released the first mechanical characterisation study performed on human hearts exported from patients whose death was not related to cardiovascular disease. The samples analysed were 114 removed from 12 patients. Planar biaxial mechanical tests and histological methods were used to characterise the mechanical and structural properties of the tissue. 40 preconditioning cycles were performed on each specimen. Subsequently, each sample was subjected to 7 biaxial test protocols, of which only one was equibiaxial. The test protocols were applied equally to MV and TV tissues, and the results are shown graphically in [Figure 2.6](#). The study suggests that the parameters obtained for the MV do not adequately describe the behaviour of the TV, the latter being less rigid and more flexible. Indeed, the two valves are subjected to different loading conditions and consequently have different structural integrity from each other. Compared to the previous study conducted by K. Amini Khoiy et al. [39], the TV leaflets proved to be more extensible and isotropic. This result could be influenced by the advanced age of the subjects (70.1 ± 3.7 years old).

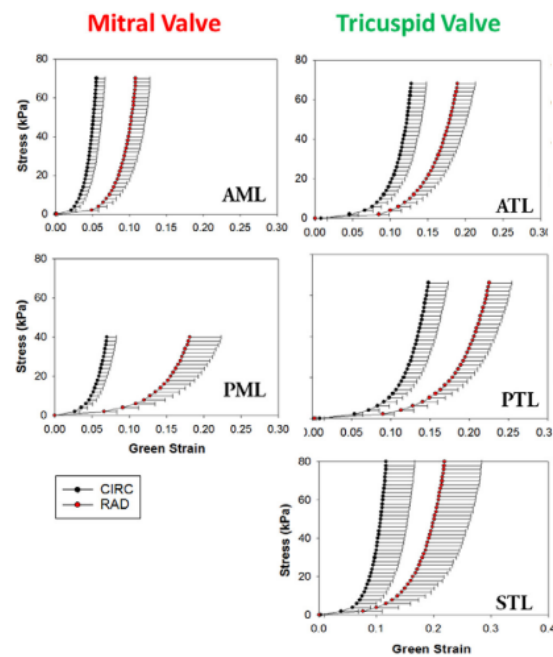


Figure 2.6: The graphs allow a direct comparison of the stress-strain curves obtained from the equibiaxial protocol of each MV and TV valve leaflet. The graphs show in blue the results obtained in the circumferential direction (CIRC) and in red in the radial direction (RAD).

Data are presented as mean \pm standard error. Images adapted from Pham et al. [40]

In 2019, Laurence et al. [41] provided a more precise characterization of the mechanics of MV and TV leaflets, than earlier research. The anterior leaflets of the two valves were divided into six regions, each sample obtained was subjected to biaxial mechanical tests with various load ratios up to a tension of 50 N/mm. The [Figure 2.7](#) shows the characterisation graphs of the six regions obtained for the tricuspid valve considering the stress-strain relationship in both radial and circumferential directions. In addition, time-dependent behaviour was evaluated on each tissue sample using stress-relaxation tests.

The results of the biaxial mechanical tests in this study showed a significant difference in the anisotropy of the material when comparing the central regions of the tissue with the marginal regions. Comparing the results obtained for the MV and TV, they found that the TV revealed more pronounced changes in material anisotropy for the central regions than for the marginal regions, compared to the MV.

The results on stress relaxation exhibited an anisotropic and exponential stress decay trend with variations in stress reduction between tissue regions. By allowing the tissue to relax for 900 seconds, the initial stress was reduced by 20-30%.

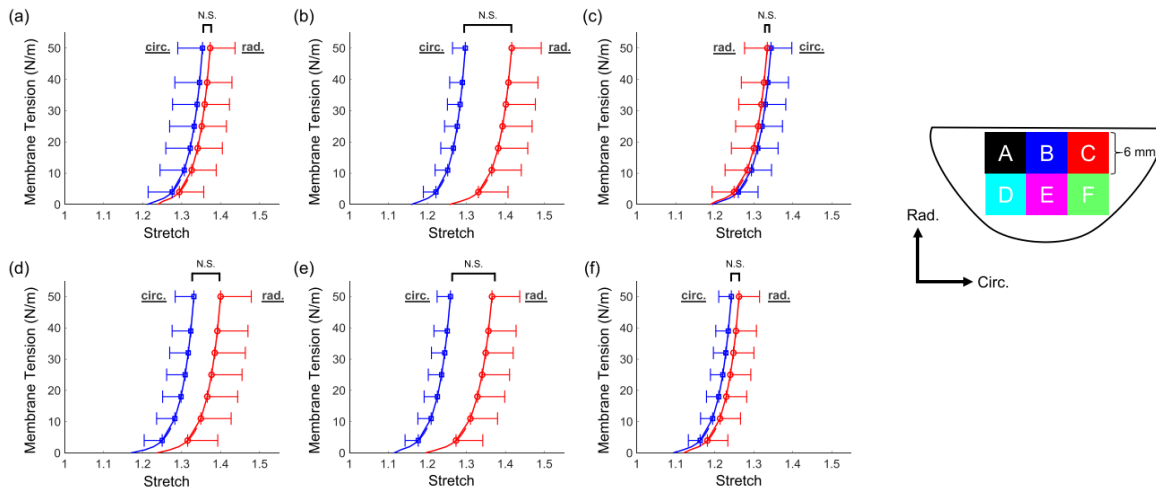


Figure 2.7: The six samples extracted from the TVAL are shown schematically on the right and the labels A-F correspond to the stressed region. The graphs depict the total tissue elongation results for the six TVAL tissue regions under equi-biaxial loading protocol. In each graph, the mean standard error of the membrane tension was averaged over the total tissue elongation results. Images adapted from Laurence et al. article [41]

The most recent study characterising TV leaflets was conducted by Meador et al. [42] in which a mechanical and microstructural analysis was performed on samples of ovine TV leaflets. From the valves, samples of only the central zone were exported, as shown in [Figure 2.8 \(A\)](#). The samples were preconditioned with an equibiaxial loading protocol at 300 mN for 10 cycles. Subsequently, 5 loading protocols were performed, both equibiaxial and non-equibiaxial. In addition, a preload of 10 mN was applied before all test protocols. The study shows a variability in microstructure and mechanical properties even between leaflets of the same subject. Tricuspid leaflet composition, collagen orientation and valve cell morphology were found to be spatially heterogeneous and varied between leaflet types. Furthermore, under biaxial tension, the mechanical behaviours of the leaflets showed unequal degrees of mechanical anisotropy between leaflets. The TVSL, as shown in [Figure 2.8 \(B\)](#), proved to be more rigid in the radial direction and not in the circumferential direction, like the other two leaflets. The differences noted in the microstructure are consistently reflected in the different mechanical responses between the leaflets.

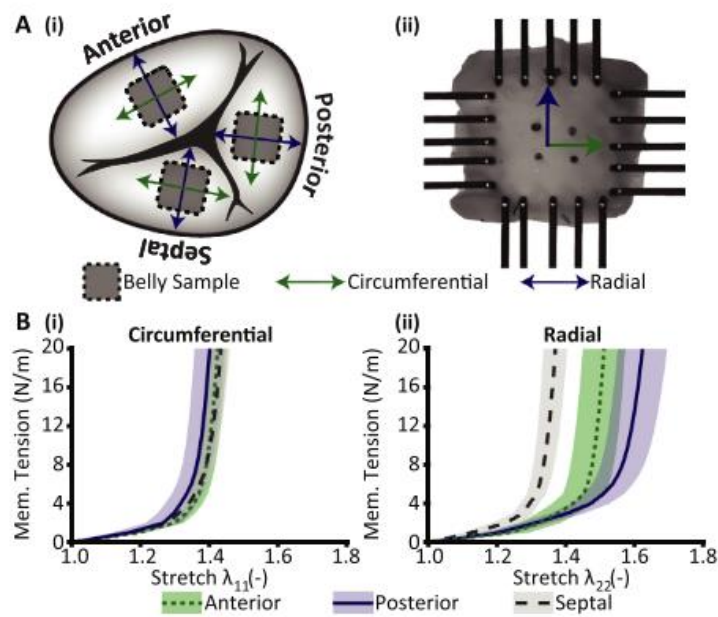


Figure 2.8: (A) (i) Schematic representation of the removal zone of the tissue samples extracted from the TVAL, TVPL and TVSL (ii) Representation of how the tissue samples were mounted in alignment with the circumferential and radial directions and tested under biaxial tension (B) Graphs of response to the application of equibiaxial membrane tension and stretching of the TVAL, TVPL and TVSL in the (i) circumferential and (ii) radial directions. Images adapted from Meador et al. article [42].

2.3.2. Leaflets: constitutive models

The characterization of leaflet materials reveals their mechanical behaviour to be predominantly elastic, non-linear, and anisotropic. This behaviour of biological materials is modelled using strain energy functions, which are scalar functions connecting the strain energy density to the strain gradient of a material.

In isotropic materials, the strain energy density function is based solely on the invariants of the Cauchy-Green strain tensor. However, anisotropic materials require additional parameters for definition. For instance, the energy function is influenced by specific reference vectors or tensors that need to be determined for each model.

2.3.2.1. Holzapfel model

The Holzapfel constitutive model [43], [44] is a biomechanical model based on an anisotropic and hyperelastic approach used to simulate the mechanical behaviour of biological tissues. The model requires the definition of the initial fibre orientation, thus considering the microscopic tissue structure of the leaflets in terms of orientation and collagen fibre distribution. The orientation of the fibres will undergo rearrangements and affect the mechanical properties of the tissue during the simulation. The model requires the definition of constitutive parameters usually obtained from experimental tests or from data published in the scientific literature.

The formulation of the strain energy function in terms of strain energy per unit of reference volume U according to Holzapfel's model is:

$$U = C_{10}(I_1 - 3) + \frac{1}{D} \left(\frac{(J^{el})^2 - 1}{2} - \ln J^{el} \right) + \frac{k_1}{2k_2} \sum_{\alpha=1}^N \{ \exp[k_2(\bar{E}_\alpha)^2] - 1 \} \quad (2.1)$$

Where:

- $\bar{E}_\alpha = \kappa (I_1 - 3) + (1 - 3\kappa) (I_{4(\alpha\alpha)} - 1)$ is a function that characterises the deformation of the family of fibers, and can describe from perfectly aligned family of fibers to randomly distributed ones.
- C_{10} , D , k_1 , k_2 and κ are material parameters dependent on temperature.
- N : number of defined fibers.
- I_1 : first deviatoric strain invariant.
- $I_{4(\alpha\alpha)}$: pseudo invariant term.
- J^{el} : elastic volume ratio.

The distribution of the N families of fibres in the model is represented by the third term of the strain energy function, while the first and second terms describe the distortional and volumetric contribution of isotropic non-collagenous material.

2.3.2.2. Lee model

Lee's constitutive model [45] is a formulation based on invariants and was first formulated to describe the stress-strain behaviour of MV tissues. Later, this formulation also found applications in the description of TV leaflets [37].

The general formulation of the model is:

$$W(I_1, I_4) = C_{10} [e^{c_{01}(I_1-3)} - 1 + \frac{c_0}{2} [(1 - \beta)e^{c_1(I_1-3)^2} + \beta(I_4 - 1)^2 - 1]] \quad (2.2)$$

where:

- I_1 and I_4 are the first and fourth deviatoric strain invariants of Cauchy-Green tensor.
- β : parameter for the level of anisotropy of the material.
- C_{10} , C_{01} , c_0 and c_1 : material constants.

The parameter β allows to define the response of the tissue in the direction orthogonal to the fibres. This parameter can take a value between 0 and 1: 0 corresponds to a purely isotropic material, 0.5 is a transversely isotropic material and can be related to the strength of the fibre alignment.

2.3.2.3. Fung model

Fung's model [46] has various variants and allows the description of various classes of anisotropic material models. The idea on which it is based is that biological tissues can be represented as a set of elastic elements that under load are subject to complex deformations. The material behaviour is described by a strain energy function, which represents the energy stored in the material in response to a deformation. This strain

energy function depends on the main invariants of the strain tensor. Finally, its description takes into account the anisotropy of the material, i.e. the directionality of the fabric's mechanical properties.

To extend Fung's constitutive model to the description of anisotropic materials, a transformation matrix, in which the preferential orientation of the fibres is defined, is combined with the constitutive model.

If a biological tissue with directional fibres is being modelled, an anisotropic Fung model of the type can be used:

$$W = \frac{C_1}{D_1} (e^{D_1(I_1-3)} - 1) + \frac{C_2}{D_2} (e^{D_2(I_2-3)} - 1) + \frac{C_3}{D_3} (e^{D_3(I_3-3)} - 1) \quad (2.3)$$

Where all the parameters ($C_1, D_1, I_1, C_2, D_2, I_2, C_3, D_3, I_3$) are defined according to tissue structure and fibre orientation.

2.3.3. CTs: biomechanical characterisation

The mechanical response of the TV CTs is non-linear elastic, with asymmetrical behaviour in tension and compression. In fact, the CTs can withstand significant tensile loads, but are unable to sustain any load in compression. Their behaviour depends on the progressive recruitment of collagen fibres, which characterise their microstructure.

The first characterisation study of CTs was conducted by Lim et al. in 1980 [47]. In this study, human derived CTs were analysed in terms of their microstructure and dimensions using scanning electron microscopy and transmission electron microscopy, as well as in terms of their mechanical response through a uniaxial tensile test to failure. The CTs were kept moist during the tests and were tested with a strain rate of 0.05 cm/min. [Figure 2.9](#) shows the stress-strain curve obtained by Lim for the tendon CTs. It is a curve denoting non-linear behaviour typical of soft biological tissues. This exhibits a low resistance for small deformations, which gradually increases with elongation: after a deformation of approximately 8%, the curve becomes linear, and this point of transition between the first non-linear section and the constant-stiffness section is called the transition point. In the article, they report a comparison with the results of uniaxial tensile tests on MV CTs. The MV CTs were found to be less extensible with the same cross section. Data from electron micrographs show differences in mean diameter and mean fibril density compared to MV CTs. TV has an average fibril diameter of 441 ± 2 Å, in MV it is 545 ± 2 Å. The percentage of collagen fibrils on the cross-sectional area of the fibre is 30.3 % for TV, and 42.6 % for MV.

These differences explain the stiffer nature of the TV CTs.

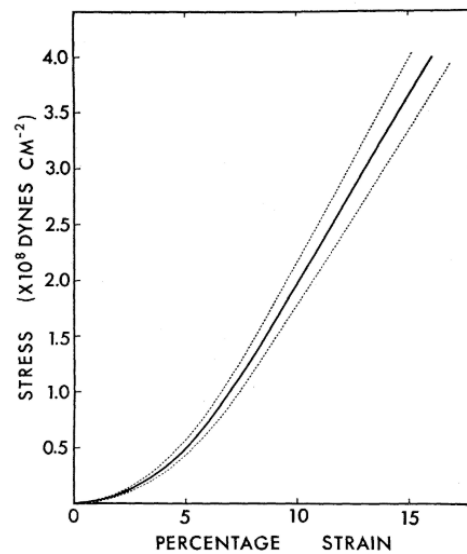


Figure 2.9: The graph represents the stress-strain curve of human TV CTs. The central line is the mean value, while the two dashed lines are the standard error. Images adapted from Lim et al. article [47]

Lim's description of the material has been widely used in the development of computational models of TV.

Following Lim's study, many years passed before another research group proposed a new characterisation of CTs. The next study, in fact, was that of Pokutta-Paskaleva et al. in 2019 [48]. The CTs were categorised and divided on the basis of the anatomical description and the position of the CTs insertion on the leaflets. Each sample of each CT type was subjected to a uniaxial tensile test under hydrated conditions until failure with a strain rate of 3 mm/min. [Figure 2.10](#) shows the stress-strain relationships for the TVAL, TVPL and TVSL CTs. The CTs on the TVAL were found to be the most rigid, while those on the TVPL and TVSL are most extensible.

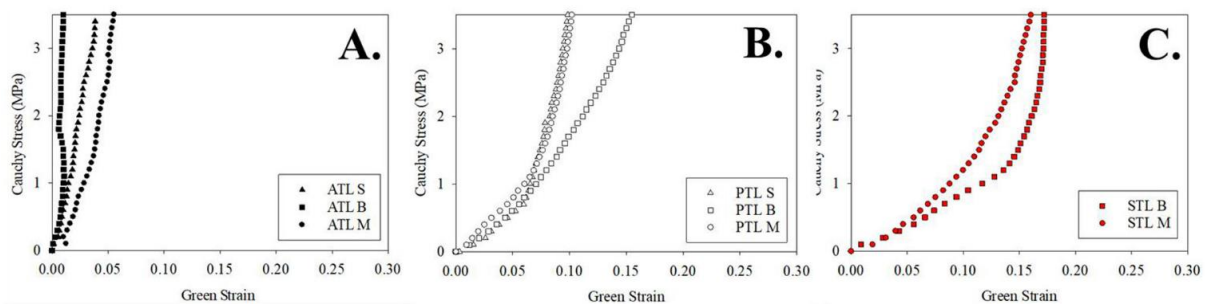


Figure 2.10: The three plots represent the mean uniaxial chordal mechanical response for (A) TVAL, (B) TVPL and (C) TVSL. The mechanical responses were then grouped by chordal insertion points and were further subdivided on the basis of anatomical description: triangles represent struct CTs, squares basal CTs and circles marginal CTs. Images adapted from Pokutta-Paskaleva et al. article [48]

The most recent study characterising CTs of the TV is that reported in the 2010 article by Smith et al. [49] In their study, they categorised TV CTs using three parameters:

leaflet of origin, insertion site and size. In the study, 53 samples derived from TVs of sheep were analysed. The samples were subjected to uniaxial tensile tests to study their stress and deformation behaviour. The [Figure 2.11](#) shows that CTs in this study also exhibit a non-linear stress-strain response typical of collagenous tissues. In addition, some variability was found depending on the insertion site and size of the CTs.

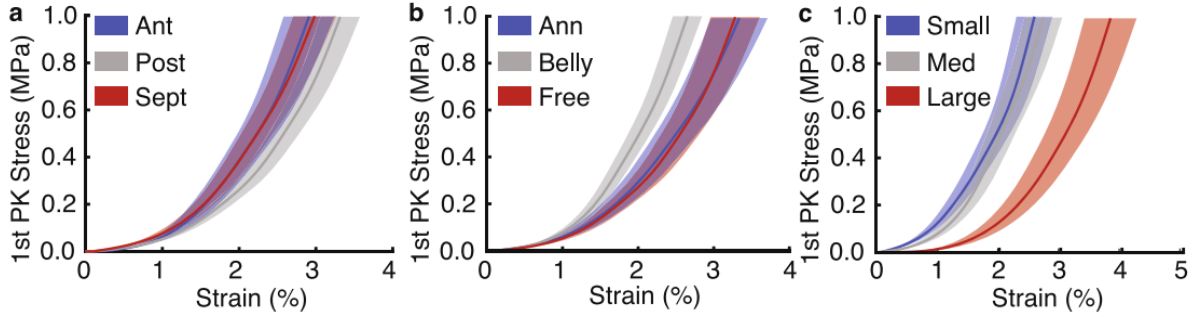


Figure 2.11: The graphs show the first PK stress-strain for all tendon chords divided by (a) leaflet, (b) insertion site, (c) tricuspid tendon chord size. For each graph, the mean value and the detected standard error are shown. Images adapted from Smith et al. article [49].

2.3.4. CTs: constitutive models

The CTs have linear elastic behaviour, which is strongly influenced by their microstructure. CTs consist of collagen fibres that are arranged parallel to the fibre axis and are gradually recruited when stressed by a tensile load. Furthermore, they exhibit asymmetrical behaviour between tension and compression; in fact, if stressed in compression, their structure does not allow them to bear any load.

The constitutive models used in the development of FE models of TV are not models specifically developed for TV CTs tissue but are models describing the behaviour of fibrous structures with a predominant direction.

2.3.4.1. Second order polynomial function

To describe the mechanical response of collagenous structure, as CTs, is possible to use the second-order polynomial energy function available in the ABAQUS/Explicit library (Simulia, Dassault Systèmes, Providence, RI, USA) [67]

The polynomial function has the following structure:

$$W = \sum_{i+j=1}^N C_{ij} (I_1 - 3)^i (I_2 - 3)^j + \sum_{i=1}^N \frac{1}{D_t} (J^{el} - 1)^{2i} \quad (2.4)$$

If $N \geq 2$, a polynomial function is obtained.

- I_1 and I_4 : first and fourth deviatoric strain invariant of Cauchy-Green tensor.
- C_{ij} and D_t are temperature-dependent model parameters.
- J^{el} : elastic volume ratio, which in the case of the incompressibility hypothesis is equal to 1.

2.3.4.2. Ogden model

In Ogden's model, which is also in the ABAQUS/Explicit library (Simulia, Dassault Systèmes, Providence, RI, USA) [B---], the strain energy potential is described using principal stretches.

The formulation within Abaqus has the following structure:

$$U = \sum_{i=1}^N \frac{2\mu_i}{\alpha_i^2} (\lambda_1^{\alpha_i} + \lambda_2^{\alpha_i} + \lambda_3^{\alpha_i} - 3) + \sum_{i=1}^N \frac{1}{D_i} (J^{el} - \mathbf{1})^{2i} \quad (2.5)$$

Where:

- $\lambda_i = J^{-\frac{1}{3}} \lambda_i$ and $\lambda_1 \lambda_2 \lambda_3 = \mathbf{1}$
- μ_i and α_i are temperature-dependent model parameters.
- J^{el} : elastic volume ratio.

2.3.4.3. Weiss model

Weiss in his PhD thesis [50] analysed the biological tissue from a mathematical point of view and proposed a new description of biological materials consisting mainly of collagen. His model describes the principle of recruitment of collagen fibrils: there is a first phase in which the fibrils are gradually recruited and a second phase in which all fibrils have been recruited and the stiffness of the material remains constant.

The strain energy function is the sum of an isotropic and an anisotropic component:

$$W = W_{iso} + W_f \quad (2.6)$$

By assuming to be in a condition of incompressibility:

$$W_{iso} = a_1 (I_1 - 3) + a_2 (I_2 - 3) \quad (2.7)$$

$$\frac{\partial W_{iso}}{\partial I_1} = a_1 \quad \frac{\partial W_{iso}}{\partial I_2} = a_2 \quad (2.8)$$

Where I_1 and I_2 are the first and second invariants of the Cauchy-Green deformation tensor. a_1 and a_2 are the constitutive parameters that will describe the isotropic component of the model.

The model is applied to structures that have a predominant length and are tested with uniaxial load tests, thus:

$$\mathbf{F} = \begin{bmatrix} \lambda & 0 & 0 \\ 0 & \frac{1}{\sqrt{\lambda}} & 0 \\ 0 & 0 & \frac{1}{\sqrt{\lambda}} \end{bmatrix} \rightarrow \mathbf{B} = \begin{bmatrix} \lambda^2 & 0 & 0 \\ 0 & \frac{1}{\lambda} & 0 \\ 0 & 0 & \frac{1}{\lambda} \end{bmatrix} \rightarrow \mathbf{B}^{-1} = \begin{bmatrix} \frac{1}{\lambda^2} & 0 & 0 \\ 0 & \lambda & 0 \\ 0 & 0 & \lambda \end{bmatrix}$$

The Cauchy effort can also be expressed as the sum of an isotropic and an anisotropic contribution:

$$t = t_{iso} + t_f \quad (2.9)$$

$$t_{iso} = 2 \mathbf{F} \frac{\partial W_{iso}}{\partial c} \mathbf{F}^T - \rho I = \dots = 2 [a_1 \mathbf{B} - a_2 \mathbf{B}^{-1}] - \rho I \quad (2.10)$$

$$t_f = \frac{1}{\lambda_f^2} \left(\lambda_f \frac{\partial W_f}{\partial \lambda_f} \right) (\mathbf{F} \hat{\mathbf{N}}_f) (\mathbf{F} \hat{\mathbf{N}}_f)^T \quad (2.11)$$

In Weiss' thesis, two assumptions were made following observations on the mechanical behaviour of collagen fibres:

- Collagen does not support compressive loads. Structures composed mainly of collagen tend to bend under very small compressive forces.
- the stress-tension relationship for collagen can be well approximated by an exponential in the region where the collagen fibres are unravelling and by a straight line in the region where all fibres are aligned with the direction of loading.

These observations led to the formulation of the deformation energy of Weiss' constitutive model for collagen fibres:

$$\lambda_f \frac{\partial W_f}{\partial \lambda_f} = \begin{cases} 0 & \lambda_f < 1 \\ a_3 [e^{a_4(\lambda_f - 1)} - 1] & 1 \leq \lambda_f \leq \lambda_f^* \\ a_5 \lambda_f + a_6 & \lambda_f > \lambda_f^* \end{cases} \quad (2.12)$$

Where λ_f^* is the stretch ratio identifying the point at which all collagen fibres are recruited and aligned with the direction of loading. This point, as shown in the [Figure 2.12](#), corresponds to the point at which the transition between the non-linear and linear regions occurs.

The parameters a_3 , a_4 , a_5 and a_6 are the constitutive parameters of the anisotropic model. Specifically, a_3 controls exponential stress and a_4 , the rate of unwinding of the collagen fibres, a_5 is the modulus of the straightened collagen fibres, a_6 is the y-axis intercept of the linear region with the exponential region.

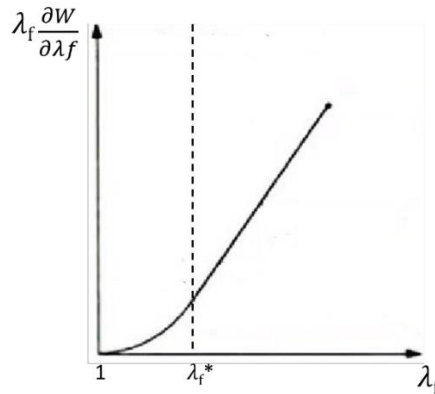


Figure 2.12: In the graph, the dotted line shows the value of λ_f^* which is the transition point between the exponential region and the linear region. Image adapted from Amicone and Dazzi thesis [30].

In Amicone and Dazzi's thesis [30], the constitutive models just described were compared. In order to allow the polynomial model of order 2, the Odgen model of order 3 and the Weiss model to be compared, the experimental data obtained from

Lim were fitted. The graph in the [Figure 2.13](#) shows that the Odgen and polynomial model curves become unrealistic for high strain values. The third order Odgen model tends to describe the stiffness as a parameter that continues to decrease. If the data were fitted with the second order Odgen model the results will be similar to that described by the second-order polynomial curve in the plot, in which above a certain threshold the stiffness of the material tends to decrease. The Weiss model, on the other hand, keeps the stiffness constant after the transition point of the curve. When all the collagen fibres have been recruited the stiffness remains constant, so this model seems to be the one that best describes the behaviour of one-dimensional collagenous elements such as CTs.

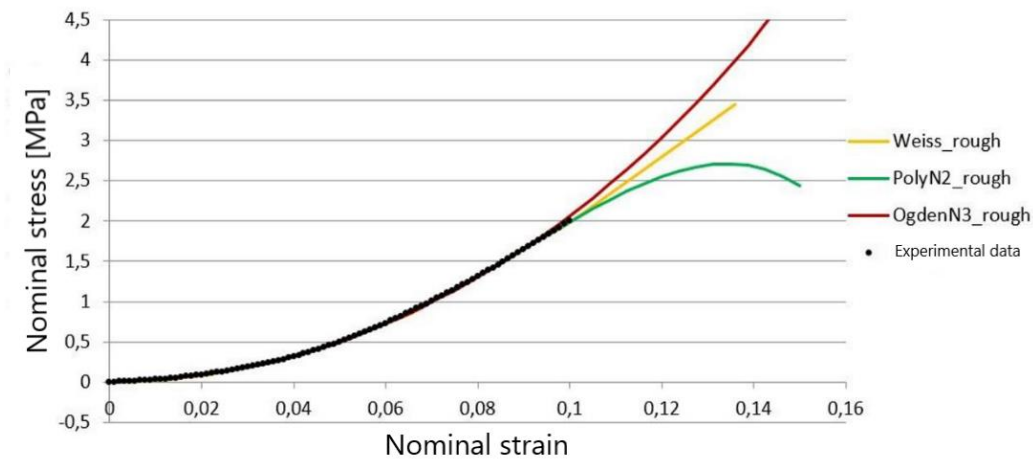


Figure 2.13: The graph allows a comparison between the curve obtained with the Weiss model shown in yellow, the curve obtained with the 3-order Odgen model in red, and the curve obtained with a 2-order polynomial model, all of which are fitted to the experimental data of Lim. Image adapted from Amicone and Dazzi thesis [30].

2.3.4.4. Saint Venant-Kirchhoff model

The Saint Venant-Kirchhoff model is a commonly used approach for describing the biomechanics of hyperelastic materials. It is based on the idea that the deformation of a material is proportional to the applied tension, while considering the anisotropic and non-linear behaviour of biological tissues.

Laurence in his Phd thesis [51] used this constitutive model, without the Poisson effect, to describe the behaviour of CTs:

$$S_{11} = (\lambda + 2\mu) E_{11} \quad (2.13)$$

Where:

- λ, μ are the Lamè constants.
- E_{11} is the Cauchy-Green tensor.

2.4. Computational models for TV

Stevanella's model [6] was the first complete model of the TV. The geometry was described in parametric terms, as previously described in [section 2.2.1 "Parametric models"](#). The discretization of the leaflets was based on triangular shell elements with a uniform thickness of 0.396 mm, which corresponds to the average value identified in their experimental campaign. The CTs were described by means of truss elements with a constant cross-sectional area and no branching. The biomechanical behaviour of the leaflets was modelled through the May-Newman constitutive material model [52], which describes the MV material as elastic, incompressible, transversely isotropic and highly non-linear. As this was the first model for the TV, much information was not available in the literature. The article therefore conducted a sensitivity study of the constitutive model parameters adopted to determine those that could best describe the behaviour of the tissue. Three significant distributions of collagen fibres were assumed in the study:

- A. a strongly circumferential fibre distribution, as occurs in the anterior leaflet of the MV.
- B. a network of collagen loosely oriented in a circumferential direction, similar to that observed in the posterior leaflet of the MV.
- C. a very low and evenly dispersed fibre distribution density, implying an isotropic tissue response.

The nominal stress distribution at the systolic peak in the three models is shown in the [Figure 2.14](#). The study shows that the displacements and stress distribution are insensitive to the fibre distribution, while the strain field is strongly influenced by it. From the results, it seems that the third hypothesis better reflects the real situation and therefore the hypothesis is that the fibres are poorly organised within the tissue of the TV leaflets. This article, highlighting the limitations of the work performed, provided an outline for subsequent work. It suggested the use of clinical imaging, an in-depth study of the materials of the main structures, including leaflets and CTs, a study of the variation in thicknesses at various points in the valve, consideration of the true nature of the CTs in terms of branching and insertion points in the leaflets, and an analysis of the spatial arrangement of pressure within the ventricle.

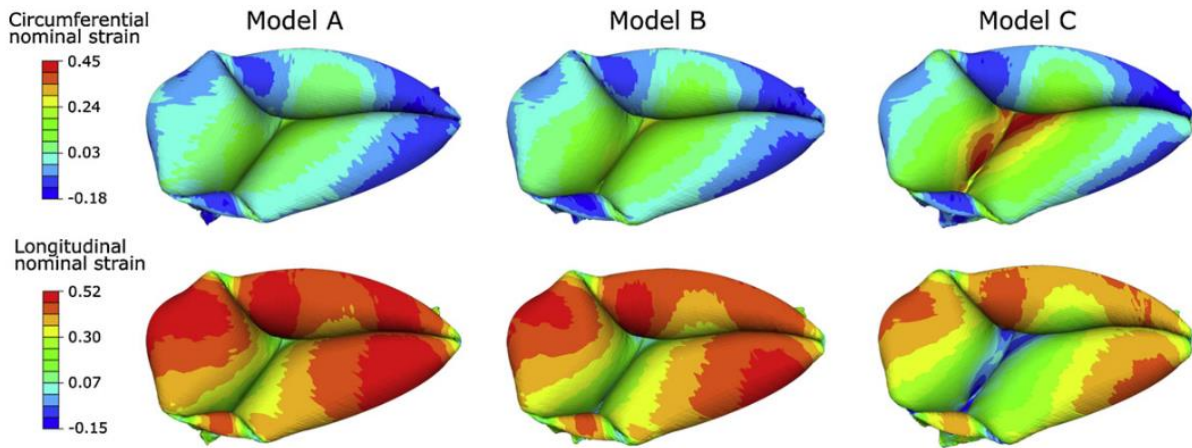


Figure 2.14: Result of systolic peak simulation in models A,B and C of nominal strain distributions in circumferential and longitudinal direction. Images adapted from Stevanella et al. article [6]

In the development of the model by Anversa and Careddu [37], efforts were made to address some limitations observed in previous models. The model's geometry is derived from manual segmentation of RT3DE echocardiographic images, as outlined in section [2.2.2. “Models based on clinical image segmentations”](#), aiming for enhanced model reliability. The chordae tendineae, invisible in the images, were modeled to approximate anatomical details as per article [13]. The CTs' material properties were described using a second-order polynomial function from the Abaqus material library, with parameters fitted using experimental data from Lim [47] specific to the TV, discussed in section [2.3.3. “CTs: biomechanical characterisation”](#). For the leaflets, a constitutive model and material description were adopted from the MV, based on the model proposed by Lee et al. [45] and experimental data from Pham et al. [40]. The leaflet surface was discretized using 3-node triangular shell elements, and the pressure load was calibrated on a test bench, peaking at 31.1 mmHg.

However, this model's primary limitations include the operator-dependent nature of manual tracking and the quality of available images. The results indicated incomplete coaptation, likely due to excessive tethering. The colorimetric map in [Figure 2.15's](#) left illustrates nodal displacement, while the right side displays systolic peak radial nominal strain from an evaluated valve. Peak stresses were observed at chordal insertions, suggesting that the observed coaptation issues might stem from the action of the CTs and their insertions.

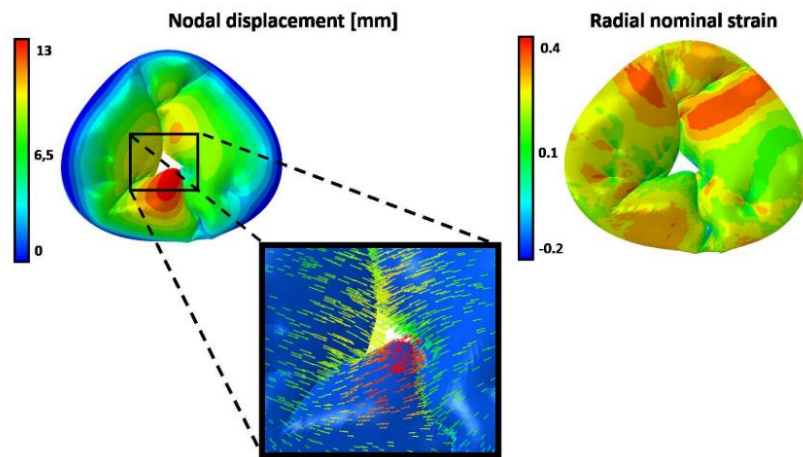


Figure 2.15: On the left is the colorimetric map of the nodal displacement in mm, and the directions of the resulting displacement vectors; on the right is the result in terms of nominal radial deformations at systolic peak. Images adapted from Aversa and Careddu thesis [37].

In 2018, Kong et al. [7] introduced a model aimed at clinical application, utilizing computed tomography images from three patients to create a computational valve model reflective of *in vivo* leaflet stresses and deformations. This model employed 8-node hexahedral elements for the valve leaflets and 2-node truss elements for the CTs, whose 3D geometry was inferred from literature due to their invisibility in CT images [13], [53]. The leaflets were modeled using the Holzapfel model with parameters fitted from material properties reported by Pham, while the CTs were described using the Ogden model [54], with parameters from uniaxial tests of human mitral valve chords. An iterative process was used to match the leaflet geometry with that observed in images. Mid-systole stress distribution, shown in [Figure 2.16](#), indicated maximum stresses in the leaflets' central regions and compression stresses near the CT insertion points and commissures, with mean stresses varying across different parts of the valve (from 37 to 80 kPa for the TVAL, from 25 to 91 kPa for the TVPL and from 24 to 63 kPa for the TVSL).

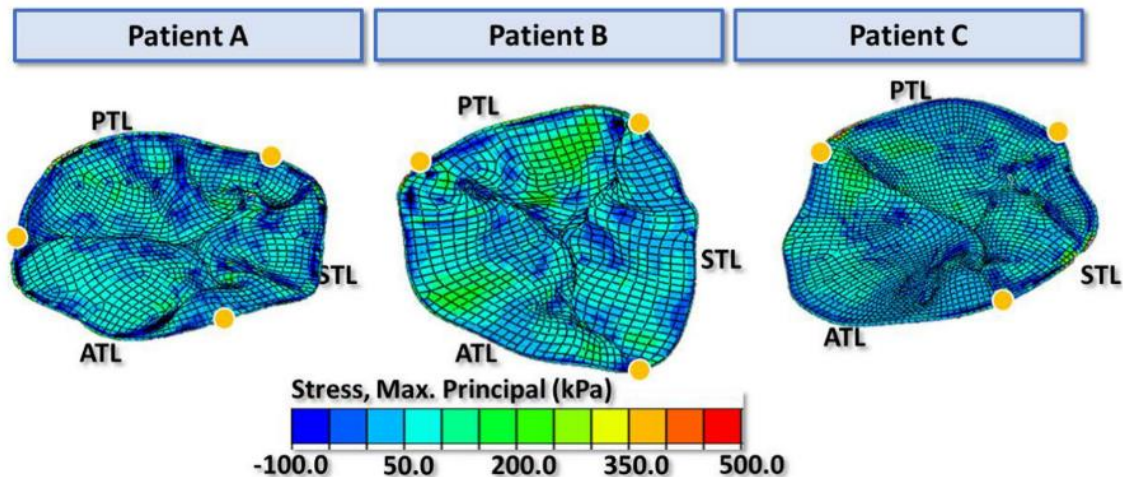


Figure 2.16: Distribution of the main maximum principal stress distribution in mid-systole on the leaflets for each of the patients. Yellow points indicating the annulus boundary between leaflets. Images adapted from Kong et al. article [7]

Locatelli and Manini [29] in 2019 developed a computational model based on images acquired by RT3DE of a porcine heart mounted on a test bench or mock loop. The valves used in the study were valves affected by regurgitation, on which they tested a new surgical repair procedure. The aim was to obtain a three-dimensional automatic valve reconstruction of both the regurgitant valve and the valves with repair. The automatic reconstruction workflow was based on a few basic steps:

- The point cloud resulting from the segmentation was recalculated using spline curves to obtain 32 parallel curves generating the curvilinear plot that describes a row version of the leaflets.
- A Butterworth low-pass filter was applied to the raw points.
- The coordinates were transformed from the local 2D system of the image plane to the global 3D system and a cylindrical reference system was defined.
- The point cloud was oversampled in the circumferential direction.
- The radial and axial coordinates were interpolated using cubic splines as a function of angular position.
- The points were resampled with 360 equally spaced points.

The commissures were traced in the images and were ordered by the two reference points: the APM and the connector inserted in the septal wall. The APM is traced in the short axis view, while the position of the other two muscles was reconstructed geometrically.

The leaflets were discretized with four-node elements and a characteristic size of 0.4 millimetres. The chords were represented with their own branches and discretized with truss elements. For each chord, the number of branches, number and point of insertion was defined based on the anatomical study conducted by Silver et al. [13]. Reinforcing elements were inserted to limit the stresses at the branching points. The leaflets were described using the Holzapfel computational model, described in [section](#)

[2.3.2.1 “Holzapfel model”](#), assuming a single family of fibres arranged in a circumferential direction. The constitutive parameters were defined based on the biaxial tests conducted by Amini et al., described in [section 2.3.1 “Leaflets: biomechanical characterisation”](#). The material of the CTs is described with a polynomial function of second-order strain energy, described in [section 2.3.4.1. “Second order polynomial function”](#), based on the data of Lim et al., described in the section 2.3.3 [“CTs: biomechanical characterisation”](#).

[Figure 2.17](#) shows that the computational model failed to describe the geometry of the TV in systolic configuration. Indeed, the regurgitant area between the actual images of the valve and the reconstructed model are very different. The images refer to a single valve, the images on the left refer to the regurgitant valve, the other two are tests of the repair procedure.

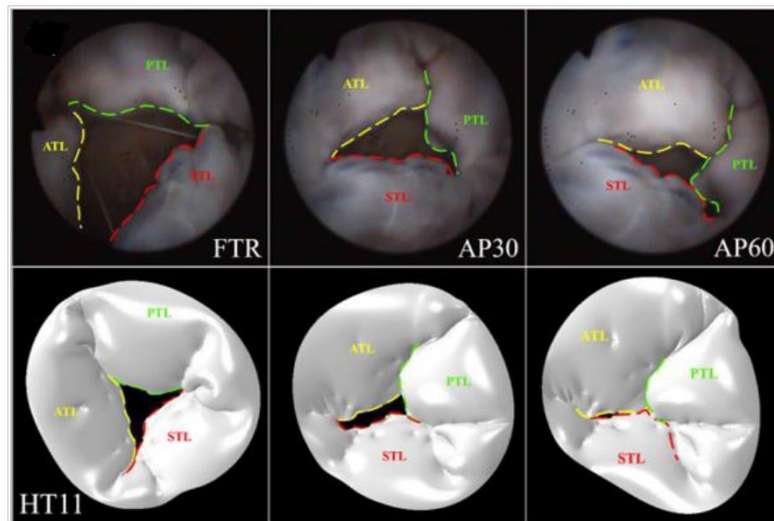


Figure 2.17: The images in the upper part of the table are images from experimental video taken during the movement of the heart on a test bench. The images at the bottom are the TV reconstructions with the automatic workflow. The images on the left refer to the original valve with regurgitation, the two configurations on the right (AP30 and AP60) are the result of the application of reconstruction surgery. Images adapted from Locatelli and Manini thesis [29]

The modelling approach studied by Locatelli and Manini [29] was exploited in the thesis by Amicone and Dazzi [30], who started from an already well-founded work and focused on improving the model. The thesis work focused on certain aspects:

- The definition and implementation of a filter to obtain temporal trends of the annulus displacement as natural as possible.
- The definition of a precise orientation of the collagen fibres to be given as input to the Holzapfel model. The fibres were arranged following a study proposed by Cochran et al. [55] for the mitral valve, shown in the [Figure 2.18](#). A direction was assigned circumferentially to the centre of the leaflet and in the annulus-margin free direction in the commissure regions. In the transition zones from

the centre of the leaflet to the commissure zone, a double sigmoid was defined to orientate the individual fibres according to the position of the element's centre of gravity. In the insertion zones, where the reinforcing elements are present, the fibres were oriented radially.

- For CTs, was proposed the use of the Weiss model, described in [section 2.3.4.3 “Weiss model”](#). This model describes a more natural fibre behaviour, i.e. once all collagen fibres have been recruited, the stiffness remains constant.

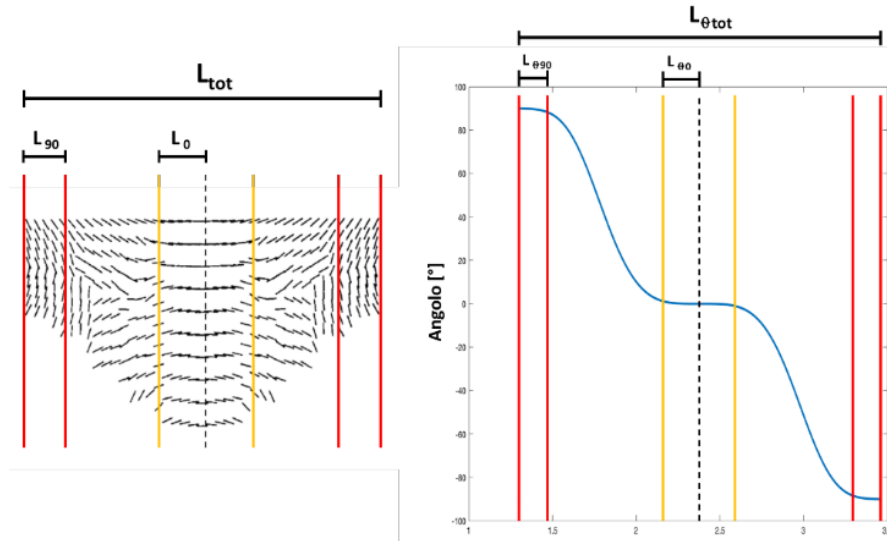


Figure 2.18: The figure shows the fibre orientation proposed and implemented in the Holzapfel model for describing the material in the leaflets. Images adapted from Amicone and Dazzi thesis [30]

In 2022, Laurence published his PhD thesis [51] entitled 'The tricuspid valve: mechanics, microstructure, modelling and simulation'. This is a complex and comprehensive work on all the most important TV features from engineering point of view. The valve was analysed starting with experimental tests to identify the characteristics of the tissues. The material characterisation was carried out at several levels. It started from a macroscopic characterisation of the leaflets by means of biaxial tests, described in [section 2.3.1 “Leaflets: biomechanical characterisation”](#), to the analysis of the architecture of the collagen fibres in the leaflets at the mesoscale and microscale level.

The second part of the thesis focused on the development of an in-silico model of the TV that incorporated the experimentally derived data. The geometry of the valve was described in parametric terms, according to the B-spline method described in [section 2.1.1. “Parametric models”](#). The leaflet surfaces were described as a shell element with a thickness of 0.396 mm and discretized with quadrangular S4 elements whose characteristic dimension was defined at 0.25 mm. The CTs were described as T3D2 truss elements of radius 0.23 mm. The leaflets were described as Lee's model, featured in [section 2.3.2.2 “Lee model”](#), assuming the tissue as transversely isotropic and incompressible. For the CTs, the Saint Venant-Kirchhoff model described in section

[2.3.4.4. “Saint Venant-Kirchhoff model”](#) was used without the Poisson effect. Young's modulus was set to $E = 40$ MPa and $\nu = 0$, and Lamé constants $\lambda = 0$ MPa and $\mu = 20$ MPa. The trans-valvular pressure was simplified to a linear expression with a maximum at 25 mmHg in 0.005 s and the peak being held for 0.4 s.

The biaxial tests, conducted in the first part of the work, showed that the pre-strains are related to the microstructure of the underlying tissue. In the computational model, was conducted an analysis on several isotropic and anisotropic configuration combinations to reproduce the circumferential and radial pre-strains as best as possible.

[Figure 2.19](#) shows the predicted systolic TV configurations for various isotropic combinations of pre-strains. The stresses on the leaflets increase as the pre-strains increase. In the first model, which does not consider pre-strains, it reaches a tension on the leaflets of 60 kPa, increasing to 20% the pre-strains reach 100 kPa. Furthermore, the systolic configuration of the TV changes substantially, considering a pre-strain of 20%, a valve with TR is obtained.

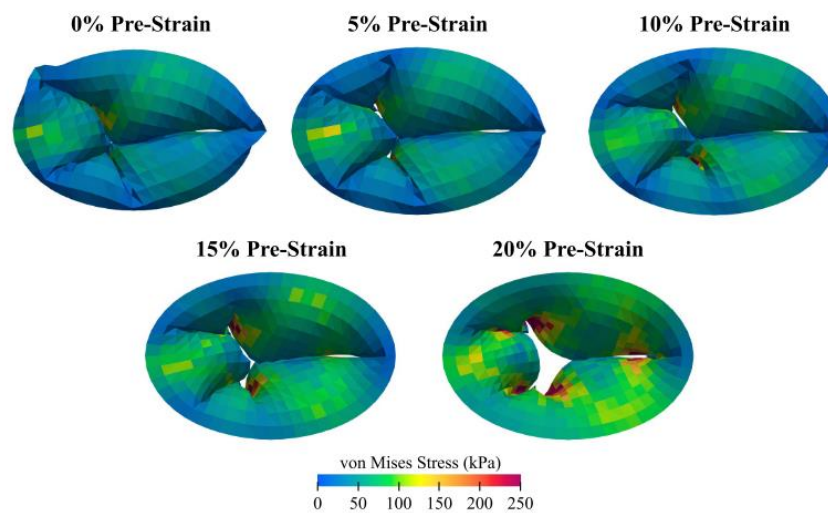


Figure 2.19: Results of FE models considering four levels of isotropic pre-strains. The analysed TV configuration is the systolic peak configuration. Images adapted from Laurence PhD thesis [51].

In the same year, Mrudang Mathur et al. [9] published another study on TV reconstruction. In their study, they used a totally new approach. As described in [Figure 2.20](#), they use a reverse engineering pipeline on a healthy TV in order to reconstruct a FE model. A healthy, beating human right heart was incorporated into an organ-preserving system to recreate a realistic haemodynamic environment for the valve. The dynamics of the annulus during the cardiac cycle were measured by markers and transvalvular pressure by miniaturised pressure sensors. To reconstruct the geometry, they combined information from the sensors with in vitro images of the valve leaflets. Material properties were extracted from the valves themselves using biaxial tests on leaflet tissue, reported in [section 2.3.1 “Leaflets: biomechanical characterisation”](#) and

described in Meador's article, and uniaxial tests on CTs. Tests showed that the level of anisotropy in TV leaflets is minimal, so an isotropic model could be used to describe the material with good results. The constitutive model used for the description of the leaflets was proposed by Kamensky et al. [56] that is based on Lee's model, described in [section 2.3.2.2 "Lee model"](#). The Ogden model, described in [section 2.3.4.2 "Ogden model"](#), was used to describe the CTs. The leaflets were discretized with C3D8R hexahedral elements and a uniform thickness of 0.78 mm, the CTs as T3D2 truss elements, and different diameters depending on the type of CT: 0.65 mm for CTs for TVAL, 0.64 for TVPL and 0.71 for TVSL. To validate the model, valve closure was simulated, and the geometry obtained was then compared with ultrasound images.

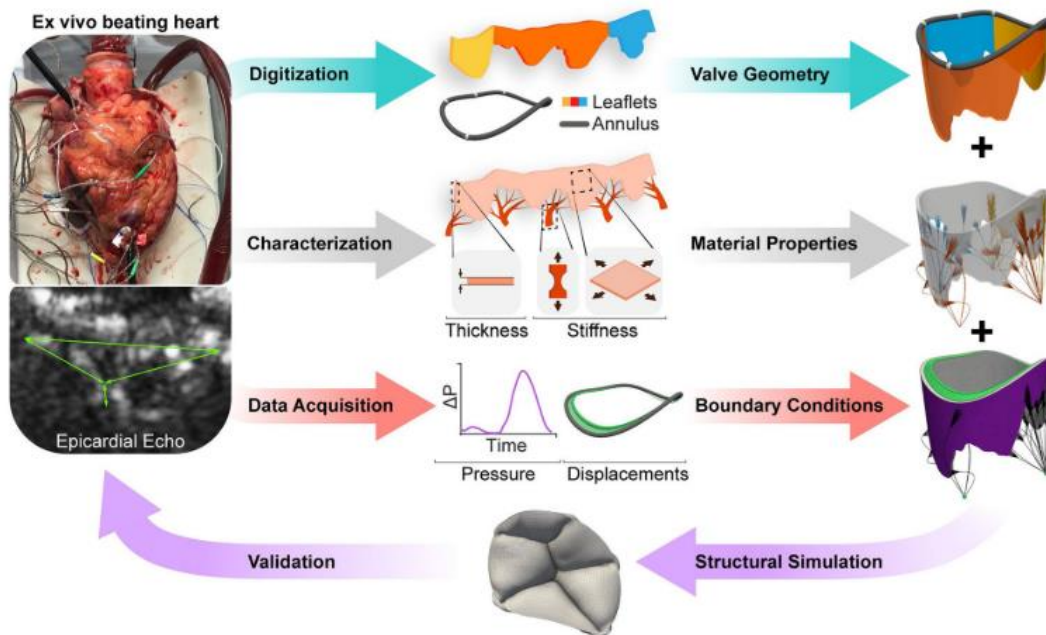


Figure 2.20: Schematic representation of the engineering process (inverse). the geometry of the model was obtained by digitising the motion of the valve ring the geometry of the leaflets. The material properties were obtained from in vitro mechanical tests on each leaflet on the CTs. Transvalvular pressure was acquired using a pressure microsensors. The FE model was used to predict valve closure, and the result was validated using epicardial echocardiographic images of the beating heart. Images adapted from Mrudang Mathur et al. article [9].

3 Methodology

3.1. Aims and objectives of the thesis

The TV has garnered increased importance in the clinical context, and the need has arisen for a thorough understanding of its biomechanics to deal pathological conditions such as TR. Most of the models available today are based on simplistic assumptions, which are not always adequately justified by functionally equivalent behaviour of its structures and are hardly adequate to simulate a real clinical application. Finite-element models can be used on a large scale and for multiple purposes such as predicting valve behaviour under pathological conditions, improving existing surgical techniques, and assessing their impact in advance, developing new medical devices and optimising prosthesis design.

The aim of this thesis is to implement a reliable reconstruction workflow ([Figure 3.1](#)) for the development of a finite element (FE) model of the regurgitant valve that is as accurate as possible to the patient-specific geometry detected using echocardiography. The software used in the development of the workflow are MATLAB (Version R2023a, The MathWorks, Inc., Natick, MA, USA) and Abaqus/Explicit (SIMULIA, Dassault Systèmes).

The echocardiographic images used were acquired in the Locatelli and Manini's thesis [29]. These images were specifically collected to study the biomechanics of porcine TVs affected by regurgitation. In the same thesis, they simulated the in-vitro TV repair idea proposed in the article by Jaworek et al. [10], and described in section [1.2.3. "New approach"](#).

Post-operative ultrasound images of the valve, in which the APM, PPM and annulus points have been brought closer together, will be used to verify the impact that the idea of moving the free wall of the ventricle closer to the septum has on the biomechanics of the valve.

This chapter will describe the strategy, assumptions and techniques used to obtain an accurate 3D model of the TV with regurgitation, the generation of the computational grid or mesh, the description of the tissue properties and the boundary conditions imposed to obtain the most accurate simulations possible. The end of the chapter will also discuss the in-silico test method applied to test the idea of Jaworek et al. [10]

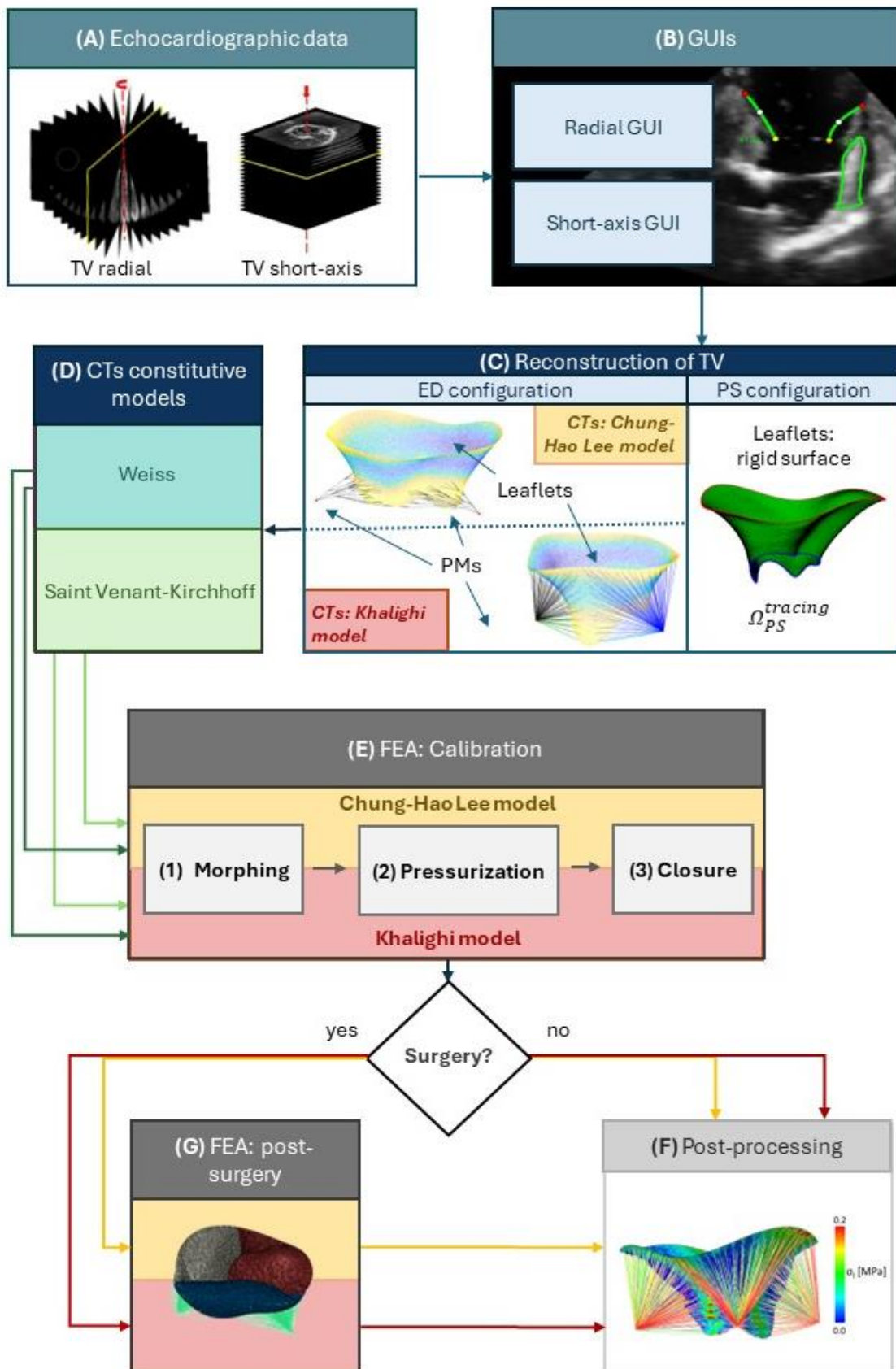


Figure 3.1: Overview of the project workflow

3.2. Echocardiographic Data

The initial data are images acquired by RT3D ultrasound of porcine TV with TR placed in a mock circulation loop system. The aim of the system was to simulate pulmonary circulation to study TV behaviour. This system had some limitations, e.g. the pump connector was placed in the septal wall at the level of the septal leaflet and during the simulation of the cardiac cycle caused a non-physiological behaviour of the right ventricle, which contracts during diastole and enlarges during systole. In addition, to place the connector properly in the septal wall, part of the left heart was removed, losing some widely known landmarks used in clinical practice when analysing echocardiographic images.

Images were acquired with a Philips iE33 system with TEE trans-oesophageal probe (CX7-2t, Philips, Eindhoven, The Netherlands). The probe was positioned in contact with the epicardium, between the afterload and preload connectors to allow an atrial view of the valve.

The parameters set were:

- Temporal resolution: 30 frames/cycle
- Spatial resolution: 0.70x0.69x0.54
- Data extraction: Cartesian DICOM

These measurements were carried out and constitute a key aspect of the thesis by Locatelli and Manini [29].

3.3. Data preparation workflow

The ultrasound data obtained using the Philips system are raw data that must be converted before they can be visualised and processed. The acquisition of 3D ultrasound data is guided by a DICOM "Enhanced US Volume" standard that provides information on how to save 3DE data. Despite its existence, this standard is not widely used by machine manufacturers Philips Medical is one of the few, perhaps the only one, that partially uses it. The standard requires the construction of a regular orthogonal volume, i.e. a Cartesian system, and that the data is saved in DICOM format.

The workflow for processing basic ultrasound data to obtain image planes that can be used for manual segmentation of the main anatomical valve structures was defined in Locatelli and Manini's thesis [29]. This workflow was used, without modification, and is therefore reported below:

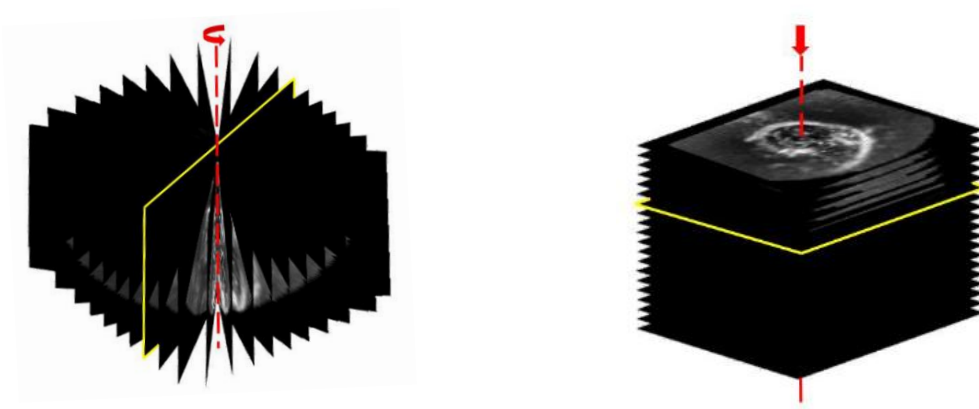
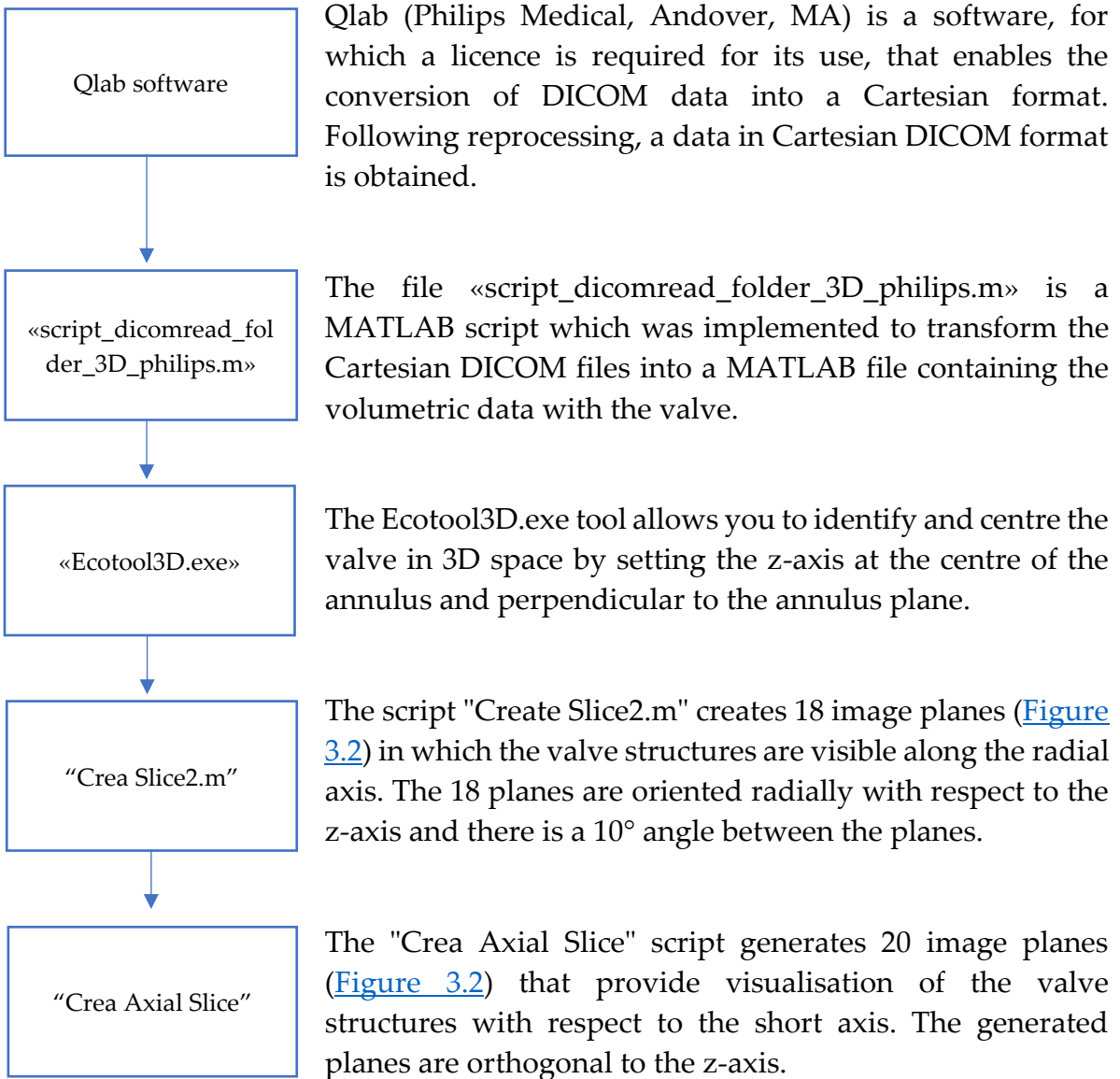


Figure 3.2: The two images represent the 18 planes (left) along the radial axis and the 20 planes (right) along the short axis of the valve structures generated at the end of the workflow. Images adapted from Locatelli and Manini's thesis [29]

3.4. Radial segmentation

The MATLAB (Version R2023a, The MathWorks, Inc., Natick, MA, USA) environment provides tools for the creation in simplified terms of a graphical user interface allowing a 'point and click' type of control. Although the most recent versions of the MATLAB software provide a new tool called 'App Designer', a graphical user interface (GUI) was used for the development of the graphical user interface. This choice made it possible to exploit part of the code, which had already been implemented, and simply extend it to suit the needs of this project.

The aim was to obtain an interface that would allow the manual segmentation of certain specific regions of the image planes obtained at the end of the workflow described in the paragraph [3.3 “Data preparation workflow”](#). In the case of TV, it was essential to trace its main structures; thus, the annulus, free margin, leaflets and PMs.

The peculiarity of the images making available for this work is that the mock loop configuration used, and the positioning of the probe did not refer to scans of clinically common standard planes. Furthermore, the removal of a large part of the left heart and the focus on the valve meant that the images did not contain the main structures that are identified and used as clinical landmarks. For example, the valvular plane was not complete in the images, and the aortic and mitral valves were not present.

This introduced the need to identify other reference points specific to the set-up used. In the mock loop chosen configuration the heart was set in motion via a system of pumps and connectors. One of these connectors was inserted into the septal wall of the ventricle and is clearly identifiable from the images. This artificially introduced element became an important reference point during the reconstruction.

3.4.1. Radial GUI development

The GUI was developed starting from a previously developed version, showed in the left side of [Figure 3.3](#). The GUI ([Figure 3.3](#)) and the algorithms for identifying structures were then modified to obtain useful data. For example, the APM was identified with a single point, this methodology was based on very simplistic assumptions; so, it was replaced with a point cloud that also allowed information to be obtained on the shape and orientation in space of the papillary itself. In addition, only a single PM was traced, whereas at least two PMs were usually visible from the images; therefore, the possibility of tracing all visible PMs was added.



Figure 3.3: Left: menu of the starting GUI version. Right: new version of the GUI specially developed to allow a good segmentation of echocardiographic images of a TV. This version is the one that was used for manual image segmentation on this thesis work.

Within the GUI, a tool called viewer was added. The viewer allows to display in the three-dimensional space all the points drawn in the various image ([Figure 3.5](#)). Manual tracing inherently introduces inaccuracies, and the images were frequently unclear ([Figure 3.4](#)). However, the viewer tool enabled instant verification of the traced structures, allowing for the assessment of their accuracy in the 3D reference system based on anatomical understanding.

Additionally, the viewer also incorporated the feature of displaying, through a 4th order Fourier approximant, in real-time what the conformation of the valvular annulus could be, based on the points already traced. In this way, it was possible to obtain a useful indication on the quality of the tracing of the annulus points and a reference for those planes where the structures are not clearly identifiable. The mathematical manipulations on the point clouds required to apply the Fourier transform will be discussed in the section [3.6.1.1. “Reference system and 3D point-cloud orientation”](#)

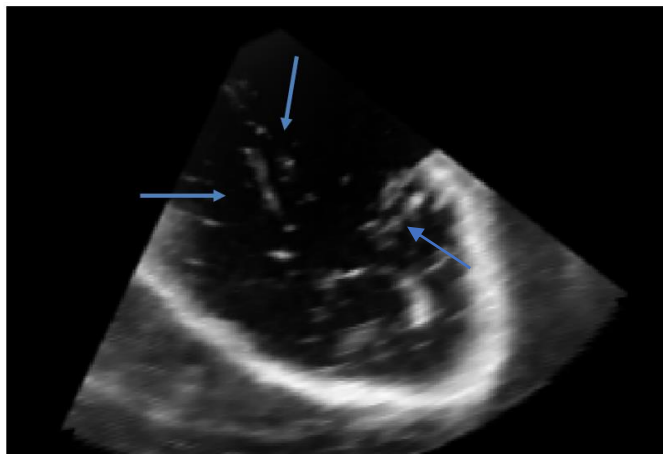


Figure 3.4: the blue arrows identified three leaflets that are visible in the image. It is possible that one of the two leaflets visible on the left of the image is a shadow or an artefact.

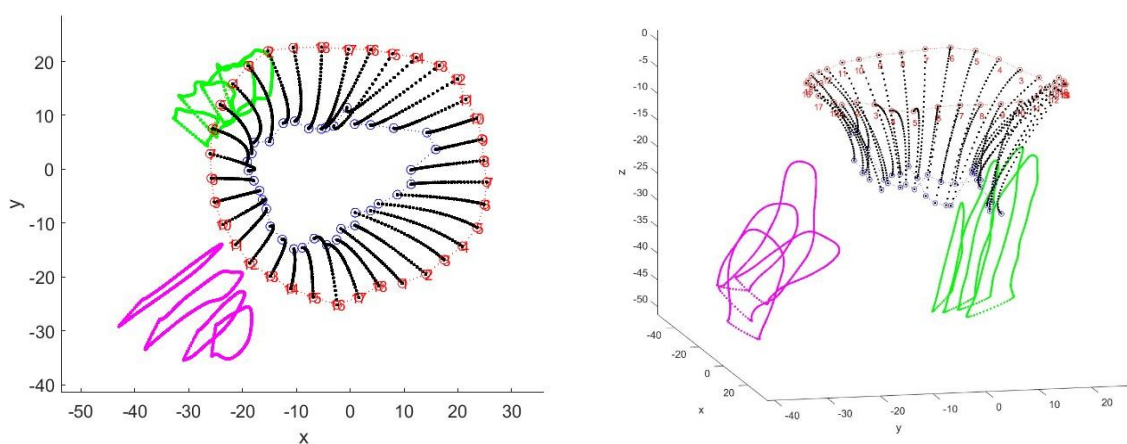


Figure 3.5: Tool viewer: allows you to view plotted points in three-dimensional space. In the images in red are the annulus points, in black the leaflets and in blue the free margin. The elements in green and pink are the tracings in the various planes of the PMs. In the image on the left, the center of mass of the point cloud has been positioned at the origin of the reference system.

3.4.2. Identification and tracing of reference structures

The GUI displayed the substructures of the TV and landmarks along the radial axis of the valve. Multiple frames can be displayed for each cardiac cycle, the characteristics of the echocardiograph used during the recording the mean is 30 frames for cycle. On each of the 18 previously derived 2D image planes, the GUI was implemented to provide the possibility of manually trace the structures of interest. For the purposes of this work, the frame of ED when the valve is in open configuration and SP when the valve is in close configuration were traced. The valves available were all pathological with TR; therefore, at the systolic frame the valve is never completely closed.

Depending on the frame of interest, the tracings were performed in a single plane or in several planes.

The GUI gives the possibility to identify the annulus, leaflets, free margin, connector and PMs.

3.4.2.1. Annulus

The annulus, as described in the section [1.1.1. “Annulus”](#), is an anatomical structure that works as a transition element between the leaflets and the myocardial wall. On each plane, a pair of points representing the right and left parts of the annulus were identified.

In echocardiographic images, the structure is not always clearly identifiable, due to poor image quality and the orientation of the planes not always ideal. Manual segmentation is therefore easily susceptible to errors. To improve the quality of the tracings, it was decided to be allowed to visualise the individual points in the viewer with the red colour in [Figure 3.6](#). In addition, it is possible to characterise how these points are interpolated by the fourth-order Fourier transform with a much larger number of points than traced, as shown with the blue colour in [Figure 3.6](#). The fourth-order Fourier transform is also used in the reconstruction phase, to limit the noise resulting from manual tracing. This mathematical technique is not commonly used as an regularization tool, but previous studies of mitral valve annulus [57] reconstruction have used it successfully.

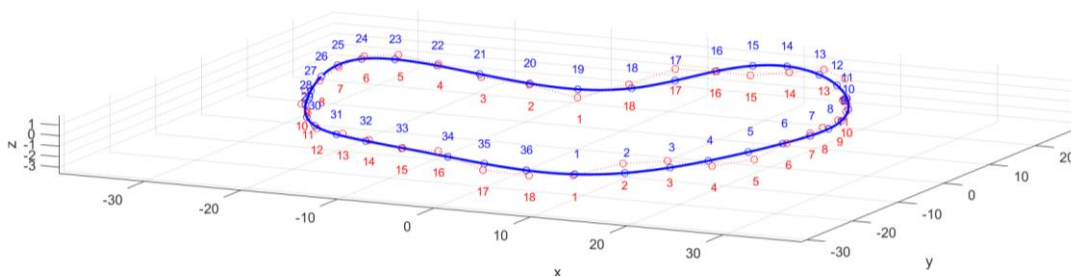


Figure 3.6: The graph shows in red the manual traces for each plane, in blue the position the corresponding points assume after applying the fourth-order Fourier transform.

3.4.2.2. Free margin and leaflets

The free margin was identified as the cluster of the last points belonging to each segmented leaflet; therefore, on the radial planes, two points were also identified in each plane, one for each visible leaflet profile. After plotting the annulus, free margin and leaflet points, all points are interpolated by a cubic spline ([Figure 3.7](#)). The spline is resampled to 32 evenly distributed points. At the end of the tracing of the three structures (annulus, free margin and leaflets), an $18 \times 2 \times 32$ matrix is obtained. This matrix defines the coordinates of the tracing points in the 2D image plane of the TV leaflets geometry.

To compare the tracing with previous planes and identify whether the traced length is consistent with the anatomical information available, the length of each segmented profile is plotted on the image, together with each new segmentation ([Figure 3.7](#)).

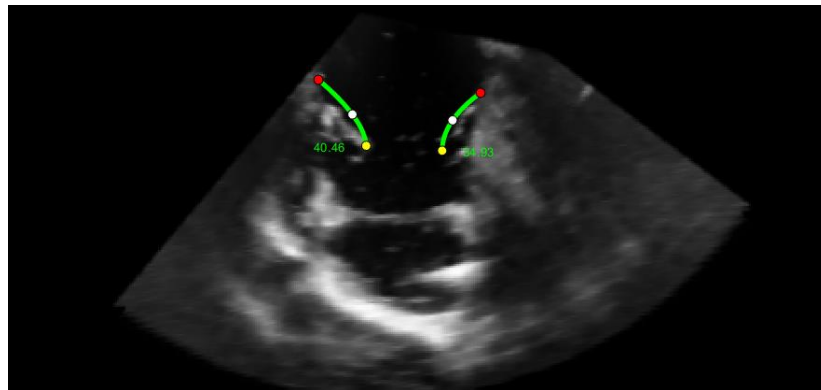


Figure 3.7: In the image the red dots identify the annulus, the yellow dots the free margin and in green the leaflets with their lengths

3.4.2.3. Connector

The connector that has been artificially inserted into the wall of the ventricular septum is easily identifiable on echocardiographic images. This element was traced by a point on each plane where visible ([Figure 3.8](#)).

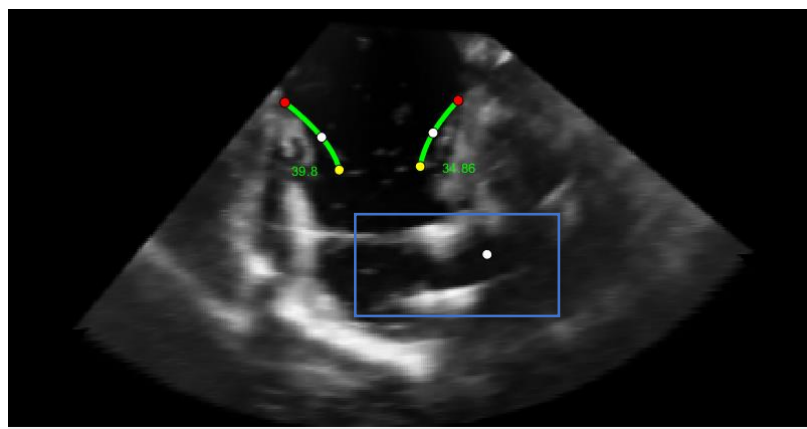


Figure 3.8: Tracing of the connector with a white dot.

3.4.2.4. PMs

From the pictures, it is possible to clearly identify some of the PMs. The APM is distinguished by its size and is always present. It is often possible to identify a second muscle, which usually corresponds to the PPM. The SPM is more difficult to identify, its morphology is not always well defined, and in 20% of subjects it is not present.

For the identification of the PMs, a Matlab *drawfreehand* function was exploited ([Figure 3.9](#)). This function allows a freehand drawing to be created around the region of interest (ROI). At the end of the drawing, a matrix of size $N \times 3$ containing a number N

of coordinates defined by the speed of the drawing and the extent of the area of interest is generated for each PM. The reported coordinates correspond to the plotted line.

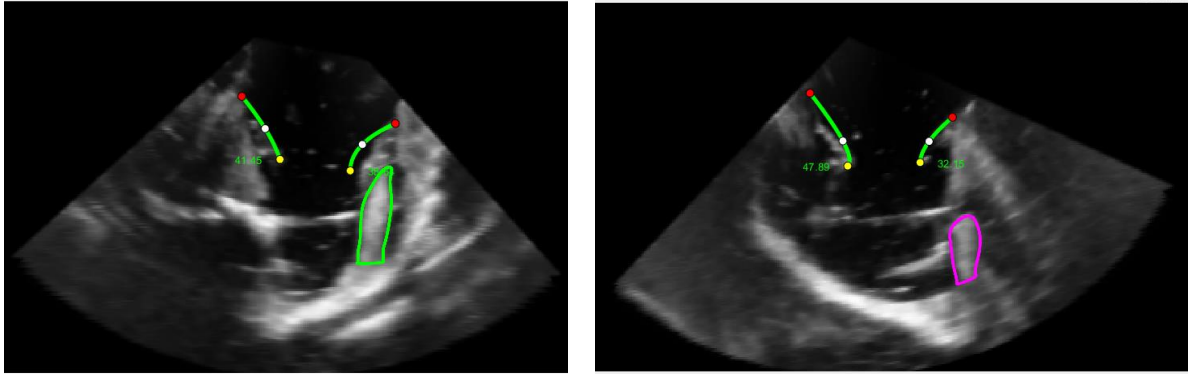


Figure 3.9: In the pictures, one can see how the “drawfreehand” function works. The papillary muscles traced are in green the anterior PM, in magenta the second PM.

The connector and papillary muscles are important landmarks and has been exploited in the reconstruction phase for the definition of leaflets and for the orientation of the valve in 3D local reference system.

3.5. Short-axis segmentation

The short-axis GUI or axial GUI, as in the case of the radial axis GUI, was developed from an existing GUI with similar purposes. The short-axis GUI is able to move through the 20 axial planes previously identified, for each one of the recorded frames. The previous version of short-axis GUI allowed only to trace the commissures, while the possibility of identifying PMs sections has been added (Figure 3.10). Again, the images have been segmented only to the frames of interest: the ED and the SP.

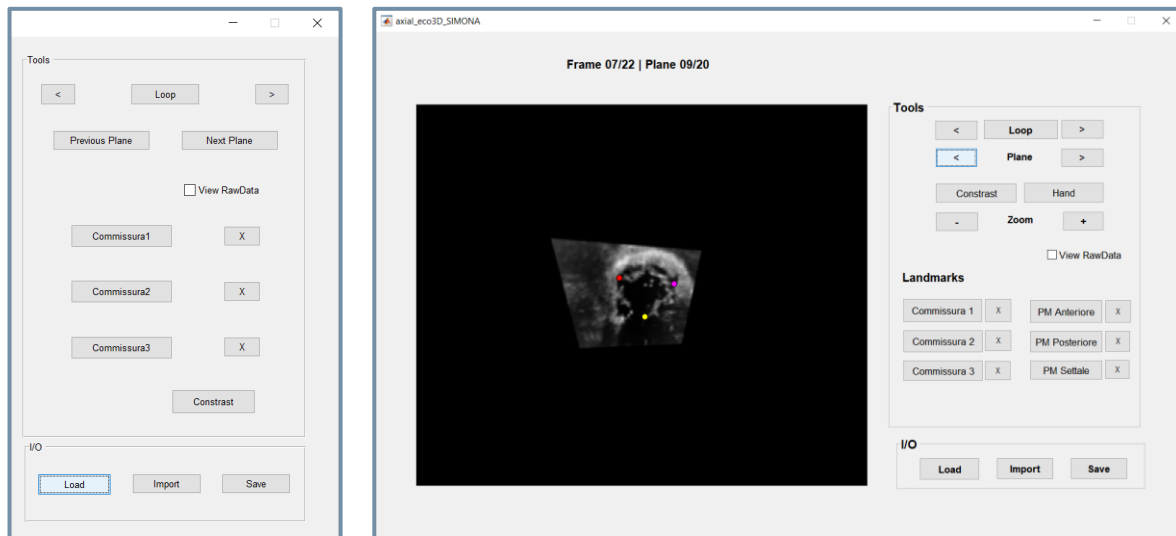


Figure 3.10: Left: Initial version of the short axis GUI. This only allows identification of the three commissures with red, magenta and yellow dots. Right: Improved version that also allows the ROI to be traced around the area of visible PMs.

3.5.1.1. Commissures

The commissures were drawn only on the plane closest to the annulus, where the information from the coaptation of the leaflets was still visible. In fact, the simplest and least error-prone method is to identify the commissures as the points where the coaptation of the leaflets is visible. Each commissure was identified by a single point.

3.5.1.2. PMs

This point is an improvement on the previous version of the GUI. In the case of HT11 valve, two of the three muscles were visible. This information, which proved important in the reconstruction phase, was saved, as in the case of the radial GUI by identifying the ROI of each papillary, on each plane where it was visible and clearly identifiable.

3.6. TV model generation

The data acquired from the tracing of the main TV structures were processed using the software Matlab (Version R2023a, The MathWorks, Inc., Natick, MA, USA). The TV was reconstructed in ED configuration and in SP configuration. The CTs, not visible from the images, were modelled parametrically following previous studies in the literature [58], [8], [59].

3.6.1. TV open surface, at ED

The reconstruction of the leaflets' surface in ED configuration required a series of steps, which will be described in detail below. The points plotted on the various planes of the ultrasound images were oriented in Matlab's local reference system; they were also filtered and resampled to obtain a uniform point cloud. The point cloud was the basis for the definition of a triangulated surface to which the characteristics of a TV were associated.

3.6.1.1. Reference system and 3D point-cloud orientation

At the end of the segmentation, both along the radial and short axis, the matrices extracted contain the image plane information and the x and y coordinates of each point plotted. The points are then defined in two co-ordinates. In order to use the information, it is necessary to transform the co-ordinates of the plotted points from the 2D reference system of the image plane to a 3D reference system. The 3D reference system in which the coordinates will be defined will first be a global reference system, corresponding to the Cartesian DICOM reference system, then a local reference system that is convenient for working on the data in the Matlab environment.

The first step is to convert the coordinates from the image plane reference system to the three-dimensional reference system. This transformation requires these data:

- O_i = vector containing the coordinates of the origin of the i -th image plane with respect to the global reference system
- res_x and res_y = number of pixels along the local directions x and y
- V_{x_i} and V_{y_i} = versors defining the orientation of the local x and y directions of the i -th image plane with respect to the global reference system

Considering a generic point P , belonging to any of the structures drawn on the i -th image plane, the relation proposed in the thesis of Locatelli and Manini [29] is:

$$[X, Y, Z] = O_i + x res_x V_{x_i} + y res_y V_{y_i} \quad (3.1)$$

The annulus point-cloud in the diastolic frame, inserted into the global reference system, was used as a reference to position the valve in space. The centre of gravity of the diastolic annulus was centred in the origin of the global reference system, and all other points shifted accordingly.

A Principal Components Analysis (PCA) function in Matlab was used to define the valve orientation in space. This function PCA is based on a statistical technique called the principal component technique and was first described by mathematician Karl Pearson in the early 1900s. This technique is based on the relationships between variables and makes it possible to reduce the size of data matrices. In data processing, orthogonal axes describing the maximum variance of the data are defined. The PCA function exploited in the Matlab environment provides more information, the one of interest to us are the coefficients of the principal components [67]. The coefficients were used to obtain a right-handed cylindrical reference system and to invert, if necessary, the ventricle in the negative z -direction.

In the thesis by Locatelli and Manini Manini [29] and Amicone and Dazzi [30], in which the experimental setup is described, it is known that the connector is placed in the septal wall. From the tracing of echocardiographic images, the positions of the connector and the commissure are known. The angular coordinate of the midpoint of the leaflets between these the antero-septal commissure and the postero-septal commissure was used as the rotation angle in radians for the definition of the rotation matrix. Applying the rotation matrix to the points plotted all the valve was rotated so that the midpoint of the septal leaflet had zero angular co-ordinate.

$$rot = \begin{bmatrix} \cos(\theta_{rot}) & -\sin(\theta_{rot}) & 0 \\ \sin(\theta_{rot}) & \cos(\theta_{rot}) & 0 \\ 0 & 0 & 1 \end{bmatrix} \quad (3.2)$$

[Figure 3.11](#) shows on the xy plane the orientation of the valve leaflets represented by the black, red and green points. The central black star corresponds to the origin of the reference system and the centre of mass of the annulus point cloud. Applying the rotation matrix, it is obtained that the midpoint of the septal leaflet, identified by the blue star, is always at zero theta (i.e. to the right), being the theta of the cylindrical reference system between $-\pi$ and $+\pi$.

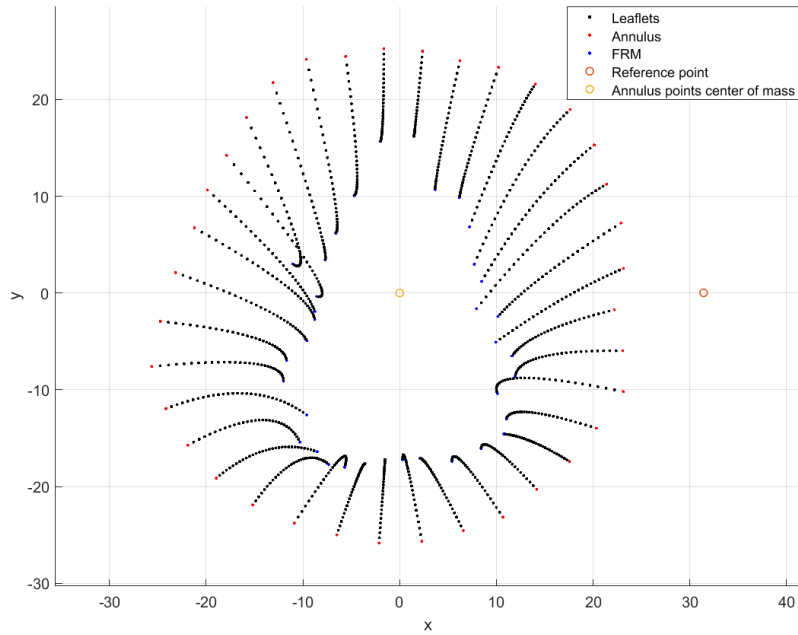


Figure 3.11: view of the valve leaflets in the xy plane, represented by the black, red and green points. The centre of gravity of the annulus point cloud corresponds to the origin of the reference system and is identified by the yellow circle. The orange circle is the midpoint of the septal leaflet, used as reference point.

[Figure 3.12](#) depicts the outcome of applying the mathematical tools just described to the matrices containing the coordinates of the points traced in the image planes.

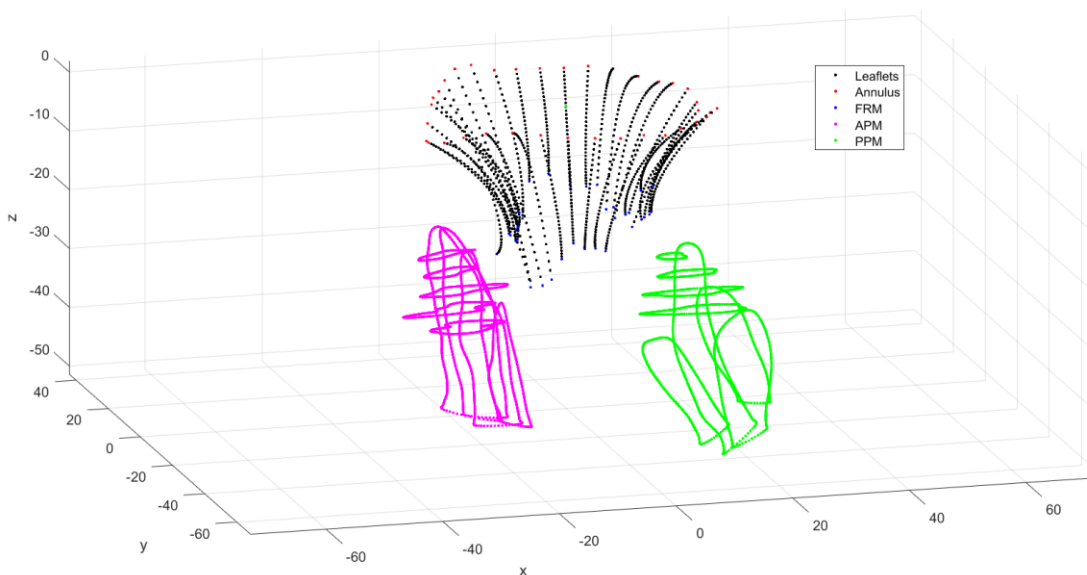


Figure 3.12: Three-dimensional plot of the points drawn on the image planes. The black dots are the leaflets, at the ends the red dots are the annulus and the green dots are the free margin. The green and magenta lines are the traces of the ROIs along the short axis and along the radial axis of the APM and PPM.

3.6.1.2. Filtering and resampling

The points describing the leaflets are subject to noise caused by both manual segmentation and reference system transformations. Tondi in his thesis [57] used a 4th order Fourier transform to filter and resample the point cloud describing the MV annulus with good results. In this work, the same principle was exploited, but applied to the entire point cloud describing the leaflets, from the annulus to the free edge ([Figure 3.13](#)).

The point cloud is described in a cylindrical reference system, knowing the radial p and axial h positions of the points and in coefficients a_k , b_k , c_k and d_k used in the Fourier function:

$$\begin{cases} \rho(\vartheta) = a_0 + \sum_{k=1}^4 [a_k \cos(k\vartheta) + b_k \sin(k\vartheta)] \\ h(\vartheta) = c_0 + \sum_{k=1}^4 [c_k \cos(k\vartheta) + d_k \sin(k\vartheta)] \end{cases} \quad (3.3)$$

The application of this function requires special expediency. The centre of gravity of the points to be filtered and resampled must coincide with the origin of the reference system. To obtain the desired result, the point cloud characterising the leaflets was divided into 32 sub-clouds corresponding to the 32 interpolation levels of the radial axis GUI spline. Each sub-point-cloud was first translated so that its centre of mass corresponded to the origin of the reference system, the Fourier transform was applied and then it was relocated to its original position. The number of points with which each curve was resampled is constant and is strictly dependent on the characteristic dimension defined in the triangular mesh creation phase.

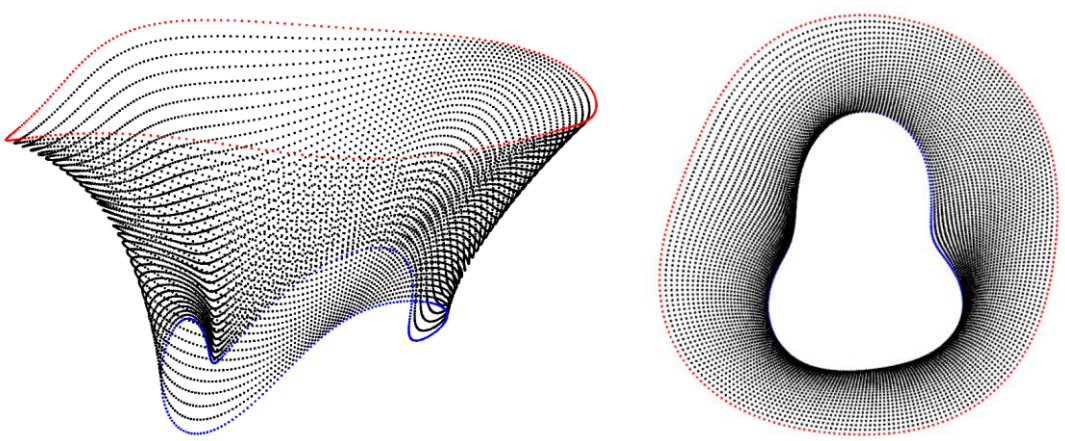


Figure 3.13: (left) three-dimensional plot of the points obtained after applying the 4th order Fourier transform to the 32 levels of the leaflets. (right) plot of the same points in the xy plane

3.6.1.3. Surface triangulation

Leaflets were defined as three-node shell elements (ABAQUS, S3R type elements).

For the definition of the triangulation, a preliminary connectivity matrix was generated ([Figure 3.14](#)).

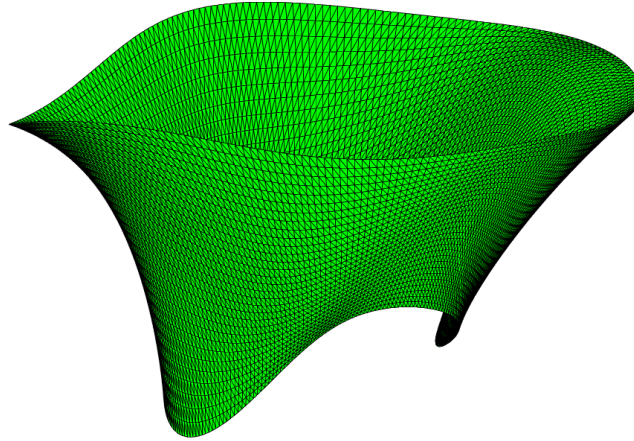


Figure 3.14: Mesh generated after application of the Triangulation algorithm

The triangulated point cloud (see [Figure 3.14](#)) underwent smoothing through a Python script utilizing a Taubin filter. This filter, known for improving mesh quality by minimizing surface irregularities, preserves the mesh's overall geometry and crucial features like edge shapes.

The script required an STL file of the mesh, specifying the number of iterations and the bandwidth frequency for the Taubin filter. Each iteration involved smoothing operations influenced by the selected frequency.

To enhance mesh quality post-smoothing, another Python script leveraging the *gmsh* library was employed for remeshing, establishing the final mesh ([Figure 3.15](#)).

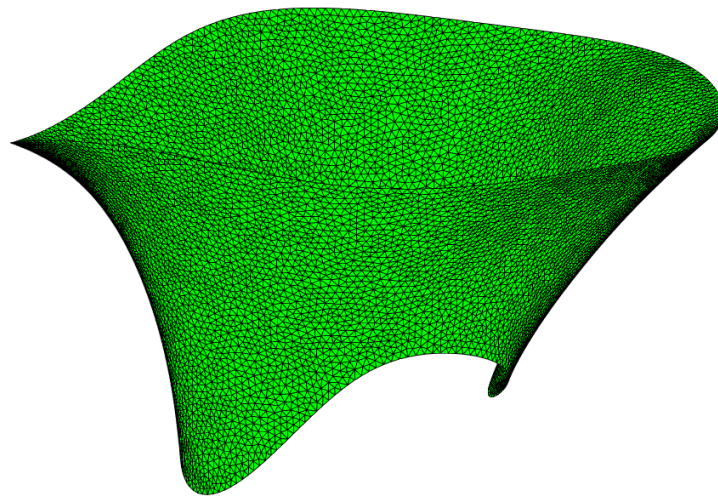


Figure 3.15: Mesh obtained after the application of Taubin's filter to smooth out surface irregularities and applying the remeshing of the triangulation.

3.6.1.4. Commissures and leaflets identification

In the literature, there are two criteria for the identification of commissures:

- A. Geometric Criterion [A]: Utilized by Johnson et al. [36], this method identifies commissures at the intersection points of two leaflets along the free margin. Mathematically, these points are at the curve's maximums describing the free margin, emphasizing the geometrical configuration of the leaflets.
- B. Echocardiographic Identification [B]: This approach, applied in the thesis by Locatelli and Manini, locates commissures based on the leaflets' coaptation points, which are observed at the annulus level in echocardiographic images, focusing on the clinical imaging aspect [29].

The criterion based on the geometry of the free margin represents a common practice used in the TV in-silico parametric models [36], [51], but it does not match the clinical identification of commissures on echocardiographic images. On the other hand, the identification of commissures on echocardiographic images is done manually, so it is operator-dependent and susceptible to error. Neither criterion provides total assurance of the position of commissures, and both have a certain margin of error; therefore, both were evaluated ([Figure 3.16](#)).

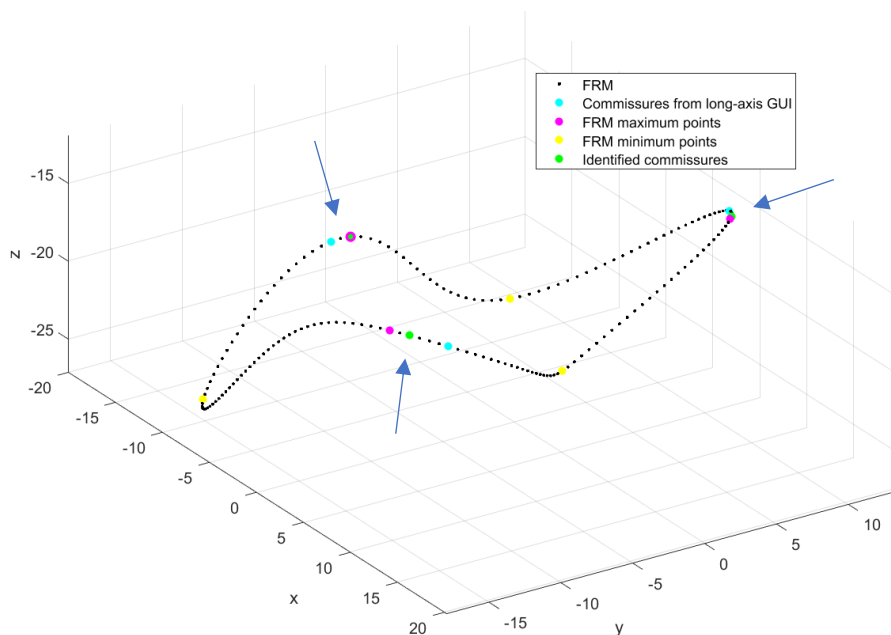


Figure 3.16: The curve plotted is the free margin curve. The points in yellow represent the curve's minimum points. The magenta stars are the maximum points. The blue, red and green stars are the points resulting from plotting along the short-axis view of the valve. The points in green, also indicated by the blue arrows, are the points calculated using the weighted average of the two.

By analysing the shape of the reconstructed free margin, the maximum points of the curve were calculated for the identification of the commissures according to criterion

To identify commissures, the maximum points on the curve of the reconstructed free margin were calculated using geometric criterion. Additionally, information regarding the commissures' positions was derived from the segmentation performed using the SA GUI, mapped to the free margin level according to the echocardiographic identification criterion. When the data from both criteria showed reasonable consistency, the manually traced information was retained. However, if the manual tracing significantly diverged from Criterion A, the latter's data was prioritized. In cases where the data fell between these extremes, a weighted average of both values was used.

The preference for data from the free margin curve analysis over segmentation-derived information was due to the short-axis ultrasound images being marred by substantial noise and low pixel count, which compromised the precision of point identification. With higher quality images, a reversal in the weighting of the information types might be more appropriate, underscoring the reliance on the quality of imaging in determining the most reliable method for commissure identification.

Mathematically, the minimum points of the free margin curve were calculated. The incremental ratio of the point plotted in the SA GUI from the calculated maximum point (Δ_{max}) and the incremental ratio of the point plotted in the short-axis GUI from the calculated minimum point (Δ_{min}) was calculated. At this point, the weight parameter was calculated.

$$\Delta_{max}(i) = \frac{|z_{com_{GUI}}(i) - z_{point_{max}}(i)|}{|\theta_{GUI}(i) - \theta_{max}(i)|} \quad (3.4)$$

$$\Delta_{min}(i) = \frac{|z_{com_{GUI}}(i) - z_{point_{min}}(i)|}{|\theta_{GUI}(i) - \theta_{min}(i)|} \quad (3.5)$$

$$weight(i) = \frac{\Delta_{max}(i)}{\Delta_{max}(i) + \Delta_{min}(i)} \quad (3.6)$$

If:

- $weight < 0.2$: the commissure is defined according to the information derived from manual tracing.
- $weight > 0.4$: the commissure calculated as the maximum point of the FRM.
- $0.2 < weight < 0.4$: calculation of the weighted average of the two information items:

$$theta_{final}(i) = theta_{GUI}(i) * weight(i) + theta_{max}(i) * (1 - weight(i)) \quad (3.7)$$

The commissures, once identified, were ordered and named. The way the valve was orientated theta equals zero corresponds to the midpoint of the TVSL, so the two commissures with the lowest angular position modulus were the two commissures at the TVSL. Viewing the valve from the xy plane ([Figure 3.17](#)) is in a configuration that is consistent with the en-face observation of the valve in echocardiographic images. This factor, together with the definition of a right-handed cylindrical reference system,

makes it possible to identify the commissure with negative theta as the antero-septal commissure, the commissure with positive theta as the postero-septal commissure, and the third commissure is the antero-posterior. Hence the identification of the sets of the three leaflets ([Figure 3.17](#)).

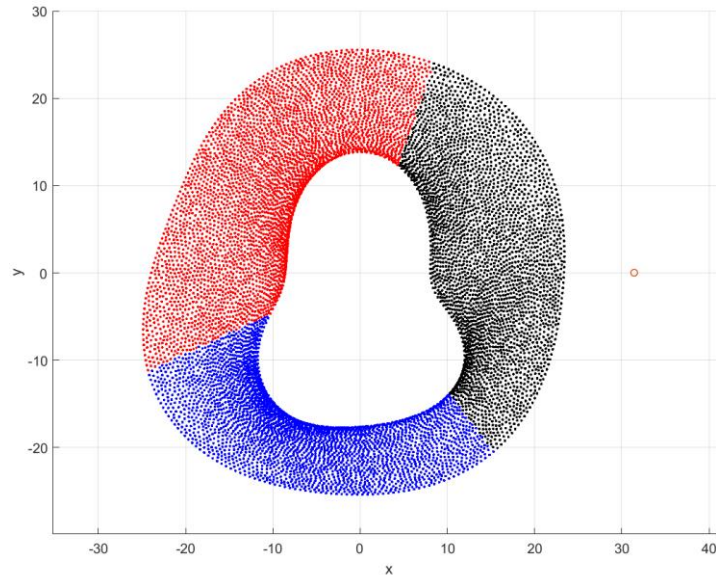


Figure 3.17: The orange circle is reference point for the rotation matrix that provides information on the midpoint of the TVSL; so, in black the TVSL, in red the TVPL and in blue the TVAl.

3.6.1.5. Mesh characteristics

All present models of the tricuspid valve describe the thickness as constant throughout the valve. This assumption is not consistent with the anatomical information [13], and could bias the stress distribution on the leaflets derived from the in-silico models.

[Table 1.2](#) shows the thickness data measured in the article by Heyden et al. [18]. It can be seen from the data that the average valve thickness varies, although to a small value, from leaflet to leaflet. In addition, it is known that the clear zone is the least thick area of the leaflets, and the thickness increases moving towards the ends because towards the annulus it goes into the myocardial walls, while at the level of the free edge most of the chordal insertions are located [13].

The model for describing thickness is based on the proximity to specific characteristic points, where thickness values are explicitly defined. For each commissure, a point 3 mm below the annulus was pinpointed to bypass the rough zone. From this commissure point, the midpoint in the clear zone was determined, serving as the model's minimum point. This process was repeated for each commissure. Along the curve that interpolated these points and mirrored the leaflets' shape, midpoints within the clear zones of the three leaflets were identified. These midpoints were assigned a thickness value, 10% less than the average leaflet thickness suggested by Heyden et al.

[18], At each commissure point, the thickness value was averaged between the two neighbouring leaflets.

From these six points, thickness values were progressively increased circumferentially through a linear function, capping at the highest mean value reported by Heyden et al.[18] for the TVAL, further increased by 10%. Given the high variability in Heyden's reported values, using these as a variability measure was deemed unsuitable; instead, the minimum and maximum values were defined as the average values $\pm 10\%$. This methodology allows for a detailed mapping of thickness across the valve, considering both specific anatomical landmarks and averaged empirical data.

The pattern then starts the minimum value assigned in one of the 6 points and grows to the maximum following a linear function (Figures 3.18). If the leaflet is large enough then it will reach the value of maximum thickness; the larger the leaflet, the more extensive the region of maximum thickness will be. If the extent is less, a thin leaflet will result. The reason for this modelling is based on the principle that under physiological conditions one can assume that the systolic and diastolic pressure is the same in all individuals, neglecting small variations; therefore, the pressure difference between the ventricle and atrium also remains approximately the same. If a leaflet is large, this means that it will have to cover a large area of the orifice and be subjected to intense stress and strain; if a leaflet is small, the area to be covered is smaller and therefore the stress and strain are less. This model takes into account the fact that physiologically, tissue tends to remodel itself based on the stresses to which it is subjected. If a leaflet is small, it will be subjected to reduced efforts, and it does not make sense for it to have the same thickness as a very large leaflet.

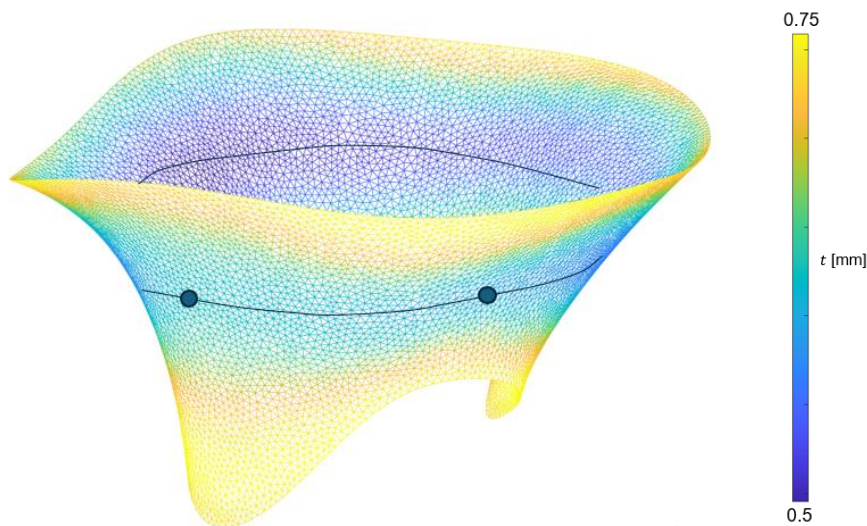


Figure 3.18: Plot of the thicknesses along the leaflets. The line indicates the area in which the minimum points have been identified, the two dots indicate two of the points in which the minimum values have been defined. One is located at the radial coordinate of the commissure and one at the radial coordinate midpoint of the leaflet.

The biomechanical response of the TV leaflets was described using the hyperelastic Holzapfel constitutive model, already described in section [2.3.2.1. "Holzapfel model"](#). The constitutive parameters of the model, specific to each leaflet, were derived on the basis of data obtained from biaxial tensile tests on porcine tricuspid valves by Khoiy et al. [39], reported in section [2.3.1. "Leaflets: biomechanical characterisation"](#) ([Figure 2.5](#)). For the description of fibre orientation, following the work done in the thesis by Amicone and Dazzi [30], the idea was made to reproduce the architecture and physiological rearrangement of collagen.

Cochran et al. [60] analysed and mapped the architecture of collagen fibres in the anterior leaflet of porcine MVs using the techniques of small angle light scattering and polarised light microscopy. [Figure 3.19](#) shows the normalised and averaged graph of the 4 samples reported in the article.

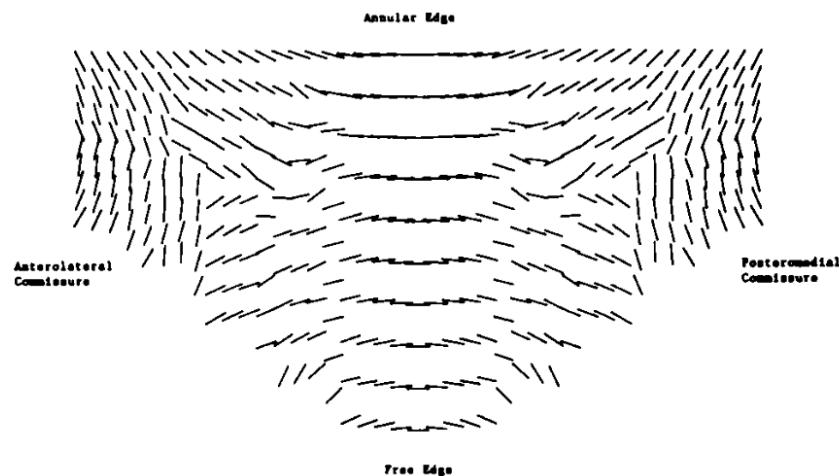


Figure 3.19: Normalised graph of collagen architecture in porcine MV anterior leaflets. Image adapted from Cochran et al. article [60]

The article indicates is that the fibres tend to lie parallel to the annulus in the central portion of the leaflet and then gradually orient themselves orthogonally as they approach the commissures. From a physiological point of view, near the commissures most of the chordal insertions are present and this orientation should preserve a continuity between leaflet and chord. The study was taken as a reference as there is no similar study in the literature for TV leaflets. In the work of Amicone and Dazzi [30], the orientation of the fibres was calculated for each individual element and was associated with the position of its centre of gravity. A double sigmoid working as a function of the angular coordinate of the single element's centre of gravity was used to describe the particular fibre arrangement.

In the final step of triangulation, nodes were arranged such that the surface normals pointed outward from the atrial surface ([Figure 3.20](#)). This arrangement facilitates the specification of surfaces for force and pressure application in simulations.

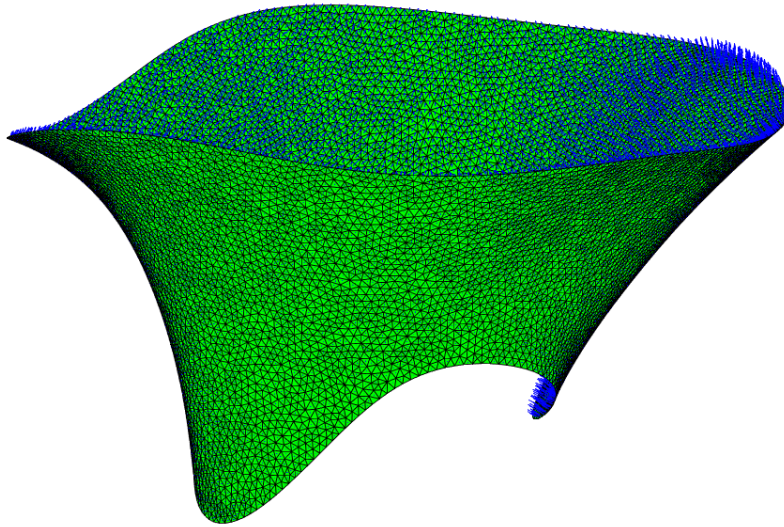


Figure 3.20: The surface normals were evaluated to determine if they were all oriented in the same direction and, if not, to rearrange them correctly. This step is fundamental for the simulation pipeline.

3.6.2. TV close surface, at SP

The TV was modelled at both ED and SP. The valve configuration at SP will play a key role in the simulations, as will be explained in section [3.7.2. "Systolic closure with CTs calibrations"](#). The data for the SP reconstruction of the TV is derived from the tracings performed at the SP frame using the two implemented GUIs. To achieve consistency between the two valve configurations in the local reference system, the point clouds were roto-translated using the same logics and parameters derived from the TV ED configuration. The point clouds were translated towards the origin of the reference system corresponding to the centre of mass of the ED annulus, rotated with respect to the z-axis so that the ventricle is in the negative z-direction, inserted into a right-handed cylindrical reference system and rotated with respect to the xy-plane using the rotation matrix identified on the basis of the midpoint of the TVSL in the ED configuration.

The point cloud belonging to the leaflets, once appropriately oriented in the local reference system, was filtered and resampled ([Figure 3.21](#)) with the 4th-order Fourier transform, following the same process as described in section [3.6.1.2. "Filtering and resampling"](#)

A little foresight has been taken into account in this step. In the simulation described in section [3.7.2. "Systolic closure with CTs calibrations"](#), a shift of the annulus points from the ED configuration to SP was imposed. In order to obtain a homogeneous distribution of deformations in the transition between diastole and systole, the points in the ED and SP configuration had to correspond in number and distance variation between consecutive points. The reference pattern for the arrangement of the annulus nodes is the ED configuration where the nodes were positioned using 4th-order

Fourier transform, where the dependent variable is theta, i.e. the angular coordinate. To this purpose, an algorithm has been implemented that calculates the distance between two consecutive points of the annulus in the ED configuration in terms of the displacement ratio with respect to the angular coordinate. The displacement ratio is then applied to the arrangement of the points of the annulus in SP configuration, rescaled with respect to the overall length of the annulus.

Algorithm 1 change ratio of the length of n^{th} element of the annulus

- 1: Initialisation of the vector containing the ED annulus nodes;
 - 2: Calculation of distance between two points belonging to two consecutive rows of the vector
 $d = \text{Punti}(2:\text{id}_{\text{pt_end}}-1,:) - \text{Punti}(1:\text{id}_{\text{pt_end}}-2,:);$
 - 3: Calculation of cumulative sum of segment lengths, with the function *cumsum*;
 $L = \text{sqrt}(\text{dot}(d,d,2));$
 - 4: $L_{\text{cum}} = \text{cumsum}([L]);$
 - 5: Calculation of the fraction of length for each segment, dividing the cumulative length of each segment by the total length of the route. The relative length of each segment has a value between 0 and 1.
 $\text{fraz} = [\emptyset; L_{\text{cum}}/L_{\text{cum}}(\text{end})];$
-

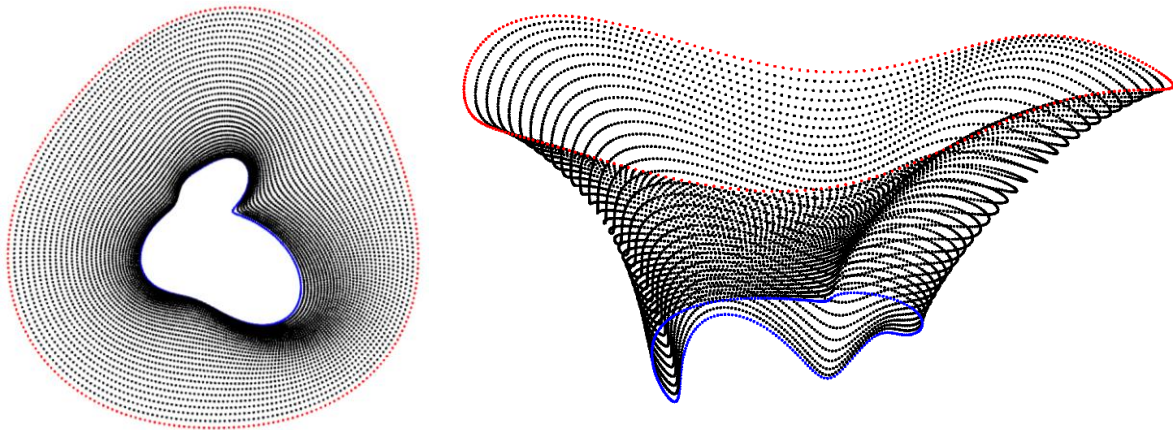


Figure 3.21: Representation of the point clouds obtained for SP TV after being filtered and resampled. In the image the points in red represent the annulus, those in blue the free margin and in black the leaflets.

The point cloud was subjected to [Algorithm 1: Triangulation](#). For the SP configuration ([Figures 3.21](#)), the quality of the mesh is not crucial; therefore, it was decided to apply the smoothing phase of the valve surface only in the case where, considering all the location variations in position of the annulus points before and after the application of smoothing, the difference was not significant. For the maximum value detected, the

ratio of this value to the dimension defined per infinitesimal element was calculated. Smoothing is only applied in the case where the ratio is less than 0.1 ([Figure 3.22](#)).

In the case of the TV in SP configuration, the orientation of the normal of each individual element was also verified graphically.

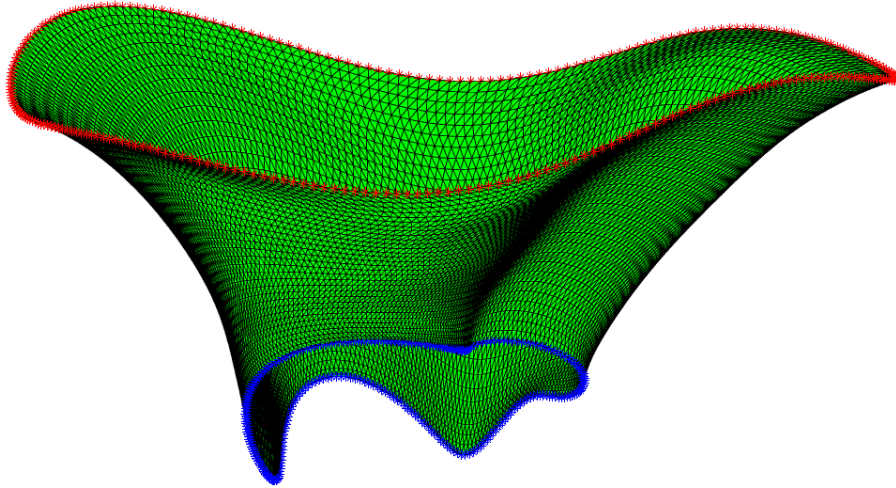


Figure 3.22: the image represents the TV to SP following triangulation. The annulus is highlighted in red and the free margin in blue.

3.6.3. PMs

The description of the PMs was obtained by combining the information from the tracings and that from the anatomical knowledge of the TV.

Two of the three PMs were clearly identifiable in the images. These PMs were segmented with respect to both the radial axis and the short axis of the TV. In the literature, even the most recent articles, identify the PMs as a single point that corresponds to the PM head coordinate, assuming that all PM CTs originate from that point [36], [61]. Also in this work, information from the tracings was used to define the coordinates of three points corresponding to APM, PPM e SPM.

For the two traced PMs, the centre of mass of the point cloud closest to the commissure was calculated and that point was identified as the PM ([Figure 3.23](#)).

The third PM was not evident from the images, so its position had to be defined on the basis of certain assumptions. In Locatelli and Manini's thesis [29], the angular position of the PMs was associated with that of the corresponding commissures. A circumference centred in the origin of the axes and with a radius equal to the average of the two distances of the two PMs was calculated in order to define the PMs' ρ and height (z). The circumference was then translated at z equal to the average of the height of the two PMs ([Figure 3.23](#)).

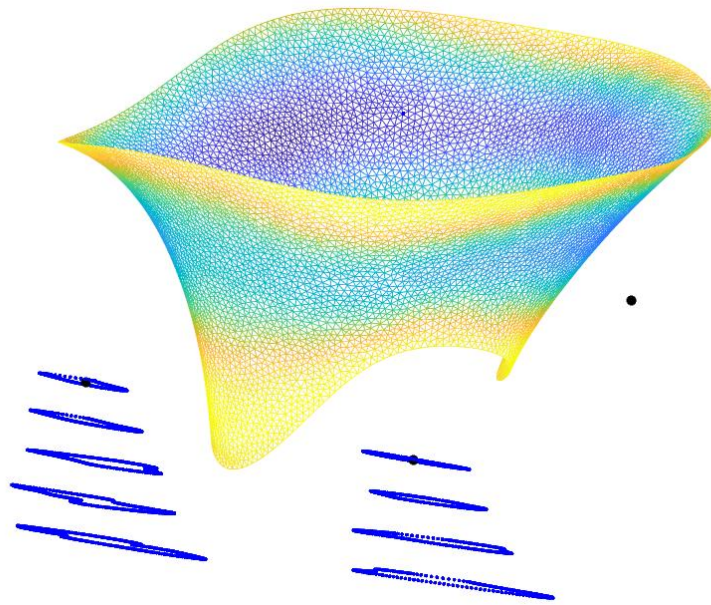


Figure 3.23: The figure displays the TV in ED configuration, in blue are the PMs traces from the segmentation through the short-axis GUI. The points in black are the APM, PPM and SPM. As the third PM is not visible from the images, the position was calculated based on the information from the other two PMs and considering the theta of the reference commissure.

The same approach was used for both ED and SP papillary identifications. ([Figure 3.24](#))

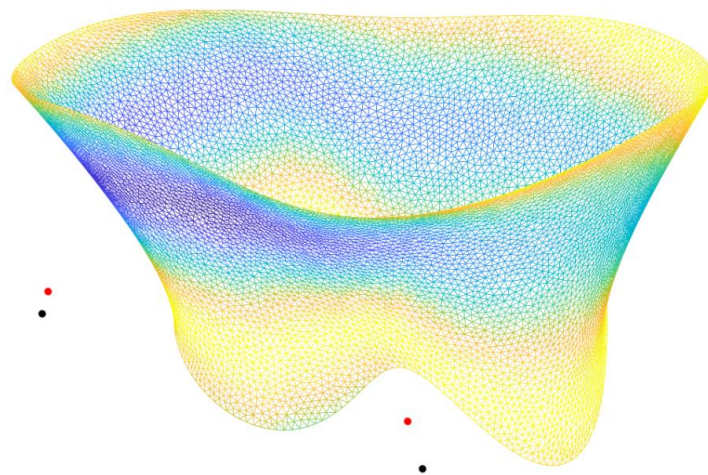


Figure 3.24: In the figure, the black dots represent the PMs calculated for the ED configuration, the black ones the PMs calculated for the SP configuration. The way the TV is oriented, only 2 of the 3 PMs are visible.

CTs

Anatomically CTs can have different shapes and conformations as described in section [1.1.4. "Chordae Tendinea"](#).

Typically, CTs originate from PMs, branching out to attach on the ventricular surface of the leaflets, primarily to support the leaflets during systole when the valve closes. In imaging modalities like ultrasound, Cardiac CT, or MRI, chordal structures are not visible, leading to various modeling approaches discussed in literature. This thesis focuses on the challenge posed by pathological valve conformations, specifically examining TV affected by TR. The issue of valve coaptation failure or incompleteness is critical for simulations, as it significantly contributes to the instability of the entire TV system.

In the current work, two parametric models of CTs found in the literature were tested:

- Model proposed by Kamensky et al. [56] for atrio-ventricular valves and amplified by Chung-Hao Lee et al. [8] to the specific case of TV;
- Functionally equivalent model of CTs proposed by Khalighi et al. [58] for the MV

Both models were used to describe the biomechanical characteristics of CTs and were tested with two constitutive models: the constitutive Weiss model, described in section [2.3.4.3. "Weiss model"](#) and the Saint Venant-Kirchhoff model, described in section [2.3.4.4. "Saint Venant-Kirchhoff model"](#).

For the Weiss constitutive model, the constitutive parameters reported by Amicone and Dazzi [30] were used after sampling the data obtained from uniaxial theses by Lim et al.[47]. The parameters have been reported in [Table 3.1](#).

| a_1 [MPa] | a_2 [MPa] | a_3 [MPa] | a_4 [-] | a_5 [MPa] | a_6 [MPa] |
|-------------|-------------|-------------|-----------|-------------|-------------|
| 16.8521 | -1.6506 | 16.15996 | -5.68092 | -57.57986 | 56.57986 |

Table 3.1: Values of the 6 constitutive parameters identified for the CTs of the TV, reported in Amicone and Dazzi's thesis [30] and obtained by fictitious data from Lim[47]. Parameters a_1 and a_2 refer to the isotropic description of the Weiss model, while parameters a_3 , a_4 , a_5 and a_6 are the parameters calculated for the anisotropic component.

The transition point of the curve was identified as $\lambda_f^* = 1.063$.

The Saint Venant-Kirchhoff model was used considering the parameters given in Laurence's PhD thesis [51]; therefore, Poisson's coefficient was considered to be 0, Young's modulus $E = 40$ MPa, and consequently Lamé's constants assumed value $\lambda = 0$ MPa and $\mu = 20$ MPa.

3.6.3.1. Chung-Hao Lee parametric model for TV CTs

The basic model was described using geometries typical of computer-aided design (CAD). In this work, the parametric description was reported in the Matlab working environment. There are many studies in the literature in which parametric descriptions of natural [62], [63] and prosthetic [64], [65] valves have been performed. Here too, however, there is a limited presentation of parametric design-based TV modelling. The parametric model of Chung-Hao Lee et al. [8] is an extension of Kamensky's et al. [56] model based on information from clinical data and parametric inputs ([Figure 3.25](#)).

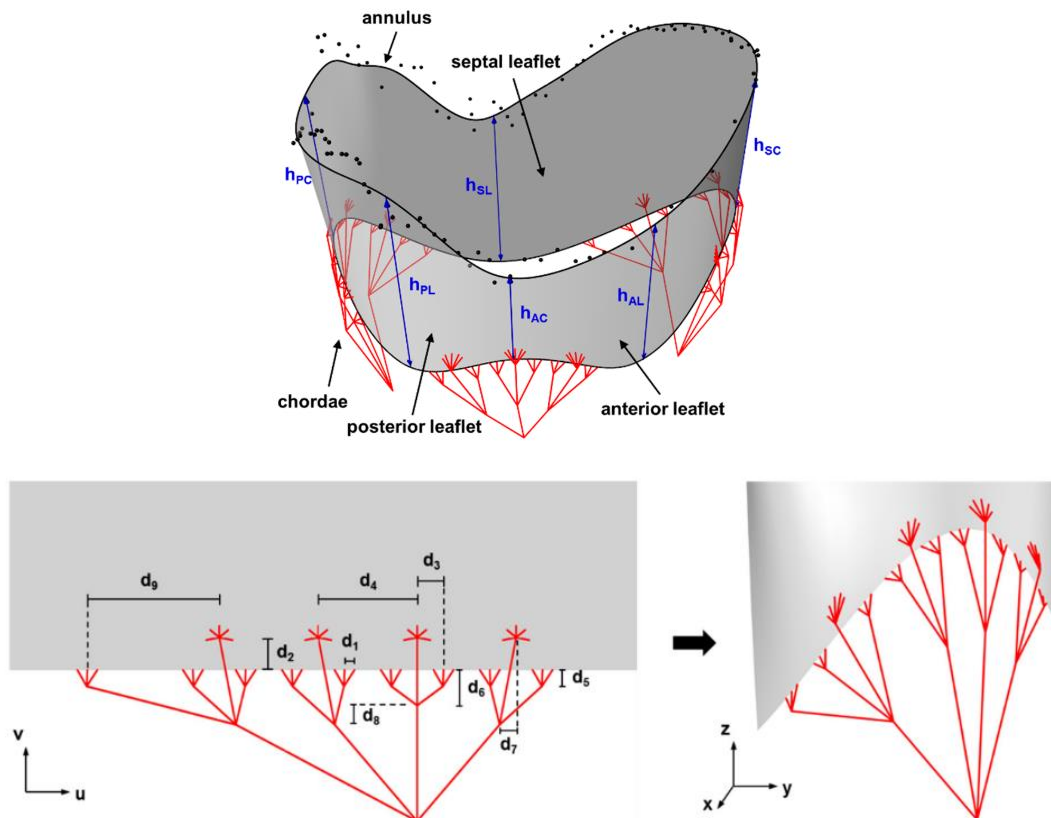


Figure 3.25: Parametric representation of the CTs proposed by Chung-Hao Lee et al. [8] The image also shows the distances (d_1 , d_2 , d_3 , d_4 , d_5 , d_6 , d_7 , d_8 and d_9) of the chordal insertions from the free margin. In addition, there are three groups of CTs that originate from the PMs and insert on the anterior and posterior leaflets, and four groups of CTs originate from the PMs that have CTs that insert on the septal leaflet.

The same model was adopted in the article by Laurence et al. [59] in which a computational model of the TV was developed to study how different pathological conditions can influence the overall biomechanics of the valve, including the simulated TR in terms of displacement of the PMs and variation in the conformation of the annulus. In the article, 11 chord groups originating from the three PMs were used.

The model used in this thesis has 11 chordal groups, 3 per PM to which an additional group is added if the PM has insertions on the TVSL ([Figure 3.26](#)). The reason is that

the TVSL is anatomically much more stable and less mobile, as it is anchored to the septum. This feature is simulated by the use of an extra set of chords. As in the article by Laurence et al. [59], the chords were described as truss elements with a cross area of 0.17 mm^2 .

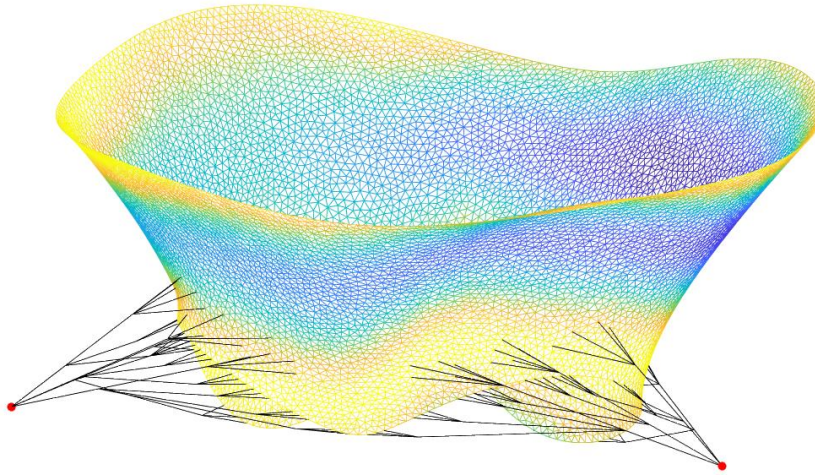


Figure 3.26: Representation of CTs reconstruction following Chung-Hao Lee et al. [8] parametric model.

3.6.3.2. Khalighi parametric model for TV CTs

Khalighi et al. [58] developed a model of the MV CTs that matches the functionality of the native structure. The process began with a high-resolution 3D anatomical reconstruction of the MV. Following the creation of a model close to the anatomical structure, major components were systematically simplified, assessing the effects on stress, strain, and the MV shape. Their findings demonstrated the feasibility of achieving accurate results and stable simulations by representing CTs as straight, non-branching structures of uniform cross-section. Additionally, the practice of specifying precise insertion points on the leaflets was gradually eliminated.

For healthy MVs, the study uncovered significant redundancy in the native valve's CT apparatus. They also established that the closing actions of healthy, diseased, or surgically modified MVs could be accurately mimicked using a simplified CT apparatus. This apparatus consists of individual chords emanating from two papillary muscles, attaching to the leaflets at a density of $15 \text{ insertions/cm}^2$, thereby simplifying the complex native CT structure without compromising functional accuracy ([Figure 3.27](#)).

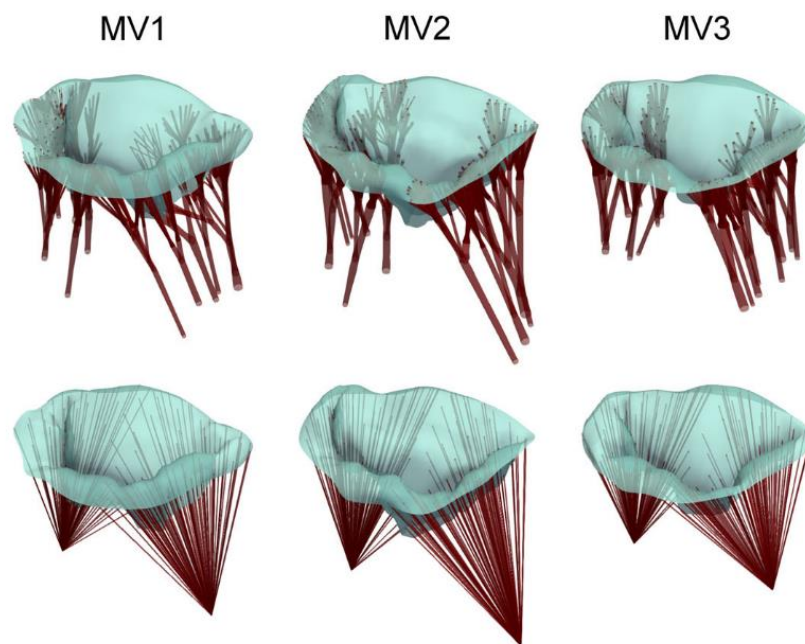


Figure 3.27: The images represent the 3 MVs on which the theory of applying a functionally equivalent model for valve closure simulations was tested. The top row represents the anatomically accurate model of the native valve, while the second row shows for each of the valves the functionally equivalent model in which only 2 PMs were conserved, the CTs are straight and insert randomly into the leaflets but with an insertion density defined at 15 insertions/cm².

Although this model is based on an in vivo extracted imaging dataset, it provides guidelines for defining a CT apparatus of MV when working with ex-vivo imaging methods, where no information of CTs is available.

Based on the results of Khalighi et al. [58] for MV, it was decided to develop a functionally equivalent model of the CTs of TV. In this case, the origin points of the CTs were 3, which corresponded to the 3 PMs of the TV. For chordal insertion density in leaflets, an iterative study was conducted to evaluate the parameter in two case studies: TV with TR and the same valve following the surgical repair proposed by Jaworek et al. [10]. Of the three proposed modalities, only the AP repair, i.e. the FWA technique in the antero-posterior direction, was tested, with a 60% reduction.

In Tondi's thesis [57], an algorithm from the ISO2MESH library's *meshresample* function was employed to establish chordal insertion points. This function creates a new triangulation with fewer nodes than its predecessor from an original triangulation, resulting in larger elements belonging to the valve's defined mesh. This process ensures evenly distributed points at the required insertion density, aligning with points within the system.

Once the insertion points on the leaflets were obtained, they were divided into six groups based on their position on the TV. The first 3 groups were defined according to the PMs of origin. Each group was then divided into 2 to identify the CTs with

insertion point in the free margin (FRM) and those inserting in the remaining part of the leaflets (BULK).

After pinpointing the origin and insertion points, a linear interpolation was executed between these two points, defining the CTs as T3D2 elements with a cross-sectional area of 0.17 mm^2 . (Figure 3.28)

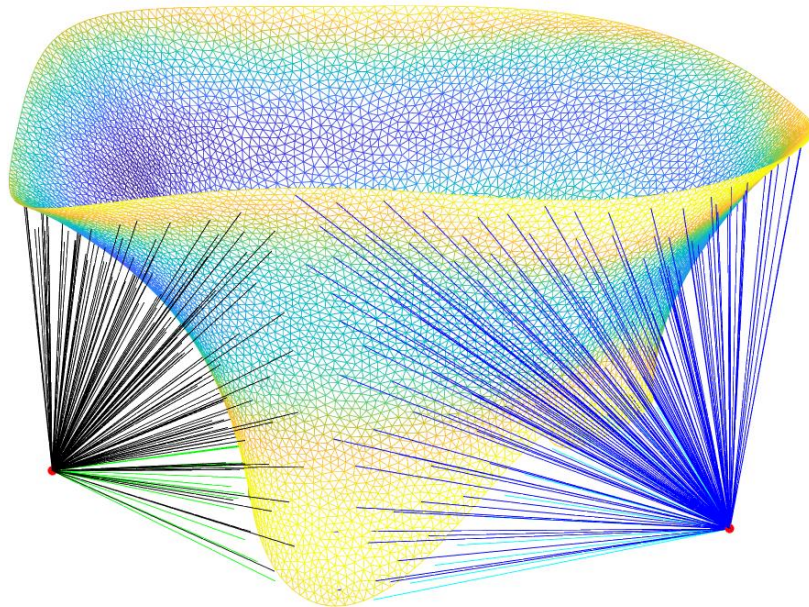


Figure 3.28: representation of the CTs architecture defined following the model of Khalighi et al. [58]. The image shows 2 of the 3 PMs identified by a red dot and 4 of the 6 groups of CTs. The green and light blue CTs are the CTs that fit on the free edge, the blue and black CTs are the CTs defined as BULK. In the image it can be seen that some CTs pass through the leaflets to reach their insertion point, this issue was not considered relevant as the contact between these two elements is not considered in the simulations.

3.7. Simulation of systolic TV closure: TR case

The systolic TR closure under pathological conditions was assessed by means of two distinct FE pipelines. All simulations were conducted with the commercial software Abaqus/Explicit. The input information required for the simulations was provided by writing INPUT files using MATLAB software.

One FE procedure consisted of a single-step simulation in which the valve was tested by reconstructing the valve with the chords described according to the model of Chung-Hao Lee et al. [8]. Using this procedure, two constitutive models were tested for the description of the CTs material.

The other FE procedure consists of three steps with the aim of determining the optimal length of each CT at the initial instant. This procedure was optimised for TV, following the procedure described earlier by Khalighi et al. [58] and applied in Tondi's thesis [57]. Also in this case, two constitutive material models were tested.

In both FE procedures, the time-dependent pressure load measured experimentally during the in-vitro test protocol described in Locatelli and Manini's thesis [29] was used ([Figure 3.29](#)).

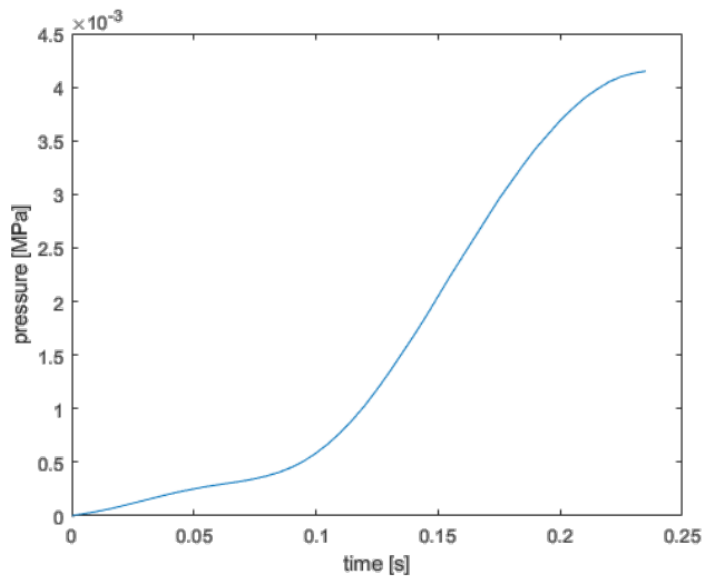


Figure 3.29: Transvalvular pressure measured experimentally during Locatelli and Manini's thesis. Image adapted from Locatelli and Manini thesis [29].

For the sake of clarity, the following symbols will be used from now on

- $\Omega_{ED}^{tracing}$: surface at ED used at the beginning of the simulations.
- $\Omega_{PS}^{FE,closure}$: surfaces extracted at the end of the systolic closure simulation.
- $\Omega_{PS}^{tracing}$: reconstructed surface resulting from the tracing of the echocardiographic images at SP.

3.7.1. Systolic closure with single step FE

The systolic closure was simulated with a single step length of 0.235 s (Figure 3.30). The CTs geometry was described using the parametric model of Chung-Hao Lee et al. [8] testing the Weiss and Saint Venant-Kirchhoff constitutive models. The valve was loaded with experimental pressure values (Figure 3.29).

The materials were described with the following constitutive models and parameters:

- Leaflets: Holzapfel model, with a description of the leaflets direction according to the model of Cochran et al. [60] and the constitutive parameters reported by Amicone and Dazzi [30] after sampling the data obtained from biaxial theses by Khoiy et al. [39].
- CTs:
 - A. Weiss model, with constitutive parameters reported by Amicone and Dazzi [30] after sampling data from uniaxial theses by Lim et al. [47]
 - B. Saint Venant-Kirchhoff model, with constitutive parameters defined in Laurence PhD thesis [51]

The boundary conditions established were:

- The displacement of nodes belonging to PMs from the ED configuration to the SP configuration. Both coordinates are derived from manual segmentation and TV reconstruction. To simulate the displacement, the calculated differences from the coordinates of the i -th PMs were provided:

$$du_{i,PM} = (x_{i,PS} - x_{i,ED} , y_{i,PS} - y_{i,ED} , z_{i,PS} - z_{i,ED}) \quad (3.8)$$

- The points belonging to the annulus were shifted from the ED configuration to the SP configuration, again information derived from the segmentation and reconstruction of the two instants of the cardiac cycle and again calculated as the difference between the coordinates of the i -th point:

$$du_{i,ANN} = (x_{i,PS} - x_{i,ED} , y_{i,PS} - y_{i,ED} , z_{i,PS} - z_{i,ED}) \quad (3.9)$$

A surface interaction with a friction parameter of 0.05 and a contact between the atrial surfaces with a scale penalty of 2 was defined for the atrial surface of the leaflets.

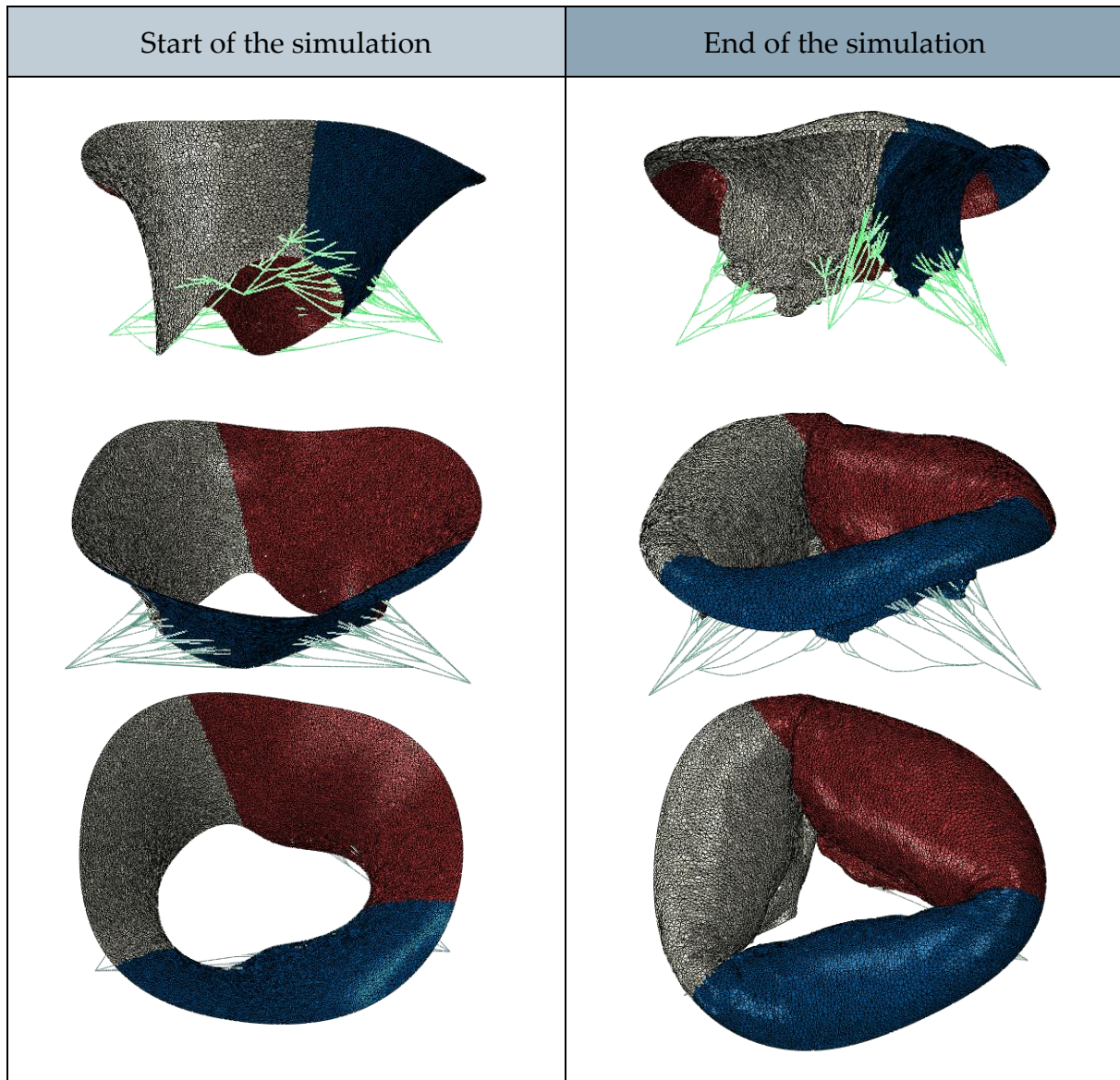


Figure 3.30: The plots represent the TV at the beginning and end of the simulation. The first line highlights the CTs, the second line represents the TV in its entirety and the third line shows the behaviour of the three leaflets. In red the TVPL, in grey the TVAL and in blue the TVSL.

3.7.2. Systolic closure with CTs calibration

In order to reproduce the pathological TV movement and acquire data at the systolic peak, it was decided to test a workflow that was successful on MV, the method presented by Khalighi et al. [58]. The FE process consists of three simulations:

A. Morphing

The TV was reconstructed from the segmentation of the ED frame of the cardiac cycle. From the echocardiographic images the CTs are not visible; therefore, neither their morphology nor length can be defined. At ED it is possible to assume that the CTs are unloaded and relaxed, whereas at SP they are fully extended and in tension. The CTs, due to their conformation, are only able to support tensile loads.

To overcome this problem during the first simulation, the ED TV leaflets were loaded with a pressure ramp on the ventricular side until they lay on the $\Omega_{PS}^{tracing}$ (Figure 3.31). The goal was to capture the leaflets' node coordinates at SP without CTs restricting leaflet movement or causing erratic behavior, achieved by modeling the CT material as highly elastic. After adjusting for displacement, the distance between papillary muscles (PMs) and chordal insertion points on the leaflets at SP could be determined, thus estimating CT lengths at SP.

The simulation was divided into two steps:

First step

The start-step configuration of the TV requires the description of two elements: the $\Omega_{ED}^{tracing}$ and the $\Omega_{SP}^{tracing}$.

The valve in ED configuration was reconstructed using the workflow described in section 3.6.1. "TV open surface, at ED". The Holzapfel model for the leaflets was used to describe the materials, while the CTs were described as linear elastic with Poisson's coefficient $\nu = 0.3$ and very low elastic modulus $E = 5\text{kPa}$.

The function of the valve in SP configuration is to act as a mould during valve closure, when pressure load is applied. For this reason, it has been discretised as a rigid surface. The ED and SP configuration, if placed at the same point in space could interpenetrate. To avoid problems during simulation at the initial instate, the TV described as a rigid surface in SP configuration is positioned 3 mm above the valve in ED configuration, considering the z-axis of the cylindrical system in which the geometries are described.

The first step has a duration of 1s. The boundary conditions set are:

- Block the translational degrees of freedom of the points describing the PMs ($u_i^{PMs} = 0$, with $i = 1, 2, 3$).
- Block of rotations of the rigid valve in SP configuration ($u_i^{\Omega^{PS}} = 0$, with $i = 4, 5, 6$).

- Translation along the z-axis of the rigid surface at SP of the TV, to position it inside the valve in ED configuration.
- Displacement of points belonging to the annulus from the position in the ED to the configuration in SP, calculated as a variation of x, y and z coordinates:

$$du_{i,ANN} = (x_{i,PS} - x_{i,ED} , y_{i,PS} - y_{i,ED} , z_{i,PS} - z_{i,ED})$$
- A series of characteristic points were identified on the free edge of both configurations. 1 node was identified for each commissure, 1 node for each leaflets' minimum points and 2 nodes at a distance of 3 mm from the minimum points, one on the right and one on the left. The corresponding nodes of the ED and SP configurations were connected by a set of CONNECTOR elements. By means of these elements, they were driven to contact with $\Omega_{PS}^{tracing}$.

This step is a step of only displacement of the TV elements to position them in the correct place for the start of step 2 ([Figure 3.31](#)). Contacts between different points on the atrial surface of the valve in the ED configuration and between the ventricular surface of the rigid surface in the SP configuration and the atrial surface of the ED configuration were modelled using the scale penalty method, set equal to 2, and a friction coefficient of 0.05.

Second step

The second step also has a duration of 1 s. The boundary conditions are:

- Enclosure of the rigid surface in SP configuration
- Block of the translational degrees of freedom of the points belonging to the annulus and free margin sets ($u_i^{ANN} = 0$ and u_i^{FRM} , with $i = 1, 2, 3$)
- Block the translational degrees of freedom of the points describing the PMs ($u_i^{PMs} = 0$, with $i = 1, 2, 3$).

In this step, a pressure ramp from 0 to 5 mmHg is applied to the ventricular surface of the TV in ED configuration. The aim of the simulation is to guide the contact between the ventricular surface of the rigid TV in SP configuration and the atrial surface of the other valve ([Figure 3.31](#)).

The same contact description as in step 1 was used during the simulation.

At the end of the simulation, the coordinates of the leaflets were extracted from Abaqus. The coordinates are then imported into a MATLAB script, which has the function of recalculating the points belonging to the chords with the starting point the PMs in systolic configuration and insertion on the SP valve leaflets.

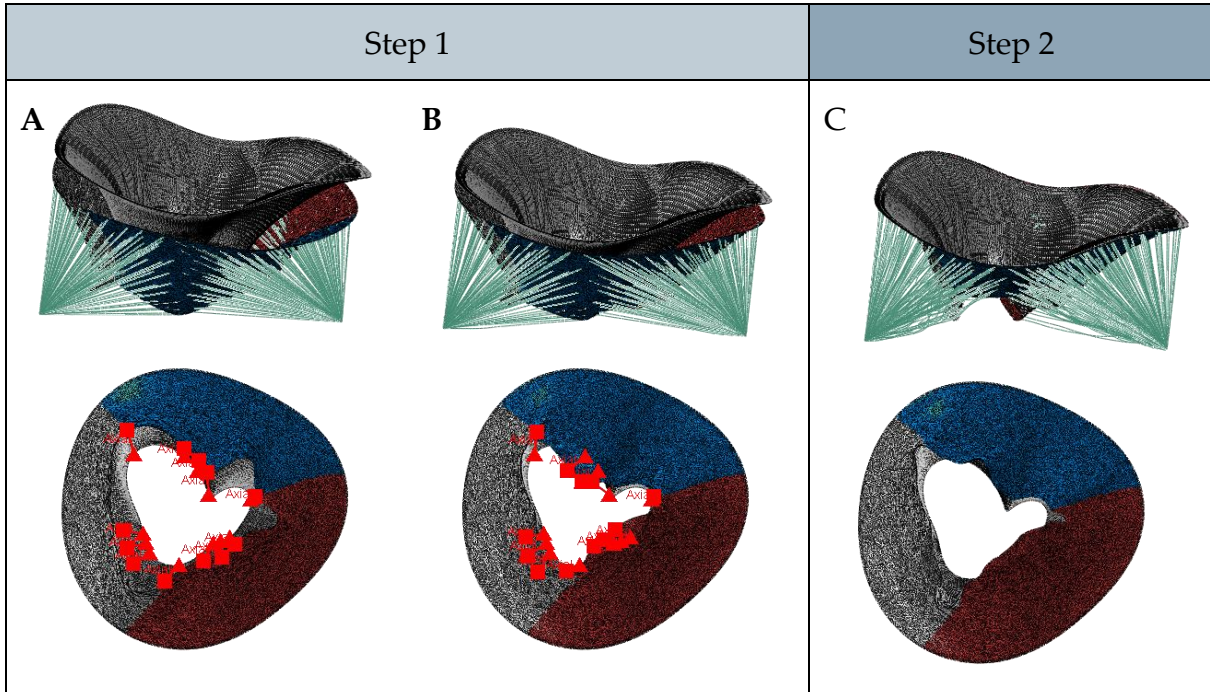


Figure 3.31: Morphing simulation. (A) Initial configuration: the rigid surface in SP configuration is located 3 mm relative to the z-axis above the valve in ED configuration. The CONNECTOR elements are positioned at the defined points at the free edge and ready to bring the leaflets closer together. (B) Configuration at 0.5 of step 1: The rigid surface is approaching the valve, and the CONNECTOR elements are shortening. (C) End of step 2: The valve has been pressurised and the valve leaflets have moved closer together. Blocking the translations of the free edge points prevents the leaflets from assuming unphysiological conformations. In red the TVPL, in grey the TVAL and in blue the TVSL.

B. Calibration of CTs

The TV was held in the position extracted from the previous configuration, then in the simulated SP configuration. The CTs are fully stretched and described as hyper-rigid and the ventricular surface was pressurised to the experimentally measured peak value (Figure 3.29). From the simulation, it is possible to extract the reaction force (RF) of each individual chord at the PMs. Using a reverse engineering approach, the deformation of each CT was calculated by inverting the constitutive model of the material.

The calibration takes place in a single step of 1s duration (Figure 3.32). At the initial time, the valve is in the configuration extracted from the morphing step. In this case, a new constitutive model was assigned to the CTs in order to extract the RF of the CTs: The CTs were described as a linearly elastic but hyper-rigid tissue, with Poisson's coefficient $\nu = 0.475$ and elastic modulus $E = 100\text{GPa}$, simulating the condition in which all collagen fibres were recruited.

The boundary conditions imposed were:

- Block of the translational degrees of freedom of the points belonging to the annulus set ($u_i^{ANN} = 0$, with $i = 1, 2, 3$)
- Block the translational degrees of freedom of the points describing the PMs ($u_i^{PMs} = 0$, with $i = 1, 2, 3$).

The contacts between different points on the atrial valve surface were modelled using the scale penalty method, set equal to 3, and a friction coefficient of 0.05.

At the end of the simulation, through Abaqus, it was possible to extract the RF values acting on the CTs. The RF values were extracted at the last 4 instants of the step. The extracted values for each CT component were then used to calculate the average RF value and exclude peak or minimum values, removing possible oscillations of the leaflets caused by the applied pressure drop.

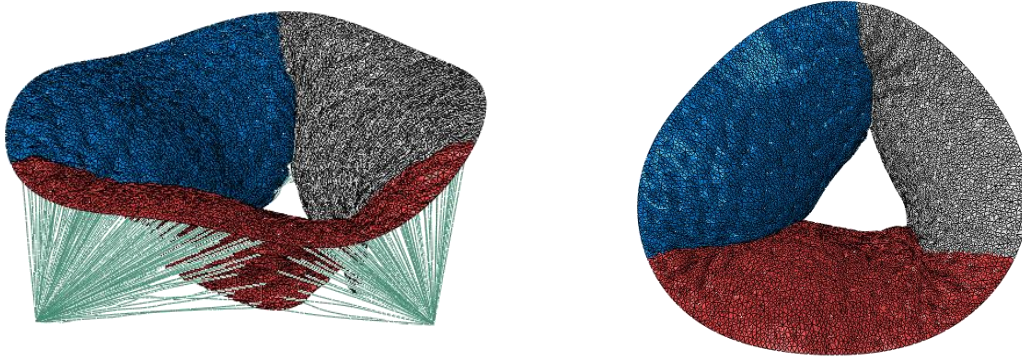


Figure 3.32: Simulation set-up for TV RF extraction. The applied pressure load is that measured during the experimental tests. The leaflets respond to the load by swelling. Their dotted shape is due to the chordal insertions. In red the TVPL, in grey the TVAL and in blue the TVSL.

RF is used to calculate the First Piola-Kirchhoff tensor stress (P_{11}) by dividing RF with the cross section of the CT. In the model, all CTs were associated with the same cross section equal to 0.17 mm^2 .

$$P_{CT} = P_{11} = \frac{RF}{A_{CT}} \quad (3.11)$$

The true axial stress t_{11} of the CT can be calculated by multiplying P_{CT} by the value of the axial stretch ratio λ_{11} . The value of λ_{11} is unknown and in the case of the constitutive Saint Venant-Kirchhoff model, the value of λ_{11} can be determined directly by solving the equation:

$$(\lambda + 2 * \mu) * \frac{1}{2} * (\lambda_{11}^2 - 1) * \lambda - P_{11} = 0 \quad (3.12)$$

In the case of Weiss constitutive model for describing CTs and the iterative *Algorithm 2* was defined to calculate λ_{11} .

Algorithm 2 Iterative estimation of λ_{11}

Value of RF_{ax} and cross section of the CT and parameters of constitutive model are known.

- 1: Initialisation of arbitrary values of λ_{ref} and λ_{11} (e.g. $\lambda_{ref} = 1000$ and $\lambda_{11} = 2$)
- 2: Initialization of threshold value $\varepsilon = 0.005$
- 3:
$$P_{11} = \frac{RF_{ax}}{cross\ section}$$
- 4:
$$t_{11} = P_{11} * \lambda_{11}$$
- 5: **While** $(\lambda_{ref} - \lambda_{11}) > \varepsilon$
- 6:
$$\lambda_{ref} = \lambda_{11};$$
- 7: **If** $\lambda_{11} < \lambda_f^*$ % λ_f^* is the transition value for the Weiss constitutive model
- 8:
$$eqn = 2 * \left(a_1 * \left(\lambda^2 - \left(\frac{1}{\lambda} \right) \right) - a_2 * \left(\left(\frac{1}{\lambda} \right)^2 - \lambda \right) + a_3 * (e^{a_4 * (\lambda - 1) - 1}) - t_{11} = 0 \right.$$

% Constitutive model
- 9: % The solution was calculated using the *vpasolve* function and limiting the calculated value of lambda between 0.9 and 2, at the end the new value of λ_{11} is obtained
- 10: **else**
- 11:
$$eqn = 2 * \left(a_1 * \left(\lambda^2 - \left(\frac{1}{\lambda} \right) \right) - a_2 * \left(\left(\frac{1}{\lambda} \right)^2 - \lambda \right) + a_5 * \lambda + a_6 - t_{11} = 0 \right.$$
- 12: % Constitutive model
- 13: % The solution was calculated using the *vpasolve* function and limiting the calculated value of lambda between 0.9 and 2, at the end the new value of λ_{11} is obtained.
- 14: **end**
- 15:
$$t_{11} = P_{11} * \lambda_{11};$$
- 16: **end**
- 16:
$$l_0 = l_{end} * \lambda_{11}$$

l_0 will be the length of the chordae projected onto the leaflet in the final closure simulation. For each CT the node at the origin was shifted along the CT axis to obtain the correct initial length.

C. Closure of the TV

The last FE flow simulation simulates the closure of the CT as it would occur in a pathological cardiac cycle ([Figure 3.33](#)). In this simulation, the CTs were described using the reference constitutive model.

The simulation consists of two steps.

First step

Step of 1s duration. In this step, the displacement conditions of the individual points are applied to obtain the desired basic configuration for the start of the second step ([Figure 3.33](#)).

The kinematic conditions are:

- Displacement of the new CTs origin points to the coordinates of the reference PM at ED configuration. Displacement calculated as the change in x, y and z coordinates:

$$du_{i,CTOR} = \left(x_{i,PM_{ED}} - x_{i,NEWCTOR}, y_{i,PM_{ED}} - y_{i,NEWCTOR}, z_{i,PM_{ED}} - z_{i,NEWCTOR} \right) \quad (3.13)$$

- Encaster of leaflet points in ED configuration

Second step

Step duration of 0.235 s. At the beginning of the step, the chords were slack due to the shifting of the origin point ([Figure 3.33](#)). During the step, the origin of the CTs is shifted towards the position of the PM in the SP configuration, the annulus is shifted from the ED configuration to SP, and at the same time the experimentally measured pressure load is applied ([Figure 3.29](#)).

The kinematic conditions are:

- Displacement of the CTs origin points from the coordinates of the reference PM in the ED configuration to that in the SP configuration. Displacements are calculated as the change in x, y and z coordinates:

$$du_{i,CTOR} = (x_{i,PM_{PS}} - x_{i,PM_{ED}}, y_{i,PM_{PS}} - y_{i,PM_{ED}}, z_{i,PM_{PS}} - z_{i,PM_{ED}}) \quad (3.14)$$

- Displacement of points belonging to the annulus from the position in the ED to the configuration in SP, calculated as a variation of x, y and z coordinates:

$$du_{i,ANN} = (x_{i,PS} - x_{i,ED}, y_{i,PS} - y_{i,ED}, z_{i,PS} - z_{i,ED}) \quad (3.15)$$

The contacts between different points on the atrial surface, the ventricular surface and between the atrial and ventricular surface were modelled using the scale penalty method, set equal to 5, and a friction coefficient of 0.05.

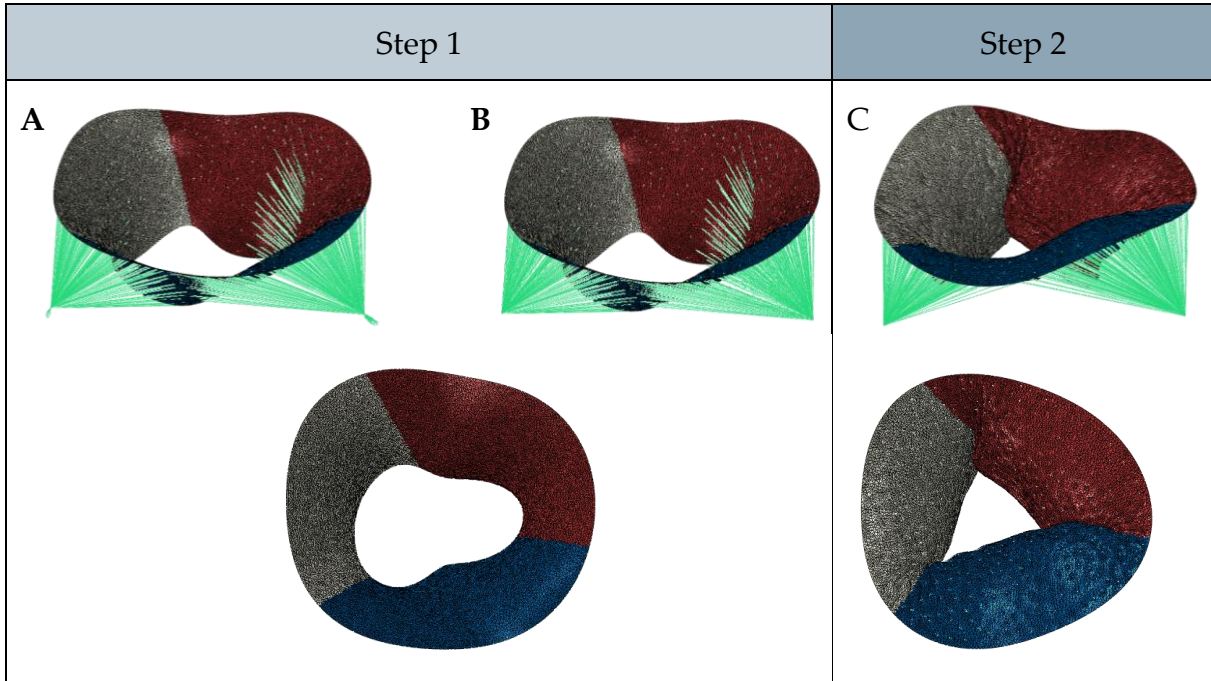


Figure 3.33: Closure simulation. (A) Start point of the first step. The CTs have been redefined to have an initial length of l_0 and must pass through the reference PM in their construction. The points of the leaflets are embedded. (B) At the end of the first step, the origin point of the CTs was shifted to the coordinate of the reference PM at ED configuration. At this step, the CTs are relaxed. (C) End of the second step. The CT was loaded with the pressure load and the SP configuration of the valve was obtained. During the simulation, the annulus and PM points were shifted from the ED configuration to the reconstructed SP configuration. In red the TVPL, in grey the TVAL and in blue the TVSL.

In this simulation, a small variation was considered. In step 1, the distance between the recalculated point of origin of the CTs and the insertion in the leaflet was evaluated. The displacement of the nodes to the PM in ED configuration is only applied if the calculated distance is greater than the distance between PM in ED configuration and the insertion point of the leaflet. Otherwise, what would happen is that at the initial instant, the CT would already be in tension and the shape of the leaflets would be modified. In the second step, these points are shifted from the new origin points calculated from l_0 data to the position of the systolic PM.

3.7.2.1. Applications

The described 3-simulation workflow was applied to evaluate:

- The geometric model of CTs described in the section [3.6.4.1. “Chung-Hao Lee parametric model for TV CTs”](#).
- The geometric model of CTs described in the section [3.6.4.2. “Khalighi parametric model for TV CTs”](#), considering different values of chordal insertion density

- Weiss' constitutive model for the CTs material
- Saint-Venant Kirchhoff's constitutive model for the CTs material

At the end of the morphing simulation, in the case of the geometric model described by Khalighi et al. model it is possible to extract the magnitude of the RFs for each CT from Abaqus. In the case of the application to the Chung-Hao Lee et al. model it was decided to calculate the l_0 only for the first part of the CTs, without therefore varying the length of the branches. In this case it was necessary to do a few more steps to obtain the RF on each initial part of the CTs.

The RF_x , RF_y and RF_z value is extracted from Abaqus at the level of the insertion points of the leaflet branches. Also in this case, the three RF components were extracted for the last 4 instants and the average value was calculated.

The section of CT on which the elongation will be calculated is from the section connected to the associated papillary muscle up to the first branch. The RFs have been divided based on the stretch of rope to which the branches belong ([Figure 3.34](#)).

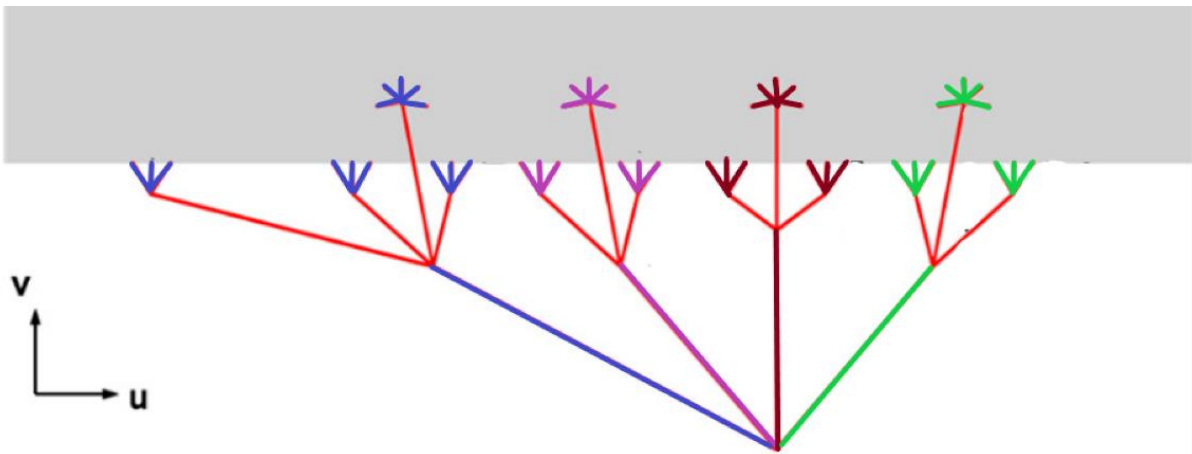


Figure 3.34: schematic representation of how the RFs extracted for each insertion were associated with the section of CT on which the value of l_0 will be calculated. In the image, the shorter blue branches at the level of the leaflet, represented in grey, are all the points where the RFs were extracted and have been associated with the long blue segment that originates from the PM, which is the meeting point of the blue CTs, purple, brown and green. The same reasoning can be done for the colours purple, brown and green.

The total force acting along the main branch of the rope is given by the sum of the components acting on the individual branches:

$$F_{tot} = [F_{x_1} + F_{x_2} + \dots + F_{x_n}, F_{y_1} + F_{y_2} + \dots + F_{y_n}, F_{z_1} + F_{z_2} + \dots + F_{z_n}] \quad (3.16)$$

$$F_{tot} = [F_{tot}(x), F_{tot}(y), F_{tot}(z)] \quad (3.17)$$

The F_{tot} was then projected in the direction parallel to the chord to obtain the acting in the F_{ax} direction.

3.8. Simulation of systolic TV closure: post-surgery

To simulate the surgical intervention proposed in the article by Jaworek et al. [10] the ultrasound images acquired in Manini and Locatelli's thesis [29] in which they tested an AP FWA of 60% were used.

Using the radial axis GUI, the annulus was segmented in ED and SP configuration, while the PMs and the position of the commissures were traced on the SA planes.

Following the reconstruction, the structures of the TV with TR and those of the post-surgery on the same valve appeared of different proportions; therefore, the dimensions were modified so that their proportion was consistent.

The closure of TV following the application of the idea of Jaworek et al. [10] was simulated as it would occur in a physiological cardiac cycle ([Figure 3.35](#)). The CTs were described according to the parametric model of Khalighi [58], also in this case multiple values of chordal insertion density were tested. Furthermore, the simulations were carried out with both the Weiss and Saint-Venanti Kirchhoff constitutive models for the description of the CTs material.

The simulation is composed of two steps.

First step

Step duration of 1s. In this phase, the PMs and Annulus points were moved from the TV configuration with TR at ED to the TV configuration following the application of the 60% AP FWA. All imposed displacements derive from reprocessed data but acquired from echocardiographic images.

The kinematic boundary conditions are:

- Displacement of the points belonging to the annulus from the valve position with TR to the post-intervention position, both ED, calculated as a variation of the x, y and z coordinates:

$$du_{i,ANN} = (x_{i,AP60_ED} - x_{i,TR_{ED}} , y_{i,AP60_ED} - y_{i,TR_{ED}} , z_{i,AP60_ED} - z_{i,TR_{ED}}) \quad (3.18)$$

- Displacement of the new points of origin of the CTs in TV configuration with TR to the position of the PMs post-surgery, both in ED configuration. The displacement calculated as a change in the x, y and z coordinates:

$$du_{i,PM} = (x_{i,AP60_ED} - x_{i,TR_{ED}} , y_{i,AP60_ED} - y_{i,TR_{ED}} , z_{i,AP60_ED} - z_{i,TR_{ED}}) \quad (3.19)$$

Second step

Step duration of 0.235 s. In this step, the closure of the TV post-surgery was simulated.

The kinematic boundary conditions are:

- Displacement of the points belonging to the annulus from the position of the post-intervention valve in ED configuration to those in SP configuration, calculated as a variation of the x, y and z coordinates:

$$du_{i,ANN} = (x_{i,AP60PS} - x_{i,AP60ED} , y_{i,AP60PS} - y_{i,AP60ED} , z_{i,APP60PS} - z_{i,AP60ED}) \quad (3.20)$$

- Displacement of the PMs from the position of the post-intervention valve in ED configuration to those in SP configuration, calculated as a variation of the x, y and z coordinates:

$$du_{i,PM} = (x_{i,AP60PS} - x_{i,AP60ED} , y_{i,AP60PS} - y_{i,AP60ED} , z_{i,APP60PS} - z_{i,AP60ES}) \quad (3.21)$$

The valve was loaded with the physiological pressure load ([Figure 3.29](#)).

In both simulation steps, the contacts between different points of the atrial surface, the ventricular surface and between the atrial and ventricular surfaces were modelled with the scale penalty method, set equal to 5, and with a friction coefficient equal to 0.05.

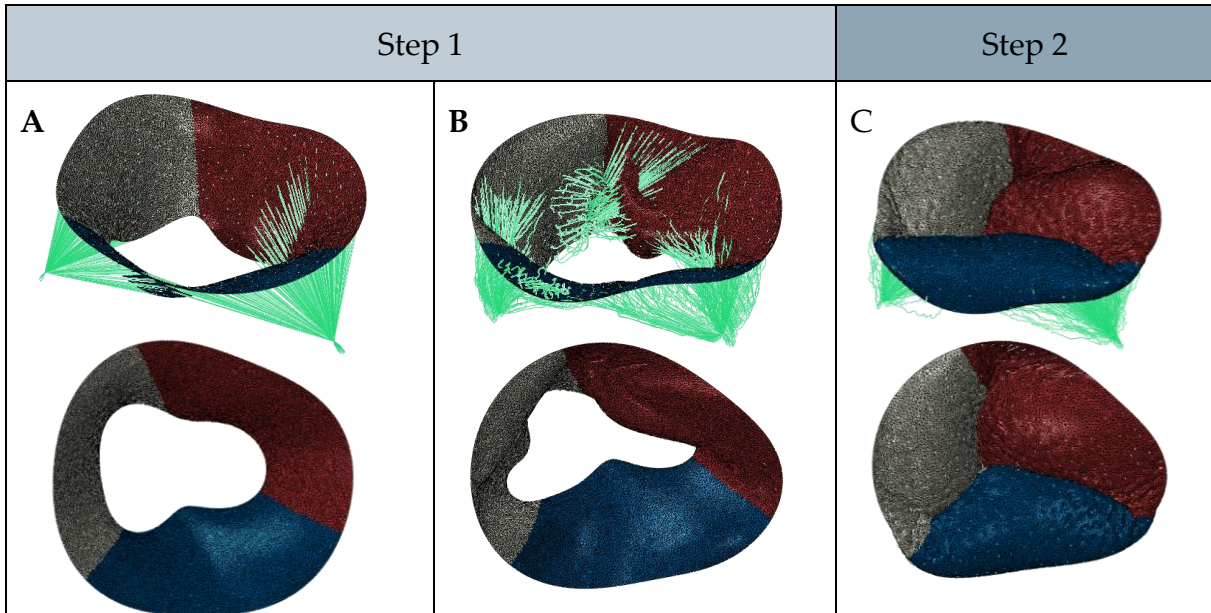


Figure 3.35: (A) Configuration of the TV at the beginning of step 1. The configuration of the TV is the one reconstructed at ED with TR, evaluating the starting position of the CTs calculated in the calibration phase. (B) At the end of step 1 the post-intervention valve configuration is obtained. The shape of the annulus was modified, and the position of PMs was translated. The CTs appear much more relaxed. (C) End of the loading step showing the result of applying the idea of Jaworek et al. [10].

4 Results

This chapter will present the main results obtained in this thesis work.

In the first section, the results obtained because of the reconstruction work on TV HT11 with TR will be reported. Several pathological valve closure configurations were tested, [Figure 4.1](#) summarises the acronyms and parameters chosen for the configurations deemed relevant, the results of which will be presented in the following sections.

The development of a reconstruction workflow required the detailed analysis of some valve structures, such as CTs. The FEA results on the TV will define the importance of the various parameters analysed in the biomechanical characterisation of the valve.

The focus of the work was on the simulation workflow. For the TR valve two workflows were tested: a single-step valve closure simulation, literature *gold-standard* simulation for TV, and the CTs calibration workflow proposed in the work of Khalighi et al [58] for the MV. For the sake of clarity, from now on the first will be called *single step* simulation and the second *calibration* simulation.

Two different configurations of the chordal apparatus have been tested: the first chordal model was taken from the work of Chung-hao Lee et al. [8], developed specifically on the feature of the TV (it will be called *Chung-Hao Lee geometry*), and thus, describing in a more anatomically-faithful way the general ramifications of the CTs; the second chordal model was inspired by the work of Khalighi et al. [58], in which a functionally equivalent parametric model is developed (this will be called *Khalighi geometry* or *functionally equivalent model*).

Lastly, the CTs material of each configuration was evaluated by applying the constitutive Weiss model and the Saint-Venant Kirchhoff model, presented in sections [2.4.4.3 "Weiss model"](#) and [2.3.4.4 "Saint Venant-Kirchhoff model"](#), respectively.

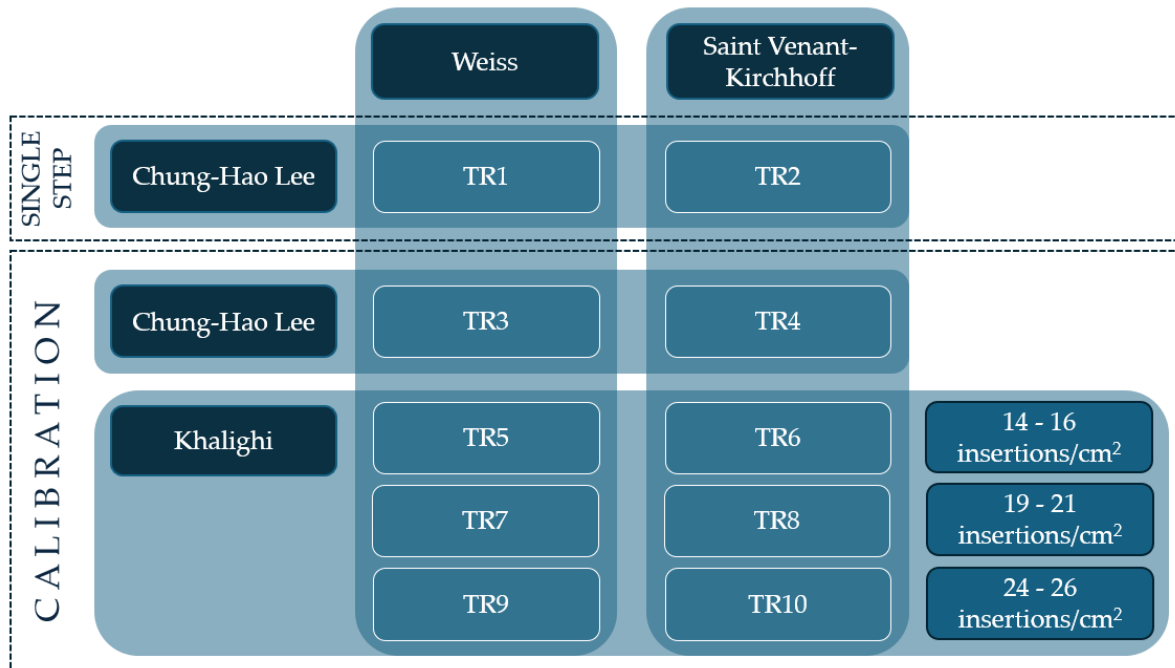


Figure 4.1: Framework of tested configurations for TV with TR and definition of acronyms.

The double-entry table, although with atypical configuration, provides the necessary information to understand the differences between the various configurations. For example, in the TR2 configuration the CTs were described geometrically with the Chung-Hao Lee model, the material used was Saint Venant-Kirchhoff and the simulation was carried out in a single step. For the TR5 to TR10 simulations, an additional parameter, typical of Khalighi's functionally equivalent model, was evaluated, which is the chordal insertion density.

The second part of the chapter will report the results obtained following the application of the surgical procedure proposed in the article by Jaworek et al. [10]. The surgical procedure tested, among those proposed in the article, is the FWA in the AP direction. Starting from the configuration of the TV obtained at the end of the reconstruction phase, the new positions of the annulus and PMs were defined, based on the segmentation of the post-surgery 3D echocardiographic images. For the evaluation of the impact of the parameters on the simulations that will be called post-surgery, several configurations were evaluated. [Figure 4.2](#) shows the simulations conducted, the results of which will be presented.

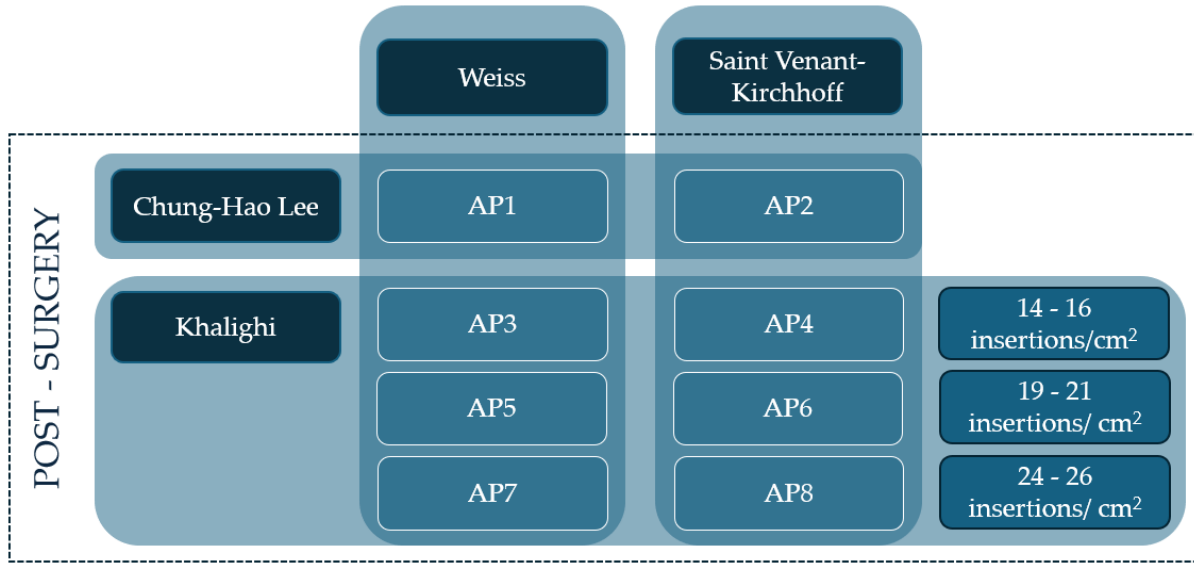


Figure 4.2: framework of the configurations tested to evaluate the biomechanical behaviour of the TV as a consequence of a 60% FWA in the AP direction and their acronyms. The double table provides information with respect to the geometric model used for the description of the CTs and the constitutive model for the description of the material. In this case, post-surgery simulation was applied to all configurations.

4.1. Analysis of TV with TR

To evaluate the parameters implemented for the TV with TR, the results will be divided into two sections. The first section will report the results of the 6 configurations, TR5 to TR10, characterized by the functionally equivalent model of CTs. A sensitivity analysis based on clinically relevant metrics will define the impact of the chordal insertion density. One of the proposed chordal densities will then be chosen and the two configurations extracted will be compared, using both engineering and clinically relevant metrics, with the other 4 configurations, TR1 to TR4.

For the evaluation of the clinically relevant characteristics of $\Omega_{PS}^{FE,closure}$, the $\Omega_{PS}^{tracing}$ was used as reference.

4.1.1. CTs insertion density: sensitivity analysis

This first section was inspired by the work conducted by Khalighi et al. [58] for MV. In this thesis work the functionally equivalent model for the CTs was analysed, slightly modified and applied to TV for the first time. The valve whose echocardiographic images were used is TV with severe TR, identified as HT11.

As the TV geometry is more complex respect the MV, three different chordal densities were implemented to evaluate the behaviour of the TV model in systolic closure simulations. [Table 4.1](#) for each configuration tested shows the chordal insertion density values and the number of CTs generated.

| ID | CTs density [insertions/cm ²] | Nr of CTs |
|------|--|-----------|
| TR5 | 14 – 16 | 412 |
| TR6 | 14 – 16 | 412 |
| TR7 | 19 - 21 | 532 |
| TR8 | 19 - 21 | 532 |
| TR9 | 24 - 26 | 607 |
| TR10 | 24 - 26 | 607 |

Table 4.1: The first column allows identification of the reference configuration; the second column shows the chordal insertion density and the third the number of CTs.

For each configuration, two clinically relevant metrics were obtained from the data extracted from the Abacus software at the end of the Closure simulation. Specifically, the regurgitant area of the $\Omega_{PS}^{FE,closure}$ in the xy plane was evaluated, compared to that of the $\Omega_{PS}^{tracing}$ and the point-to-point Euclidean distance between the $\Omega_{PS}^{tracing}$ and the $\Omega_{PS}^{FE,closure}$. Finally, the total computational time was the sum of the computational times of the 3 required simulations.

4.1.1.1. Regurgitation area

The statistical technique presented in Locatelli and Manini's thesis [29] was used to evaluate the TV regurgitation area. Both the annular area ($A_{ANN,tracing}$) and the regurgitant area ($A_{FTR,tracing}$), extracted from the $\Omega_{PS}^{FE,closure}$, shown in [Table 4.2](#), and the percentage of the regurgitation area with respect to respect the annular area was used as reference values ($\%RA_{FTR,tracing}$).

| | $A_{ANN,tracing}$ [mm ²] | $A_{FTR,tracing}$ [mm ²] | $\%RA_{FTR,tracing}$ |
|-------------------------|--------------------------------------|--------------------------------------|----------------------|
| $\Omega_{PS}^{tracing}$ | 2010.90 | 246.02 | 12,23% |

Table 4.2: Annulus and regurgitant area in the xy plane extracted from the reference configuration $\Omega_{PS}^{FE,closure}$. The last column shows the percentage ratio between $A_{FTR,tracing}$ and the $A_{ANN,tracing}$.

For each configuration was calculated ([Table 4.3](#)):

- $A_{FTR,FE}$ = the regurgitation area in the xy plane of the $\Omega_{PS}^{FE,closure}$;
- $\%RA_{FTR,FE}$ = the percentage of the regurgitation area of the $\Omega_{PS}^{FE,closure}$ respect the annulus area of the $\Omega_{PS}^{tracing}$
- ε = error calculated as the difference between the percentage of the reference regurgitant area of $\Omega_{PS}^{tracing}$ and the percentage obtained from $\Omega_{PS}^{FE,closure}$ data.

$$\varepsilon = \%RA_{FRM,tracing} - \%RA_{FRM,FE} \quad (4.1)$$

| ID | $A_{FRM,FE}$ [mm ²] | % $RA_{FRM,FE}$ (ϵ) |
|------|---------------------------------|--------------------------------|
| TR5 | 438.90 | 21.18 % (- 8.95) |
| TR6 | 211.73 | 10.53 % (1.7) |
| TR7 | 266.58 | 13.25 % (- 1.02) |
| TR8 | 209.33 | 10.41 % (1.82) |
| TR9 | 254.00 | 12.63 % (- 0.4) |
| TR10 | 206.64 | 10.27 % (1.96) |

Table 4.3: Results of the sensitivity analysis. The $A_{FTR,FE}$ in mm² was extracted for each configuration. From this value, the percentage of the $A_{FTR,FE}$ was calculated with respect to the $A_{FTR,FE}$ and the error (% $RA_{FRM,tracing}$ - % $RA_{FRM,FE}$) in brackets.

Being based on the difference between valve configuration, ϵ may acquire both positive or negative values: positive values are displayed when the $A_{FTR,FE}$ has a value smaller than the reference, while negative values are related to the $A_{FTR,FE}$ being greater in magnitude than the reference. This means that a positive value indicates a lower TR condition than the reference one, while a negative value describes a worse pathological condition than the reference. Considering the scope of the simulations, the negative sign error implies a conservative description of the patient's condition.

The modulus comparison of error values (Figure 4.3), indicate different behaviour of the two constitutive models by varying the chordal insertion density. The Saint-Venant Kirchhoff constitutive model has error values that are stable for the three chordal densities tested but tend to increase. In all cases, the errors have a positive sign. Weiss' constitutive model makes it possible to obtain, by increasing the chordal insertion density, a regurgitation area that is always closer to the reference ones and always with a negative sign.

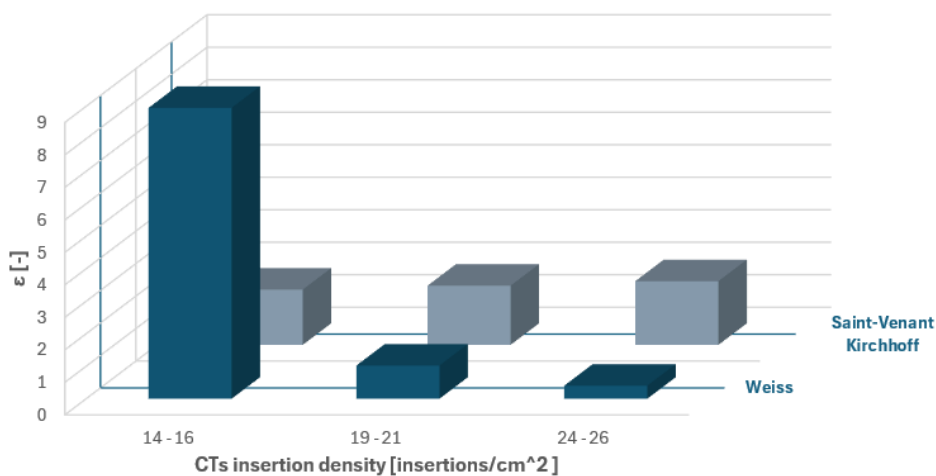


Figure 4.3: plot of the value of ϵ , on the z-axis, for the 6 configurations tested. The x-axis shows the chordal insertion density and the y-axis the type of constitutive model used for the CTs.

4.1.1.2. Euclidean distance between $\Omega_{PS}^{tracing}$ and $\Omega_{PS}^{FE,closure}$

For each configuration, the Euclidean distance (D) between the leaflet nodes in the configuration $\Omega_{PS}^{tracing}$ and the $\Omega_{PS}^{FE,closure}$ was calculated. Values were extracted for each point. From the distribution, the median, 25th and 75th percentiles were evaluated ([Table 4.4](#)).

| ID | D [mm] |
|------|--------------------|
| TR5 | 1.20 (0.47 ÷ 2.33) |
| TR6 | 1.29 (0.57 ÷ 2.26) |
| TR7 | 1.18 (0.48 ÷ 2.07) |
| TR8 | 1.18 (0.57 ÷ 2.10) |
| TR9 | 1.11 (0.46 ÷ 1.91) |
| TR10 | 1.15 (0.55 ÷ 1.97) |

Table 4.4: Results of sensitivity analysis against Euclidean distance values calculated point-to-point along the entire leaflet surface.

Values are reported as median (25th percentile ÷ 75th percentile).

Echocardiographic images have a spatial resolution of 0.70x0.69x0.54. The median values are therefore all above the pixel size, hence the best configuration is the one with the lowest median value.

The median values were compared ([Figure 4.4](#)) for the 6 configurations tested. Regardless of the material constitutive model, a reduction in D is observed as the chordal insertion density increases. The Weiss constitutive model for each configuration manages to obtain lower values.

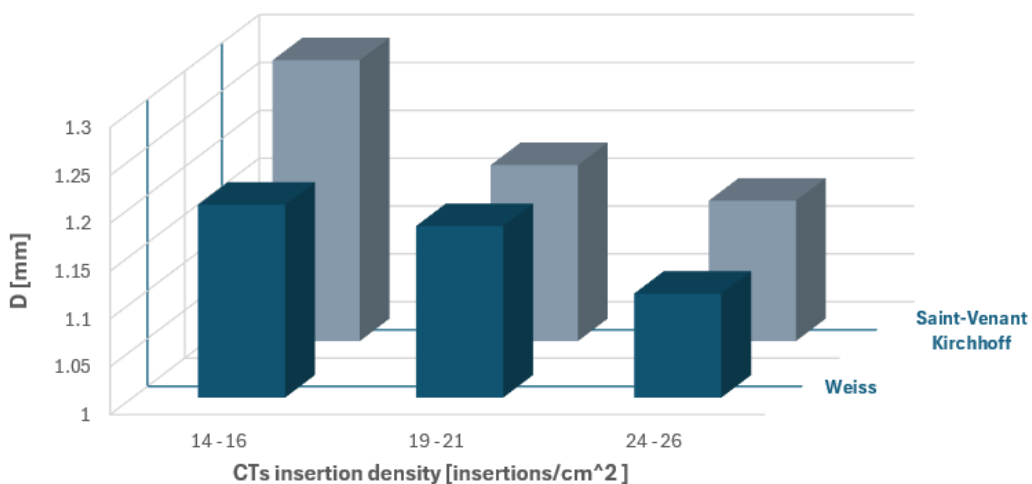


Figure 4.4: plot of the D value in mm, on the z-axis, for the 6 configurations tested. On the x-axis chordal insertion density and on the y-axis the type of constitutive model of the CTs.

4.1.1.3. Computational time

The last parameter that was considered for the sensitivity analysis was the computational time to perform the three simulations for the calibration workflow (Table 4.5). The configurations with the same chordal insertion density value shared the morphing and pressurisation simulations. Following pressurisation, the RF of the CTs was extracted and the length of the individual CTs was evaluated on the chosen constitutive model.

| ID | Morphing | Pressurization | Closure | Tot |
|------|----------|----------------|---------|-------|
| TR5 | 10:45 | 10:23 | 03:59 | 25:07 |
| TR6 | 10:45 | 10:23 | 03:31 | 24:39 |
| TR7 | 12:35 | 11:06 | 04:34 | 28:14 |
| TR8 | 12:35 | 11:06 | 04:55 | 28:36 |
| TR9 | 15:23 | 11:23 | 04:44 | 31:29 |
| TR10 | 15:23 | 11:23 | 04:58 | 31:44 |

Table 4.5: Results of sensitivity analysis: computational time for each simulation of the calibration workflow of the TV CTs. Time values are given in hours.

The total time was compared for each simulation (Figure 4.5). The result is that increasing the chordal insertion density increases the computational time required. The simulation in which the variations are most evident is the Morphing simulation. In the Closure simulation, variations occur based on the constitutive model chosen for the material of the CTs.

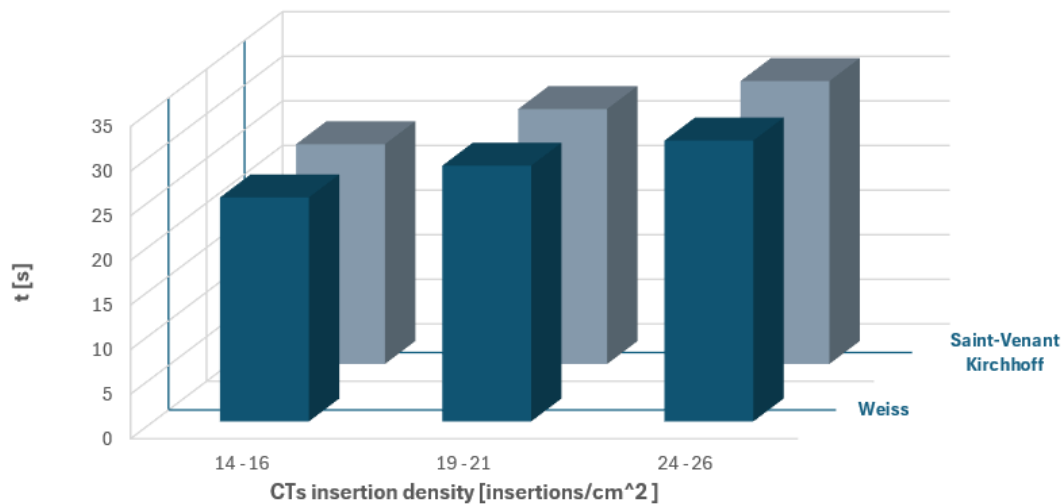


Figure 4.5: plot of the computational time in hours, on the z-axis, for the 6 configurations tested. The x-axis shows the chordal insertion density and the y-axis the type of constitutive model used for the CTs.

4.1.2. Engineering mechanics and clinically-relevant geometry metrics

This section will present key engineering and clinical metrics for TV evaluation from the analyzed configurations, enabling comparison of critical parameters in FE simulations. These findings will address core thesis questions, including the applicability of Khalighi's model for MV to TVs with TR, how it differs from Chung-Hao Lee's TV model, the impact of calibrating CTs on valve biomechanics analysis, and the effect of CTs' constitutive models on TV biomechanics.

The configurations analysed will be those shown in [Figure 4.6](#). In the specific case of the TR5, TR6, TR7, TR8, TR9 and TR10 configurations, the previous section showed that the configurations with chordal insertion densities of 24-26 insertions/cm² have a better behaviour in terms of morphological characterisation of the TV with TR; therefore, only the results obtained for the TR9 and TR10 configurations will be presented below.

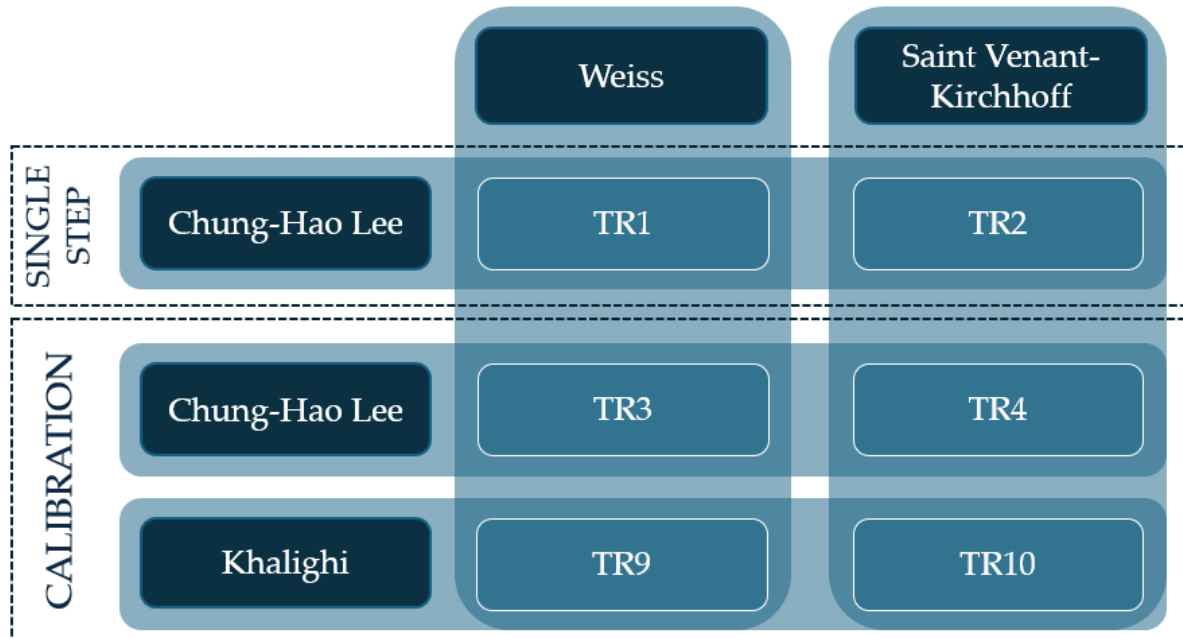


Figure 4.6: configurations chosen for parameters analysis: type of simulation, parametric model for CTs and material constitutive model of CTs.

The quantities that will be investigated for each configuration are:

- Engineering mechanics metrics:
 - Leaflets maximum principal stresses
 - CTs maximum principal stresses
 - RFs on the annulus length
 - Leaflets radial and circumferential maximum principal strains (NE11 and NE22)
- Clinically-relevant geometry metrics:
 - Regurgitation area
 - Euclidean distance between $\Omega_{PS}^{FE,closure}$ and $\Omega_{PS}^{tracing}$

4.1.2.1. Leaflets maximum principal stresses

For each configuration, the max principal stress values ([Table 4.6](#)) were extracted on the leaflets at the end of the simulation, i.e. at simulated SP.

| ID | Max principal stresses [MPa] |
|------|------------------------------|
| TR1 | 0.06 (0.038 ÷ 0.082) |
| TR2 | 0.06 (0.040 ÷ 0.091) |
| TR3 | 0.07 (0.042 ÷ 0.095) |
| TR4 | 0.07 (0.047 ÷ 0.101) |
| TR9 | 0.04 (0.014 ÷ 0.074) |
| TR10 | 0.04 (0.014 ÷ 0.074) |

Table 4.6: max principal stress values measured on the leaflets for each configuration. The values were reported as median (25th percentile ÷ 75th percentile).

For the evaluation of the maximum principal stresses, box plots were constructed based on the spectrum of values obtained by calculating the first 99 percentiles ([Figure 4.7](#)). The analysis of the percentiles allowed the exclusion of stress peaks, on the order of MPa, which were considered as outliers. The boxplots were subdivided on the basis of the constitutive model used in the description of the CTs.

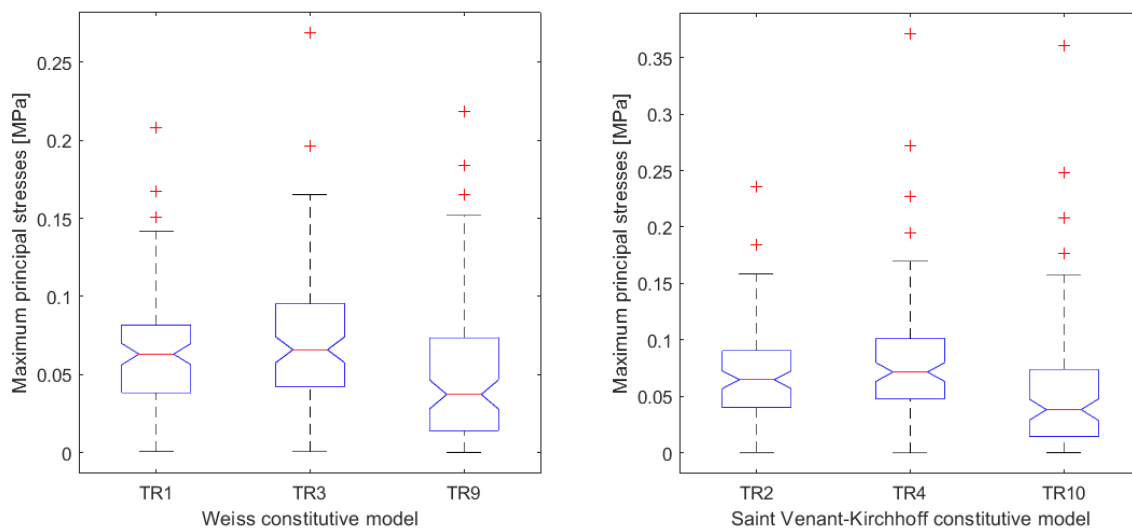


Figure 4.7: (left) box plot of the values of the leaflets maximum principal stresses in MPa of the configurations in which the CTs were described with Weiss' constitutive model. (right) configurations with the Saint Venant-Kirchhoff constitutive model.

From the values reported in [Table 4.6](#) and the box plot in [Figure 4.7](#) it is possible to observe only a little statistical variation of the max principal stress in terms of median, 25th and 75th, for the configurations in which the CTs were described using Chung-Hao Lee's model, in the case of the single step or calibration simulations. Considering one of the configuration, for example the TR3 configuration ([Figure 4.8](#)), it can be seen that

the critical point of this geometric model is the insertion points of the CTs in the leaflets.

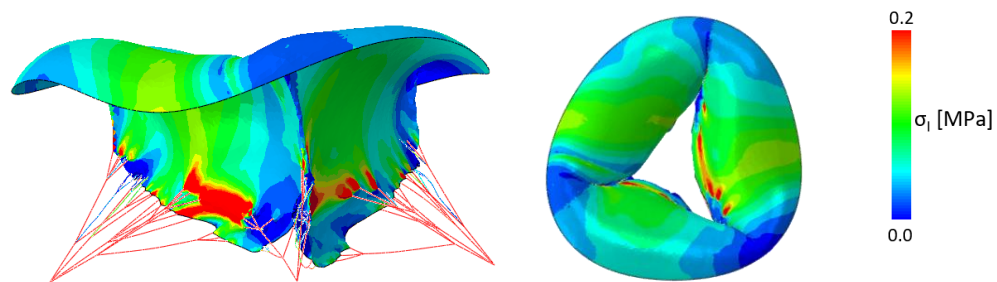


Figure 4.8: (left) lateral and (right) atrial view of the leaflets maximum principal stress of TR3 configuration at the end of systolic closure simulation.

The functionally equivalent model of the TR9 and TR10 configurations shows a significant change in the value of the median of the maximum principal stresses ([Figure 4.7](#)), compared to the previous configurations, which are reduced by half. The evenly distributed arrangement of the CTs does not allow a concentration of stresses at specific points on the leaflets. In this case, the most stressed points are in the central zone of the leaflet, a stress which tends to increase as we move from the FRM to the annulus ([Figure 4.9](#)).

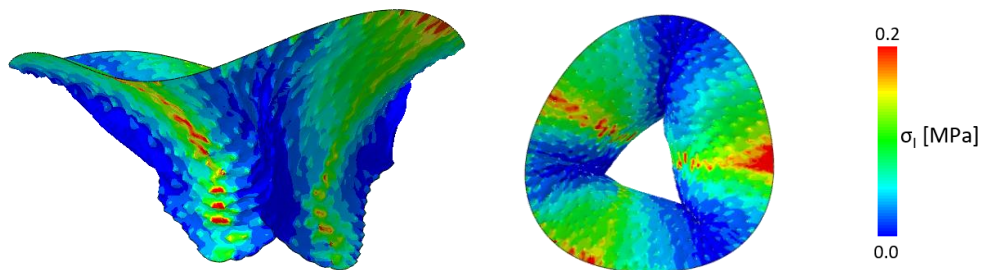


Figure 4.9: (left) lateral and (right) atrial view of leaflet max principal stress of the TR9 configuration at the end of the simulation.

4.1.2.2. CTs Maximum principal stresses

Maximum principal stresses values were also evaluated for the CTs ([Table 4.7](#)). In the case of the TR9 and TR10 configurations, the values of the two groups of CTs were also extracted: the CTs that fit into the FRM of the TV and the CTs that fit onto the leaflets.

| ID | Max principal stresses [MPa] |
|------|--------------------------------------|
| TR1 | 0.21 (0.071 ÷ 1.034) |
| TR2 | 0.27 (0.069 ÷ 1.019) |
| TR3 | 0.40 (0.123 ÷ 1.116) |
| TR4 | 0.63 (0.1306 ÷ 1.683) |
| TR9 | 0.15 (0.108 ÷ 0.220) |
| | CTs on FRM 0.06 (0.038 ÷ 0.100) |
| | CTs on leaflets 0.16 (0.113 ÷ 0.229) |
| TR10 | 0.13 (0.081 ÷ 0.202) |
| | CTs on FRM 0.04 (0.028 ÷ 0.073) |
| | CTs on leaflets 0.14 (0.089 ÷ 0.209) |

Table 4.7: CTs maximum principal stress for each configuration in MPa. The values were reported as median (25th percentile ÷ 75th percentile).

The Chung-Hao Lee model depicts a less populated chordal apparatus, in term of CTs, compared to the functionally equivalent model.

This implies that a smaller number of chords are responsible for handling a substantial load, leading to significantly lower stress values in the CTs as per the functionally equivalent model. The data from different configurations, illustrated through box plots in [Figure 4.10](#), clearly delineates the disparities between the two models.

Stress values in the functionally equivalent model are tightly grouped, indicating uniform stress across CTs, a result of calibrating unbranched CTs. Conversely, in Chung-Hao Lee's model, the stress disparity between the 25th and 75th percentiles is vast, indicating that some CT sections face high stress while others bear minimal load.

The aggregated stresses across branch levels in the box plots ([Figure 4.10](#)) for configurations TR1 through TR4 suggest that categorizing stresses by branch level could either narrow the gap between the 25th and 75th percentiles or elucidate stress distribution across each level of branches.

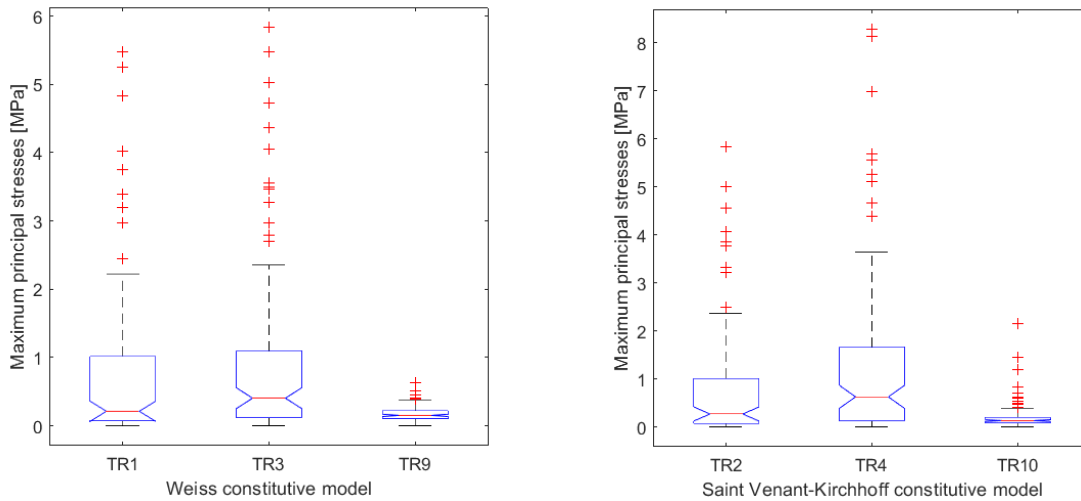


Figure 4.10: (left): box plot of CTs maximum principal stresses in MPa in which the material is described with the Weiss constitutive model. (right): box plot in which the CTs are Saint Venant-Kirchhoff constitutive model.

Applying the calibration to the model of Chung-Hao Lee shows a change in the statistic distribution of values, which becomes particularly significant when the constitutive Saint Venant-Kirchhoff model was used.

4.1.2.3. RF Annulus

For each configuration were extracted the RF along the annulus ([Table 4.8](#)).

| ID | RF [N] |
|------|----------------------|
| TR1 | 0.02 (0.011 ÷ 0.022) |
| TR2 | 0.02 (0.011 ÷ 0.021) |
| TR3 | 0.02 (0.011 ÷ 0.021) |
| TR4 | 0.02 (0.013 ÷ 0.022) |
| TR9 | 0.02 (0.011 ÷ 0.035) |
| TR10 | 0.02 (0.012 ÷ 0.044) |

Table 4.8: RF along the annulus for each configuration. The values were reported as median (25th percentile ÷ 75th percentile).

The RFs on the annulus do not show significant variations among configurations. The only aspect that can be emphasised is that, as shown in [Figure 4.11](#), the TR9 and TR10 configurations present a greater gap between the minimum and maximum peaks, respect the other configurations.

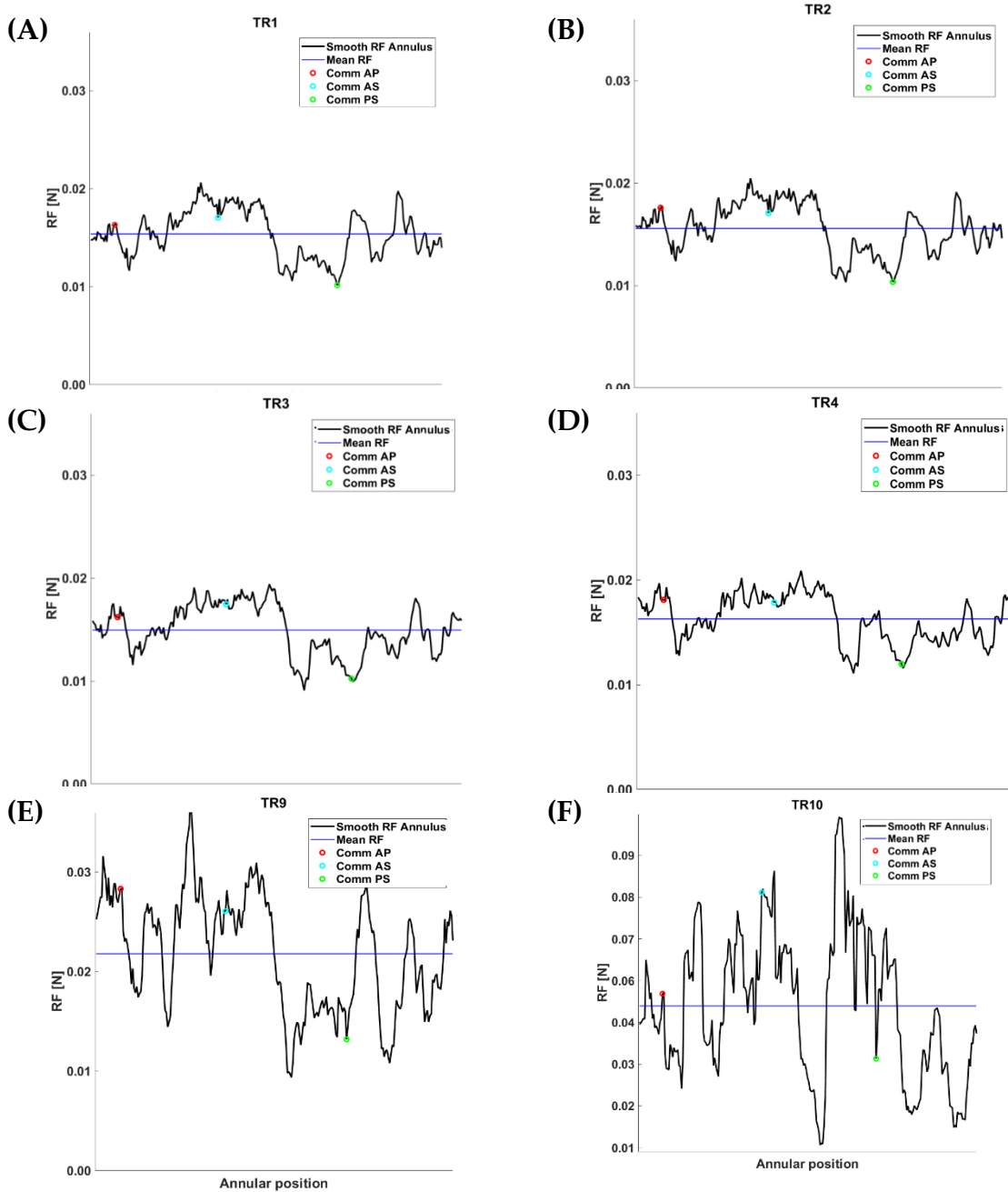


Figure 4.11: RFs graphs at the end of the valve closure simulation as a function of position on the annulus. The actual values have been filtered with a low-pass filter to make the distribution more meaningful, and are represented with a black line. The blue line is the average value of the RFs. The dots are used to determine the position of the RFs with respect to the valve annulus: red the position of the antero-posterior commissure, cyan the antero-septal commissure, green the postero-septal commissure.

4.1.2.4. Leaflets maximum principal strains

[Table 4.9](#) depicts the maximum principal strains on the leaflets. The maximum principal strains were divided into its radial (NE11) and circumferential (NE22) components, defined on the cylindrical reference system used to reconstruct the TV.

| ID | | Max principal strains [MPa] |
|------|------|-----------------------------|
| TR1 | NE11 | 0.21 (0.098 ÷ 0.293) |
| | NE22 | 0.03 (-0.025 ÷ 0.121) |
| TR2 | NE11 | 0.23 (0.102 ÷ 0.303) |
| | NE22 | 0.03 (-0.040 ÷ 0.120) |
| TR3 | NE11 | 0.23 (0.113 ÷ 0.319) |
| | NE22 | 0.03 (-0.034 ÷ 0.103) |
| TR4 | NE11 | 0.24 (0.107 ÷ 0.337) |
| | NE22 | 0.01 (-0.055 ÷ 0.109) |
| TR9 | NE11 | 0.16 (0.049 ÷ 0.246) |
| | NE22 | 0.06 (0.002 ÷ 0.132) |
| TR10 | NE11 | 0.16 (0.047 ÷ 0.250) |
| | NE22 | 0.06 (0.005 ÷ 0.125) |

Table 4.9: Leaflets maximum principal strains divided in radial (NE11) and circumferential (NE22) component for each configuration. The values were reported as median (25th percentile ÷ 75th percentile).

The NE11 consistently exhibits a higher modulus than the NE22 across all configurations, leading to greater deformation in the radial direction. This deformation results from applied pressure on the ventricular surface and restricted annulus point displacement. However, the radial deformation in the functionally equivalent model is restrained by the CTs in both the basal and clear zones. The Chung-Hao Lee model, characterized by a sparser distribution of CTs and their absence in the upper valve regions, permits greater radial deformation (see [Figure 4.12](#)). Conversely, the functionally equivalent model shows more pronounced circumferential deformation, attributed to the evenly distributed CT insertion points, which increase surface tension.

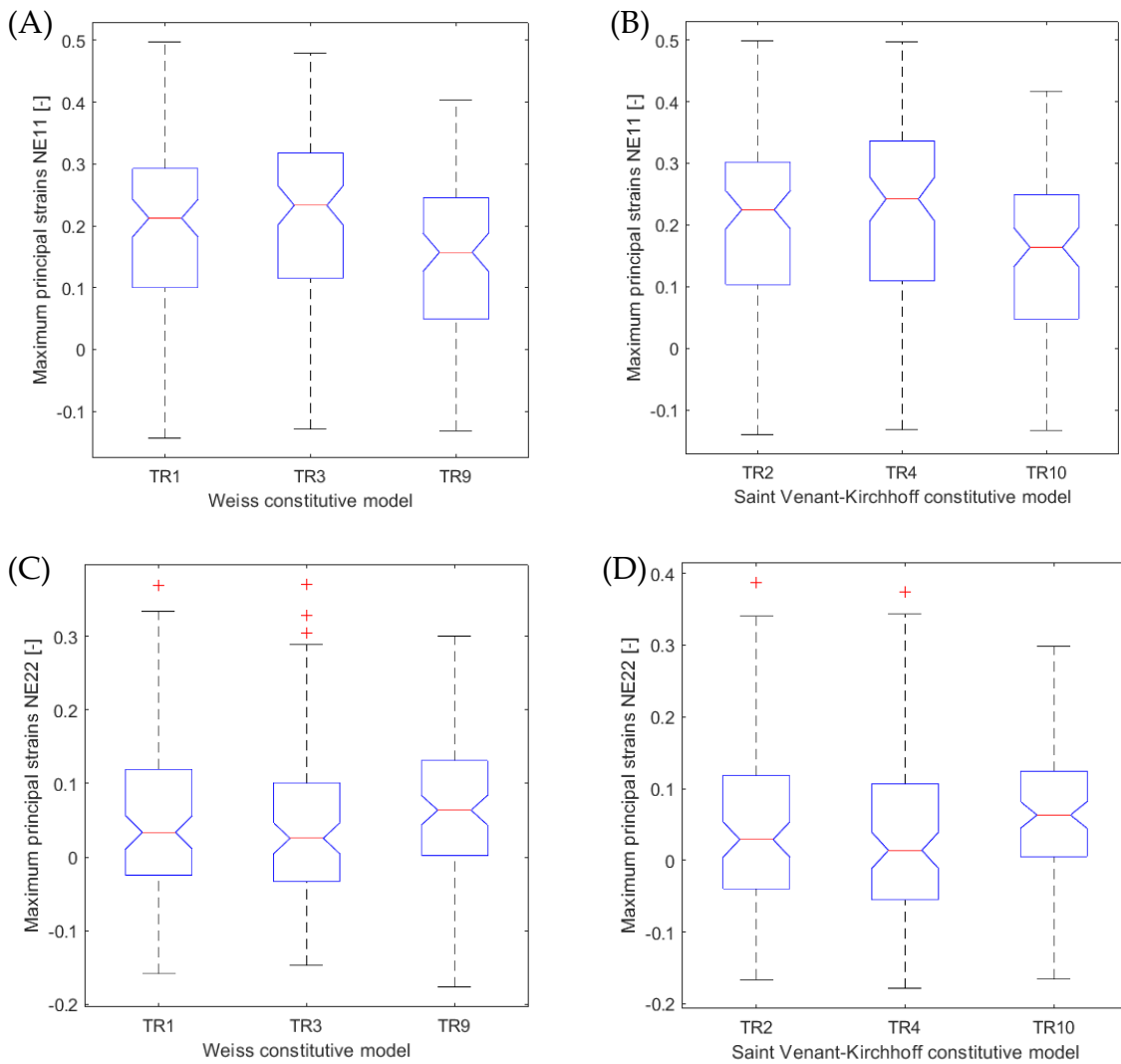


Figure 4.12: Box plot leaflets maximum principal strain (A) NE11 with CTs described with Weiss constitutive model (B) NE11 with CTs described with Saint Venant-Kirchhoff constitutive model (C). NE22 with CTs described with Weiss constitutive model (D) NE22 with CTs described with Saint Venant-Kirchhoff constitutive model.

The NE11 values of the configurations with the two parametric models are also confirmed by simply observing the morphology that the valve assumes in the two cases. Observing the TR3 ([Figure 4.13](#)) and TR9 ([Figure 4.14](#)) valves, the former tends to swell with respect to the annulus plane, while the latter maintains a conformation more similar to the reference one. In the TR3 valve, a peak of NE11 values is observed at the central zone of the leaflet, on the contrary NE22 strain peaks, although of a much smaller magnitude, can be observed at the insertion of the CTs at the level of the FRM.

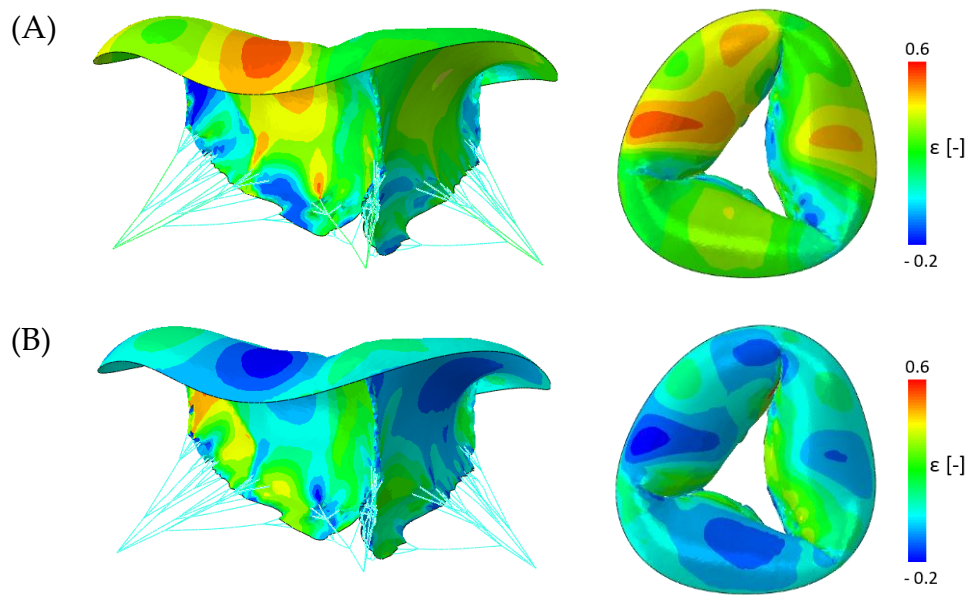


Figure 4.13: (A) (left) lateral and (right) atrial view of leaflets NE11 of TR3 configuration at the end of closure simulation. (B) (left) lateral and (right) atrial view of leaflets NE22 of TR3 in the same condition.

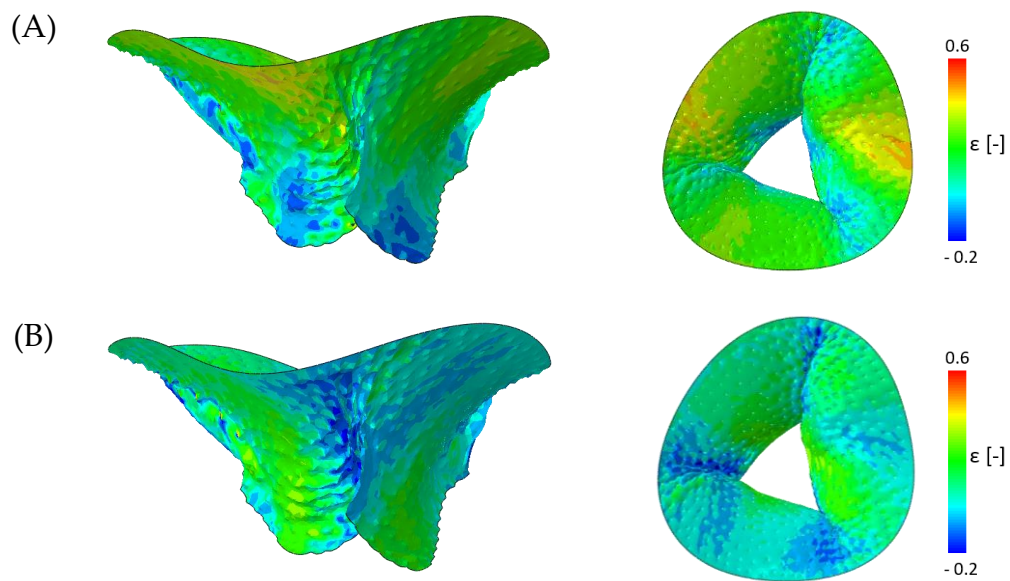


Figure 4.14: (A) (left) lateral and (right) atrial view of leaflets NE11 of TR9 configuration at the end of closure simulation. (B) (left) lateral and (right) atrial view of leaflets NE22 of TR9 in the same condition

4.1.2.5. Regurgitation area

The regurgitation area was assessed following the statistical technique described in section 4.1.1.1 "Regurgitation area" and using the values given in Table 4.2 as references (Table 4.10).

| ID | $A_{FRM,FE}$ [mm ²] | % $RA_{FRM,FE}$ (ϵ) |
|------|---------------------------------|--------------------------------|
| TR1 | 212.29 | 10.55 % (1.68) |
| TR2 | 200.80 | 9.99 % (2.24) |
| TR3 | 209.93 | 10.44 % (1.79) |
| TR4 | 266.16 | 13.24 % (- 1.01) |
| TR9 | 254.00 | 12.63 % (- 0.4) |
| TR10 | 206.64 | 10.27 % (1.96) |

Table 4.10: for each configuration was evaluated the regurgitation area of $\Omega_{PS}^{FE,closure}$, moreover the percentage of the regurgitation area extracted of $\Omega_{PS}^{FE,closure}$ was calculated with respect to the annular area of $\Omega_{PS}^{tracing}$ (% $RA_{FRM,tracing}$ - % $RA_{FRM,FE}$).

In the case of the configuration in which the parametric Chung-Hao Lee model is used, the calibration shows an effect that varies according to the constitutive model used. As was the case in section 4.1.1.1 "Regurgitation area", the constitutive model of the material appears to play a significant role in the regurgitation area obtained. The error between the various models was represented graphically in Figure 4.15.

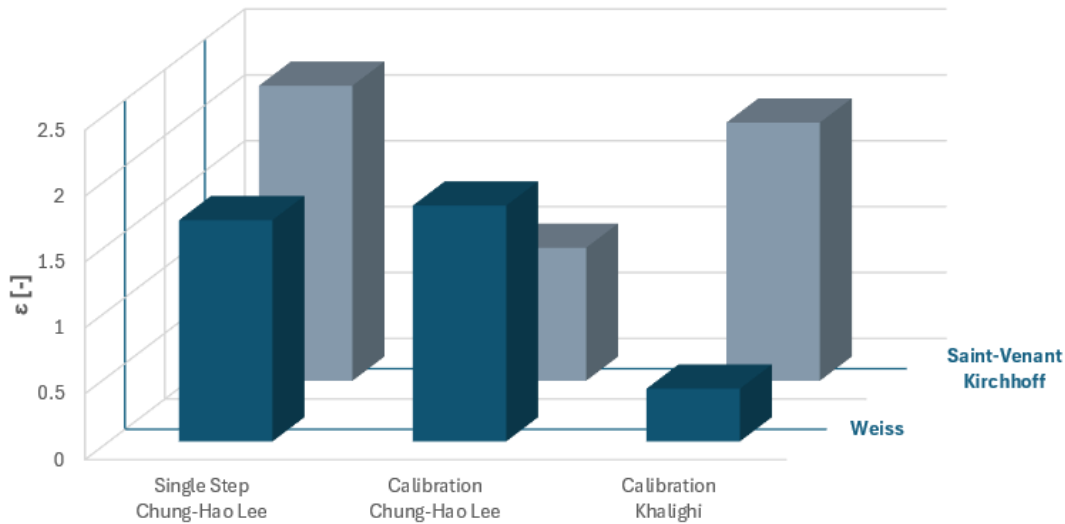


Figure 4.15: plot of the value of ϵ , on the z-axis, for the 6 configurations tested. The x-axis shows the simulation workflow used and the y-axis the type of constitutive model used for the CTs.

4.1.2.6. Euclidean distance between $\Omega_{PS}^{tracing}$ and $\Omega_{PS}^{FE,closure}$

This parameter was calculated as reported in the section [4.1.1.2. “Euclidean distance between \$\Omega_{PS}^{FE,closure}\$ and \$\Omega_{PS}^{tracing}\$ ”](#) (Table 4.11)

| ID | D [mm] |
|------|--------------------|
| TR1 | 3.89 (2.03 ÷ 5.93) |
| TR2 | 3.49 (1.69 ÷ 5.33) |
| TR3 | 3.29 (1.82 ÷ 5.11) |
| TR4 | 2.59 (1.14 ÷ 4.42) |
| TR9 | 1.11 (0.46 ÷ 1.91) |
| TR10 | 1.15 (0.55 ÷ 1.97) |

Table 4.11: Euclidean distance values calculated point-to-point along the entire leaflet surface. Values are reported as median (25th percentile ÷ 75th percentile).

The parametric model of the CTs determines the morphology of the leaflets at the end of the SP closure simulation ([Figure 4.16](#)). Considering Chung-Hao Lee et al.'s model, the calibration acted by reducing the error caused by the chordal apparatus ([Figure 4.16](#)).

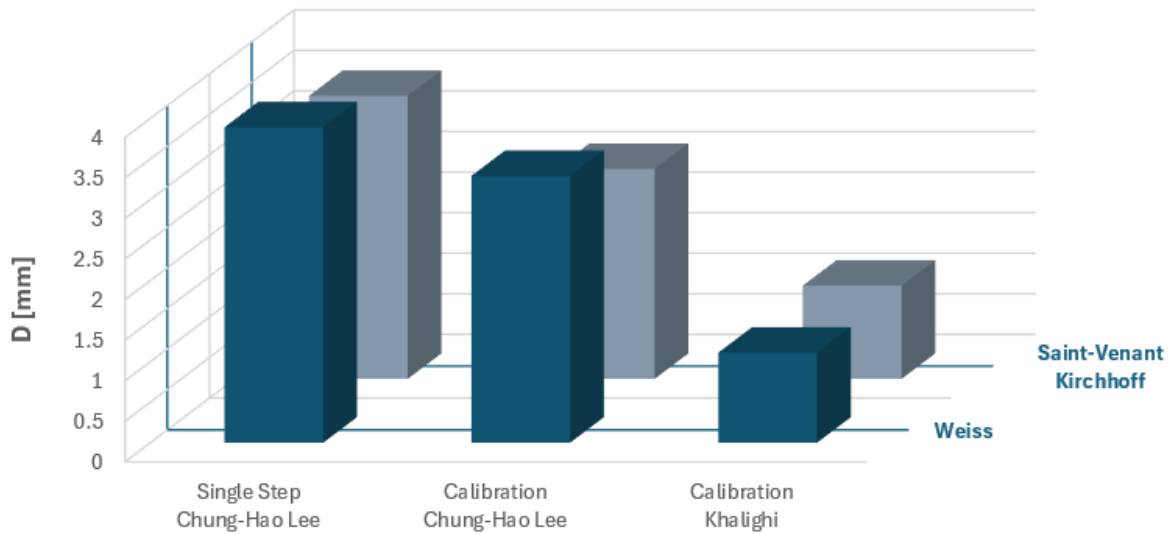


Figure 4.16: plot of the D value in mm, on the z-axis, for the 6 configurations tested. On the x-axis chordal insertion density and on the y-axis the type of constitutive model of the CTs.

As already shown by the values of the maximum principal strains, the two parametric models for the description of the CTs determine the biomechanical behaviour of the TV leaflets. [Figure 4.17](#) plots the TR3 (A) and TR9 (B) configurations against the reference surface. The TR3 valve tends to inflate, and the centre of the leaflets progressively moves away from the reference surface. The TR9 valve, thanks to the contribution of the CTs, acquires a morphology very similar to the reference one.

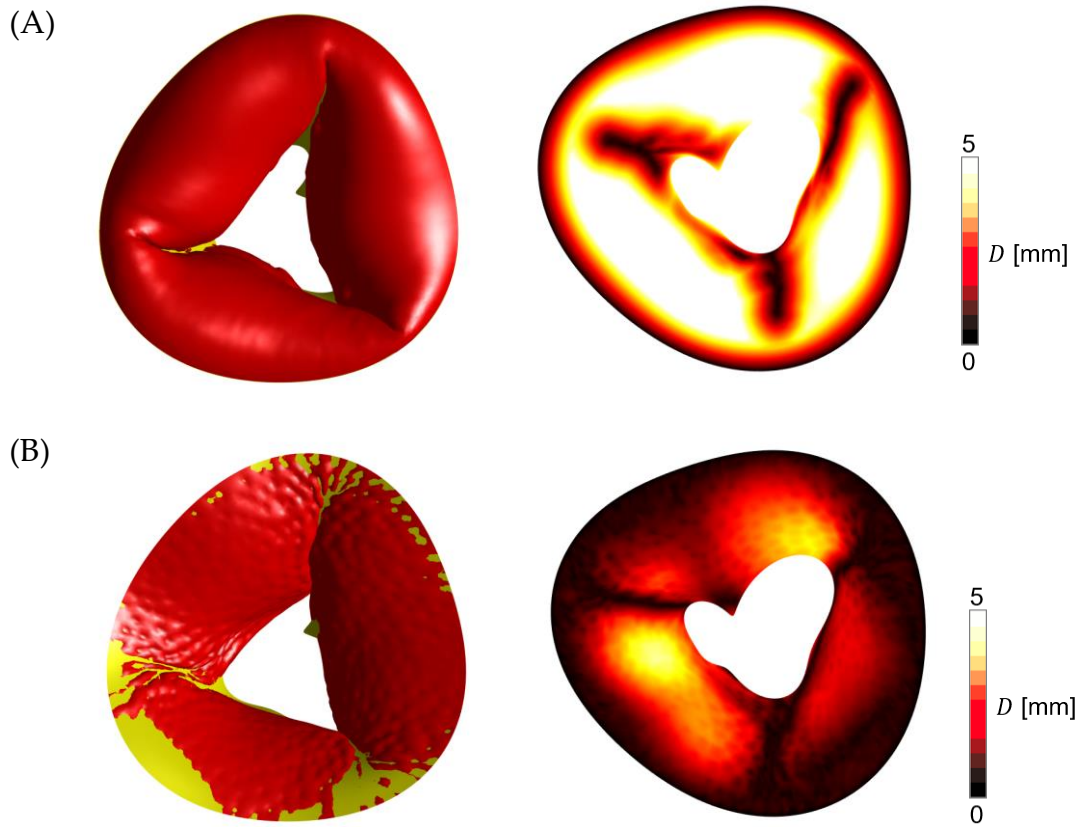


Figure 4.17: (A) (left) plot of the $\Omega_{PS}^{FE,closure}$ TR3 in red on the $\Omega_{PS}^{tracing}$ reference valve in yellow. (right) plot of the point-to-point distance between $\Omega_{PS}^{FE,closure}$ and $\Omega_{PS}^{tracing}$. Black means the distance is approximately 0, white in says the distance is 5 mm or more. (B) (left) plot of the $\Omega_{PS}^{FE,closure}$ TR9 in red on the $\Omega_{PS}^{tracing}$ reference valve, in which the interpenetration of surfaces is visible. (right) plot of the point-to-point distance between the $\Omega_{PS}^{FE,closure}$ and the $\Omega_{PS}^{tracing}$ reference valve.

4.2. Analysis of TV after FWA AP60

During in-vitro experimental work of Manini and Locatelli thesis [29] the TVs with TR were subjected to the FWA procedure. Using the experimental data acquired in the case of 60% FWA in the AP direction on the HT11 valve was reproduced in silico. Starting from these data and following the work carried out in the previous section, a methodological study was conducted using FE analysis on the configurations shown in Table 4.2. In this section the results obtained will be discussed.

4.2.1. Quality of the images

A preliminary, macroscopic analysis of the echocardiographic images ([Figure 4.18](#)) shows that the planes that were used for radial segmentation have centring problems. In some images, part of the TV atrium was cut off and the axis of rotation of the images did not coincide with the actual axis of the valve.

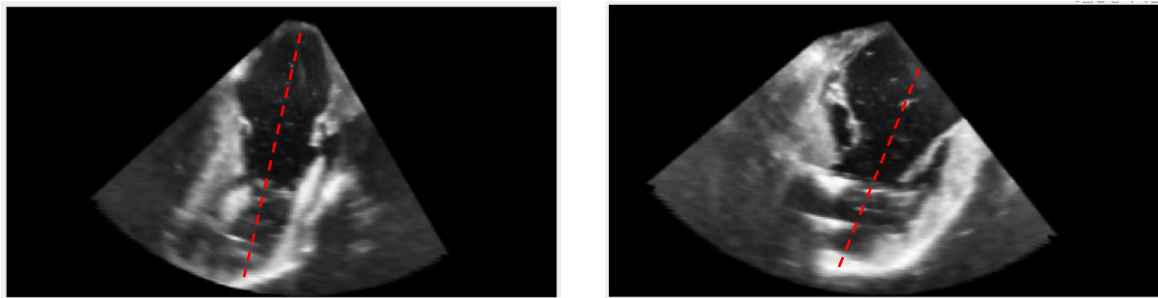


Figure 4.18: Echocardiographic planes of the long axis of the post-surgery HT11 valve. In the images the valve axis is highlighted in red, considering the ED frame of different planes of the same volumetric data.

The current tools, previously implemented in MATLAB and described in the sections [3.4. "Radial segmentation"](#) and [3.5. "Short-axis segmentation"](#), for aligning the TV and setting radial planes lack the precision needed for detailed image manipulation. Their centering capability relies on a limited set of functions for identifying key structures, leading to inaccuracies when applied to echocardiographic images from a test bench that don't follow clinical protocols. As a result, these tools often fail to produce precise and consistent data. Moreover, the process of identifying crucial structures for centering is subject to operator variability.

Observations using the "viewer" tool within the radial axis Graphical User Interface (GUI) reveal uneven distribution of points marked to outline the annulus (see [Figure 4.19](#)). Especially noticeable with annulus points on the right side of each plane-image appearing more clustered. This irregularity could potentially distort the calculated shape of the annulus after intervention.

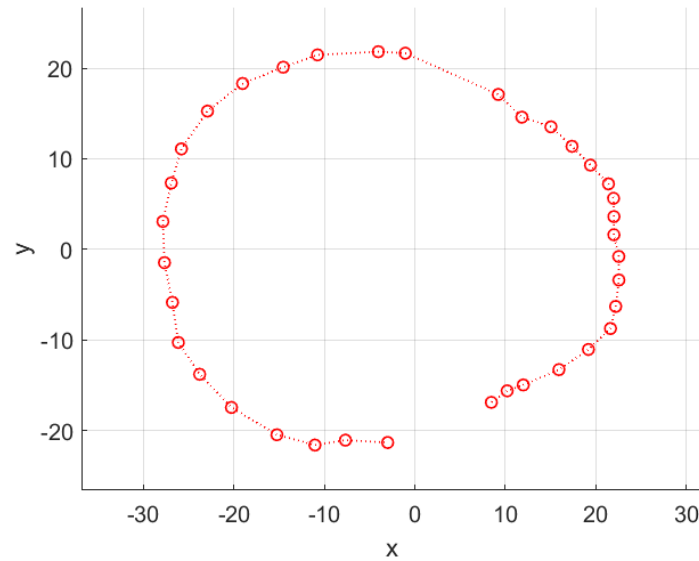


Figure 4.19: Plot in xy plane extracted following the tracing of the annulus points. There is a discrepancy between the points plotted for the annulus on the left-hand side and the specular points on the right-hand side.

The data obtained were compared graphically (Figure 4.20) with the data of the same valve before the simulation of FWA. An initial analysis reveals variation in the proportions of the main structures (annulus and PMs) pre-surgery and post-surgery.

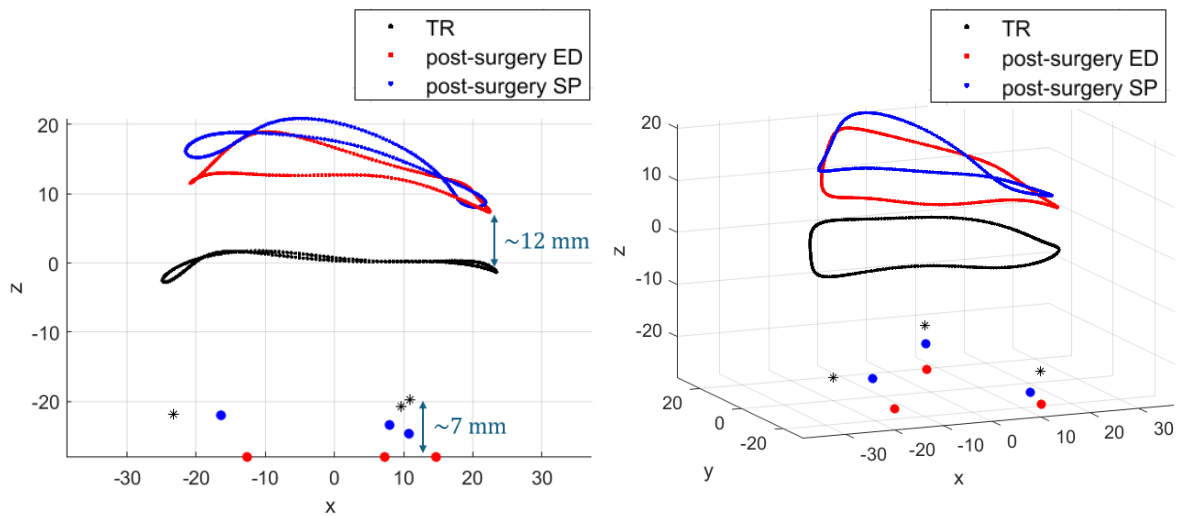


Figure 4.20: (left) plot in the xz-plane showing the difference in proportions between the annulus (black dots) and PMs (black stars) of the TV pre-surgery valve at ED and the same structure of the TV post-surgery at ED (red dots) and SP (blue dots). (right) plot of the same structures in their three-dimensionality.

Overall, it is possible to observe a certain consistency between the ED and SP structures of the post-surgery valve in that the SP PMs are in a more apical position than the ED PMs as the CTs come into tension by also stretching the head of the PM to which they are connected.

Applying the post-surgery simulation to this data, then requesting the shifting of the PMs and annulus points from the configuration of the TV with TR at ED to that of the post-surgery TV at ED, some CTs at the beginning of step 2 of the simulation are already in tension, tension which increases following the application of pressure to simulate the systolic closure of the TV. The results obtained at SP, with the actual annulus and PM positions plotted, show a particularly critical situation in terms of max principal stresses 2.53 (0.41 ÷ 6.47) MPa (Figure 4.21), NE11 strains 0.36 (0.20 ÷ 0.49) (Figure 4.22) and NE22 strains 0.05 (-0.05 ÷ 0.18). Reported data are median (25th percentile ÷ 75th percentile) (Figure 4.23).

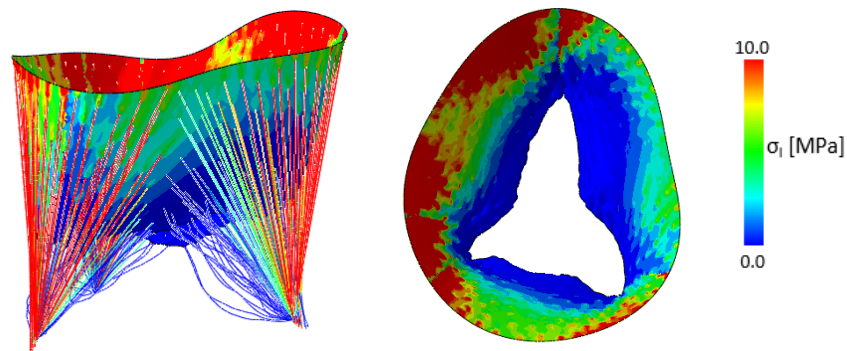


Figure 4.21: Maximum principal stresses using data extracted from the echo images.

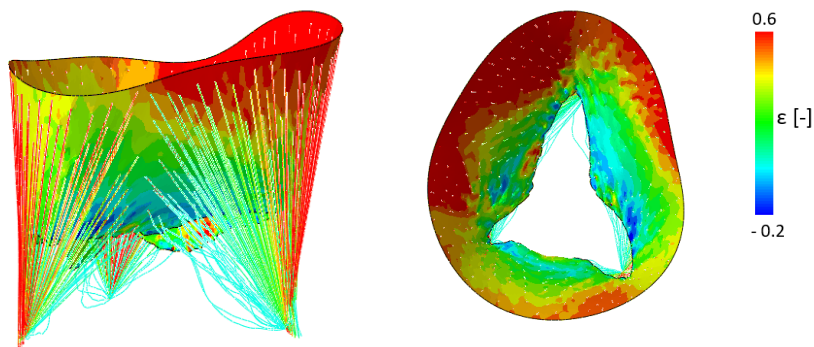


Figure 4.22: Maximum principal strains NE11 using data extracted from the echo images.

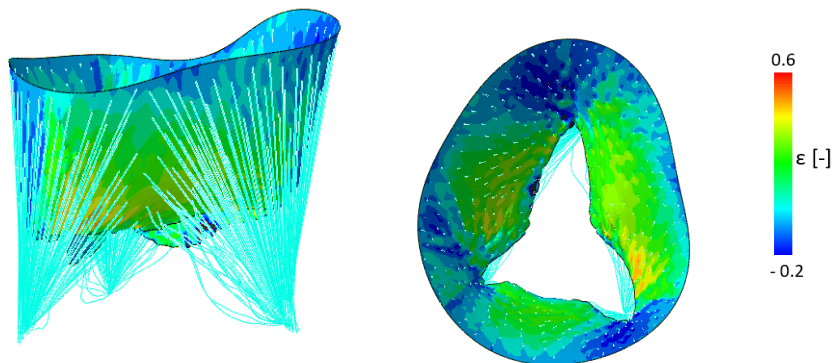


Figure 4.23: Maximum principal strains NE22 using data extracted from the echo images.

The conditions imposed on these simulations are not plausible for several reasons:

- In the approach described by Jaworek et al. [10] and as depicted in [Figure 1.10c](#), the PMs on which the distance reduction is carried out are brought closer to the xy plane of the valve, but there should be no appreciable change in height in z. The variation in z in the case of the three PMs at the TV ED with TR and TV post-surgery is reported in [Table 4.12](#).

| | PM antero-posterior | PM antero-septal | PM postero-septal |
|-----------------|------------------------|---------------------|----------------------|
| Δz [mm] | 6.14 | 8.31 | 7.22 |

Table 4.12: displacement of PMs in z direction from the TV with TR to the TV post-surgery

- The annulus may change its spatial location following surgery. When assessing all annulus coordinates in relation to the z-coordinate, the median shift is 12.73 mm, with the 25th percentile at 11.05 mm and the 75th percentile at 14.63 mm

For these reasons the initial data were manipulated to guarantee the proportional ratio between the two configurations: pre-surgery and post-surgery ([Figure 4.24](#)).

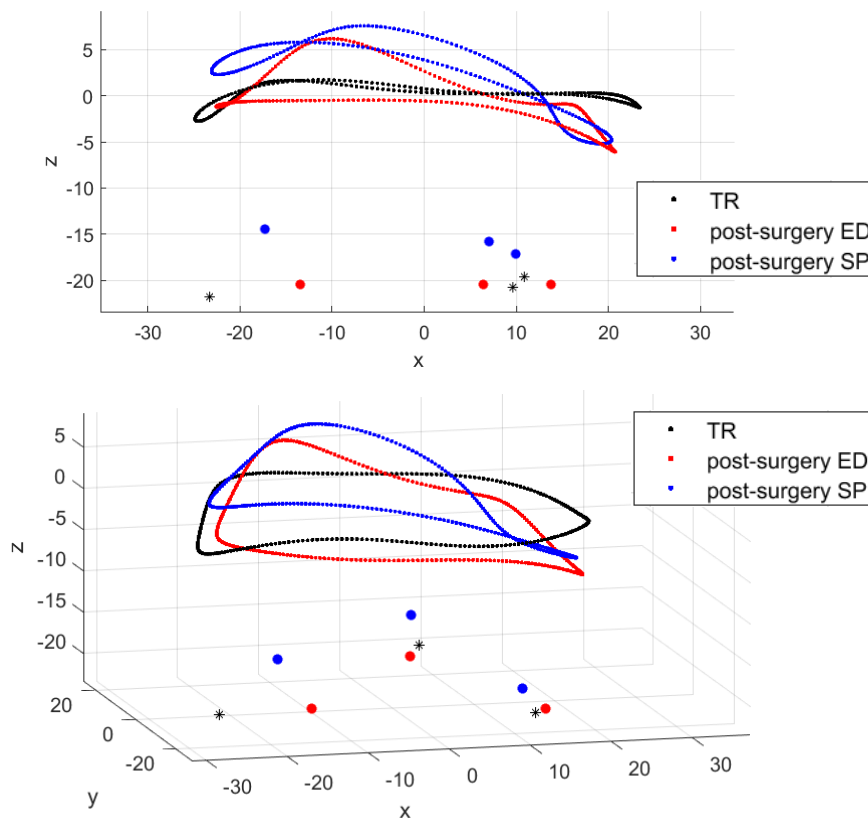


Figure 4.24: (Upper) plot in the xz-plane showing the annulus (black dots) and PMs (black stars) of the TV pre-surgery valve at ED and the same structure of the TV post-surgery at ED (red dots) and SP (blue dots) after the modification of the proportionality between the structures. (Lower) plot of the same structures in their three-dimensionality.

Finally, in the first step of the simulation, the annulus and PMs are moved to the position traced at the post-surgery ED. The displacement of the annulus also causes the displacement of the leaflets' surface ([Figure 4.25](#)). The imposed movement on the annular nodes, however, led to a change in the configuration of the leaflets, which consequently had a spatial arrangement that was not optimal for facilitating the closure of the TV.



Figure 4.25: Atrial and lateral view of the TV at the end of the first step of the post-surgery simulation. The TVPL (red) shows the most pronounced displacement, the issue is also present on the TVAL (grey) and on TVSL (blue).

4.2.2. Functional equivalent model

As with the TR valve, Khalighi's functionally equivalent model, represented by the AP3, AP4, AP5, AP6, AP7 and AP8 configurations, was tested with three distinct chordal densities: 15 ± 1 , 20 ± 1 and 25 ± 1 insertions/cm². In this section, the results obtained using engineering and clinically relevant metrics will be presented.

4.2.2.1. Leaflets maximum principal stresses and strains

The models in which the CTs were described with the Khalighi functionally equivalent model experienced problems during the post-surgery simulation. The displacement of the PMs and annulus, without intentional modifications on the CTs, caused an increase of the stresses where the distance between PMs and insertion points in the leaflets is higher than the configuration with TR and excessive leaflet deformations where the ends of the CTs were brought closer.

The models using the Khalighi functionally equivalent approach for CTs encountered issues in post-surgery simulations. The CTs, previously calibrated to precisely reproduce the regurgitant TV configuration, led to heightened stresses in areas where PMs and insertion points on the leaflets were farther apart compared to the TR configuration, and to excessive leaflet deformations when the CT endpoints were nearer.

The AP8 (chordal density of 25 ± 1 insertions/cm² and Weiss constitutive model) led to the less biased results among its family of configurations. [Figure 4.26](#) depicts the maximum principal stresses. From the image, stress peaks, in the order of 10 MPa, are denoted near the antero-posterior commissure. This high-stress area is caused by the

excessive elongation of the CTs inserted in that portion of leaflet, resulting from the imposed BCs at the annular and PM level. These CTs have to cover a greater distance than that which was calculated in the calibration phase on the TV with TR. The zones of the leaflet most affected by this issue are the clear zone and the basal zone. Analysing the SP conformation of the TV, it is observed that the TVAL and TVSL tend to bulge. This observation is supported by the radial ([Figure 4.27](#)) and circumferential ([Figure 4.28](#)) deformation maps, which show peaks in the central area of the two leaflets. The TVPL is the only one showing physiological behaviour.

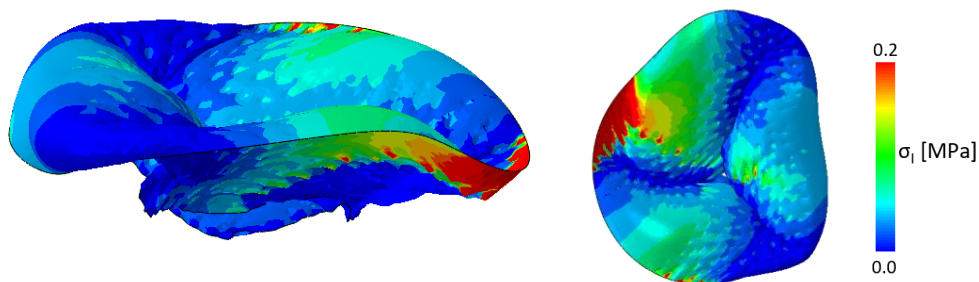


Figure 4.26: (left) lateral and (right) atrial view of leaflets maximum principal stresses on AP8 configuration.

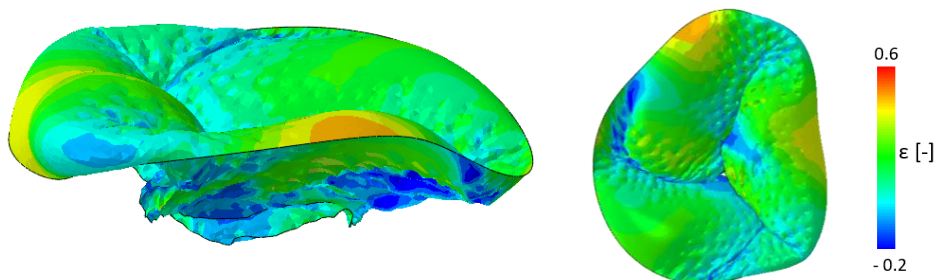


Figure 4.27: (left) lateral and (right) atrial view of leaflets maximum principal strains NE11 on AP8 configuration.

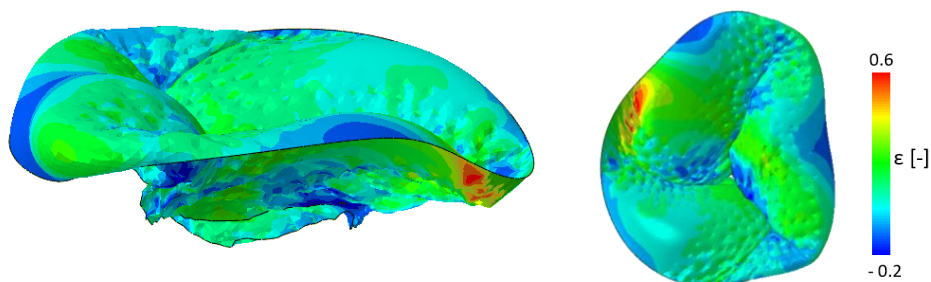


Figure 4.28: (left) lateral and (right) atrial view of leaflets maximum principal strains NE11 on AP8 configuration.

For each configuration, the median, 25th and 75th percentile ([Table 4.13](#)) of the values of maximum principal stresses and maximum principal strains in both the radial and circumferential directions were calculated. The box plots in [Figure 4.29](#) were produced

with the same values. The data showed no significant variations between the configurations tested. The chord length bias related to the displacement of the PMs and annulus points affects all tested chordal insertions with almost the same intensity.

| ID | Max principal stresses [MPa] | NE11 [-] | NE22 [-] |
|-----|------------------------------|----------------------|-----------------------|
| AP3 | 0.03 (0.008 ÷ 0.048) | 0.10 (0.008 ÷ 0.195) | 0.06 (-0.009 ÷ 0.140) |
| AP4 | 0.03 (0.008 ÷ 0.047) | 0.11 (0.018 ÷ 0.196) | 0.06 (-0.015 ÷ 0.136) |
| AP5 | 0.03 (0.008 ÷ 0.048) | 0.10 (0.008 ÷ 0.195) | 0.06 (-0.004 ÷ 0.139) |
| AP6 | 0.03 (0.008 ÷ 0.047) | 0.11 (0.014 ÷ 0.197) | 0.06 (-0.008 ÷ 0.139) |
| AP7 | 0.03 (0.008 ÷ 0.048) | 0.10 (0.008 ÷ 0.195) | 0.07 (-0.006 ÷ 0.141) |
| AP8 | 0.03 (0.008 ÷ 0.048) | 0.11 (0.013 ÷ 0.196) | 0.06 (-0.013 ÷ 0.137) |

Table 4.13: Leaflets maximum principal stresses in MPa and leaflets maximum principal strains divided in radial (NE11) and circumferential (NE22) component for each configuration. The values were reported as median (25th percentile ÷ 75th percentile).

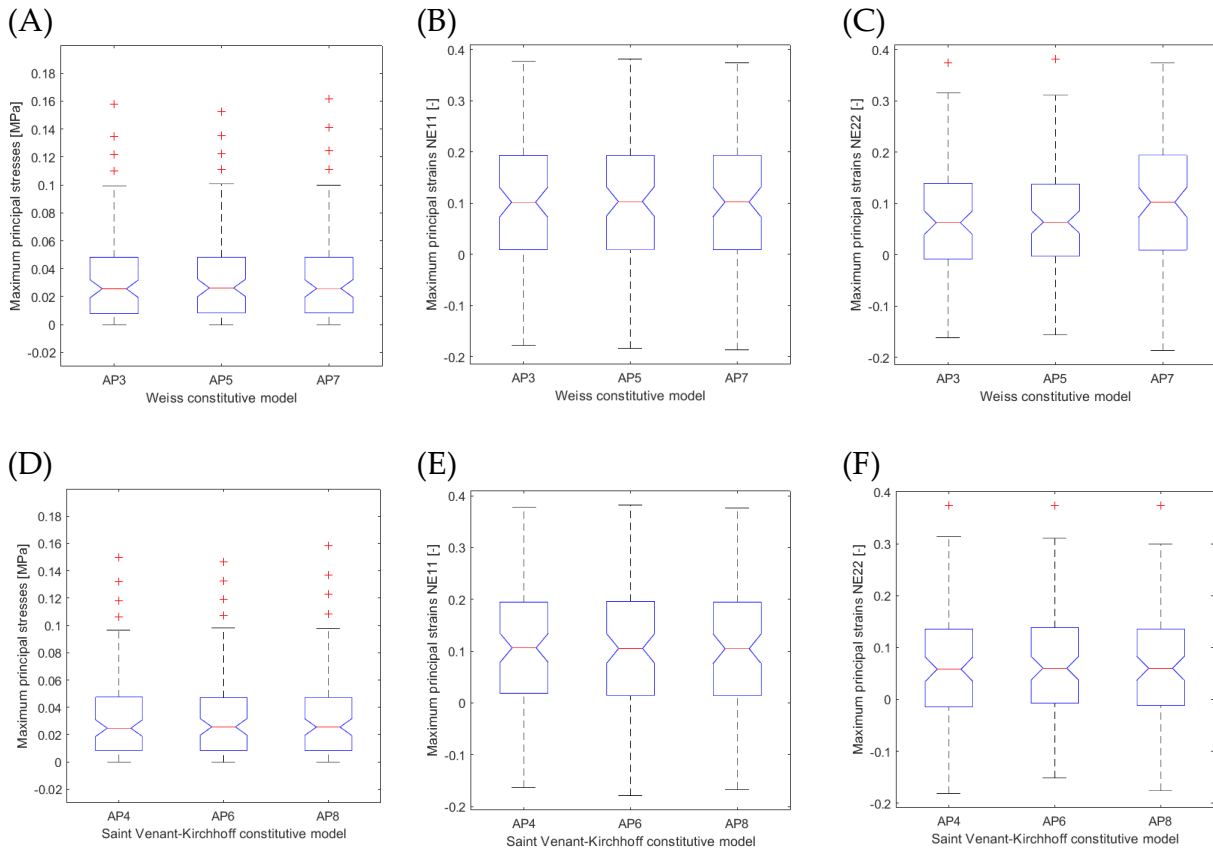


Figure 4.29: Box plot of (A) leaflets maximum principal stresses in MPa, maximum principal strain (B) NE11 and (C) NE22 with CTs described with Weiss constitutive model. Box plot of (D) leaflets maximum principal stresses in MPa, maximum principal strain (E) NE11 and (F) NE22 with CTs described with Sain Venant-Kirchhoff constitutive model.

4.2.2.2. CTs maximum principal stresses

For each configuration, the values of the maximum principal stresses were extracted ([Table 4.14](#)).

| ID | Max principal stresses [MPa] |
|-----|------------------------------|
| AP3 | 0.10 (0.011 ÷ 0.198) |
| AP4 | 0.08 (0.006 ÷ 0.182) |
| AP5 | 0.07 (0.008 ÷ 0.153) |
| AP6 | 0.06 (0.004 ÷ 0.144) |
| AP7 | 0.07 (0.007 ÷ 0.128) |
| AP8 | 0.06 (0.004 ÷ 0.122) |

Table 4.14: CTs maximum principal stresses in MPa for each configuration. The values were reported as median (25th percentile ÷ 75th percentile).

The analysis of the data ([Figure 4.30](#)) shows that by increasing the chordal insertion density, and consequently the number of CTs, the values of the maximum principal stresses tend to decrease. Furthermore, there is a discrete variation in behaviour by varying the constitutive model of the material. The configuration in which the CTs are described with the Weiss constitutive model, for each configuration, presents both in terms of median and 25th and 75th percentile values greater than those extracted for the configurations in which the material description was performed with the Saint-Venant-Kirchhoff model.

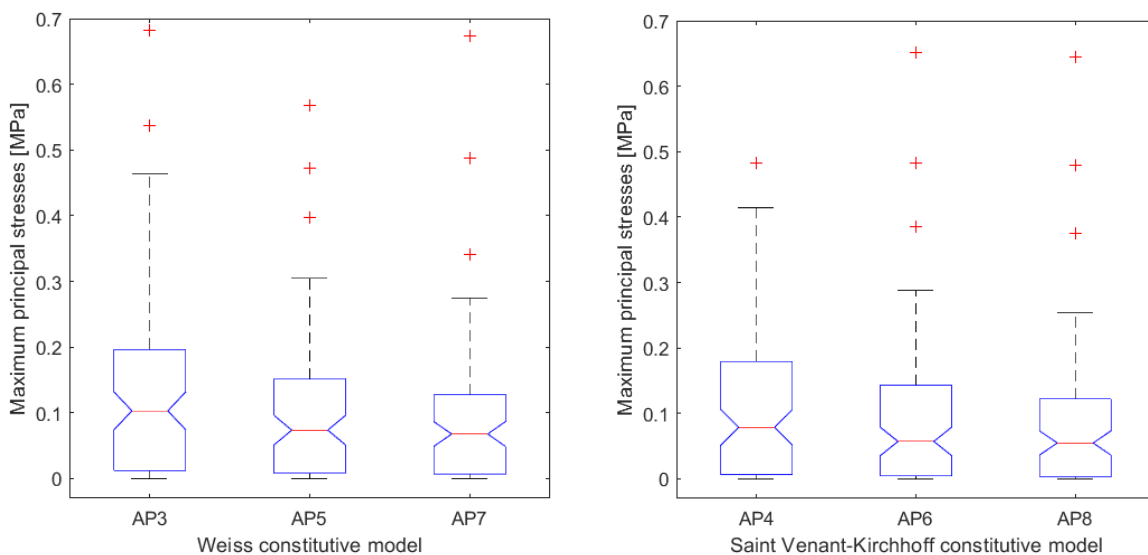


Figure 4.30: Box plot of (A) leaflets maximum principal stresses in MPa for each configuration. (left) CTs described with Weiss constitutive model. (right) CTs described with Saint-Venant constitutive model.

The decrease in the values of the maximum principal stresses as the number of CTs increases implies that the loads tend to be shared among the available CTs. Considering as an example the CTs of the AP3, AP5 and AP7 configurations which originate from the same papillary and which insert into the TVPL and TVSL ([Figures 4.31](#)), therefore in cases where the chordal density varies from 15 ± 1 insertions/cm² (A), 20 ± 1 insertions/cm² (B) to 25 ± 1 insertions/cm² (C) a reduction in the number of CTs particularly stressed is observed

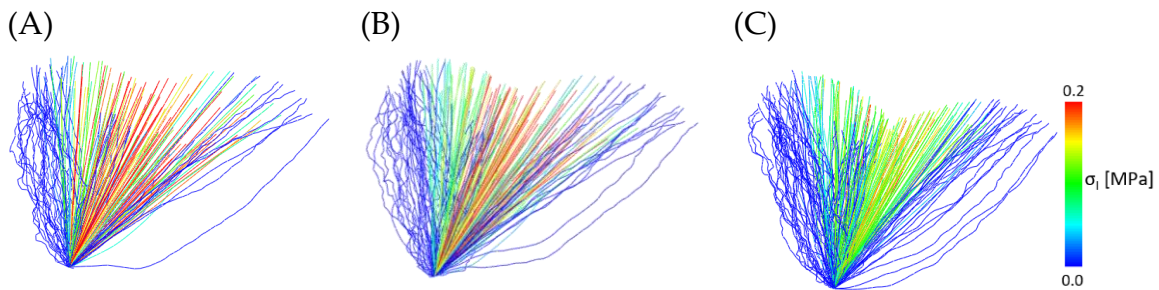


Figure 4.31: Representation of the maximum principal stresses of the CTs described with the Weiss constitutive model originating from the same PM and inserting into the TVPL and TVSL. (A) Chordal density of 15 ± 1 insertions/cm². (B) Chordal density of 20 ± 1 insertions/cm². (C) Chordal density of 25 ± 1 insertions/cm².

4.2.2.3. Regurgitation area

The evaluation of the regurgitation area has required the analysis of the valve configuration case-by-case. The conformation of the FRM in the xy plane was extracted at the end of the closure simulations. The extracted area was the sum of the regurgitation area and the area between the leaflets after their coaptation. If the leaflets co-apt, it is not certain that the FRM points will also coincide perfectly. Three-dimensional conformation of the valve was analysed on a case-by-case and the sections of area in which leaflets coaptation is present were excluded ([Figure 4.32](#)).

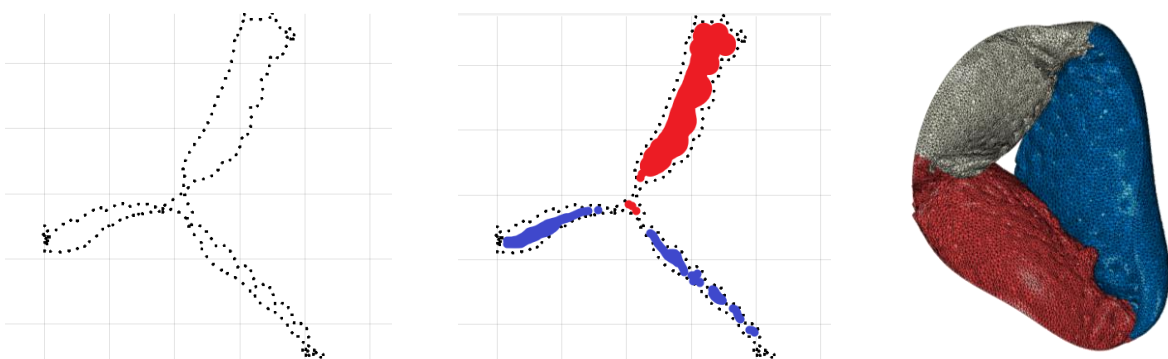


Figure 4.32: (A) FRM points on the xy plane (B) the red colour is used to define the TV regurgitation area, in blue the areas that were excluded from the total area calculation after the analysis in the three-dimensional configuration (C).

The effective area value was obtained after the processing of the data and the percentage of regurgitation area was calculated as defined in section [4.1.1.1 "Regurgitation area"](#). (Table 4.15)

| ID | $A_{FRM,FE}$ [mm ²] | % $RA_{FRM,FE}$ |
|-----|---------------------------------|-----------------|
| AP3 | 35.6 | 1.77% |
| AP4 | 23.9 | 1.18% |
| AP5 | 32.5 | 1.61% |
| AP6 | 27.7 | 1.38% |
| AP7 | 32.1 | 1.59% |
| AP8 | 30.3 | 1.51% |

Table 4.15: The effective area of regurgitation of the $\Omega_{PS}^{FE,closure}$ in mm² was extracted for each configuration. From this value, the percentage of the regurgitated area of $\Omega_{PS}^{FE,closure}$ was calculated with respect to the annular area of $\Omega_{PS}^{tracing}$.

Analysing the data, it is possible to observe an opposite behaviour in the case of the two constitutive models ([Figure 4.33](#)). In the case of the Weiss model, passing from the AP3 configuration to AP7, therefore increasing the chordal insertion density, a slight reduction in the regurgitation area is observed. In the case of the Saint Venant-Kirchhoff model, increasing the number of CTs increases also the regurgitation area.

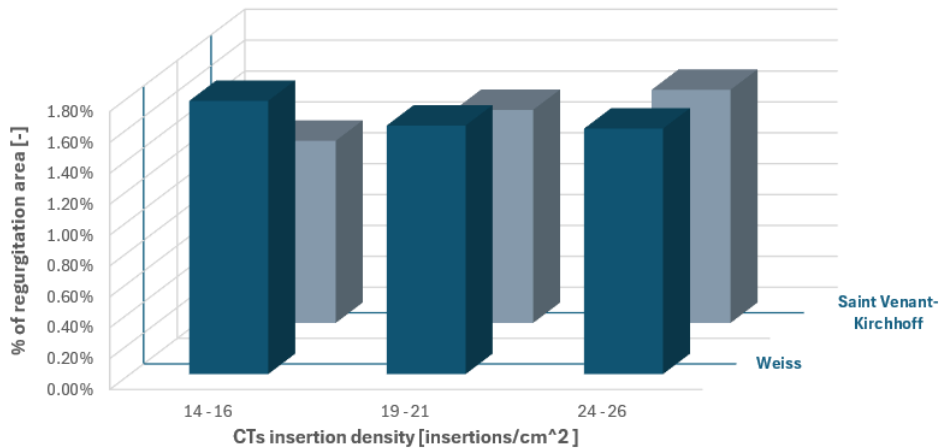


Figure 4.33: plot of the value of % of regurgitation area, on the z-axis, for the 6 configurations tested. The x-axis shows the chordal insertion density and the y-axis the type of constitutive model used for the CTs.

4.2.3. Chung-Hao Lee parametric model

The setups using the functionally equivalent model for CTs faced challenges due to adjustments in the positions of the PMs and the annulus. These changes led to a valve structure and varied stress and strain distributions that rendered the biomechanical data incompatible for comparison. This section will exclusively detail and compare results from post-surgery simulations of the AP1 and AP2 configurations, which were modeled according to the Chung-Hao Lee approach for CT geometry.

4.2.3.1. Leaflets maximum principal stresses and strains

The Chung-Hao Lee model showed no issues related to the shifting of the PMs and annulus points, demonstrating a stress distribution that aligns with the leaflets' loading conditions ([Figure 4.34](#)). As in the cases of the TV with TR, in which the CTs were described with the Chung-Hao Lee model, stress peaks are focused at the CT insertion points on the leaflets, where the maximum NE22 values are observed ([Figure 4.36](#)). The posterior leaflet presents higher stress levels than the other leaflets. The same leaflet also shows the highest values of NE11 ([Figure 4.35](#)).

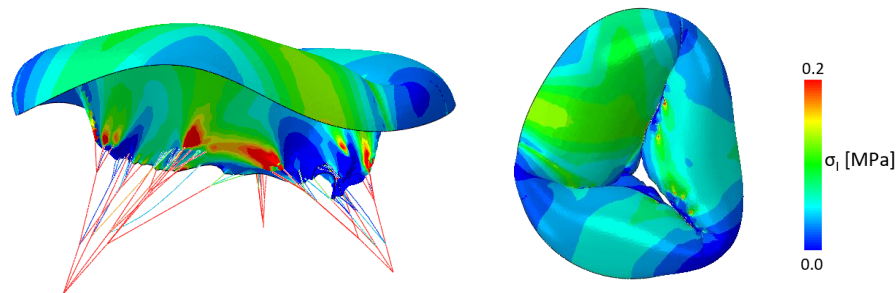


Figure 4.34: (left) lateral and (right) atrial view of leaflets maximum principal stresses in AP1 configuration.

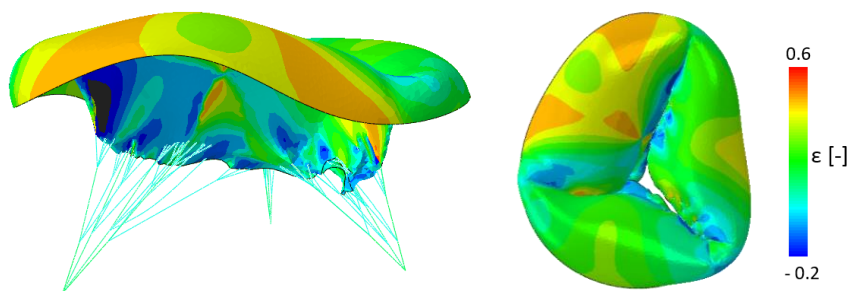


Figure 4.35: (left) lateral and (right) atrial view of leaflets maximum principal strains NE11 on AP1 configuration.

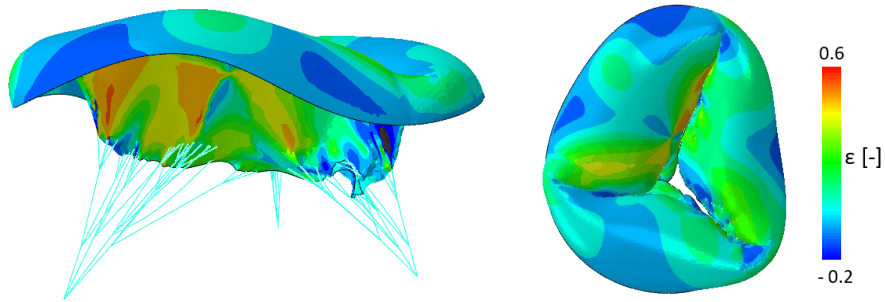


Figure 4.36: (left) lateral and (right) atrial view of leaflets maximum principal strains NE11 on AP1 configuration.

Table 4.16 shows the values of maximum principal stresses and maximum principal strains in the radial and circumferential directions for the AP1 and AP2 configurations. These values were analysed in the box plots in Figure 4.37.

| ID | Max principal stresses [MPa] | NE11 [-] | NE22 [-] |
|-----|---------------------------------|----------------------|-----------------------|
| AP1 | 0.05 (0.030 ÷ 0.069) | 0.18 (0.076 ÷ 0.269) | 0.04 (-0.025 ÷ 0.119) |
| AP2 | 0.05 (0.031 ÷ 0.073) | 0.15 (0.025 ÷ 0.263) | 0.02 (-0.023 ÷ 0.106) |

Table 4.16: Leaflets maximum principal stresses in MPa and leaflets maximum principal strains divided in radial (NE11) and circumferential (NE22) component for each configuration. The values were reported as median (25th percentile ÷ 75th percentile).

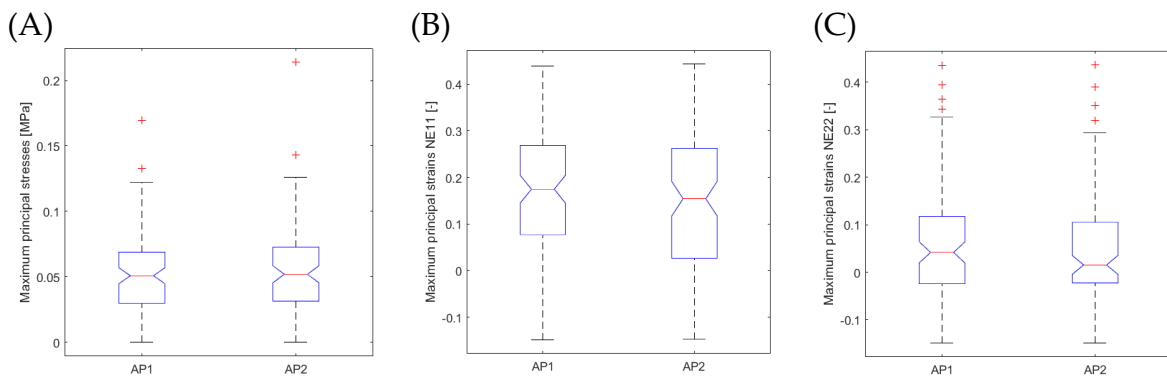


Figure 4.37: Box plot of (A) leaflets maximum principal stresses in MPa, maximum principal strain (B) NE11 and (C) NE22 of the configuration AP1 and AP2.

4.2.3.2. CTs maximum principal stresses

[Table 4.17](#) shows the median, 25th and 75th percentile values of the maximum principal stresses extracted from the CTs. The only variation between the AP1 and AP2 configuration is the constitutive model. The Saint Venant-Kirchhoff constitutive model has larger values of stresses and a wider distribution between the median and the 75th percentile ([Figure 4.38](#)).

| ID | Max principal stresses [MPa] |
|-----|------------------------------|
| AP1 | 0.19 (0.038 ÷ 0.824) |
| AP2 | 0.24 (0.053 ÷ 0.872) |

Table 4.17: CTs maximum principal stresses in MPa for AP1 and AP2 configurations. The values were reported as median (25th percentile ÷ 75th percentile).

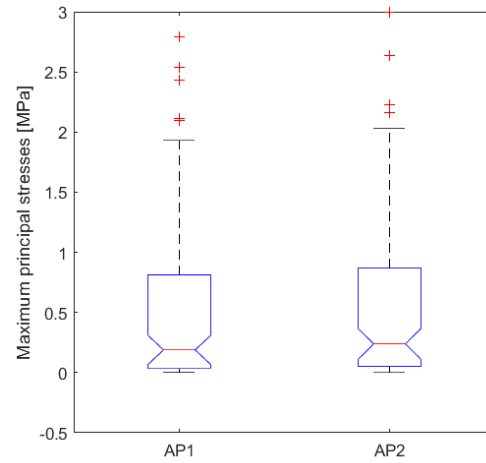


Figure 4.38: Box plot of CTs maximum principal stresses in MPa for AP1 and AP2 configurations

4.2.3.3. Regurgitation area

The identification of the regurgitation area required the application of the same procedure as applied in section [4.2.2.3. "Regurgitation area"](#), to exclude the area of the free margin where the leaflets went into coaptation in an apical side of the leaflets themselves.

Relying upon $A_{FRM,FE}$, $\%RA_{FRM,FE}$ was computed as defined in section [4.1.1.1 "Regurgitation area"](#).

| ID | $A_{FRM,FE}$ [mm ²] | $\%RA_{FRM,FE}$ |
|-----|---------------------------------|-----------------|
| AP3 | 9.63 | 0.47% |
| AP4 | 27.42 | 1.36% |

Table 4.18: The effective area of regurgitation of the $\Omega_{PS}^{FE,closure}$ in mm² was extracted for AP1 and AP2 configurations. From this value, the percentage of the regurgitated area of $\Omega_{PS}^{FE,closure}$ was calculated with respect to the annular area of $\Omega_{PS}^{tracing}$.

5 Discussion

The chapter will analyse the results, limitations and possible future developments of three macro-areas on which the thesis work was focused. Firstly, it will analyse the issues and weaknesses found in the echocardiographic data and the in tools that were used to make the data exploitable in the next steps. The second part will deal with the topic of manual tracing of the main structures of the TV, its current limitations and suggestions for reducing inaccuracies. The last part will discuss the reconstruction and simulation phases, the heart of the thesis.

5.1. Initial data

The ultrasound data is the basic element of all thesis work. On its quality and reliability relies the consistency and fairness of the results obtained by applying the reconstruction and simulation workflow.

5.1.1. Limitation

The available echocardiographic images were derived from previous thesis work [29], [30], and showed some weaknesses:

- The quality of the images did not always allow a clear and precise segmentation of TV reference structures.
- Between images from different valves or the same TV before and after surgery, there are differences between the proportions of the various structures, probably due to different positioning of the probe.

These issues required modifications on the data or on the information derived from it to obtain theoretically and physiologically correct results. For example, in the case of post-surgery TV, the segmentation proportions were modified so to be consistent with the pre-intervention proportions of the same valve ([Figures 4.21](#) and [Figure 4.25](#)). This limited the validity of the results obtained because the actual proportions are unknown, and the modifications were made simply following realistic anatomical proportions. Therefore, the true biomechanical impact of the FWA procedure could not be assessed.

The acquired data were modified using a series of tools defined in the protocol described in section [3.2 “Echocardiographic Data”](#). The protocol makes it possible to obtain image-planes that rotate around the valve's long axis or run along its short axis. The tools available are operator dependent and allow limited handling of the volumetric echocardiographic data. The consequence is that the orientation is not always correct; e.g., in the case of the postoperative valve the rotation of the planes in

the radial axis GUI did not take place exactly along the radial axis of the valve, which resulted in a probably incorrect description of the annulus shape ([Figure 4.20](#)).

5.1.2. Future developments

The issues reported could be a symptom of using images acquired following a non-standardised protocol with limited repeatability. To support this idea, the information available in the Locatelli and Maini thesis [29], are limited. The next step should be to define an acquisition protocol from which new images can be obtained.

The images were initially captured in-vitro using a porcine heart. With the current availability of a complete reconstruction and simulation workflow, it's now feasible to obtain images and quickly generate simulation outcomes. This enables a direct comparison between actual conditions and simulation results, facilitating an in-depth evaluation of the model's effectiveness, limitations, and flaws. The logical progression of this research involves its application to clinical echocardiographic images from patients.

Moreover, enhancements are needed in the ultrasound data preparation process. The accuracy of TV segmentation and reconstruction depends on precisely aligning the valve within the imaging planes. By adopting a specific image acquisition protocol, the TV can be aligned systematically within the reference system, centered around its key structures, allowing for more accurate and refined manipulation of ultrasound data.

5.2. Manual tracing

Manual image segmentation relies heavily on the operator's anatomical expertise and their skill in distinguishing between actual TV structures and imaging artifacts like shadows or defects.

To mitigate tracing bias, the current workflow incorporates several strategies for identification, analysis, and correction. The viewing tool enables the 3 visualization of newly traced TV structures, offering insights into the annulus shape, leaflet orientation, and PM positioning. Additionally, a fourth-order Fourier transform predicts the annulus's final shape post-reconstruction, based on the traced information.

5.2.1. Future developments

Some of the potential future developments related to 3DE images and segmentation could include, but are not limited to:

- By applying a 4th order Fourier transform to create a three-dimensional model of the TV annulus in a healthy valve, it can be compared with its expected physiological shape. This comparison may not only highlight tracing inaccuracies but could also reveal previously overlooked issues with the TV.

- If annulus points are traced across a defined set of image planes, showing the annulus's position as determined by the 4th order Fourier transform on each plane could help identify any uncertainties about the annulus's correct location. It might also verify if the overall tracing aligns with anatomical data.
- The commissures during reconstruction are calculated as the weighted average of the information from two criteria, as described in section [3.6.1.4. "Commissures and leaflets identification"](#). With good quality of echocardiographic images, the information from tracing the commissures along the short axis of the valve should be consistent with the minimum points calculated on FRM shape. Considering the identification of the commissures in the short-axis GUI as the correct information, if the discrepancy between the two criteria exceeds a certain threshold the free margin tracking should be re-evaluated.

In the future, one could evaluate the implementation of software capable of performing an automatic or semi-automatic segmentation of images, perhaps based on an artificial intelligence system capable of recognising real anatomical structures and excluding image defects.

5.3. Reconstruction and Simulations

The present work aimed to the definition of a complete TV reconstruction workflow to analyse valve biomechanics in two case studies:

1. Pathological TV with secondary TR.
2. TV following FWA surgical procedure.

The reconstruction phase required a detailed study of the anatomy and morphology of the TV. In addition, all information available to date from the literature was considered. The TV reconstructed with the present workflow presents peculiarities not yet considered in in-silico studies:

- The definition of a variable thickness in the radial and circumferential direction of the valve, described on anatomical information of the TV.
- The evaluation of both paradigms for defining the position of commissioners.

In the literature, the critical point in simulations is the description of the CTs. These structures are not visible through the main imaging methods, and anatomical descriptions based on ex-vivo analysis show great variability in terms of the number and position of the insertion points on the leaflets. For this reason, it was decided in the present work to investigate in detail the impact of the geometric and material characterisation of CTs. Among the articles in the literature, the one that attracted the most interest was that proposed by Laurence et al. [59], which was followed by the publication of his PhD thesis [51]. This gave rise to the idea of using Chung-Hao Lee's model as a reference, described with the Saint Venant-Kirchhoff constitutive model.

CTs are not clearly visible using the main in vivo imaging methods; therefore, the development of a specific patient apparatus loses importance. Based on this idea and inspired by the work of Khalighi et al. [58], a functionally equivalent model of CTs was developed and calibrated. The TV has a different morphology and spatial arrangement from the MV, from which the model originates, three chordal insertion densities on the leaflets were tested: 15 ± 1 , 20 ± 1 and 25 ± 1 insertions/cm². Finally, in the Amicone and Dazzi [30] thesis, applying Weiss's constitutive model resulted in an improvement of the valve's biomechanical behaviour, so this constitutive model was also tested.

TV with TR

The analysed TV presented severe TR; the work was based on the actual features traceable from echocardiographic image.

The reconstruction of the $\Omega_{PS}^{tracing}$ provided a clear reference for studying the behaviour of the TV structures at the end of the simulation of valve closure.

Khalighi's workflow was first tested on a TV affected by TR. Analysing the TV leaflets morphology obtained at SP, in terms of point-to-point distance from the $\Omega_{PS}^{tracing}$ and area of regurgitation, the result is that increasing the importance of the chordal insertion density, the error reduces ([Figures 4.3](#) and [Figure 4.4](#)). The Khalighi et al. [58] model applied to TV therefore required a higher chordal density than in the case of MV. The reference value of the chordal insertion density for both the healthy and the pathological MV was 15 insertions/cm². Sensitivity analysis, considering parameters regarding morphology and shape of the TV obtained at SP showed that for this specific case the best results are obtained with a chordal insertion density of 25 ± 1 insertions/cm².

The sensitivity analysis regarding the chordal attachment point elucidated a distinct differential response contingent upon the selected constitutive model for the chordae' material. Specifically, under the Weiss constitutive model, all evaluated configurations manifested an increase in regurgitant area relative to the baseline model. Notably, augmenting the chordal insertion point progressively ameliorated this discrepancy, approximating the baseline regurgitant area. Conversely, the application of the Saint-Venant Kirchhoff constitutive model consistently yielded a regurgitant area inferior to the baseline, with incremental increases in chordal attachment similarly reducing this deviation ([Table 4.3](#)). Thus, in the case of the Weiss model, a worse situation is obtained compared to reality and is therefore more conservative.

In the context of configurations employing the Khalighi model, the TR9 setup emerged as the most morphologically representative of the TV.

Moreover, the TR2 configuration was evaluated against the backdrop of existing tricuspid valve literature, particularly building upon the work of Laurence et al. [59] with several enhancements such as adopting an anisotropic and hyperelastic constitutive model for the leaflet material and a more anatomically accurate

arrangement of collagen fibres. However, the simulation results pointed out that TR2 was the least reflective of actual valve behaviour among the tested configurations.

Modifying the constitutive model of the material and using the Weiss model fitted on the data of Lim et al. [47] it is observed that the TR1 and TR2 configurations have similar behaviour in terms of stresses ([Figures 4.7](#)) and deformations ([Figures 4.13](#)), while slight variations are noted in terms of valve morphology. There is an improvement in the D parameter moving from TR2 to TR1 ([Figures 4.17](#)).

The application of the initial chord length calibration defined for the Chung-Hao Lee model, performed in the TR3 and TR4 configurations, showed variations in terms of both stresses ([Figure 4.7](#)) and deformations ([Figure 4.13](#)), as well as a slight improvement in the morphological characteristics of the valve ([Figure 4.16](#) and [Figure 4.17](#)), compared to the TR1 and TR2 configurations.

The analysis on all the models shows that the TR9 and TR10 configurations, which propose the functionally equivalent model, show significantly better results. The presence of a high number of CTs and uniform chordal insertions allowed the reduction of the stress peaks concentration on the leaflets ([Figure 4.10](#)), bringing the median of the maximum principal stresses on the leaflets to a value which is half the value obtained in the Chung-Hao Lee's configurations ([Figure 4.7](#)). The RF data were not statically significant to analyse the differences between the configurations.

Weiss' constitutive model, from a formal point of view, allows a correct description of the behaviour of collagen fibres, and thus of the tissue of CTs. CTs deform elastically as long as it is possible to recruit fibres; when all the fibres are recruited, the stiffness remains constant.

Of the simulations tested, in the case of a TV with TR, of which information can be extracted from echocardiographic images at both ED and SP, the most significant configuration is TR9. The functionally equivalent model proposed by Khalighi et al. [58] for MV is therefore also applicable to the case of TV with good results. The calibration of the CTs and the possibility of acting on the chordal insertion density allows a reliable patient-specific model. The Weiss constitutive model also accurately simulates the material behaviour of the CTs. The Euclidean distance between the simulated configuration of the closed CT and the surface reconstructed from the reconstructed images slightly increases the spatial resolution of the data ([Figures 4.18](#)). This represents a significant improvement over current models that exhibit excessive leaflet bulging [51], [61]. In addition, the stress distribution at the leaflets, despite the pathological conformation of the TV, is in accordance with the loading conditions, and more significant of the results found in the literature [30], [59]. Nevertheless, the applicability of the equivalent chordal apparatus combined with chordal calibration requires further study to understand the actual potential of this tool in evaluating the reproduction of TV patient-specific configurations and the associated biomechanics.

TV post-surgery

The same reconstructed valve was used to study the impact of the surgical repair strategy proposed by Jaworek et al. [10]. The study was based on post-surgery echocardiographic images, so it is not a predictive study, but a validation of the in-vitro tests.

The repair strategy consists of moving some of the PMs in a specific direction. Starting from the regurgitant baseline configuration, the simulation had to replicate the effect of the device. In the post-intervention simulation, the displacement of the PMs, as reported on the echocardiographic images, was imposed. As a result of the displacement of the PMs, the annulus changes its shape and arrangement in space; therefore, the displacement of the annulus points was also defined. The other structures of the TV are not affected during the repair procedure.

At this point, the questions to be addressed were: i) whether the CTs, calibrated solely in the pathological configuration, would permit the TV to close; and ii) whether the resultant biomechanical characterization of the valve would be useful in assessing the surgical procedure.

The validity of the functionally equivalent model diminishes when modifications are made to the underlying structures of the simulation. The findings revealed that certain CTs were overly tense, while others remained nearly unburdened even at systolic pressure ([Figure 4.31](#)). These conditions led to high stress at specific leaflet locations ([Figure 4.27](#)), and, conversely, excessive movement and deformation at others ([Figure 4.28](#)). Of particular concern, highlighted by the stress peak locations, were the CTs integrating into the basal and clear zones. These challenges persisted across all tested densities of chordal insertion ([Figure 4.30](#)), rendering the biomechanical characterization of the TV using the functionally equivalent model as unreliable.

The Chung-Hao Lee model, utilized for calibrating the first branch length of the CTs, demonstrates markedly improved performance. Notably, it exhibits no artifacts arising from the displacement of the PMs and the annulus ([Figure 4.35](#)). However, the model's limitation is the localized stress peaks at the CTs' insertion points. The choice of material model for the CTs significantly affects their biomechanical behaviour ([Figure 4.39](#)), and, more crucially, influences how the leaflets respond to pressure stress ([Figure 4.38](#)).

[Figure 5.1](#) compares the regurgitant area observed in echocardiographic images (A) with the PS configurations of AP1 (B) and AP2 (2). The regurgitant area in the AP2 configuration more closely mirrors the shape seen in the reference image, and there is a notable difference in the regurgitant area between the AP1 and AP2 configurations ([Table 4.18](#)).

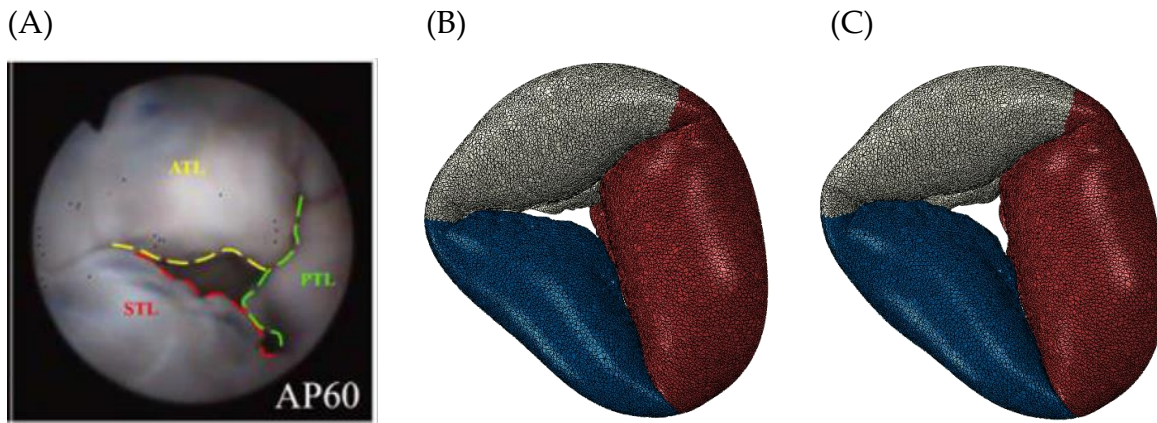


Figure 5.1: (A) experimental image of the HT11 valve after 60% FWA in AP direction adapted from Manini and Locatelli thesis [29].

FWA strategy

The simulations, after adjusting the initial data, align with the goal of employing FWA: minimizing the area of regurgitation. Given the severe TR associated with the valve in question, while regurgitation is not entirely eliminated, it is significantly reduced from a regurgitation area percentage of 12.23% to less than 1.5%.

This study represents progress beyond the current computational modelling practices for the TV. It offers a methodological framework for the characterization of CT models, establishing guidelines for modelling a diseased TV and predicting surgical outcomes. The developed reconstruction and simulation workflow lays the groundwork for a tailored approach based on echocardiographic data, which is instrumental in evaluating TV biomechanics effectively.

5.3.1. Limitations and future developments

In spite of the great results obtained, the present work has some limitations that provide the starting point for future developments.

First, the reconstruction and simulation workflow were applied only to the echocardiographic images of a single TV. To assess the repeatability of the workflow, a larger amount of data would have to be applied and it would be interesting to translate it to clinical images from patients.

Secondly, the CTs calibration workflow is a good technique to obtain a TV behaviour as close as possible to $\Omega_{PS}^{tracing}$. The application of the calibration method to Chung-Hao Lee's model turned out to be simplistic and approximate. An in-depth study of calibration on the different levels of branching could allow a model with morphological characteristics more closely matching the $\Omega_{PS}^{tracing}$.

Thirdly, the results obtained from the two models for defining the geometry of CTs applied to the case of the pathological and post-surgery valve are particularly

interesting. The implementation of a mixed model that exploits the strengths and solves the main issues of the two models could be considered. The patient-specific description of CTs is not allowed as the information from imaging is limited. Khalighi's model completely solves this problem. Of interest in Chung-Hao Lee's model is the positioning of the chordal insertions consistent with the anatomical characterisation of the CTs. A functionally equivalent model could be considered, but with unevenly distributed chordal insertions. A higher density could be defined in the rough zone to stabilise the TV, but a reduction of density might be applied to the clear and basal zone of the valve. This should make it possible to obtain a model that correctly describes the biomechanical characteristics of the TV with TR, on which the calibration of the CTs is performed, and limit artefacts in the post-surgery simulation.

Bibliography

- [1] Y. Topilsky *et al.*, “Burden of Tricuspid Regurgitation in Patients Diagnosed in the Community Setting,” *JACC Cardiovasc. Imaging*, vol. 12, no. 3, pp. 433–442, 2019, doi: 10.1016/j.jcmg.2018.06.014.
- [2] E. Yucel, P. B. Bertrand, J. L. Churchill, and M. Namasivayam, “The tricuspid valve in review: Anatomy, pathophysiology and echocardiographic assessment with focus on functional tricuspid regurgitation,” *J. Thorac. Dis.*, vol. 12, no. 5, pp. 2945–2954, 2020, doi: 10.21037/jtd.2020.02.42.
- [3] M. Gerçek and V. Rudolph, “Secondary Tricuspid Regurgitation: Pathophysiology, Incidence and Prognosis,” *Front. Cardiovasc. Med.*, vol. 8, no. July, 2021, doi: 10.3389/fcvm.2021.701243.
- [4] G. Benfari *et al.*, “Excess Mortality Associated With Functional Tricuspid Regurgitation Complicating Heart Failure With Reduced Ejection Fraction,” *Circulation*, vol. 140, no. 3, pp. 196–206, 2019, doi: 10.1161/CIRCULATIONAHA.118.038946.
- [5] J. D. Romeo *et al.*, “TOUCH MEDICAL MEDIA Current Status of Transcatheter Tricuspid Valve Therapies,” *J. Publ. Date*, no. June, pp. 49–58, 2022.
- [6] M. Stevanella, E. Votta, M. Lemma, C. Antona, and A. Redaelli, “Finite element modelling of the tricuspid valve: A preliminary study,” *Med. Eng. Phys.*, vol. 32, no. 10, pp. 1213–1223, 2010, doi: 10.1016/j.medengphy.2010.08.013.
- [7] F. Kong *et al.*, “Finite Element Analysis of Tricuspid Valve Deformation from Multi-slice Computed Tomography Images,” *Ann. Biomed. Eng.*, vol. 46, no. 8, pp. 1112–1127, 2018, doi: 10.1007/s10439-018-2024-8.
- [8] C. Lee *et al.*, *Mechanics of the Tricuspid Valve – From Clinical Diagnosis / Treatment , In-Vivo and In-Vitro Investigations , to Patient-Specific Biomechanical Modeling*. 2019.
- [9] M. Mathur, W. D. Meador, M. Malinowski, T. Jazwiec, T. A. Timek, and M. K. Rausch, “Texas TriValve 1.0: a reverse-engineered, open model of the human tricuspid valve,” *Eng. Comput.*, vol. 38, no. 5, pp. 3835–3848, 2022, doi: 10.1007/s00366-022-01659-w.
- [10] M. Jaworek *et al.*, “Treatment of Tricuspid Regurgitation at Subvalvular Level: Hemodynamic and Morphological Assessment in Ex-Vivo Beating Heart Model,” *Struct. Hear.*, vol. 4, no. 1, pp. 36–45, 2020, doi:

- 10.1080/24748706.2019.1686555.
- [11] A. Dahou, D. Levin, M. Reisman, and R. T. Hahn, "Anatomy and Physiology of the Tricuspid Valve," *JACC Cardiovasc. Imaging*, vol. 12, no. 3, pp. 458–468, 2019, doi: 10.1016/j.jcmg.2018.07.032.
- [12] C. Besler, C. U. Meduri, and P. Lurz, "Transcatheter treatment of functional tricuspid regurgitation using the Trialign device," *Interv. Cardiol. Rev. Res. Resour.*, vol. 13, no. 1, pp. 8–13, 2018, doi: 10.15420/icr.2017:21:1.
- [13] M. D. Silver, J. H. Lam, N. Ranganathan, and E. D. Wigle, "Morphology of the human tricuspid valve.," *Circulation*, vol. 43, no. 3, pp. 333–348, 1971, doi: 10.1161/01.CIR.43.3.333.
- [14] F. Maffessanti *et al.*, "Three-dimensional dynamic assessment of tricuspid and mitral annuli using cardiovascular magnetic resonance," *Eur. Heart J. Cardiovasc. Imaging*, vol. 14, no. 10, pp. 986–995, 2013, doi: 10.1093/ehjci/jet004.
- [15] P. Lama, B. K. Tamang, and J. Kulkarni, "Morphometry and aberrant morphology of the adult human tricuspid valve leaflets," *Anat. Sci. Int.*, vol. 91, no. 2, pp. 143–150, 2016, doi: 10.1007/s12565-015-0275-0.
- [16] M. Misfeld and H. H. Sievers, "Heart valve macro- and microstructure," *Philos. Trans. R. Soc. B Biol. Sci.*, vol. 362, no. 1484, pp. 1421–1436, 2007, doi: 10.1098/rstb.2007.2125.
- [17] K. E. Kramer *et al.*, "An investigation of layer-specific tissue biomechanics of porcine atrioventricular valve anterior leaflets," *Acta Biomater.*, vol. 96, pp. 368–384, 2019, doi: 10.1016/j.actbio.2019.06.049.
- [18] S. Heyden *et al.*, "Material modeling of cardiac valve tissue: Experiments, constitutive analysis and numerical investigation," *J. Biomech.*, vol. 48, no. 16, pp. 4287–4296, 2015, doi: 10.1016/j.jbiomech.2015.10.043.
- [19] A. Colombo, "Modellazione della valvola tricuspide: ricostruzione della geometria valvolare a partire da misurazioni sperimentali e simulazione della funzione valvolare tramite metodo degli elementi finiti," 2007.
- [20] A. Saha and S. Roy, "Papillary muscles of right ventricle—morphological variations and its clinical relevance," *Cardiovasc. Pathol.*, vol. 34, pp. 22–27, 2018, doi: 10.1016/j.carpath.2018.01.007.
- [21] G. R. Nigri, L. J. A. Di Dio, and C. A. C. Baptista, "Papillary muscles and tendinous cords of the right ventricle of the human heart: Morphological characteristics," *Surg. Radiol. Anat.*, vol. 23, no. 1, pp. 45–49, 2001, doi: 10.1007/s00276-001-0045-7.
- [22] C. H. A. Jost, H. M. Connolly, J. A. Dearani, W. D. Edwards, and G. K. Danielson, "Ebstein's anomaly," *Circulation*, vol. 115, no. 2, pp. 277–285, 2007, doi:

- 10.1161/CIRCULATIONAHA.106.619338.
- [23] K. A. Holst *et al.*, "Improving Results of Surgery for Ebstein Anomaly: Where Are We After 235 Cone Repairs?," *Ann. Thorac. Surg.*, vol. 105, no. 1, pp. 160–168, 2018, doi: 10.1016/j.athoracsur.2017.09.058.
- [24] P. M. Shah and A. A. Raney, "Tricuspid Valve Disease," *Curr. Probl. Cardiol.*, vol. 33, no. 2, pp. 47–84, 2008, doi: 10.1016/j.cpcardiol.2007.10.004.
- [25] N. Saran and J. A. Dearani, "Strategies for tricuspid valve repair," *Indian J. Thorac. Cardiovasc. Surg.*, vol. 36, no. January, pp. 123–130, 2020, doi: 10.1007/s12055-019-00826-x.
- [26] F. Campelo-Parada *et al.*, "First-in-Man Experience of a Novel Transcatheter Repair System for Treating Severe Tricuspid Regurgitation," *J. Am. Coll. Cardiol.*, vol. 66, no. 22, pp. 2475–2483, 2015, doi: 10.1016/j.jacc.2015.09.068.
- [27] A. Latib *et al.*, "First-in-man implantation of a tricuspid annular remodeling device for functional tricuspid regurgitation," *JACC Cardiovasc. Interv.*, vol. 8, no. 13, pp. e211–e214, 2015, doi: 10.1016/j.jcin.2015.06.028.
- [28] M. Castagna and G. Lentini, "A mock circulation loop for the right heart," 2016.
- [29] C. M. G. Locatelli, "Tricuspid Valve Finite Element Modeling based on 3D Ultrasound Imaging: Development of an Improved Method and Application to the Study of Papillary Muscle Approximation as a mean to treat Functional Tricuspid Regurgitation," 2018.
- [30] C. D. A. Amicone, "Sviluppo, verifica e applicazione di nuove soluzioni per la simulazione ad elementi finiti della biomeccanica della valvola tricuspide a partire da imaging clinico: verso una modellazione più dettagliata di geometria, microstruttura e biomeccanica valvola," 2020.
- [31] S. Singh-Gryzbon, V. Sadri, M. Toma, E. L. Pierce, Z. A. Wei, and A. P. Yoganathan, "Development of a Computational Method for Simulating Tricuspid Valve Dynamics," *Ann. Biomed. Eng.*, vol. 47, no. 6, pp. 1422–1434, 2019, doi: 10.1007/s10439-019-02243-y.
- [32] M. S. Hamid, H. N. Sabbah, and P. D. Stein, "Vibrational analysis of bioprosthetic heart valve leaflets using numerical models: Effects of leaflet stiffening, calcification, and perforation," *Circ. Res.*, vol. 61, no. 5, pp. 687–694, 1987, doi: 10.1161/01.RES.61.5.687.
- [33] M. E. Hiro *et al.*, "Sonometric study of the normal tricuspid valve annulus in sheep," *J. Heart Valve Dis.*, vol. 13, no. 3, pp. 452–460, 2004.
- [34] S. Fukuda *et al.*, "Three-dimensional geometry of the tricuspid annulus in healthy subjects and in patients with functional tricuspid regurgitation: A real-time, 3-dimensional echocardiographic study," *Circulation*, vol. 114, no. SUPPL.

- 1, pp. 492–498, 2006, doi: 10.1161/CIRCULATIONAHA.105.000257.
- [35] T. T. Ton-Nu *et al.*, “Geometric determinants of functional tricuspid regurgitation: Insights from 3-dimensional echocardiography,” *Circulation*, vol. 114, no. 2, pp. 143–149, 2006, doi: 10.1161/CIRCULATIONAHA.106.611889.
- [36] E. L. Johnson *et al.*, “Parameterization, geometric modeling, and isogeometric analysis of tricuspid valves,” *Comput. Methods Appl. Mech. Eng.*, vol. 384, p. 113960, 2021, doi: 10.1016/j.cma.2021.113960.
- [37] A. Aversa and E. Careddu, “Image-based analysis of tricuspid valve biomechanics: towards a novel approach integrating in vitro 3D-echocardiography and finite element modelling,” 2016.
- [38] A. M. Pouch *et al.*, “Image segmentation and modeling of the pediatric tricuspid valve in hypoplastic left heart syndrome,” *Lect. Notes Comput. Sci. (including Subser. Lect. Notes Artif. Intell. Lect. Notes Bioinformatics)*, vol. 10263 LNCS, pp. 95–105, 2017, doi: 10.1007/978-3-319-59448-4_10.
- [39] K. A. Khoiy and R. Amini, “On the biaxial mechanical response of porcine tricuspid valve leaflets,” *J. Biomech. Eng.*, vol. 138, no. 10, pp. 1–6, 2016, doi: 10.1115/1.4034426.
- [40] T. Pham, F. Sulejmani, E. Shin, D. Wang, and W. Sun, “Quantification and comparison of the mechanical properties of four human cardiac valves,” *Acta Biomater.*, vol. 54, pp. 345–355, 2017, doi: 10.1016/j.actbio.2017.03.026.
- [41] D. Laurence *et al.*, “An investigation of regional variations in the biaxial mechanical properties and stress relaxation behaviors of porcine atrioventricular heart valve leaflets,” *J. Biomech.*, vol. 83, pp. 16–27, 2019, doi: 10.1016/j.jbiomech.2018.11.015.
- [42] W. D. Meador *et al.*, “A detailed mechanical and microstructural analysis of ovine tricuspid valve leaflets,” *Acta Biomater.*, vol. 102, pp. 100–113, 2020, doi: 10.1016/j.actbio.2019.11.039.
- [43] G. A. Holzapfel, T. C. Gasser, and R. W. Ogden, “A new constitutive framework for arterial wall mechanics and a comparative study of material models,” *J. Elast.*, vol. 61, no. 1–3, pp. 1–48, 2000, doi: 10.1023/A:1010835316564.
- [44] T. C. Gasser, R. W. Ogden, and G. A. Holzapfel, “Hyperelastic modelling of arterial layers with distributed collagen fibre orientations,” *J. R. Soc. Interface*, vol. 3, no. 6, pp. 15–35, 2006, doi: 10.1098/rsif.2005.0073.
- [45] C. Lee *et al.*, “A High-Fidelity and Micro-anatomically Accurate 3D Finite Element Model for Simulations of Functional Mitral Valve,” pp. 416–424, 2013, doi: 10.1007/978-3-642-38899-6.
- [46] M. H. Friedman, *Biomechanics: Mechanical Properties of Living Tissues*. Y. C. Fung

- , vol. 69, no. 4. 1994.
- [47] K. O. Lim, "Mechanical properties and ultrastructure of normal human tricuspid valve chordae tendineae," pp. 455–464, 1980.
- [48] A. Pokutta-Paskaleva, F. Sulejmani, M. DelRocini, and W. Sun, "Comparative mechanical, morphological, and microstructural characterization of porcine mitral and tricuspid leaflets and chordae tendineae," *Surg Oncol Clin N Am.*, vol. 176, no. 3, pp. 139–148, 2018, doi: 10.1016/j.actbio.2018.12.029.Comparative.
- [49] K. J. Smith *et al.*, "Tricuspid Chordae Tendineae Mechanics: Insertion Site, Leaflet, and Size-Specific Analysis and Constitutive Modelling," *Exp. Mech.*, vol. 61, no. 1, pp. 19–29, 2021, doi: 10.1007/s11340-020-00594-5.
- [50] J. A. Weiss, "A Constitutive Model and Finite Element Representation for Transversely Isotropic Soft Tissues," no. December, pp. 1–111, 1994.
- [51] D. Laurence, "The tricuspid valve: mechanics, microstructure, modeling and simulation," 2022.
- [52] K. M. Newman and F. C. P. Yin, "A constitutive law for mitral valve tissue," *J. Biomech. Eng.*, vol. 120, no. 1, pp. 38–47, 1998, doi: 10.1115/1.2834305.
- [53] S. Gunnal, R. Wabale, and M. Farooqui, "Morphological Study of Chordae Tendinae in Human Cadaveric Hearts," *Hear. Views*, vol. 16, no. 1, p. 1, 2015, doi: 10.4103/1995-705x.152994.
- [54] T. Pham, "Finite element analysis of patient-specific mitral valve with mitral regurgitation," *Physiol. Behav.*, vol. 176, no. 3, pp. 139–148, 2017, doi: 10.1007/s13239-016-0291-9.Finite.
- [55] K. S. Kunzelman and R. P. Cochran, "Stress/strain characteristics of porcine mitral valve tissue: Parallel versus perpendicular collagen orientation," *J. Card. Surg.*, vol. 7, no. 1, pp. 71–78, 1992, doi: 10.1111/j.1540-8191.1992.tb00777.x.
- [56] D. Kamensky, F. Xu, C. H. Lee, J. Yan, Y. Bazilevs, and M. C. Hsu, "A contact formulation based on a volumetric potential: Application to isogeometric simulations of atrioventricular valves," *Comput. Methods Appl. Mech. Eng.*, vol. 330, pp. 522–546, 2018, doi: 10.1016/j.cma.2017.11.007.
- [57] D. Tondi, "Patient-specific analysis of Mitral Valve Prolapse biomechanics : a novel automated workflow based on Cardiac MRI and FEA," 2023.
- [58] A. H. Khalighi, B. V. Rego, A. Drach, R. C. Gorman, J. H. Gorman, and M. S. Sacks, "Development of a Functionally Equivalent Model of the Mitral Valve Chordae Tendineae Through Topology Optimization," *Ann. Biomed. Eng.*, vol. 47, no. 1, pp. 60–74, 2019, doi: 10.1007/s10439-018-02122-y.
- [59] D. W. Laurence, E. L. Johnson, M. Hsu, R. Baumwart, and A. Mir, "A pilot in-silico modeling-based study of the pathological effects on the biomechanical

- function of tricuspid valves Devin,” *Heal. Res. Alliance*, vol. 33, no. 8, pp. 1089–1091, 2020, doi: 10.1007/BF01945988.
- [60] R. P. Cochran, K. S. Kunzelman, C. J. Chuong, M. S. Sacks, and R. C. Eberhart, “Nondestructive Analysis of Mitral Valve Collagen Fiber Orientation,” pp. 7823–7830, 1991.
- [61] M. Mathur, W. D. Meador, M. Malinowski, T. Jazwiec, T. A. Timek, and M. K. Rausch, “Texas TriValve 1.0: a reverse-engineered, open model of the human tricuspid valve,” *Eng. Comput.*, vol. 38, no. 5, pp. 3835–3848, 2022, doi: 10.1007/s00366-022-01659-w.
- [62] M. Thubrikar, *The Aortic Valve Author*. .
- [63] M. R. Labrosse, C. J. Beller, F. Robicsek, and M. J. Thubrikar, “Geometric modeling of functional trileaflet aortic valves: Development and clinical applications,” *J. Biomech.*, vol. 39, no. 14, pp. 2665–2672, 2006, doi: 10.1016/j.jbiomech.2005.08.012.
- [64] F. Xu *et al.*, “A framework for designing patient-specific bioprosthetic heart valves using immersogeometric fluid–structure interaction analysis,” *Physiol. Behav.*, vol. 176, no. 1, pp. 139–148, 2017, doi: 10.1002/cnm.2938.A.
- [65] K. Li and W. Sun, “Simulated Transcatheter Aortic Valve Deformation: A Parametric Study on the Impact of Leaflet Geometry on Valve Peak Stress,” *Physiol. Behav.*, vol. 176, no. 1, pp. 100–106, 2016, doi: 10.1002/cnm.2814.Simulated.
- [66] Kunzelman KS, Cochran RP, Chuong C, Ring WS, Verrier ED, Eberhart RD. Finite element analysis of the mitral valve. *J Heart Valve Dis*. 1993 May;2(3):326-40. PMID: 8269128.
- [67] Dassault Systèmes, “Abaqus Analysis User's Guide”, 2014.

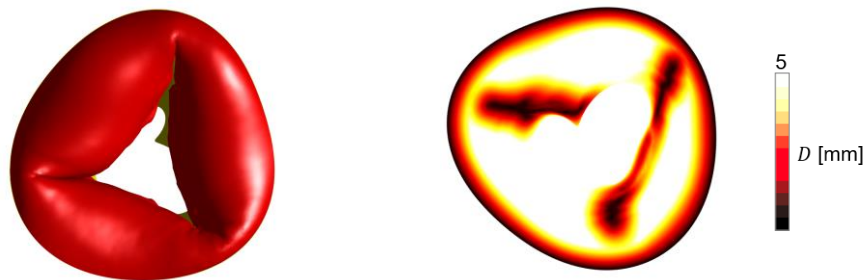
A Appendix: Additional results

A.1. TV with TR: clinically relevant analysis plots

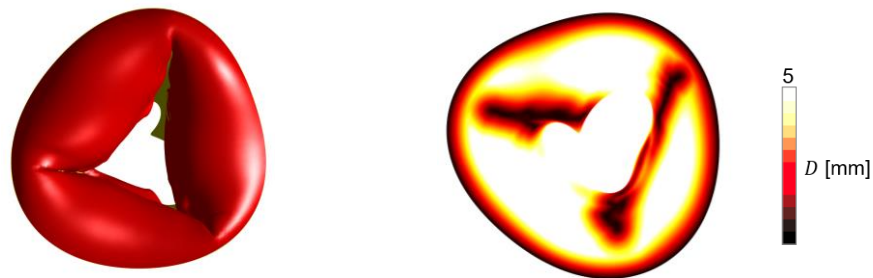
For each configuration

- Left: the atrial view of the valve obtained at the end of the simulation (in red) plotted over the reference valve $\Omega_{PS}^{tracing}$
- Right: graphic representation, in atrial view, of the distance between the valve obtained at the end of the simulation and the reference valve $\Omega_{PS}^{tracing}$. The colour scale on the side suggests that black means a distance between the two configurations of approximately zero, white a distance greater than 5 mm.

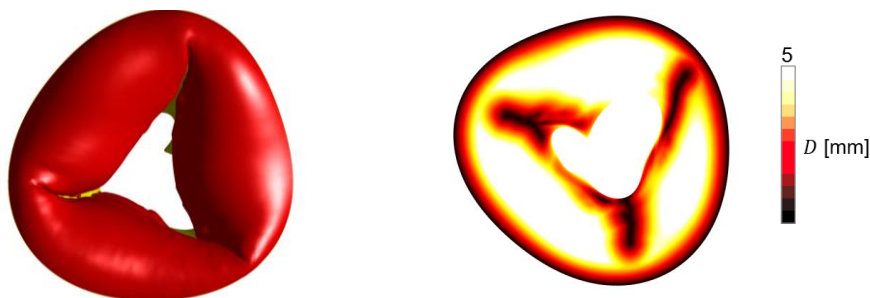
TR1



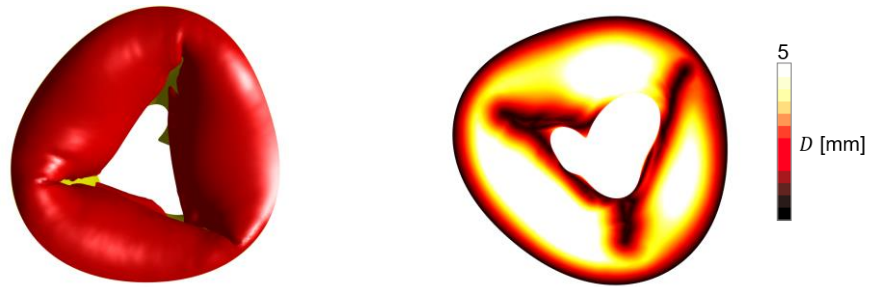
TR2



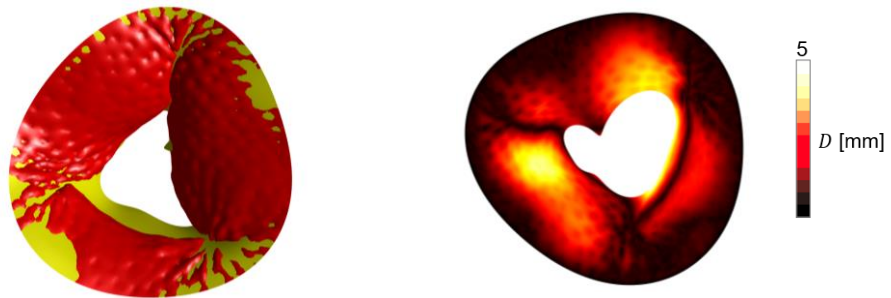
TR3



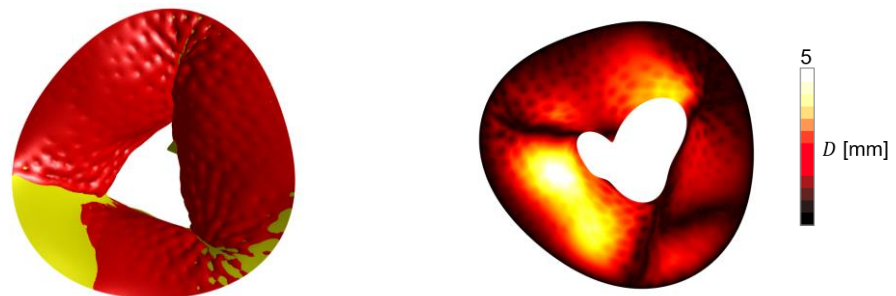
TR4



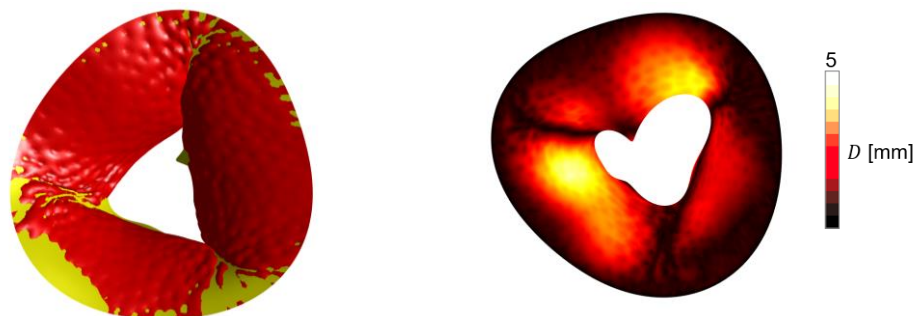
TR5



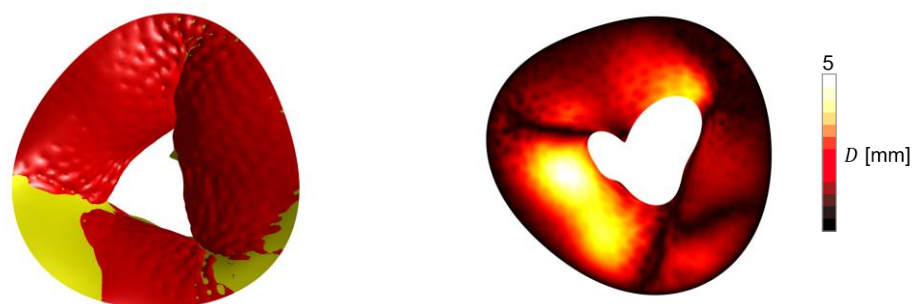
TR6



TR7



TR8



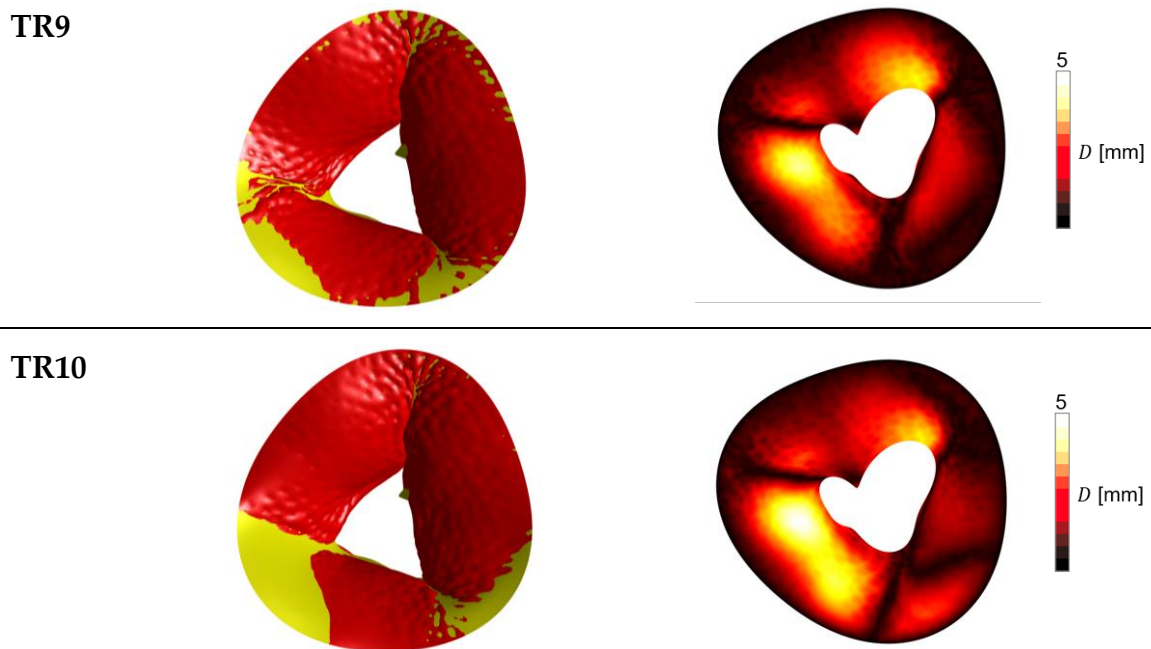
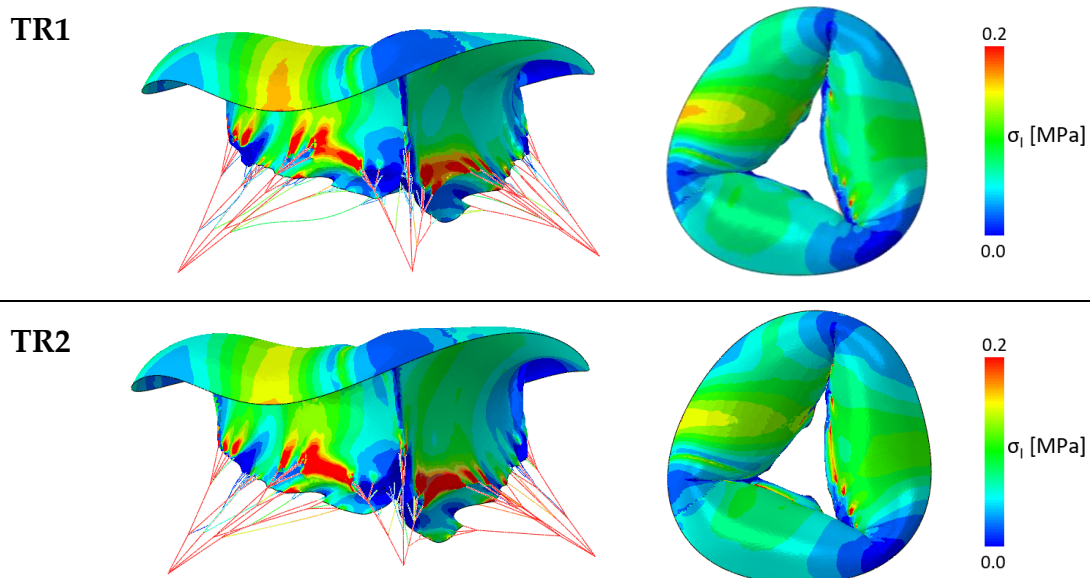


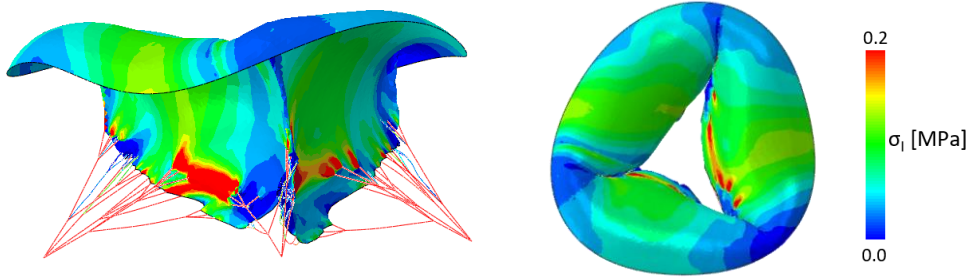
Figure A.1: graphic representation of the distance between the valve obtained at the end of the simulation and the reference valve $\Omega_{ps}^{tracing}$.

A.2. TV with TV: leaflets maximum principal stresses

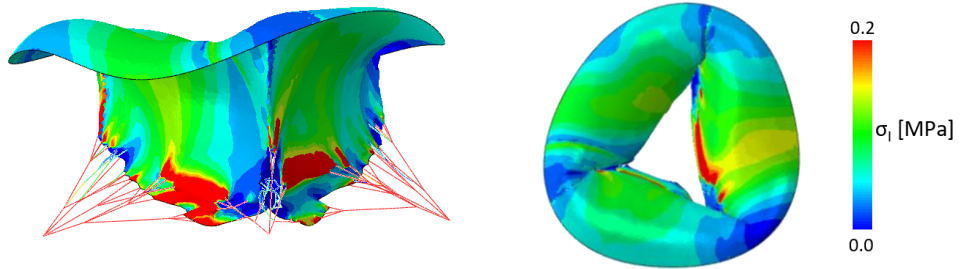
For each configuration, the lateral and atrial views of the valve are shown with their respective maximum principal stresses. The colour scale is shown to the side.



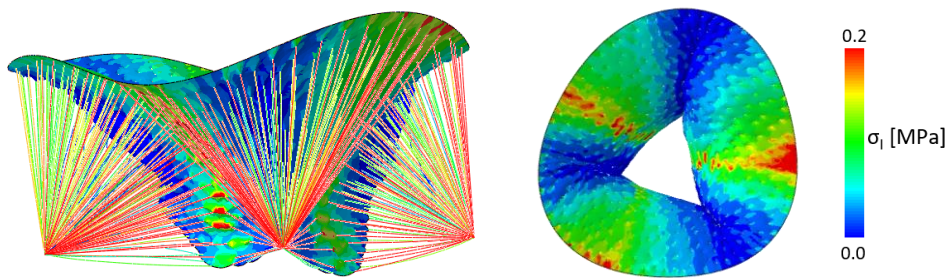
TR3



TR4



TR9



TR10

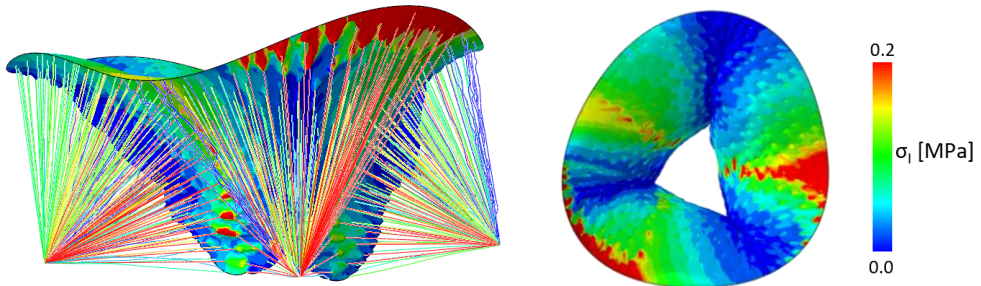


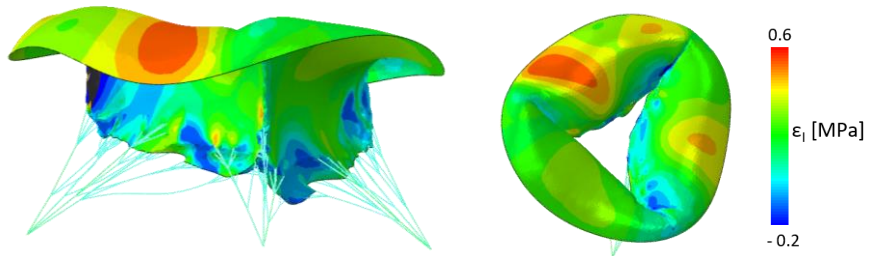
Figure A.2: the lateral and the atrial views of the valve are shown with their respective maximum principal stresses.

A.3. TV with TR: leaflets maximum principal strains

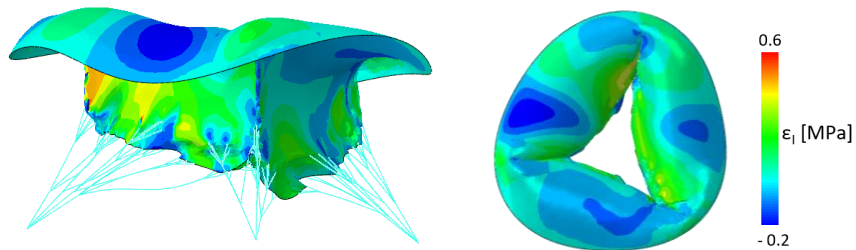
For each configuration, the lateral and atrial views of the valve are shown with their respective maximum principal strains. The colour scale is shown to the side.

TR1

NE11

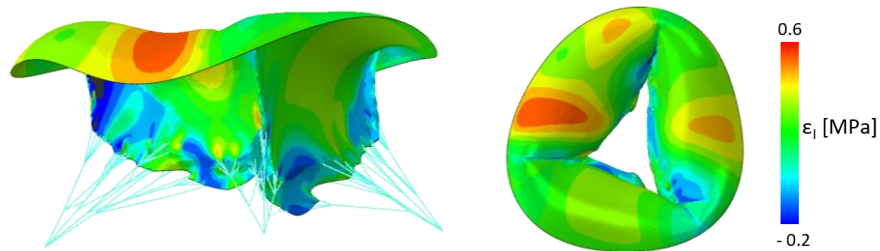


NE22

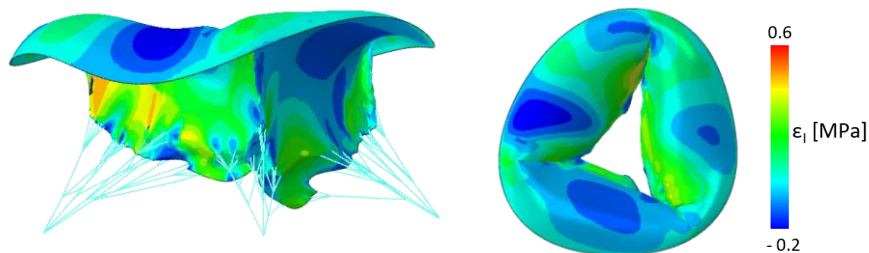


TR2

NE11

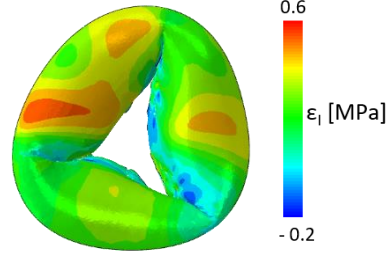
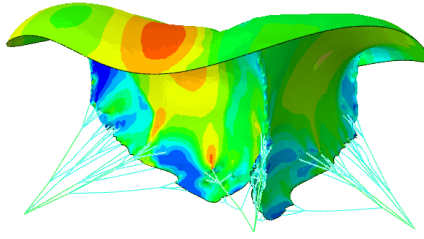


NE22

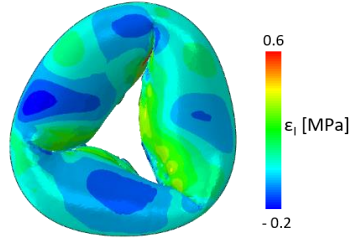
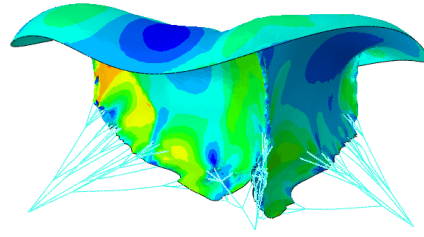


TR3

NE11

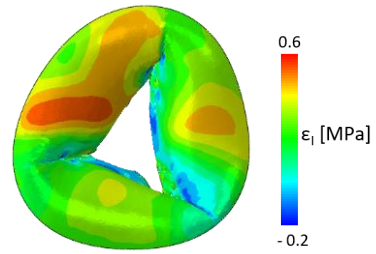
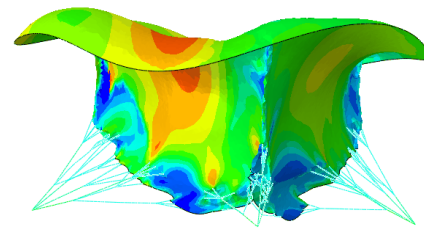


NE22

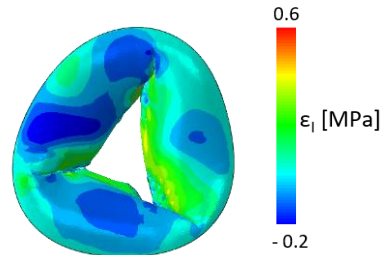
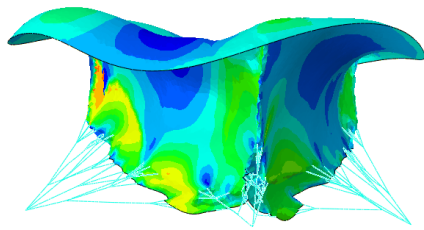


TR4

NE11

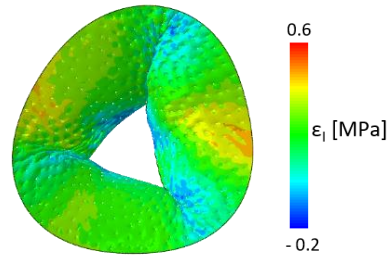
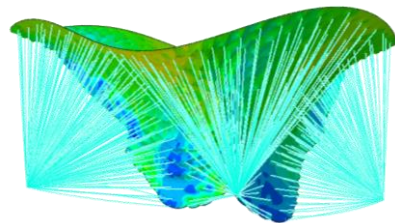


NE22

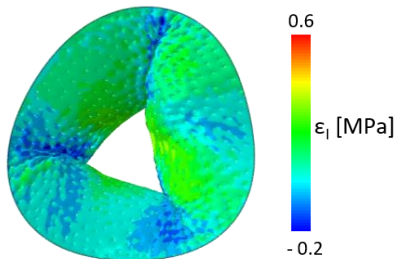
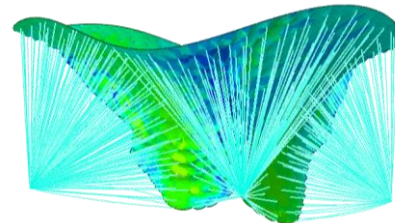


TR9

NE11



NE22



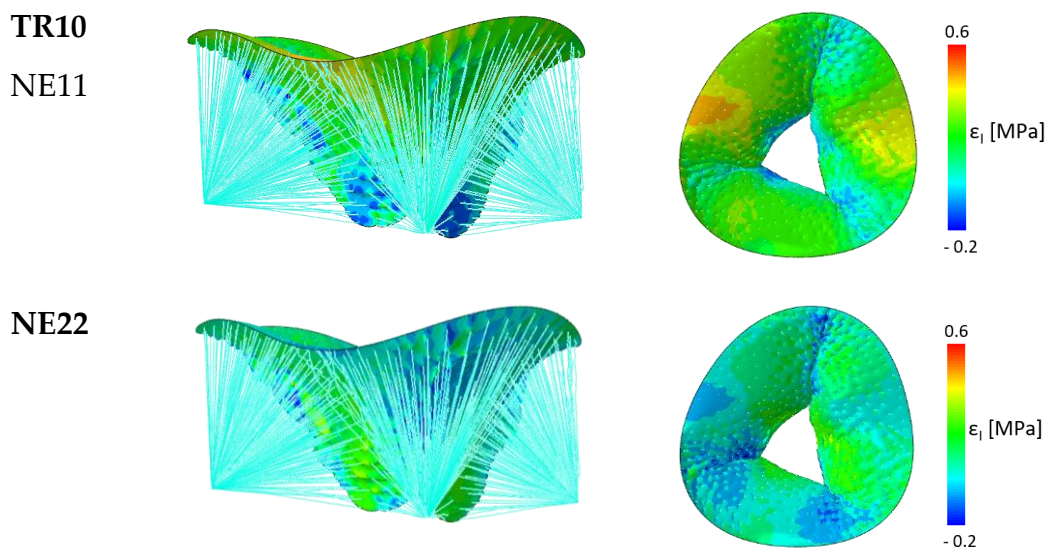
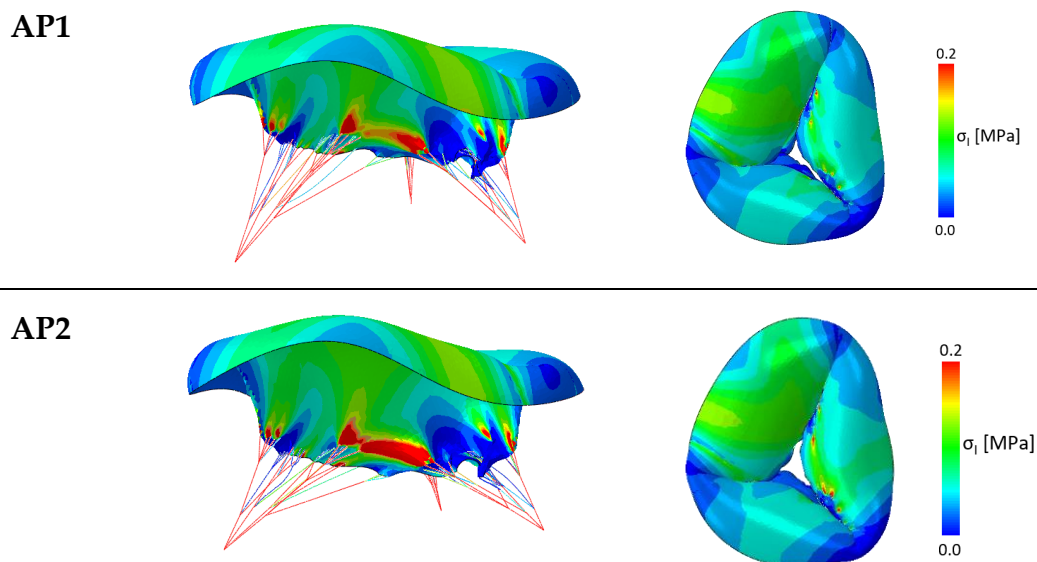


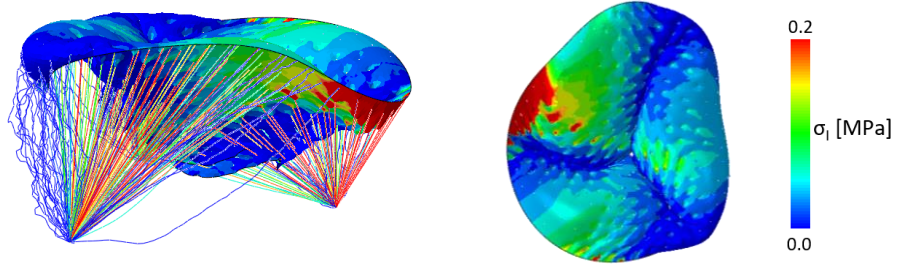
Figure A.3: the lateral and the atrial views of the valve are shown with their respective maximum principal strains.

A.4. TV-AP60: leaflets maximum principal stresses

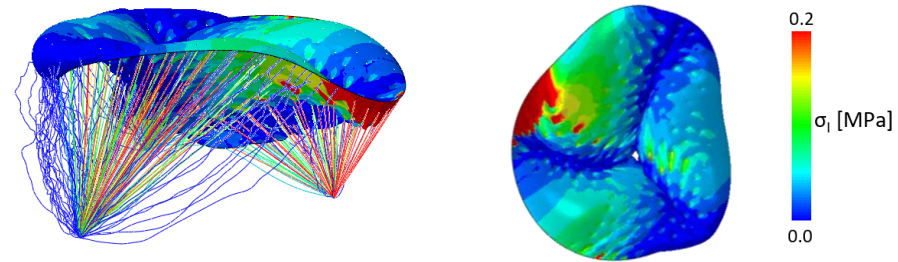
For each post-surgery configuration, the lateral and atrial views of the valve are shown with their respective maximum principal stresses. The colour scale is shown to the side.



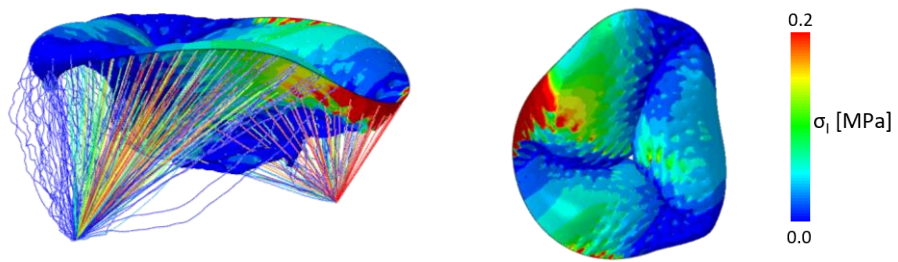
AP3



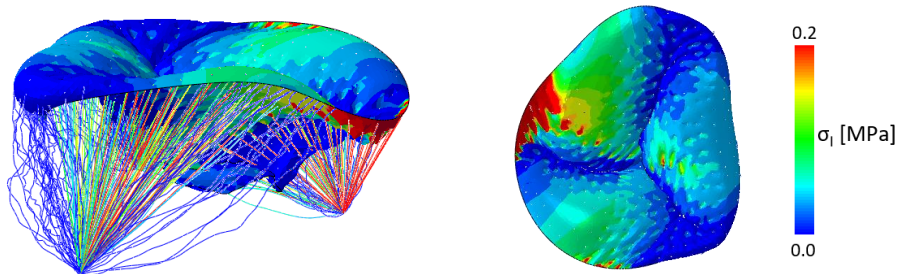
AP4



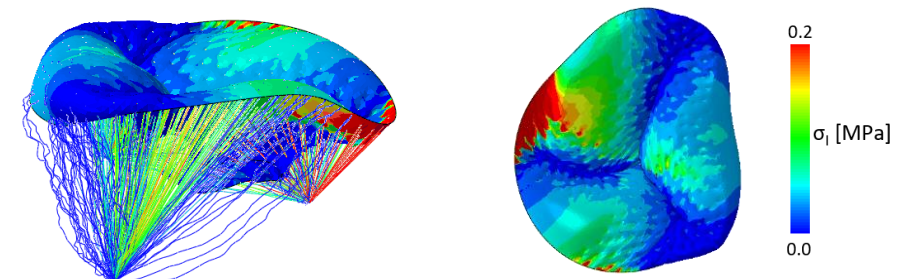
AP5



AP6



AP7



AP8

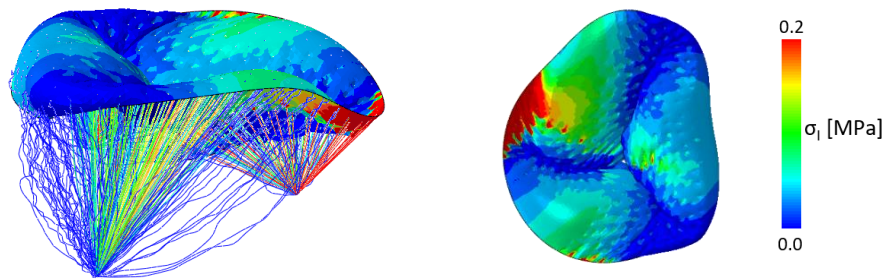


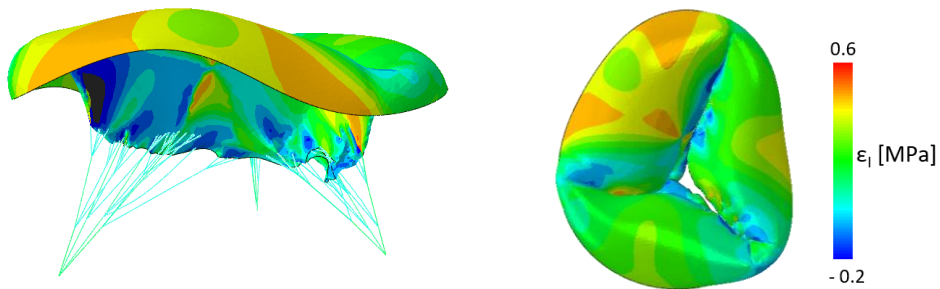
Figure A.4: the lateral and the atrial views of the post-surgery valve are shown with their respective maximum principal stresses.

A.5. TV-AP60: leaflets maximum principal strains

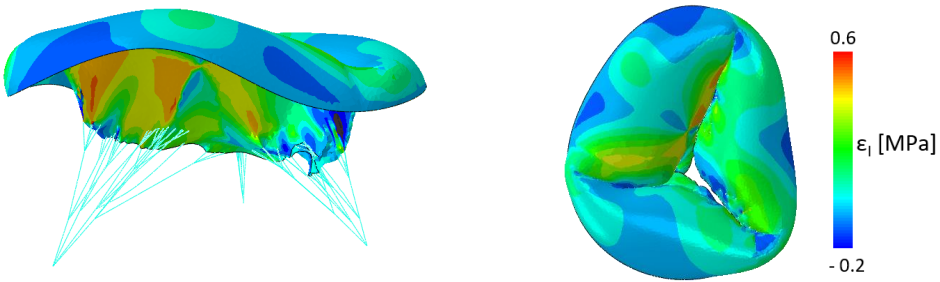
For each post-surgery configuration, the lateral and atrial views of the valve are shown with their respective maximum principal strains. The colour scale is shown to the side.

AP1

NE11

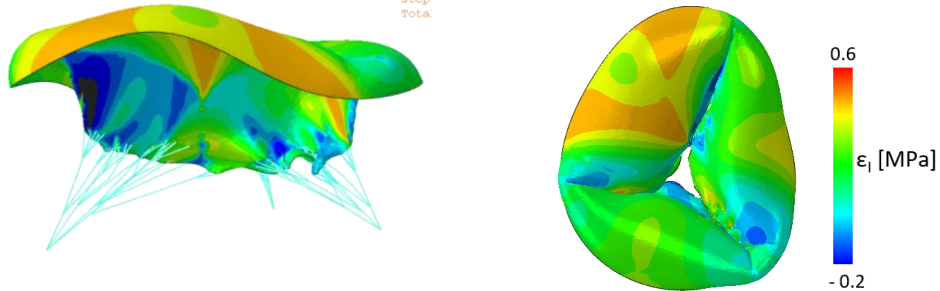


NE22

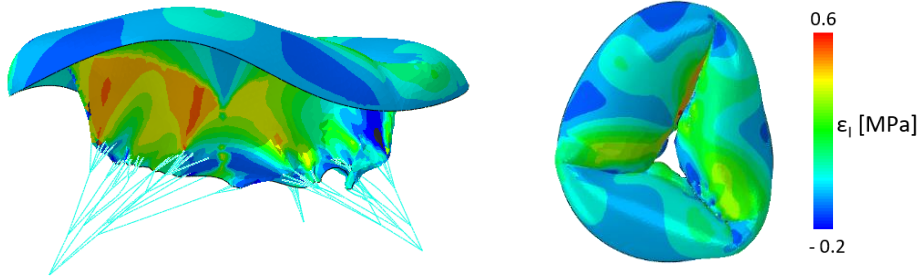


AP2

NE11

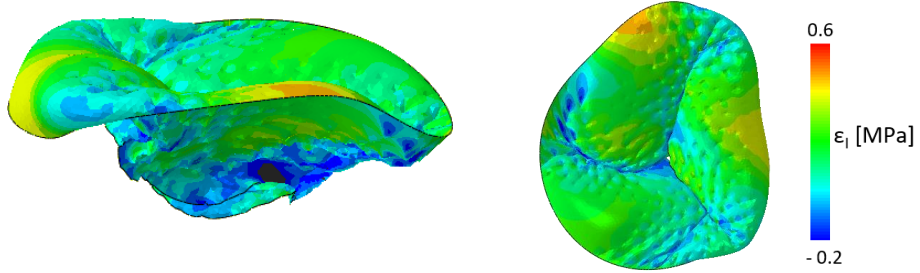


NE22

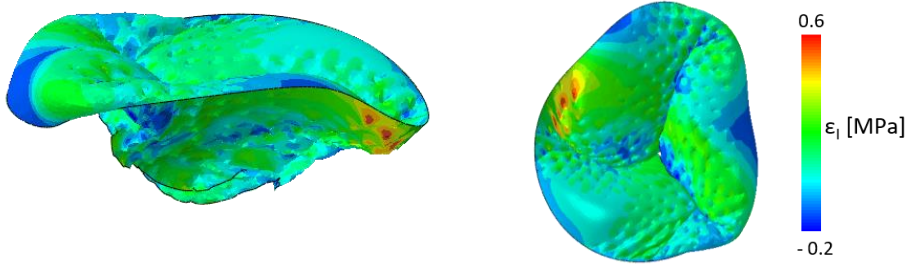


AP3

NE11

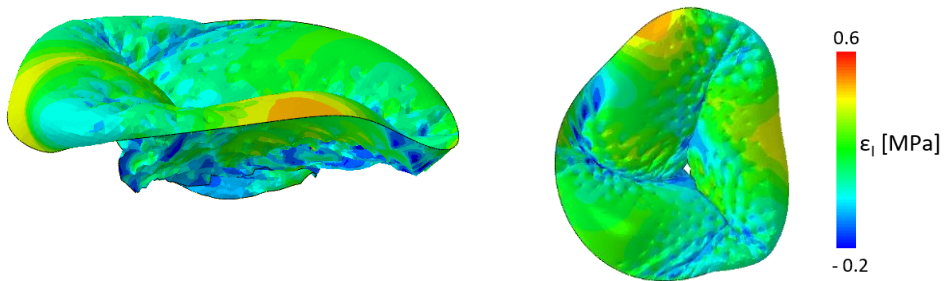


NE22

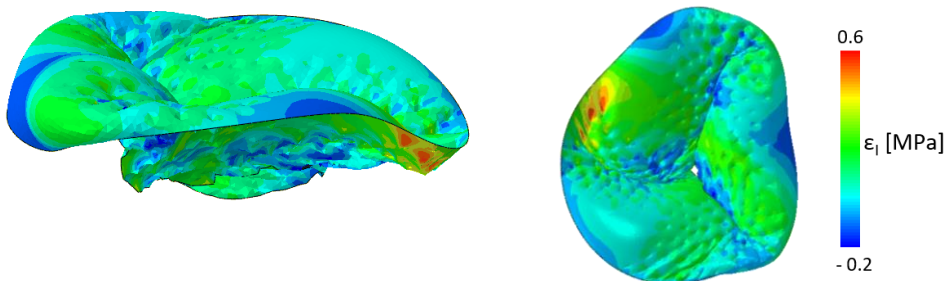


AP4

NE11

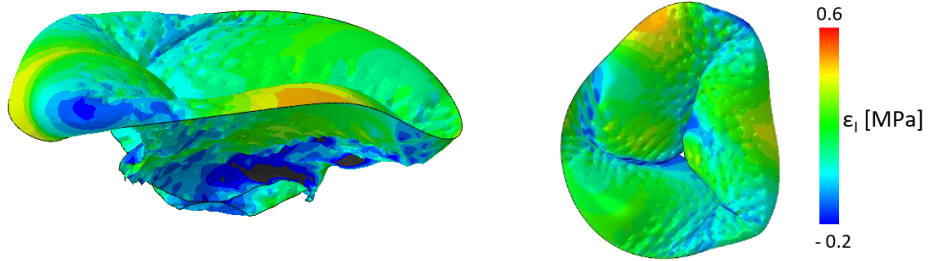


NE22

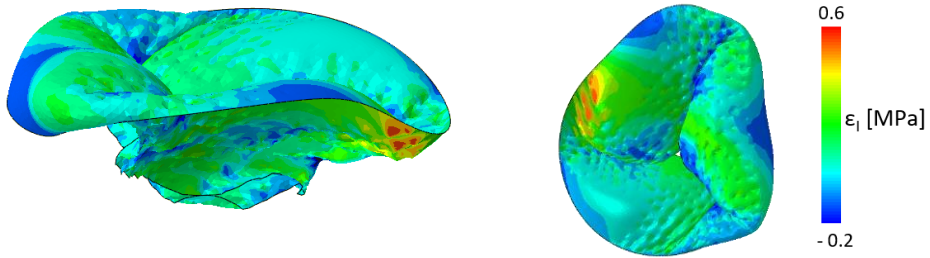


AP5

NE11

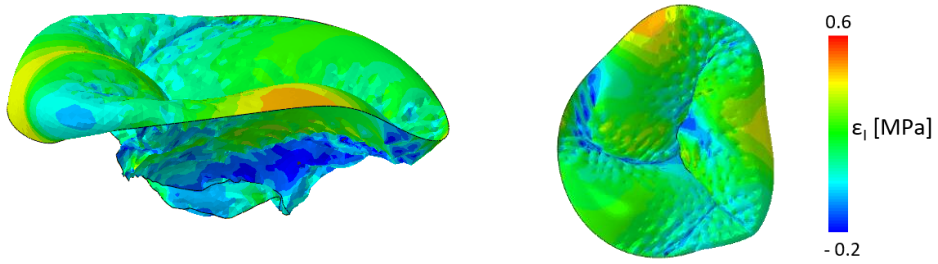


NE22

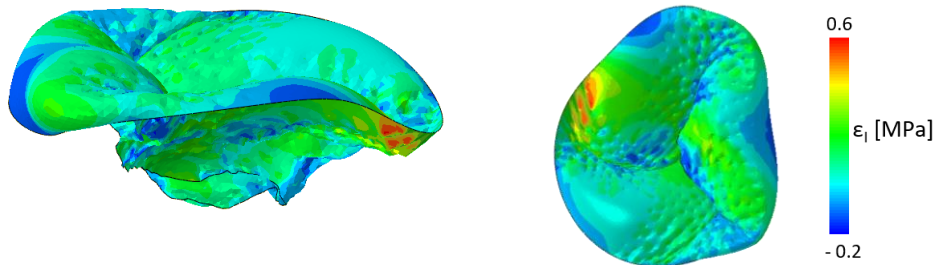


AP6

NE11

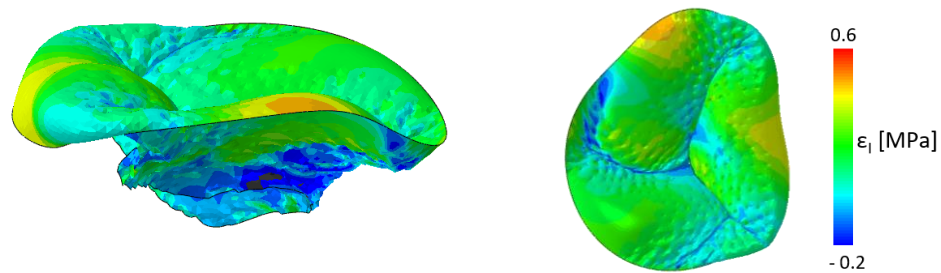


NE22



AP7

NE11



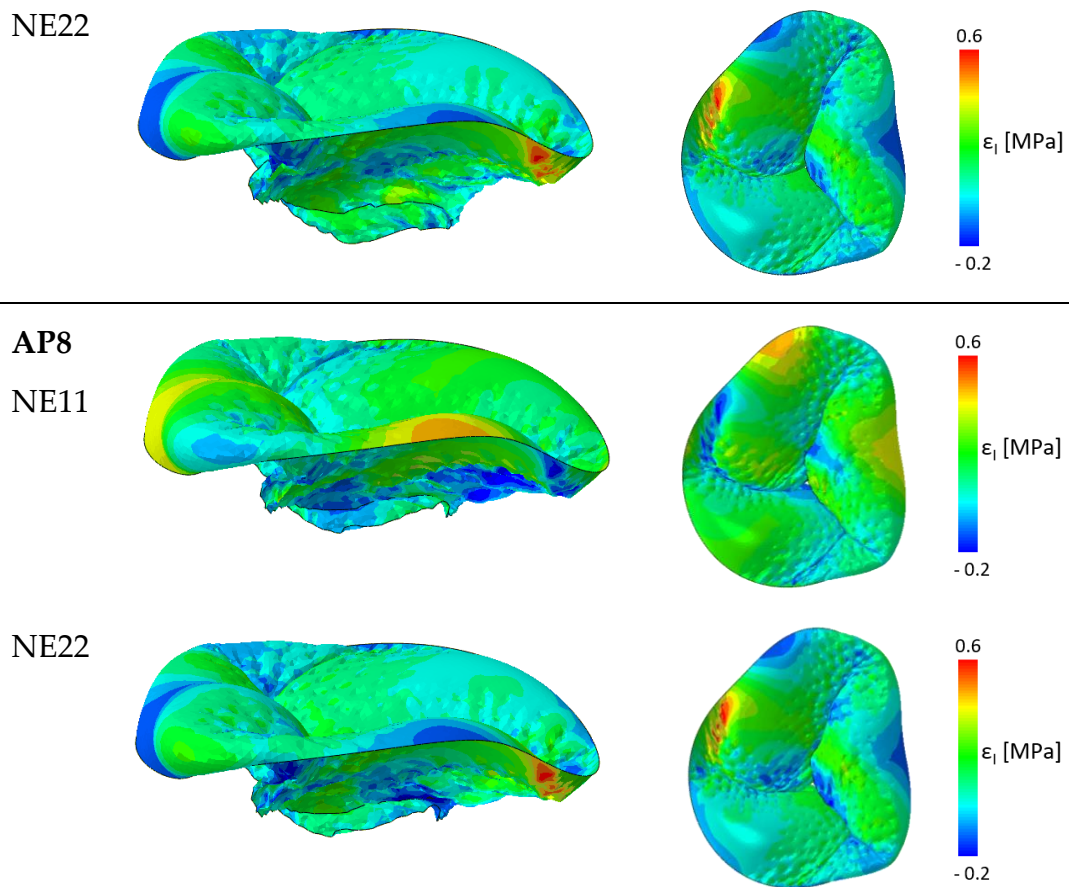


Figure A.5: the lateral and the atrial views of the post-surgery valve are shown with their respective maximum principal strains.

List of Figures

- Figure 1.1: Left: representation of the valvular plane and all four valves of the heart: the TV is at the bottom right of the sketch; the three leaflets of the TV are indicated: P=posterior leaflet, A=anterior leaflet, S=septal leaflet; MV=mitral valve; PV=pulmonary valve; AV= aortic valve. Right: cross-section of the right ventricle, where the TV is visible. The three leaflets of the TV are highlighted again, the PMs and the chordae that connect the TV to the ventricular wall are also represented. Image adapted from Evin Yucel et al. [2]..... 13
- Figure 1.2: Left: non-planar shape of the physiological tricuspid valve: the highest and lowest points of the annular profile with respect to RA and RV, are highlighted; Right: positions of points in the TV annulus line with respect to AV. Image adapted from Besler et al. [12] 13
- Figure 1.3: (A) Valve plan: identification of the TV with the leaflets. The dotted lines point out the direction of expansion during the cardiac cycle; (B) Frontal view of the heart: the dotted lines show the direction of expansion of the right heart structures. Image taken from Dahou et al. [11] 14
- Figure 1.4: The number of leaflets of the TV may vary. (A) The three-leaflet configuration: the white line indicates the TVPL, the yellow line the TVSL and the blue line the TVAL. (B) Case with 4 leaflets. Image taken from Dahou et al. [11] 16
- Figure 1.5: Representation of the TV leaflets cut open and distended on a planar surface. E-F = antero-septal commissure; C-D = postero-septal commissure, where fan-shaped chordae (fc) insert; G-H = antero-septal commissure at the Anterior Papillary Muscle (APM,) where fan-shaped chordae (fc) insert; H-C = TVPL with its multiple indentations, each one characterized by the insertion of fan-shaped chordae (fc); D-E = TVSL identified by the presence of the fold (sf); F-G = TVAL. In the illustration, the basal zone is stippled, the rough zone is dotted, and the area in between is the zone. Image taken from the Silver et al. [13]..... 17
- Figure 1.6: (A) Photograph of the APM and SPM. The morphology of the APM is atypical, but the difference in size between the anterior and SPM is clear. (B) Picture of a PPM with four heads. Image taken from the Silver et al. article [13] 19
- Figure 1.7: (A) Fan-shaped chordae (the arrow indicates the sub-branches of this chord just before insertion into the leaflet); (B) rough zone chordae (the arrow indicates the rough zone); (C) free-edge chordae (the arrow indicate the only free-edge chordae with its thin structure); (D) deep chordae (the arrow indicated the triangular fold); (E) basal

| | |
|--|----|
| chordae (the arrow indicated this type of CTs). Image adapted from the Silver et al. article [13] | 20 |
| Figure 1.8: On the left is a representation of the physiological annulus with its typical cell shape. On the right is a representation of a more planar and circular annulus typical of the TR. Image adapted from Besler et al. [12]..... | 24 |
| Figure 1.9: (A) Ring Annuloplasty, (B and C) Surgical reconstruction of the leaflet. Images adapted from Nishant Saran et al. [25]..... | 25 |
| Figure 1.10: (a) Illustration of the directions of the FWA technique. i. View with respect to the valve levels. ii. View with respect to the short axis on the PMs level; (b) Representation of the experimental set-up; (c) Experimental protocol: for each heart sample, data were recorded in three pre-FWA or TR conditions, post-FWA with 30% and 60% approximation. Below are the acronyms shown in the figure: TV = tricuspid valve, RA = right atrium, RV = right ventricle, SW = septal wall, AL = anterior leaflet, PL = posterior leaflet, SL = septal leaflet, APM = anterior papillary muscle, PPM = posterior papillary muscle, SPM = septal papillary muscle, A-P = anterior-posterior approximation direction, A-S = anterior-septal approximation direction, A-SW = anterior-septal wall approximation direction, MV = mitral valve, LA = left atrium, LV = left ventricle..... | 26 |
| Figure 1.11: Schematic representation of the experimental set-up developed in [28]. The pump (A) is connected to the heart by means of a connector (B) which was inserted directly into the septal wall. The preload simulator is connected to the atrium (C), while the afterload simulator (I) was connected downstream of the PV (M). | 28 |
| Figure 1.12: Left: RV restraining bands to control the RV motion. Right: Connector positioning in the septal wall and removing the LV. Images adapted from Castagna and Lentini's thesis [28] | 28 |
| Figure 2.1: Representation of the TV unloaded configuration using a parametric model developed by Stevanella et al. Image adapted from Stevanella et al. article [6] | 34 |
| Figure 2.2: Basic sequence for the realization of the parametric model proposed by Johnson. The promo step is the definition of the 18 characteristic points of the annulus, which are interpolated by a B-spline. The initial point of the curve corresponds to the antero-septal commissure. Identifying the position of the commissures is fundamental to defining the annulus-free margin extension. Parametrically, the position of the papillary muscles and the characteristics of the main tendon groups are defined. Image adapted from Johnson et al. article [36] | 35 |
| Figure 2.3: steps leading from acquisition of echocardiographic data to three-dimensional valve reconstruction. Image adapted from Aversa and Careddu thesis [37]. | 36 |
| Figure 2.4: The first column represents the source image, the second the manual segmentation and the third column the result obtained with the MALF (multi-atlas | |

- label fusion) technique, the fourth column the model obtained. Image adapted from Pouch article [38]. 36
- Figure 2.5: The graphs shown are the results of biaxial tests on the TVAL, TVPL and TVSL respectively, imposing different levels of tension. The circumferential direction (Circ) is highlight in red and the radial direction (Radial) in blue. The main line is the average value obtained and the horizontal bars are the standard errors. The green horizontal line indicates the maximum level of physiological tension, while the tests go up to 100N/m to simulate the condition of hypertension. Images adapted from K. Amini Khoiy et al. article [39]..... 38
- Figure 2.6: The graphs allow a direct comparison of the stress-strain curves obtained from the equibiaxial protocol of each MV and TV valve leaflet. The graphs show in blue the results obtained in the circumferential direction (CIRC) and in red in the radial direction (RAD). Data are presented as mean \pm standard error. Images adapted from Pham et al. [40]..... 39
- Figure 2.7: The six samples extracted from the TVAL are shown schematically on the right and the labels A-F correspond to the stressed region. The graphs depict the total tissue elongation results for the six TVAL tissue regions under equi-biaxial loading protocol. In each graph, the mean standard error of the membrane tension was averaged over the total tissue elongation results. Images adapted from Laurence et all. article [41] 40
- Figure 2.8: (A) (i) Schematic representation of the removal zone of the tissue samples extracted from the TVAL, TVPL and TVSL (ii) Representation of how the tissue samples were mounted in alignment with the circumferential and radial directions and tested under biaxial tension (B) Graphs of response to the application of equibiaxial membrane tension and stretching of the TVAL, TVPL and TVSL in the (i) circumferential and (ii) radial directions. Images adapted from Meador et al. article [42]. 41
- Figure 2.9: The graph represents the stress-strain curve of human TV CTs. The central line is the mean value, while the two dashed lines are the standard error. Images adapted from Lim et al. article [47]..... 44
- Figure 2.10: The three plots represent the mean uniaxial chordal mechanical response for (A) TVAL, (B) TVPL and (C) TVSL. The mechanical responses were then grouped by chordal insertion points and were further subdivided on the basis of anatomical description: triangles represent struct CTs, squares basal CTs and circles marginal CTs. Images adapted from Pokutta-Paskaleva et al. article [48] 44
- Figure 2.11: The graphs show the first PK stress-strain for all tendon chords divided by (a) leaflet, (b) insertion site, (c) tricuspid tendon chord size. For each graph, the mean value and the detected standard error are shown. Images adapted from Smith et al. article [49]. 45

| | |
|--|----|
| Figure 2.12: In the graph, the dotted line shows the value of $\lambda f *$ which is the transition point between the exponential region and the linear region. Image adapted from Amicone and Dazzi thesis [30]. | 47 |
| Figure 2.13: The graph allows a comparison between the curve obtained with the Weiss model shown in yellow, the curve obtained with the 3-order Odgen model in red, and the curve obtained with a 2-order polynomial model, all of which are fitted to the experimental data of Lim. Image adapted from Amicone and Dazzi thesis [30]. | 48 |
| Figure 2.14: Result of systolic peak simulation in models A,B and C of nominal strain distributions in circumferential and longitudinal direction. Images adapted from Stevanella et al. article [6]..... | 50 |
| Figure 2.15: On the left is the colorimetric map of the nodal displacement in mm, and the directions of the resulting displacement vectors; on the right is the result in terms of nominal radial deformations at systolic peak. Images adapted from Aversa and Careddu thesis [37]. | 51 |
| Figure 2.16: Distribution of the main maximum principal stress distribution in mid-systole on the leaflets for each of the patients. Yellow points indicating the annulus boundary between leaflets. Images adapted from Kong et al. article [7]..... | 52 |
| Figure 2.17: The images in the upper part of the table are images from experimental video taken during the movement of the heart on a test bench. The images at the bottom are the TV reconstructions with the automatic workflow. The images on the left refer to the original valve with regurgitation, the two configurations on the right (AP30 and AP60) are the result of the application of reconstruction surgery. Images adapted from Locatelli and Manini thesis [29] | 53 |
| Figure 2.18: The figure shows the fibre orientation proposed and implemented in the Holzapfel model for describing the material in the leaflets. Images adapted from Amicone and Dazzi thesis [30] | 54 |
| Figure 2.19: Results of FE models considering four levels of isotropic pre-strains. The analysed TV configuration is the systolic peak configuration. Images adapted from Laurence PhD thesis [51]...... | 55 |
| Figure 2.20: Schematic representation of the engineering process (inverse). the geometry of the model was obtained by digitising the motion of the valve ring the geometry of the leaflets. The material properties were obtained from in vitro mechanical tests on each leaflet on the CTs. Transvalvular pressure was acquired using a pressure microsensor. The FE model was used to predict valve closure, and the result was validated using epicardial echocardiographic images of the beating heart. Images adapted from Mrudang Mathur et al. article [9]..... | 56 |
| Figure 3.1: Overview of the project workflow | 58 |

- Figure 3.2: The two images represent the 18 planes (left) along the radial axis and the 20 planes (right) along the short axis of the valve structures generated at the end of the workflow. Images adapted from Locatelli and Manini's thesis [29]..... 60
- Figure 3.3: Left: menu of the starting GUI version. Right: new version of the GUI specially developed to allow a good segmentation of echocardiographic images of a TV. This version is the one that was used for manual image segmentation on this thesis work..... 62
- Figure 3.4: the blue arrows identified three leaflets that are visible in the image. It is possible that one of the two leaflets visible on the left of the image is a shadow or an artefact..... 63
- Figure 3.5: Tool viewer: allows you to view plotted points in three-dimensional space. In the images in red are the annulus points, in black the leaflets and in blue the free margin. The elements in green and pink are the tracings in the various planes of the PMs. In the image on the left, the center of mass of the point cloud has been positioned at the origin of the reference system..... 63
- Figure 3.6: The graph shows in red the manual traces for each plane, in blue the position the corresponding points assume after applying the fourth-order Fourier transform. 64
- Figure 3.7: In the image the red dots identify the annulus, the yellow dots the free margin and in green the leaflets with their lengths 65
- Figure 3.8: Tracing of the connector with a white dot. 65
- Figure 3.9: In the pictures, one can see how the “drawfreehand” function works. The papillary muscles traced are in green the anterior PM, in magenta the second PM. .. 66
- Figure 3.10: Left: Initial version of the short axis GUI. This only allows identification of the three commissures with red, magenta and yellow dots. Right: Improved version that also allows the ROI to be traced around the area of visible PMs. 67
- Figure 3.11: view of the valve leaflets in the xy plane, represented by the black, red and green points. The centre of gravity of the annulus point cloud corresponds to the origin of the reference system and is identified by the yellow circle. The orange circle is the midpoint of the septal leaflet, used as reference point. 70
- Figure 3.12: Three-dimensional plot of the points drawn on the image planes. The black dots are the leaflets, at the ends the red dots are the annulus and the green dots are the free margin. The green and magenta lines are the traces of the ROIs along the short axis and along the radial axis of the APM and PPM..... 70
- Figure 3.13: (left) three-dimensional plot of the points obtained after applying the 4th order Fourier transform to the 32 levels of the leaflets. (right) plot of the same points in the xy plane..... 71

- Figure 3.14: Mesh generated after application of the Triangulation algorithm 72
- Figure 3.15: Mesh obtained after the application of Taubin's filter to smooth out surface irregularities and applying the remeshing of the tringulation..... 72
- Figure 3.16: The curve plotted is the free margin curve. The points in yellow represent the curve's minimum points. The magenta stars are the maximum points. The blue, red and green stars are the points resulting from plotting along the short-axis view of the valve. The points in green, also indicated by the blue arrows, are the points calculated using the weighted average of the two. 73
- Figure 3.17: The orange circle is reference point for the rotation matrix that provides information on the midpoint of the TVSL; so, in black the TVSL, in red the TVPL and in blue the TVAL. 75
- Figure 3.18: Plot of the thicknesses along the leaflets. The line indicates the area in which the minimum points have been identified, the two dots indicate two of the points in which the minimum values have been defined. One is located at the radial coordinate of the commussure and one at the radial coordinate midpoint of the leaflet. 76
- Figure 3.19: Normalised graph of collagen architecture in porcine MV anterior leaflets. Image adapted from Cochran et al. article [60]..... 77
- Figure 3.20: The surface normals were evaluated to determine if they were all oriented in the same direction and, if not, to rearrange them correctly. This step is fundamental for the simulation pipeline..... 78
- Figure 3.21: Representation of the point clouds obtained for SP TV after being filtered and resampled. In the image the points in red represent the annulus, those in blue the free margin and in black the leaflets..... 79
- Figure 3.22: the image represents the TV to SP following triangulation. The annulus is highlighted in red and the free margin in blue..... 80
- Figure 3.23: The figure displays the TV in ED configuration, in blue are the PMs traces from the segmentation through the short-axis GUI. The points in black are the APM, PPM and SPM. As the third PM is not visible from the images, the position was calculated based on the information from the other two PMs and considering the theta of the reference commissure. 81
- Figure 3.24: In the figure, the black dots represent the PMs calculated for the ED configuration, the black ones the PMs calculated for the SP configuration. The way the TV is oriented, only 2 of the 3 PMs are visible..... 81
- Figure 3.25: Parametric representation of the CTs proposed by Chung-Hao Lee et al. [8] The image also shows the distances (d1, d2, d3, d4, d5, d6, d7, d8 and d9) of the chordal insertions from the free margin. In addition, there are three groups of CTs that originate from the PMs and insert on the anterior and posterior leaflets, and four

- groups of CTs originate from the PMs that have CTs that insert on the septal leaflet.
 83
- Figure 3.26: Representation of CTs reconstruction following Chung-Hao Lee et al. [8] parametric model. 84
- Figure 3.27: The images represent the 3 MVs on which the theory of applying a functionally equivalent model for valve closure simulations was tested. The top row represents the anatomically accurate model of the native valve, while the second row shows for each of the valves the functionally equivalent model in which only 2 PMs were conserved, the CTs are straight and insert randomly into the leaflets but with an insertion density defined at 15 insertions/cm². 85
- Figure 3.28: representation of the CTs architecture defined following the model of Khalighi et al. [58]. The image shows 2 of the 3 PMs identified by a red dot and 4 of the 6 groups of CTs. The green and light blue CTs are the CTs that fit on the free edge, the blue and black CTs are the CTs defined as BULK. In the image it can be seen that some CTs pass through the leaflets to reach their insertion point, this issue was not considered relevant as the contact between these two elements is not considered in the simulations. 86
- Figure 3.29: Transvalvular pressure measured experimentally during Locatelli and Manini's thesis. Image adapted from Locatelli and Manini thesis [29]. 87
- Figure 3.30: The plots represent the TV at the beginning and end of the simulation. The first line highlights the CTs, the second line represents the TV in its entirety and the third line shows the behaviour of the three leaflets. In red the TVPL, in grey the TVAL and in blue the TVSL. 89
- Figure 3.31: Morphing simulation. (A) Initial configuration: the rigid surface in SP configuration is located 3 mm relative to the z-axis above the valve in ED configuration. The CONNECTOR elements are positioned at the defined points at the free edge and ready to bring the leaflets closer together. (B) Configuration at 0.5 of step 1: The rigid surface is approaching the valve, and the CONNECTOR elements are shortening. (C) End of step 2: The valve has been pressurised and the valve leaflets have moved closer together. Blocking the translations of the free edge points prevents the leaflets from assuming unphysiological conformations. In red the TVPL, in grey the TVAL and in blue the TVSL. 92
- Figure 3.32: Simulation set-up for TV RF extraction. The applied pressure load is that measured during the experimental tests. The leaflets respond to the load by swelling. Their dotted shape is due to the chordal insertions. In red the TVPL, in grey the TVAL and in blue the TVSL. 93
- Figure 3.33: Closure simulation. (A) Start point of the first step. The CTs have been redefined to have an initial length of l_0 and must pass through the reference PM in their construction. The points of the leaflets are embedded. (B) At the end of the first

step, the origin point of the CTs was shifted to the coordinate of the reference PM at ED configuration. At this step, the CTs are relaxed. (C) End of the second step. The CT was loaded with the pressure load and the SP configuration of the valve was obtained. During the simulation, the annulus and PM points were shifted from the ED configuration to the reconstructed SP configuration. In red the TVPL, in grey the TVAL and in blue the TVSL. 96

Figure 3.34: schematic representation of how the RFs extracted for each insertion were associated with the section of CT on which the value of l_0 will be calculated. In the image, the shorter blue branches at the level of the leaflet, represented in grey, are all the points where the RFs were extracted and have been associated with the long blue segment that originates from the PM, which is the meeting point of the blue CTs, purple, brown and green. The same reasoning can be done for the colours purple, brown and green..... 97

Figure 3.35: (A) Configuration of the TV at the beginning of step 1. The configuration of the TV is the one reconstructed at ED with TR, evaluating the starting position of the CTs calculated in the calibration phase. (B) At the end of step 1 the post-intervention valve configuration is obtained. The shape of the annulus was modified, and the position of PMs was translated. The CTs appear much more relaxed. (C) End of the loading step showing the result of applying the idea of Jaworek et al. [10]. 99

Figure 4.1: Framework of tested configurations for TV with TR and definition of acronyms. The double-entry table, although with atypical configuration, provides the necessary information to understand the differences between the various configurations. For example, in the TR2 configuration the CTs were described geometrically with the Chung-Hao Lee model, the material used was Saint Venant-Kirchhoff and the simulation was carried out in a single step. For the TR5 to TR10 simulations, an additional parameter, typical of Khalighi's functionally equivalent model, was evaluated, which is the chordal insertion density..... 101

Figure 4.2: framework of the configurations tested to evaluate the biomechanical behaviour of the TV as a consequence of a 60% FWA in the AP direction and their acronyms. The double table provides information with respect to the geometric model used for the description of the CTs and the constitutive model for the description of the material. In this case, post-surgery simulation was applied to all configurations. 102

Figure 4.3: plot of the value of ε , on the z-axis, for the 6 configurations tested. The x-axis shows the chordal insertion density and the y-axis the type of constitutive model used for the CTs..... 104

Figure 4.4: plot of the D value in mm, on the z-axis, for the 6 configurations tested. On the x-axis chordal insertion density and on the y-axis the type of constitutive model of the CTs. 105

- Figure 4.5: plot of the computational time in hours, on the z-axis, for the 6 configurations tested. The x-axis shows the chordal insertion density and the y-axis the type of constitutive model used for the CTs..... 106
- Figure 4.6: configurations chosen for parameters analysis: type of simulation, parametric model for CTs and material constitutive model of CTs. 107
- Figure 4.7: (left) box plot of the values of the leaflets maximum principal stresses in MPa of the configurations in which the CTs were described with Weiss' constitutive model. (right) configurations with the Saint Venant-Kirchhoff constitutive model. 108
- Figure 4.8: (left) lateral and (right) atrial view of the leaflets maximum principal stress of TR3 configuration at the end of systolic closure simulation. 109
- Figure 4.9: (left) lateral and (right) atrial view of leaflet max principal stress of the TR9 configuration at the end of the simulation. 109
- Figure 4.10: (left): box plot of CTs maximum principal stresses in MPa in which the material is described with the Weiss constitutive model. (right): box plot in which the CTs are Saint Venant-Kirchhoff constitutive model. 111
- Figure 4.11: RFs graphs at the end of the valve closure simulation as a function of position on the annulus. The actual values have been filtered with a low-pass filter to make the distribution more meaningful, and are represented with a black line. The blue line is the average value of the RFs. The dots are used to determine the position of the RFs with respect to the valve annulus: red the position of the antero-posterior commissure, cyan the antero-septal commissure, green the postero-septal commissure. 112
- Figure 4.12: Box plot leaflets maximum principal strain (A) NE11 with CTs described with Weiss constitutive model (B) NE11 with CTs described with Saint Venant-Kirchhoff constitutive model (C). NE22 with CTs described with Weiss constitutive model (D) NE22 with CTs described with Saint Venant-Kirchhoff constitutive model. 114
- Figure 4.13: (A) (left) lateral and (right) atrial view of leaflets NE11 of TR3 configuration at the end of closure simulation. (B) (left) lateral and (right) atrial view of leaflets NE22 of TR3 in the same condition. 115
- Figure 4.14: (A) (left) lateral and (right) atrial view of leaflets NE11 of TR9 configuration at the end of closure simulation. (B) (left) lateral and (right) atrial view of leaflets NE22 of TR9 in the same condition 115
- Figure 4.15: plot of the value of ϵ , on the z-axis, for the 6 configurations tested. The x-axis shows the simulation workflow used and the y-axis the type of constitutive model used for the CTs..... 116

- Figure 4.16: plot of the D value in mm, on the z-axis, for the 6 configurations tested. On the x-axis chordal insertion density and on the y-axis the type of constitutive model of the CTs..... 117
- Figure 4.17: (A) (left) plot of the $\Omega PSFE, closure$ TR3 in red on the $\Omega PStracing$ reference valve in yellow. (right) plot of the point-to-point distance between $\Omega PSFE, closure$ and $\Omega PStracing$. Black means the distance is approximately 0, white in says the distance is 5 mm or more. (B) (left) plot of the $\Omega PSFE, closure$ TR9 in red on the $\Omega PStracing$ reference valve, in which the interpenetration of surfaces is visible. (right) plot of the point-to-point distance between the $\Omega PSFE, closure$ and the $\Omega PStracing$ reference valve..... 118
- Figure 4.18: Echocardiographic planes of the long axis of the post-surgery HT11 valve. In the images the valve axis is highlighted in red, considering the ED frame of different planes of the same volumetric data. 119
- Figure 4.19: Plot in xy plane extracted following the tracing of the annulus points. There is a discrepancy between the points plotted for the annulus on the left-hand side and the specular points on the right-hand side. 120
- Figure 4.20: (left) plot in the xz-plane showing the difference in proportions between the annulus (black dots) and PMs (black stars) of the TV pre-surgery valve at ED and the same structure of the TV post-surgery at ED (red dots) and SP (blue dots). (right) plot of the same structures in their three-dimensionality. 120
- Figure 4.21: Maximum principal stresses using data extracted from the echo images. 121
- Figure 4.22: Maximum principal strains NE11 using data extracted from the echo images. 121
- Figure 4.23: Maximum principal strains NE22 using data extracted from the echo images. 121
- Figure 4.24: (Upper) plot in the xz-plane showing the annulus (black dots) and PMs (black stars) of the TV pre-surgery valve at ED and the same structure of the TV post-surgery at ED (red dots) and SP (blue dots) after the modification of the proportionality between the structures. (Lower) plot of the same structures in their three-dimensionality. 122
- Figure 4.25: Atrial and lateral view of the TV at the end of the first step of the post-surgery simulation. The TVPL (red) shows the most pronounced displacement, the issue is also present on the TVAL (grey) and on TVSL (blue)..... 123
- Figure 4.26: (left) lateral and (right) atrial view of leaflets maximum principal stresses on AP8 configuration..... 124
- Figure 4.27: (left) lateral and (right) atrial view of leaflets maximum principal strains NE11 on AP8 configuration. 124

| | |
|--|-----|
| Figure 4.28: (left) lateral and (right) atrial view of leaflets maximum principal strains NE11 on AP8 configuration. | 124 |
| Figure 4.29: Box plot of (A) leaflets maximum principal stresses in MPa, maximum principal strain (B) NE11 and (C) NE22 with CTs described with Weiss constitutive model. Box plot of (D) leaflets maximum principal stresses in MPa, maximum principal strain (E) NE11 and (F) NE22 with CTs described with Sain Venant-Kirchhoff constitutive model. | 125 |
| Figure 4.30: Box plot of (A) leaflets maximum principal stresses in MPa for each configuration. (left) CTs described with Weiss constitutive model. (right) CTs described with Saint-Venant constitutive model. | 126 |
| Figure 4.31: Representation of the maximum principal stresses of the CTs described with the Weiss constitutive model originating from the same PM and inserting into the TVPL and TVSL. (A) Chordal density of 15 ± 1 insertions/cm ² . (B) Chordal density of 20 ± 1 insertions/cm ² . (C) Chordal density of 25 ± 1 insertions/cm ² | 127 |
| Figure 4.32: (A) FRM points on the xy plane (B) the red colour is used to define the TV regurgitation area, in blue the areas that were excluded from the total area calculation after the analysis in the three-dimensional configuration (C). | 127 |
| Figure 4.33: plot of the value of % of regurgitation area, on the z-axis, for the 6 configurations tested. The x-axis shows the chordal insertion density and the y-axis the type of constitutive model used for the CTs. | 128 |
| Figure 4.34: (left) lateral and (right) atrial view of leaflets maximum principal stresses in AP1 configuration. | 129 |
| Figure 4.35: (left) lateral and (right) atrial view of leaflets maximum principal strains NE11 on AP1 configuration. | 129 |
| Figure 4.36: (left) lateral and (right) atrial view of leaflets maximum principal strains NE11 on AP1 configuration. | 130 |
| Figure 4.37: Box plot of (A) leaflets maximum principal stresses in MPa, maximum principal strain (B) NE11 and (C) NE22 of the configuration AP1 and AP2. | 130 |
| Figure 4.38: Box plot of CTs maximum principal stresses in MPa for AP1 and AP2 configurations | 131 |
| Figure 5.1: (A) experimental image of the HT11 valve after 60% FWA in AP direction adapted from Manini and Locatelli thesis [29]. | 138 |
| Figure A.1: graphic representation of the distance between the valve obtained at the end of the simulation and the reference valve $\Omega_{PS}^{tracing}$ | 149 |
| Figure A.2: the lateral and the atrial views of the valve are shown with their respective maximum principal stresses. | 150 |

| | |
|--|-----|
| Figure A.3: the lateral and the atrial views of the valve are shown with their respective maximum principal strains..... | 153 |
| Figure A.4: the lateral and the atrial views of the post-surgery valve are shown with their respective maximum principal stresses..... | 155 |
| Figure A.5: the lateral and the atrial views of the post-surgery valve are shown with their respective maximum principal strains..... | 158 |

List of Tables

| | |
|---|-----|
| Table 1.1: Geometric characteristics of the TV physiological annulus from a study conducted by Maffessanti et al. [14]. The table shows the geometric characteristics expressed as median value (1 st -3 rd quartile). Data are reported for healthy subjects only. | 15 |
| Table 1.2: Average thickness of TVAL, TVPL and TVSL in porcine valves | 18 |
| Table 1.3: length and thickness of CTs evaluated in the Silver et al. study on 50 human heart. Table adapted from Silver et al [13]. The data in the table show the mean \pm standard deviation. | 22 |
| Table 1.4: Main features of cardiac echocardiography | 30 |
| Table 3.1: Values of the 6 constitutive parameters identified for the CTs of the TV, reported in Amicone and Dazzi's thesis [30] and obtained by fictitious data from Lim[47]. Parameters a1 and a2 refer to the isotropic description of the Weiss model, while parameters a3, a4, a5 and a6 are the parameters calculated for the anisotropic component. | 82 |
| Table 4.1: The first column allows identification of the reference configuration; the second column shows the chordal insertion density and the third the number of CTs. | 103 |
| Table 4.2: Annulus and regurgitant area in the xy plane extracted from the reference configuration $\Omega_{PSFE, closure}$. The last column shows the percentage ratio between $A_{FTR, tracing}$ and the $A_{ANN, tracing}$ | 103 |
| Table 4.3: Results of the sensitivity analysis. The $A_{FTR, FE}$ in mm ² was extracted for each configuration. From this value, the percentage of the $A_{FTR, FE}$ was calculated with respect to the $A_{FTR, FE}$ and the error ($\%RA_{FRM, tracing} - \%RA_{FRM, FE}$) in brackets. | 104 |
| Table 4.4: Results of sensitivity analysis against Euclidean distance values calculated point-to-point along the entire leaflet surface. | 105 |
| Table 4.5: Results of sensitivity analysis: computational time for each simulation of the calibration workflow of the TV CTs. Time values are given in hours. | 106 |
| Table 4.6: max principal stress values measured on the leaflets for each configuration. The values were reported as median (25 th percentile \div 75 th percentile). | 108 |
| Table 4.7: CTs maximum principal stress for each configuration in MPa. The values were reported as median (25 th percentile \div 75 th percentile). | 110 |

| | |
|---|-----|
| Table 4.8: RF along the annulus for each configuration. The values were reported as median (25 th percentile ÷ 75 th percentile)..... | 111 |
| Table 4.9: Leaflets maximum principal strains divided in radial (NE11) and circumferential (NE22) component for each configuration. The values were reported as median (25 th percentile ÷ 75 th percentile)..... | 113 |
| Table 4.10: for each configuration was evaluated the regurgitation area of $\Omega PSFE, closure$, moreover the percentage of the regurgitation area extracted of $\Omega PSFE, closure$ was calculated with respect to the annular area of $\Omega PStracing$ ($\%RA_{FRM, tracing} - \%RA_{FRM, FE}$). | 116 |
| Table 4.11: Euclidean distance values calculated point-to-point along the entire leaflet surface. Values are reported as median (25 th percentile ÷ 75 th percentile). | 117 |
| Table 4.12: displacement of PMs in z direction from the TV with TR to the TV post-surgery | 122 |
| Table 4.13: Leaflets maximum principal stresses in MPa and leaflets maximum principal strains divided in radial (NE11) and circumferential (NE22) component for each configuration. The values were reported as median (25 th percentile ÷ 75 th percentile). | 125 |
| Table 4.14: CTs maximum principal stresses in MPa for each configuration. The values were reported as median (25 th percentile ÷ 75 th percentile)..... | 126 |
| Table 4.15: The effective area of regurgitation of the $\Omega PSFE, closure$ in mm ² was extracted for each configuration. From this value, the percentage of the regurgitated area of $\Omega PSFE, closure$ was calculated with respect to the annular area of $\Omega PStracing$ | 128 |
| Table 4.16: Leaflets maximum principal stresses in MPa and leaflets maximum principal strains divided in radial (NE11) and circumferential (NE22) component for each configuration. The values were reported as median (25 th percentile ÷ 75 th percentile). | 130 |
| Table 4.17: CTs maximum principal stresses in MPa for AP1 and AP2 configurations. The values were reported as median (25 th percentile ÷ 75 th percentile)..... | 131 |
| Table 4.18: The effective area of regurgitation of the $\Omega PSFE, closure$ in mm ² was extracted for AP1 and AP2 configurations. From this value, the percentage of the regurgitated area of $\Omega PSFE, closure$ was calculated with respect to the annular area of $\Omega PStracing$ | 131 |

List of symbols

| Variable | Description | SI unit |
|----------------------------|--|-----------------|
| D | | mm |
| $\Omega_{PS}^{tracing}$ | reconstructed surface resulting from the tracing of the echocardiographic images at SP | - |
| $A_{ANN,tracing}$ | reconstructed annulus resulting from the tracing of the echocardiographic images at SP | mm ² |
| $A_{FTR,tracing}$ | reconstructed FRM resulting from the tracing of the echocardiographic images at SP | mm ² |
| $\%RA_{FRM,tracing}$ | percentage of the regurgitation area with respect to respect the annular area surfaces extracted at the end of the systolic closure simulation | - |
| $\Omega_{PS}^{FE,closure}$ | | - |
| $A_{FTR,FE}$ | regurgitation area in the xy plane of the $\Omega_{PS}^{FE,closure}$ | mm ² |
| $\%RA_{FTR,FE}$ | percentage of the regurgitation area of the $\Omega_{PS}^{FE,closure}$ with respect to the annular area of the $\Omega_{PS}^{tracing}$ | - |
| NE11 | Leaflets radial maximum principal strains | - |
| NE22 | Leaflets circumferential maximum principal strains | - |
| u_i^{ANN} | Displacement of annulus points | mm |
| u_i^{PM} | Displacement of PMs points | mm |
| u_i^{FRM} | Displacement of FRM points | mm |

List of acronyms

| Group | Acronyms | Description |
|--|-----------------|------------------------------------|
| Anatomy and Physiopathology | TV | Tricuspid Valve |
| | MV | Mitral Valve |
| | PV | Pulmonary Valve |
| | AV | Aortic Valve |
| | TR | Functional Tricuspid Regurgitation |
| | MR | Functional Miral Regurgitation |
| | RA | Right Atrium |
| | RV | Right Ventricle |
| | TVAL | Tricuspid Valve Anterior Leaflet |
| | TVPL | Tricuspid Valve Posterior Leaflet |
| | TVSL | Tricuspid Valve Septal Leaflet |
| | CTs | Chordae Tendineae |
| | PM | Papillary Muscle |
| | APM | Anterior Papillary Muscle |
| | PPM | Posterior Papillary Muscle |
| | SPM | Septal Papillary Muscle |
| | | MRI |
| | TTE | Transthoracic Echocardiography |
| | TEE | Transesophageal Echocardiography |
| | RT3DE | 3D Real-Time Echocardiographic |
| | CT | Computed Tomography |
| | FE | Finite Element |
| | CFD | Computational Fluid Dynamics |
| | FSI | Fluid-structure interaction |
| | GUI | Graphical User Interface |
| | ROI | Region of Interest |
| | FWA | Free Wall Approximation |
| | PCA | Principal Components Analysis |
| | ED | End Diastole |
| | SP | Systolic Peak |
| | RF | Reaction Force |

Acknowledgments

Un sincero ringraziamento al professor Votta per avermi affidato il progetto di tesi, per la passione travolgente con cui affronta il suo lavoro, per la sua capacità di spiegare argomenti complessi in modo semplice, per l'occhio critico nella risoluzione dei problemi e per i suoi consigli indispensabili.

Ringrazio infinitamente anche Davide per la costante guida in questi mesi, per l'attenzione prestata a ogni singolo step del mio percorso, per la gentilezza e l'incredibile disponibilità nei miei confronti.

